Anthony Menicucci

*Candidate*

School of Engineering - Dept. of Mechanical Engineering, University of New Mexico

*Department*

This dissertation is approved, and it is acceptable in quality and form for publication:

*Approved by the Dissertation Committee:*

Professor Andrea Mammoli, Chairperson

Professor Peter Vorobieff

Professor Svetlana V. Poroseva

Professor Emeritus Thomas Caudell

Professor Manel Martinez-Ramon

# Solar Insolation Micro-Forecasts Using Longwave Infrared Sensors and Artificial Intelligence

By Anthony Menicucci

Degrees:
B.S., Applied Mathematics

DISSERTATION
Submitted in Partial Fulfillment of the
Requirements for the Degree of

Doctor of Philosophy
Engineering

The University of New Mexico
Albuquerque, New Mexico

December, 2020

# Dedications

*I would like to dedicate this PhD and my research to my parents, David and Barbara, for their love and encouragement. They are true inspirations in the ways of life and living.*

# Acknowledgements

I would like to start by acknowledging my favorite Professors. To Professor Mammoli, thank you for always teaching me to be optimistic no matter what the grim outlook feels like, currently. I would like to acknowledge and thank Professor Caudell of the Electrical and Computer Engineering department, as he has taught me everything I know about machine learning and artificial intelligence. To Professor Vorobieff and Professor Poroseva, I would like to acknowledge and thank them for their unceasing recognition and narrative of truthful situations, no matter how brutal the conclusions may be. Special thanks go out to Professor Manel who has helped me throughout this research.

Warm regards and thoughts are directed to the National Science Foundation, the NSF STTR program and the American taxpayer who have partially funded this research in the fielded trial stage of our experiment. Special thanks also go to New Mexico bond holders and taxpayers who help support UNM infrastructure.

Solar Insolation Micro-Forecasts Using Longwave Infrared Sensors and Artificial Intelligence

By

Anthony Menicucci

B.S., Applied Mathematics

Ph.D., Engineering

# Abstract

Solar Insolation Micro-Forecasts (SIMF) are used by Independent Service Operators (ISOs) and other grid operators to maintain constant and stable electrical grid frequency, voltage, power factor and waveform across their transmission infrastructure. Intermittent, thick, dense and typically cumulus clouds negatively impact the electrical grid by quickly turning on and off power production from large solar photovoltaic (PV) fields, causing grid stability problems between generation and load. Forecasting insolation values over large PV fields allows operators the chance to anticipate and proactively implement mitigation strategies like engaging spinning

reserve from gas turbines, deploying generators, buying power in the spot market, and or engaging grid tied battery/energy storage.

This research has built and fielded a deployable SIMF system. We utilized new sensors to alter the way clouds are imaged. We also employed a machine learning code (AI) called LAPART, that learns and generates five-minute accurate predictions of PV insolation values based on the specific spatial configuration of individual fields.

# Contents

# i. List of Figures

# ii. List of Tables

# iii. List of Graphs

# iv. List of Equations

# 1. Thesis Motivation and Background of the Engineering Task

Imagine a world where the generation of electricity production is split between two choices, power production with solar panels or power production with a large gas-turbine. Figure 1-1 highlights this scenario.

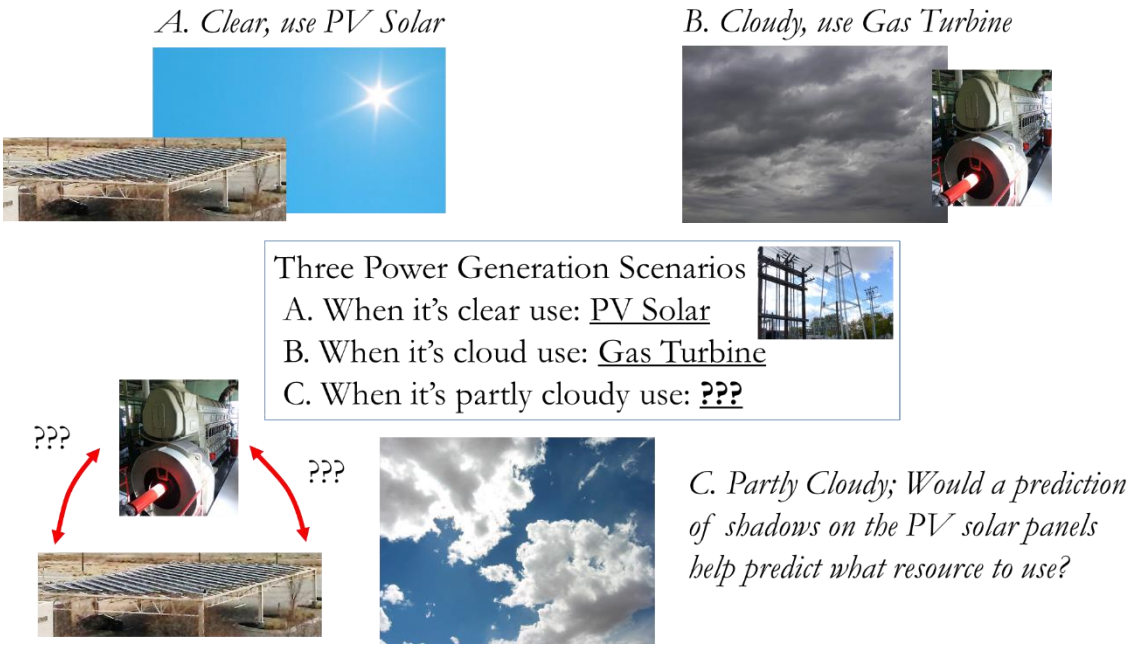


Figure 1-1. Dilemma highlighted between using an intermittent PV solar generation resource and reliable fossil fuel resources for power generation.

While trying to maximize the clean and free-fuel (after it's built) solar photovoltaics (PV) resource, the choice of generation on cloudy and sunny days is straight forward. On cloudy days utilize the gas turbine and on sunny days utilize the PV. But what does one do when the day is partly cloudy/sunny? In operation, a more complex energy generation situation occurs. Loads must meet with the correct amount of

electricity throughout the day as electricity use varies. Gas turbines and energy storage is employed to match these specific energy fluctuations. Frequency, voltage and reactive power must be kept in correct specification or the utility will become liable for damages to the consumer. In all scenarios the question is highlighted: 'Would it be helpful to have a prediction of when partially cloudy PV solar turns on or off, so the power company can tun on or off their gas turbines?' The thesis and motivation for solar irradiance microforecasts (SIMF) is an exploration of the benefits of answering "yes" to the previous question.

Though the previous scenario presented a binary situation for power production, real life decisions about power generation resources are very similar when considering solar PV. In practical use, gas turbines only need to ramp up or down power production and not turn completely on or off. Though consumer [1] and regulatory pressures continue to make photovoltaic solar an increasingly attractive option for power generation companies to meet their renewable energy portfolio standards, [2] this increase in PV generation is not without problems and cost. Because most current and new PV system installations produce intermittent power when clouds are present, it is increasingly harder to stabilize power on the grid during intermittently cloudy days. This is because most PV sites do not incorporate costly grid-connected energy storage solutions.

The intermittencies of power production are ranked among the most important challenges facing an aging electrical grid. The Edison Electric Institute, a large

corporate representative of U.S. investor-owned electric companies notes; "*Recent technological and economic changes are expected to challenge and transform the electric utility industry. These changes (or "disruptive challenges") arise due to a convergence of factors, including: falling costs of distributed generation and other Distributed Energy Resources (DER).*" [3] In combination with an ageing infrastructure [4] and a shortage of trained engineers in the power field, [5] cloud occlusion problems which cause PV power intermittencies, will continue to be a major source of technical problem for grid operators.

## 1.1. General Power Transmission and Distribution Requirements

Small scale PV farms, on the order of 0.5 to 2 MW are scalable, moderately cost-effective and easy to install. [6] However, these small-scale PV installations pose the greatest challenge in mitigating power intermittencies. This is due to their relative compact size and centralized location. [6] Currently, grid-scale power intermittencies from PV farms are manageable without SIMF because there is a low percentage of solar PV as a total of all generation sources. [7] However, geographic locations like Hawaii where solar is a large part of the total energy consumption, would greatly benefit from PV SIMF as a means to smooth power input and out to the grid [8], [9].

Wind energy also suffers from the same intermittency problem. However, strategies for mitigating intermittent power transmission from wind include the ability to attenuate output of the wind mill via altering the blade angle [10], [11] as is shown in Figure 1-2. To accomplish this in synch with the electrical grid, wind energy also has

a variety of forecasting abilities ranging form numerical weather predictions [12] to utilizing LIDAR [13] for forecasting future wind intensity.

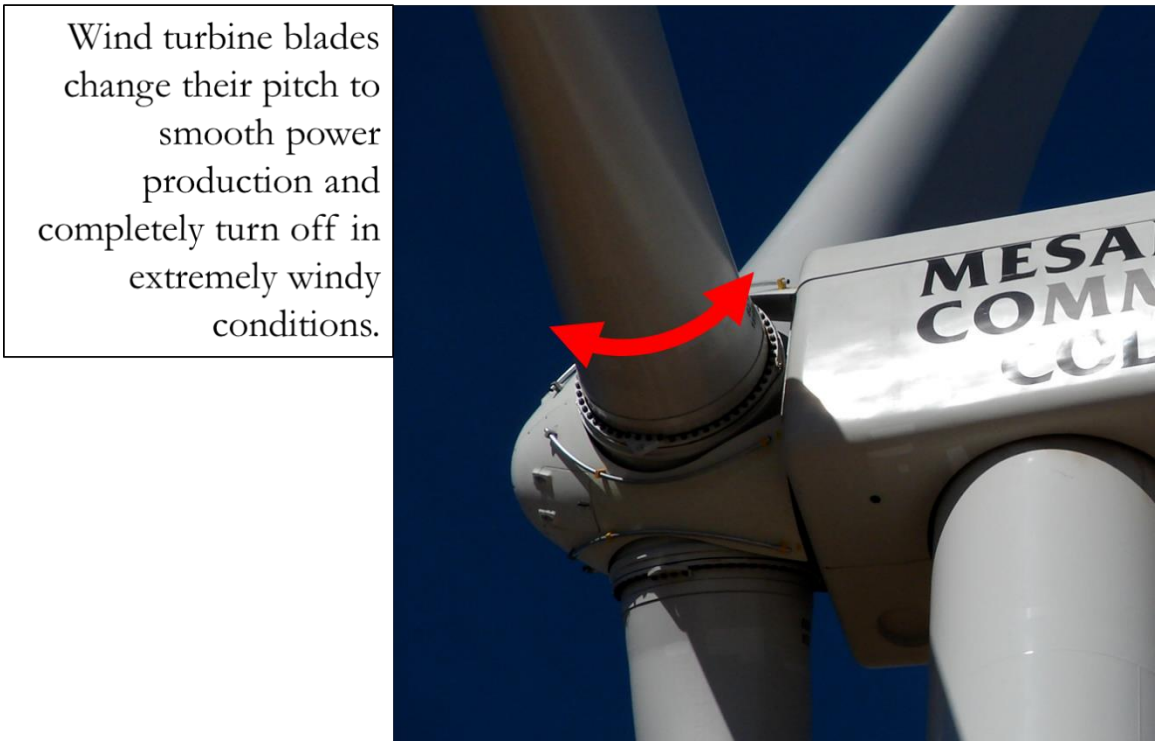


Figure 1-2. Wind blade attenuation process [14].

Wind energy can provide a quasi-energy storage function [15], [16] by forecasting day ahead minimum wind output and then change the blade angle on the day of generation, to match the minimum wind forecasted the day before. [17], [18], [19] Wind energy can be considered a reliable and stable power source with this blade smoothing process. If there is too much wind blowing at any given hour, the blade pitch will be altered, and electricity production lowered. In all cases, the minimum forecast power output must be met because market incentive exists to punish the wind farm for not supplying the minimum contracted day-ahead electricity.

There is an opportunity cost from the underutilization of the wind resources. From a market standpoint, it is more economically feasible to attenuate the wind generation resource and waste the opportunity to produce excess power then it is to produce an intermittent resource. [20]

Whether the intermittent resource is wind or solar, power fluctuations are nothing new to the industry. The constant mismatch between a varying consumer load and power supplied from the grid, ensures that daily energy production will not remain constant. Figure 1-3 shows the electricity demand in gigawatts for New England over the course of one day on 10/22/2010.

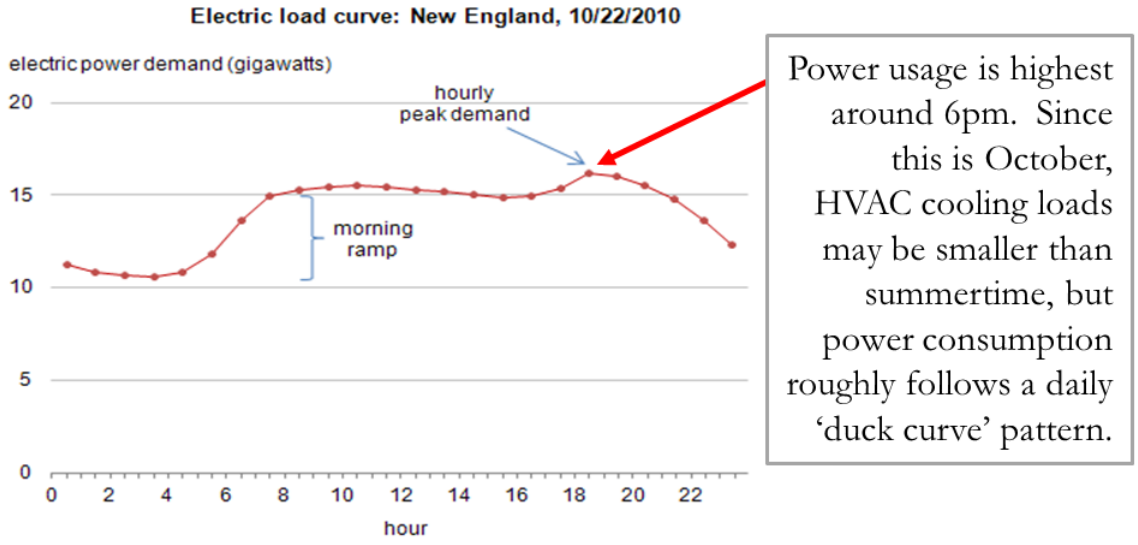


Figure 1-3. Electricity Demand for New England versus time of day [21].

This fluctuation in demand must be matched by an appropriate fluctuation of supply (up or down) to ensure that voltage, frequency and power factor remain within specification. Throughout the day, electricity must be generated by peaking power plants. Typically, "peakers" are natural gas turbines, which turn on and off or vary

output to meet any shortages/overages in electricity. [22], [23] "Peaking" power plants are specific to a fast acting temporal range and are different from coal or nuclear power plants that can take from one day to months to turn on and off. [24] A cross section of a fast acting gas turbine peaker is shown in Figure 1-1. A generic stacked version of the daily load curve [25] highlights when peaking generation occurs and is shown in Figure 1-4.

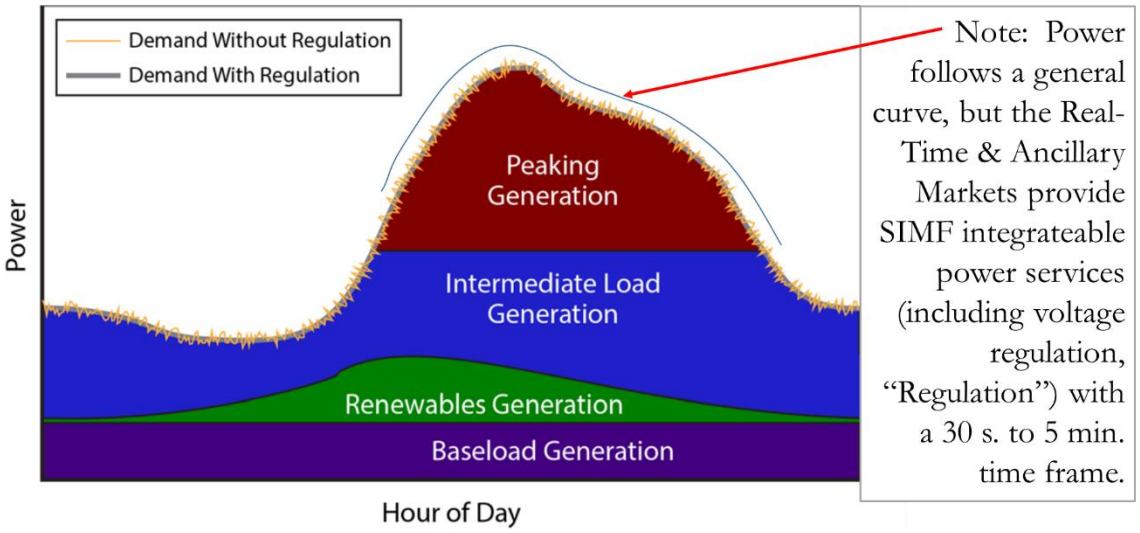


Figure 1-4. Stacked Load curve for power consumption throughout the day [25].

Sometimes peaking plants operate for only a few minutes per day based on the electrical need of an area.

Peakers can also assist in demand regulation up or down when the turbines are operating as "spinning reserve". Spinning reserve is a process where the gas turbine peaker is spinning at a minimum power. In spinning reserve turbines can act very fast (one minute) to power fluctuations and assist in grid stability operations referred to in Figure 1-4 as "Regulation". These power instabilities are sometimes caused by

intermittent cloud occlusion of PV farms, but they can also be caused by a variety of other sources like a factory or warehouse starting or stopping daily operations, among others.

The allocation of generation resources is referred to as "unit commitment". Unit commitment allocation with the integration of SIMF has been shown to greatly reduce the wear and tear on peaking equipment in the field, as well as grid scale battery storage systems [26], [6], [27].

To better illustrate a unit commitment scenario, observe the many different generation resources realized for a simulated grid operation scenario during Phase 2 of the Western Wind and Solar Integration Study (WWSIS-2) [28].

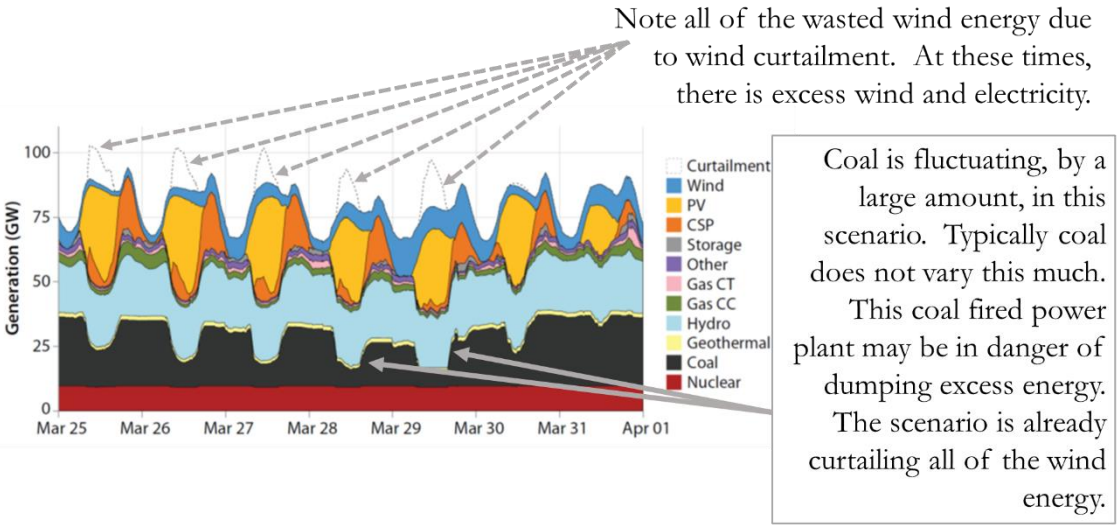


Figure 1-5. Five-minute dispatch stacks. High Solar Scenarios for a week in March in the Western Wind and Solar Integration Study (WWSIS-2) [28].

Note that in this scenario coal generation fluctuates in its electricity output, but it never turned off completely. [29], [30] However, nuclear cannot and does not change

its output at all. If too much electricity is on the grid, the power company could dump power, but such a curtailment scenario would be a last resort grid stabilization method. Unlike wind curtailment, if the coal fired power plants do not ramp up or down their electricity output fast enough, the power company may end up wasting electricity. This would be done by dumping power into energy sinks until the grid can accept the full coal unit-allocation at the grid-stable energy requirement. In this scenario, gas generation is the fastest response to power fluctuations both up and down, but the resource is limited to the number of installed units.

Because coal and nuclear do not respond very fast to fluctuations in output generation, they are considered base-load generators and only rarely fluctuate in power production. Dumping power is also a rare phenomenon as gas peakers are most likely to be curtailed first. Before wasting electricity, the spot market prices is likely to reduce and/or go negative to prevent such extreme scenarios. In the case of wind turbines, the underlying lost resource is free wind that blows over the earth. In the case of coal or nuclear, the lost resource is non-renewable. Coal and nuclear are also the most likely to be integrated with pumped hydropower storage as shown in Figure 2-8. However, coal and nuclear energy is too slow to integrate with SIMF. Instead, fast acting resources like energy storage and gas spinning reserve are better suited for SIMF.

Peaker plants are not exclusively natural gas powered but natural gas does provide a fast and cheap form of on-demand electricity. Unlike all other resources, natural gas

peaker plants can turn completely on and off multiple time throughout the day. This unit commitment scenario in Figure 1-5 illustrates the complexity of the number of generation resources that can be called upon to respond to power fluctuations on the grid. Natural gas turbines, diesel generators and grid tied battery storage are all power resources that integrate well with SIMF, as stated above.

Lastly, one should note a whole array of other so-called energy storage devices like vacuum sealed flywheels and compressed air energy storage. Though these novel ideas may have been hypothetically tested, companies in the past trying to implement such technologies have gone bankrupt. One notable example is Beacon Power's bankruptcy in 2011. [31] Beacon Power was a company that tried to make a flywheel energy storage solution. The scope of this dissertation and analysis is limited to installed and proven, legacy technology. It does not include analyzing hypothetical and unproven technologies.

## 1.2. Fast Acting Power Fluctuations

Power fluctuation events range from seconds to hours. Solar Irradiance Microforecasts (SIMF) operate to mitigate fast acting power fluctuations on the order of 1 to 10 minutes. On longer time frames, satellite imagery and weather forecasts are preferred methods for power generation predictions of PV farms. Ground based methods are investigated in this research as a means to increase the accuracy of SIMF predictions.

Though power fluctuations are not new to the industry, the rate at which electricity can fluctuate is new and presents a growing problem. These instabilities will only increase with further installations of intermittent resources [32]. To better illustrate these temporally fast acting power variations, one needs only to look at the output from a solar field on a cloudy day. Shown in the figure below, is the irradiance profile for November 26th, 2011 for the Mechanical Engineering building at the University of New Mexico in Albuquerque. This irradiance would be directly proportional to the amount of power produced by a PV field on its roof.

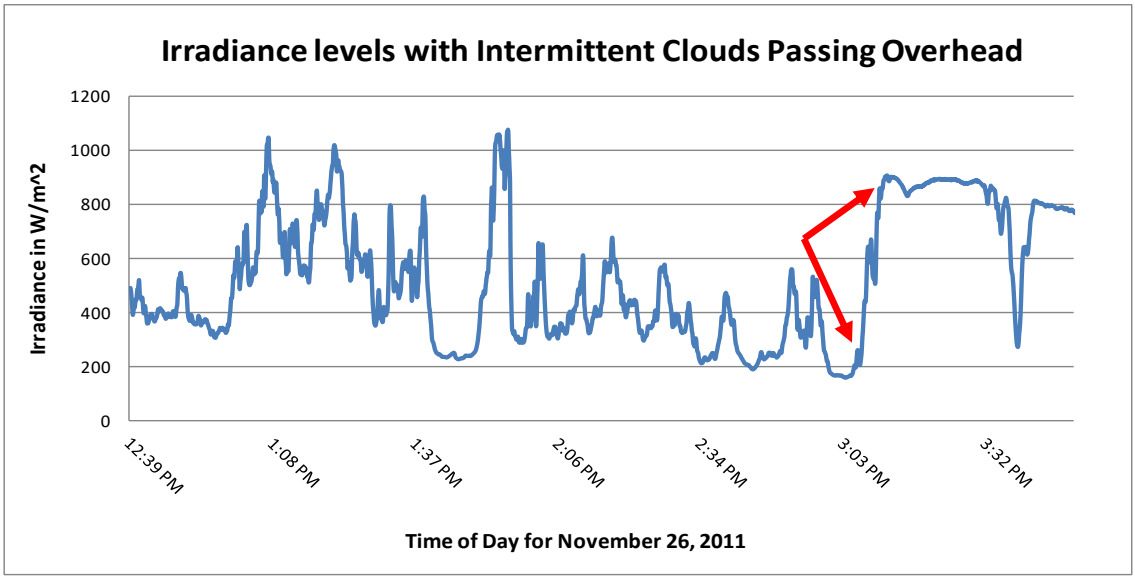


Figure 1-6. Irradiance levels with Intermittent Clouds Passing Overhead from the University of New Mexico in Albuquerque.

A close observation of time stamps 3:05pm to 3:08pm indicates that the irradiance level went from approximately 200 W/m² to around to 900 W/m². This fluctuation would equate to a solar farm producing 20%, and then ramping up to about 90% of full capacity in two minutes. The time that the ramp in electricity takes to affect the power grid is proportional to the size of the array and the velocity of the clouds. For

example, a small field can turn on and off quickly because the cloud occludes the field very fast. In larger fields with clouds moving at the same velocity, it would take longer for the field to completely turn off due to the large geographical region that it occupies. If power quality in the form of voltage, frequency and/or reactive power reaching the customer is outside of the bounds of the regulatory requirements, the power company will be held liable for damages independent of the source of the poor-quality power. This motivates a power quality correction on the part of the power supplier to help mitigate PV cloud occlusion events, among other phenomena that cause bad power quality. With SIMF, this correction can be obtained in a more cost-effective manner as this general principle applies; 'When bad things will happen, it is always better to know what's coming as opposed to dealing with it once it gets here.' An example of this principle is the reduction of battery wear and tear that occurs on battery storage with the pairing of SIMF and PV [6].

## 1.3. Legal Implications of Poor Power Quality

Even when the load is being met with enough supply, long transmission distances and other effects can lead to out of specification power quality. In general, these issues fall into one of three categories, voltage issues, frequency issues and power factor issues. These problems must be corrected before power can be delivered to the customer.

There are no nationwide standards for power quality limits, but there are agencies that write proposed standards for which different regulators have adopted for use. It

should be noted, most power quality standards are applied by state and or regional regulators. The most widely adopted standard is NEMA-C84.1 (National Electrical Manufactures Association) [33]. The figure below shows the standard limits set for normal, suboptimal and unacceptable power quality delivered as 110-120VAC service.

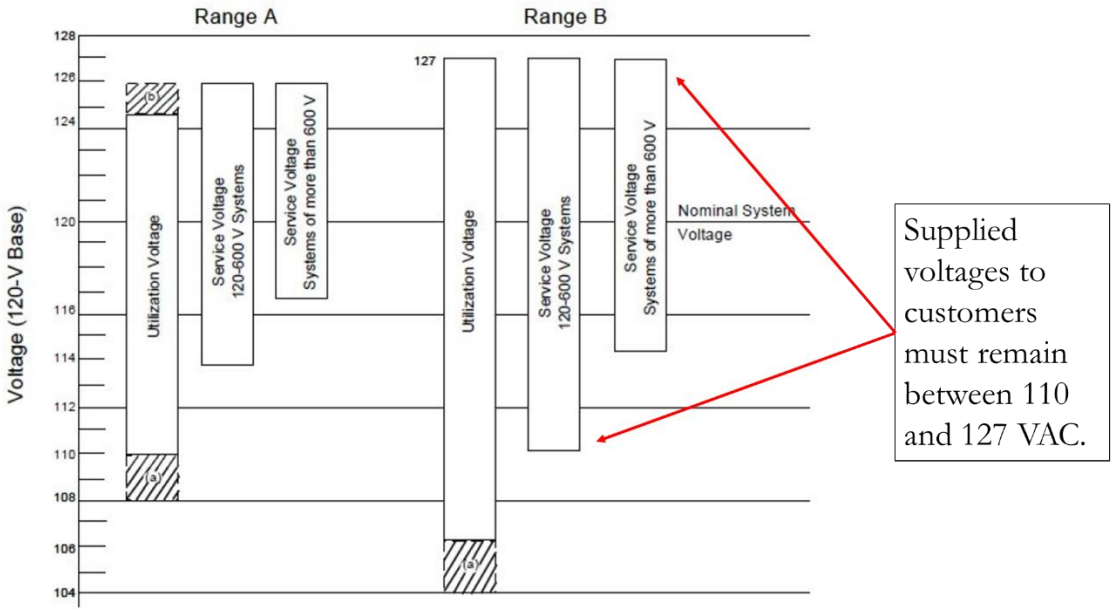


Figure 1-7. NEMA-ANSI C84.1 Voltage Ranges. Acceptable ranges of voltage for power supply to customers are shown within the bounds of the white box [34].

NEMA-C84.1 specifies limits on the upper and lower customer supplied voltages and frequencies among other power requirements. This standard is adopted by many regulatory agencies and is enforced through a variety of coercive means in the form of fines. In rare cases like the Enron scandal that became public in 2001, jail sentences for executives can also occur for nefarious actors that purposefully cause power production issues. Active power management is required by the customers who demand a constant voltage and frequency. This is important because incorrect voltages, frequencies and power factors may damage ratepayer electrically powered

products. Correct specification voltages, frequencies and power factors are also mandated by law. Because of legacy power production technology, laws do not make provisions for the source of the distortion [35]. From the law's standpoint, power companies are the only liable entity for power instabilities, even if the instability originates from an independent source, including other customers.

Since power companies are regulated to provide in-specification power, they have a vested interest to mitigate these problems as fast as possible. With the introduction of more solar without energy storage, mitigating complex power problems will require a more proactive approach rather than the current reactive mitigation strategies. SIMF can help to mitigate PV intermittencies so power companies can meet their power delivery requirements in specification and without negative legal consequences.

## 1.4. Legal Implications of Poor Quality Infrastructure

If power quality cannot be meet, or the power cannot be deliverd reliably, sometimes the power company may blackout an area. This blackout operation is occuring in record numbers by California's veriacaly intergrated power company Pacific Gas and Electric (PG&E). The Wall Stree Journal, utilzing the Freedom of Infortmation Act has revealed that PG&E revealed that at least 49 steel utility towers and their aluminum transmission lines needed immediate upgrade or replacement [36]. In 2018 a transmission line, now known as the Caribou-Palermo line, sparked a campfire in northern California that eventually killed 85 people. This was one of nearly 1,500

fires that have occurred between 2014 and 2018 [37] and was a direct result of poor maintenance. Consequently, PG&E is in litigation as a result of its failures to execute proper fiduciary obligations to its customers.

The fires that occurred are almost exclusivly due to "wind damage" [38]. This happens when the wind blows power lines into vegitation and creates fires. The solution that PG&E has implemented is widespread preemptive blackouts in northern California when windy conditions occur [39]. This provides its own problems when the power is turned back on, because every mile of transmission and distribution line must first be inspected for safety, including wildfire potential.

With an aging infrastructure, especially in California, reliable power will become more essential. As more intermittent solar power is being introduced to the power grid, especially in California, it will be crucial to have SIMF technology integrated with PV and energy storage devices.

## 1.5. Financial Markets in Power Purchase and Power Quality

Legal implications may provide a means for monetary compensation of the consumer from damages due to out-of-specification power quality. Monetary incentives exist through power-purchase markets to maintain in-specification power quality also. Before one can elaborate on the implications of financial purchase of power on the wholesale market, a summary of power markets is necessary.

Power markets are broken into three entities that generate, transmit and then deliver through distributed transmission, power within the acceptable power quality limits. These three entities are referred to as Generation, Transmission and Distribution. When one entity owns two or three of the three parts, the utility is considered vertically integrated and are typically regulated more like a monopoly than an independent resource. With each entity, temporally based markets have formed and manifest themselves in three markets called Prime Power contracts, Day-Ahead Markets and Real-Time Spot Markets. All power company entities engage in both selling and buying of power in both the Day-Ahead and Spot market also known as the Real-Time market. As the name implies, the Day-Ahead markets are for the purchase and sale of electricity to be consumed in the next day for a certain period. This day-ahead transaction enables all entities involved to transact power contracts at a discounted rate. This discounted rate is due to advanced planning of supply and demand which increases efficiency of the power grid. The Spot-market is for purchase of electricity that will be consumed very shortly (from a few minutes to immediate delivery) after purchase. Because of the need for immediate power, Spot-market prices are typically higher for consumers. Spot market power delivery is harder to deliver for producers and requires greater dispatch reliability.

With this problem in mind, a new system of settlement was designed to preserve real time incentives, by maximizing planning. In short, if the exact amount of power required day ahead (DA) is purchased in the DA market, no additional money

transacts. However, if less or more electricity is bought or consumed, respectively, then the supplier must pay the higher real-time spot-market price.

Take for example a supplier (generation) that sells $Q_1$ amount of power in the Day-Ahead market at price $P_1$. If the amount of power delivered is $Q_1$ on the contracted day ahead, then nothing about the transaction changes. However, an example from Power Economics [40] highlights what happens if the contract is not settled, either partially or in whole.

If none of the contracted power is delivered the contract is void and legal mechanisms exist to deal with that scenario. However, what if only a partial deliver of power was completed? In this scenario of a partial fulfillment of the day ahead power, the contract is treated as if the power purchased is split between what was delivered and what was contracted and billed in two different installments with a two-settlement system.

For example, a contract exists to deliver a quantity of $Q_1$ power at price $P_1$, both in the day -ahead (DA) market. The if the supplier fails to deliver some power at the time and day, they said they would. Consequently, the supplier needs to be punished monetarily, but still paid $P_1$ for $Q_1$ delivered. The difference in power delivered from what was contracted is $Q_0$. The current real time price is defined as $P_0$. The supplier will then be paid a two-settlement payment highlighted in (1-1).

$$Supplier\ is\ paid: Q_1 * P_1 + (Q_0 - Q_1) * P_0 \tag{1-1}$$

Rearranging the terms reveals the supplier is shown to be paid:

$$Supplier\ is\ paid: Q_1 * (P_1 - P_0) + Q_0 * P_0 \tag{1-2}$$

(1-2) reveals the price discrepancy of $P_1 - P_0$ at the day ahead delivery quantity. Because the DA price is almost always cheaper than the spot-market price, the incentive structure reveals the optimum operation of any grid requires optimum load forecasting.

For DA markets trying to mitigate problems with PV intermittencies, a weather forecast of cloud cover for the day ahead is most useful [41]. Historical load curves by day of year also help predict day-ahead power usage [42]. These forecasts always have too much error to be useful to mitigate PV cloud occlusion induced instabilities. Cloud occlusion intermittencies are mitigated in the spot-market. Cloudy day PV power production can be mitigated in the DA market at the hourly level, with a forecast of the percentage of sky cloud cover vs hour.

## 1.6. New Market Potentials for Solar Microforecasts

The commercial price of electricity is bought and sold in two different markets, the Spot and Day-Ahead market. Where residential customers are more likely to pay a set price for electricity based on net metering or the total amount of electricity used over the day, commercial customers usually have price incentives that vary based on the time of day and/or daily maximum usage for the month. To illustrate this,

observe that the commercial price of electricity for the New York Independent System Operator shown in Figure 1-8, varies throughout the day.

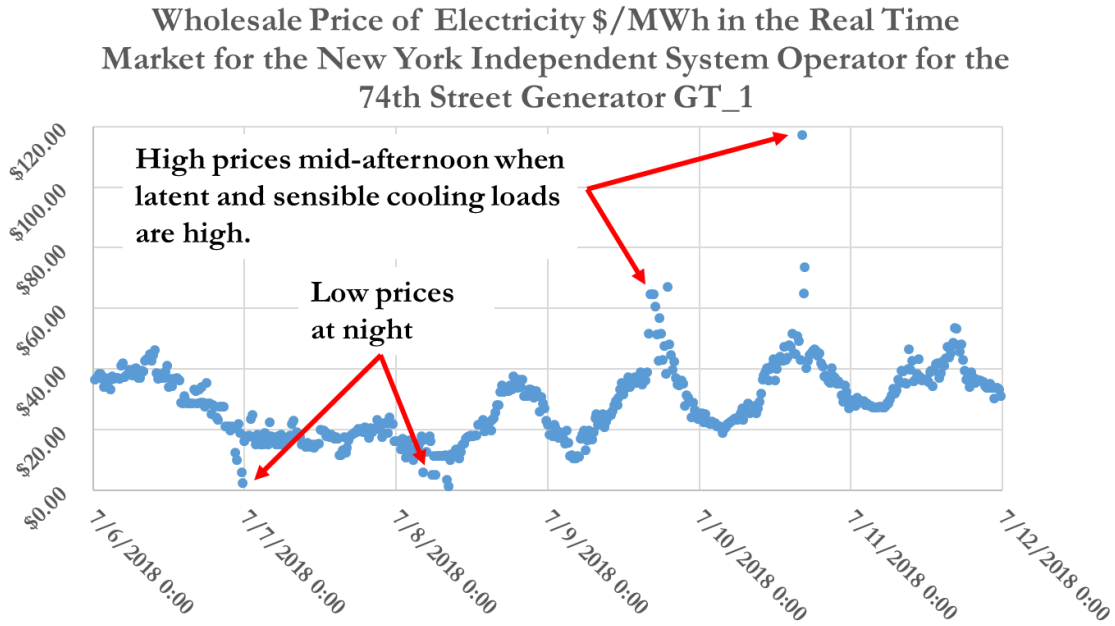


Figure 1-8. Price fluctuation illustration for the Real Time market, for one gas generator in N.Y.C., located in downtown Manhattan on 74th street [43].

Since there is small demand at night, the need for additional electricity generation resources is nearly zero, as is reflected in the price. Figure 1-8 illustrates the price for one generator for spot market operations in New York.

Bloomberg reported that the Eastern Reliability Council of Texas (ERCOT) had declared a Level 1 emergency on 8/13/2019 at 13:25 ET. A Level 1 trigger is called when operating reserves fall below 2,300 MW and they are not expected to recover within 30 minutes. When this level is reached, it allows the grid operators to purchase any and all available power supplies, including power from other grids. Since ERCOT operates on its own independent 60 cycle phase, power purchases

from another grid are technologically complex and expensive. Note in Figure 1-9, that the spot price shows about 6,850 $/MWh, but the intra-period bid topped 9,000 $/MWh [44].

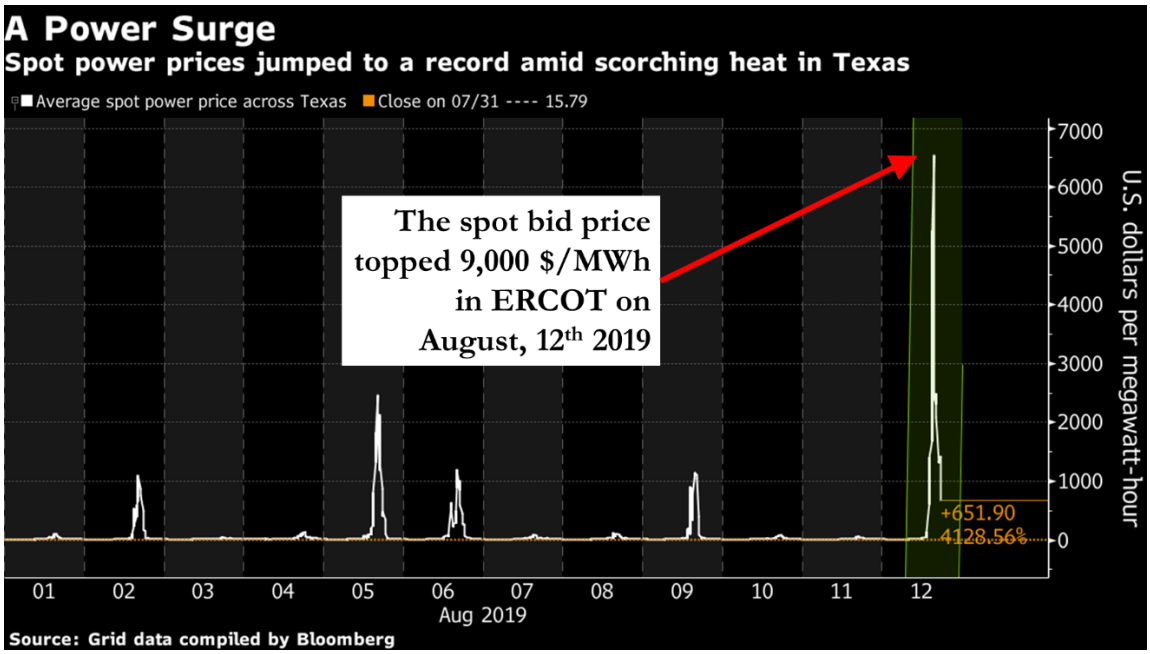


Figure 1-9, ERCOT spot market real power price as reproduced from Bloomberg on August 12th, 2019 [44].

SIMF can help with these price fluctuations by providing independent service operators with a forecast of short-term generation potential. With SIMF, PV farms once considered an intermittent resource, can now be considered for use with firm power commitments in the Spot market as supply. In combination with future knowledge of a PV farms that are about to go offline from SIMF, grid operators can proactively adjust their spot market price to match their ability to fulfill the contract.

### 1.6.1. Ancillary Services Market Potentials

Ancillary services to the power grid include but are not limited to voltage control and power regulation [21], [45]. Regulation and voltage control is the injection of mostly real (in Watts plus a power Factor) and some purely reactive power (in volt-ampere reactive) respectively, onto or off of the grid. Spot-markets exist for both reactive and real power, though many of the transactions are automated and must comply with Control Performance Standards specified by the North American Electricity Reliability Council (NERC). These integrated systems must react by both absorbing or injecting the specified contracted power at the contracted price, within seconds.

To illustrate the need for reactive power, an example of such demand is illustrated in Figure 1-10 to be meet via a grid connected battery and modern power electronics.

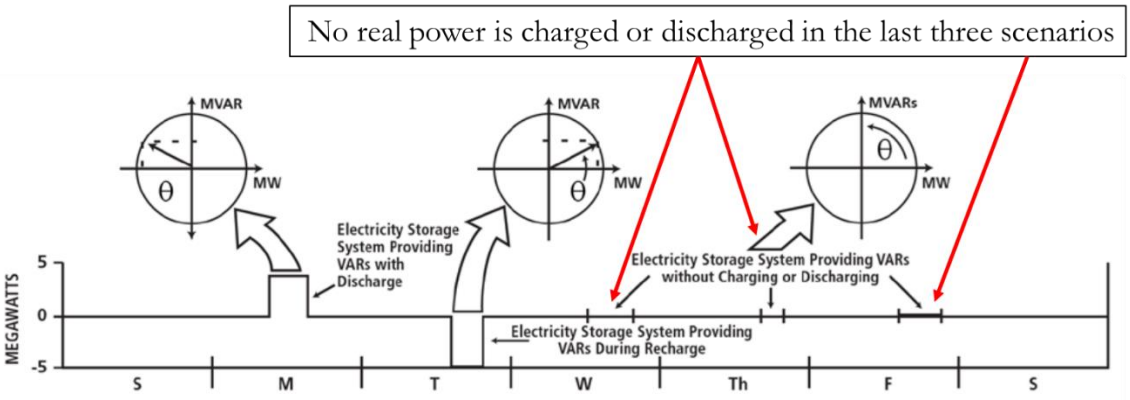


Figure 1-10. Voltage Support services example throughout the week as reproduced from EPRI [25]. Note that the battery/power electronics combination provides reactive power while both charging and discharging.

In this scenario, a grid connected battery is supplying reactive and real power mid Monday. On Tuesday it is charging on real while simultaneously supplying reactive power to the grid. The economic value of reactive power support has been

quantified. In addition, frequency and power factor are among other variables that modern PV inverters can also supply [46]. The California independent service operator (CAISO) has highlighted multiple fields with these new inverters. During excess energy production times and utilizing flexible inverters, they will often curtail real power from PV farms by as much as 60% of normal and instead utilize their inverters for frequency support [47].

Until recently, regulatory laws dictated that power electronics can only support adding real power to the grid, despite power electronics being able to provide other support. Two key takeaways remain that provide SIMF as an enabling technology for the utilization of PV fields for ancillary power services.

1. The modern-day power electronics that provide reactive power when connected to a grid sized battery, are that same technology as those that are utilized when connected to a PV farm. Thus, utilization of PV inverters for reactive power support would only be limited by the reliability of the PV farm's output and not the technology. The technology exists for PV inverters to provide ancillary power services, but legacy regulatory laws prevent it.
2. SIMF would increase the reliability of many PV installation thus enabling their use for ancillary services in the power market.

### 1.6.2. Regulatory Problems Preventing the Full Utilization of PV During Outages

The technology exists to provide voltage support at a PCC (Point of Common Coupling) but interconnection standards of distributed resources that the power companies must abide by often prevent such full utilization [48]. One such standard is the IEEE Std 1547-2003. It is the standard for interconnecting inverters with electric power systems. Whereas ANSI C84.1 governs customer supplied voltage limits, IEEE Std 1547-2003 governs the acceptable behavior of inverters with the rest of the power grid.

One such limiting regulation is found in section 8.1.1 Voltage Regulation. "*The DR [(Distributed Resource)] shall not actively regulate the voltage at the PCC. The DR shall not cause the Area EPS service voltage at other Local EPSs to go outside the requirements of ANSI C84.1-1995, Range A.*" [49], [50] As a result, inverter companies cannot and do not produce inverters for PV panels that could provide reactive power. A separate discussion of islanding and an explanation of the logic of IEEE Std 1547-2003 is highlighted below.

As intermittent generation sources like PV become more popular, the ancillary services market will become increasingly more important, thus raising the prices of such services. With the price of intermittent generation resources progressing lower, these services may be a way for PV installations to further stabilize the grid and increase their profits.

Often, whether it is intentional or not, the impression of a PV system is to offer independence form the power company and the implication is that the system functions, specifically when the grid fails. New standards have prevented such an emergency utilization, often to the detriment of the customer. In operation, due to mis-matched regulation, power outages affect grid connected PV homes in the same way as non-PV homes. The rational for this regulation was so that PV panels do not energize a circuit and electrocute and electrician when the power was disconnected from the grid. Where a market could exist for SIMF at the residential level, regulatory inflexibility is one hurdle that must first be overcome. SIMF could integrate well at the residential level utilizing the new inverter technology already deployed in the wholesale market but the residential regulations would have to change first.

In what is one of the more ironic situations pertaining to the mismatch between perceived use of solar PV panels, functional use in the field and regulatory hurdles affecting consumer sentiment, is the article by Bloomberg Energy highlighted in Figure 1-11 below. [51] It was published at the time of this writing, and it highlights regulatory problems Californian PV rooftop owners are currently facing in the light of rolling blackouts.


Figure 1-11. Bloomberg Energy article highlighting the need for batteries for solar PV to work in a power outage [51].

Bloomberg [51] explicitly states that batteries are required when the power grid is non-operational for a home or business to maintain internal power. What they convey though, is a sense of disappointment that a resource designed to make free and clean power, cannot functionally make any power, unless connected to an unstable power grid.

This is another example regulatory inflexibility that is preventing a market for SIMF technology. In the case of a residential house with PV and battery storage that is disconnected from the power grid, SIMF would increase battery life by reducing the rate of charging and discharging associated with intermittent overhead clouds. A few takeaways are highlighted below.

1. By California mandating PV installations on all new residential construction, this causes more grid instabilities.
2. In order to help with these instabilities, California should have employed one of two mitigation strategies.
    a. Mandate PV connected residential storage, where the storage can react in real time to the power fluctuations caused by intermittent clouds. In combination with a grid disconnect, this scenario could provide backup power during a blackout.
    b. Incentivize PV connected storage by making the renewable energy rebate a real time rate proportional to the spot market and inversely proportional to the power put back onto the grid. If this were the case, the renewable rebates would incentivize smoothing from the storage battery by offering greater rates from reduced power fluctuations.

In all scenarios above, the common theme exists that greater power fluctuations are contributors to grid instabilities. By mandating residential solar without an energy storage mechanism, California is making their electric grid more unstable. If energy storage was incentivized or mandated, a new larger market would exist for SIMF technology, to both stabilize the grid and increase the life of the storage units. If residential customers wanted to install enough storage, they would also have the added benefit of backup power during power outages. They would also be able to participate in arbitrage opportunities when real time prices are high enough.

# 2. Microgrids, Smart Grids and a Changing Power Infrastructure Model; Current State of the Art

In recent years a new phenomenon of non-centralized power generation has emerged [52], [53], [54], [55]. While until recently a single centralized power generation station used to supply all power to a region, recent advances in PV technology as well as smaller industrial diesel and gas generators have given rise to the concept of a Microgrid with attached Distributed Generation (DG). [56] Figure 2-1 highlights this concept of a separate area on the grid that has both loads and supplies of electricity connected with a point of common coupling (PCC).

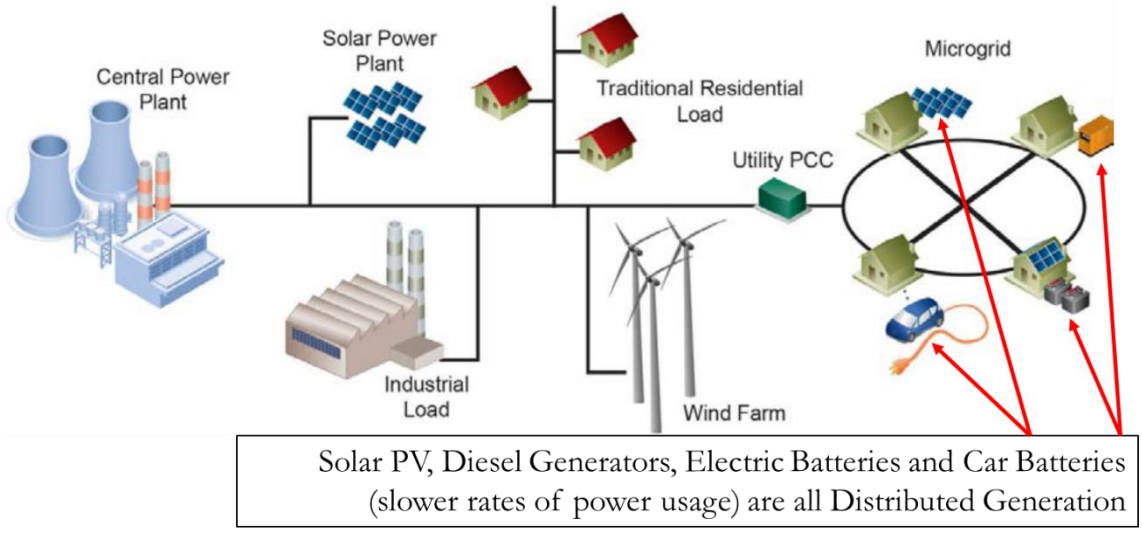


Figure 2-1. Microgrid figure from EPRI [53] highlighting multiple Distributed Generation Sources.

The region is collectively known as a microgrid region and the generation resources are called distributed because they are not a central power plant. A discussion of this

new concept of power infrastructure and the problems and advantages associated with it follows.

## 2.1. Current Electrical Infrastructure

Imagine a world in which all roads were designed to accept the maximum amount of traffic possible all the time. This is equivalent to the current electrical Infrastructure. The size of the wire needed to transmit electricity is directly proportional to the amount of maximum electricity needed at any given time [57], [58]. However, now imagine that cars can simply be generated at their destination. The number of highway roads needed would be far less. In this example, the expensive roads are like the expensive transmission lines.

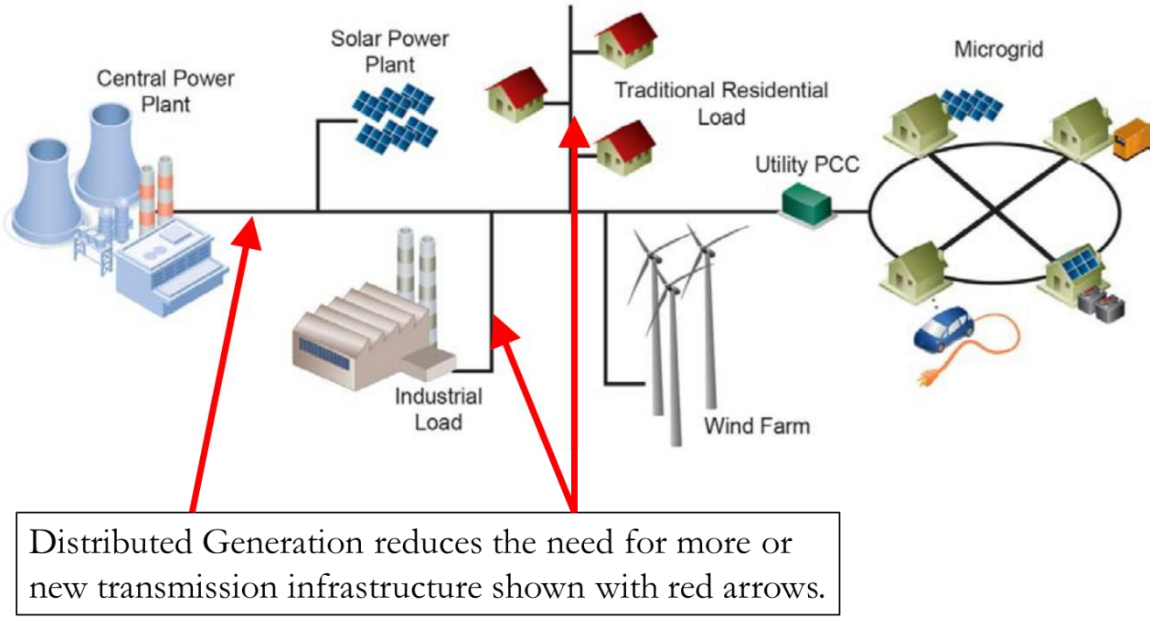


Figure 2-2. Electrical infrastructure diagram from EPRI [53] highlighting the pieces of the power delivery system.

With the assistance of Distributed Generation, the power does not have be transmitted long distances. As is shown in Figure 2-2, cost savings are realized

through decreased infrastructure need, mainly transmission and step up/down transformers.

One of the advantages of having an electrical grid is utilizing the grid to providing a battery like function for the customer. The grid can act as both a source and sink of electricity. Obviously, the electricity grid is not infinite, but is can absorb and discharge in a battery like function. This is advantageous for intermittent resources like PV. However, as the percentage of electricity generation from PV increases, which is the case for most microgrids, SIMFs will be increasingly important in stabilizing microgrids and the larger grid in general.

To better illustrate this point, PV generation on the entire grid is approximately 1.7% of total generation [59]. If 1.7% of the electricity were to disappear on the grid, voltages would drop by an average of 1.7%. If grid voltages are in the middle of the NEMA-ANSI C84.1 voltage range, then the new reduced voltage would still be in specification and in general, no mitigation strategy would be required. This extremely small percentage of PV production relative to grid size is not usually realized in a microgrid scenario. As microgrids increase around the country, SIMF will play a larger part in ensuring loads are balanced with supply and battery storage wear and tear is minimized.

## 2.2. Electrical Islanding and the Regulatory Responses from a Technological Standpoint

Though most electrical infrastructure models are based on legacy technology, new developments are beginning to study the idea of specifically disconnecting particular load regions from the grid [60], [61]. This phenomenon is known as "Islanding" and it can happen at the grid level and the individual source level [62].

Islanding is the energization of one region behind a PCC, Point of Common Coupling. It can occur for many reasons including under or overvoltage scenarios. Figure 2-1 highlights a utility scale PCC that incorporates a microgrid. Figure 2-3, shows the Public Service Company of New Mexico's (PNM) Richmond Switching Station as an example of legacy utility scale coupling technology.

Figure 2-3. Richmond Switching Station in Albuquerque, NM; similar in function and size to a utility scale Point of Common Coupling (PCC).

PNM's Richmond switching station only diverts power from different transmission lines to different parts of Albuquerque so maintenance can be done on the distribution infrastructure [63]. It does not function as a disconnect in the technical form of a PCC, but it gives the reader an example of the size of a utility PCC interacting with the grid.

In the case of a residential household with PV, the region that islands is a household disconnecting from the grid at a PCC [64], [65]. Figure 2-4 highlights a non-automated residential PCC in use.

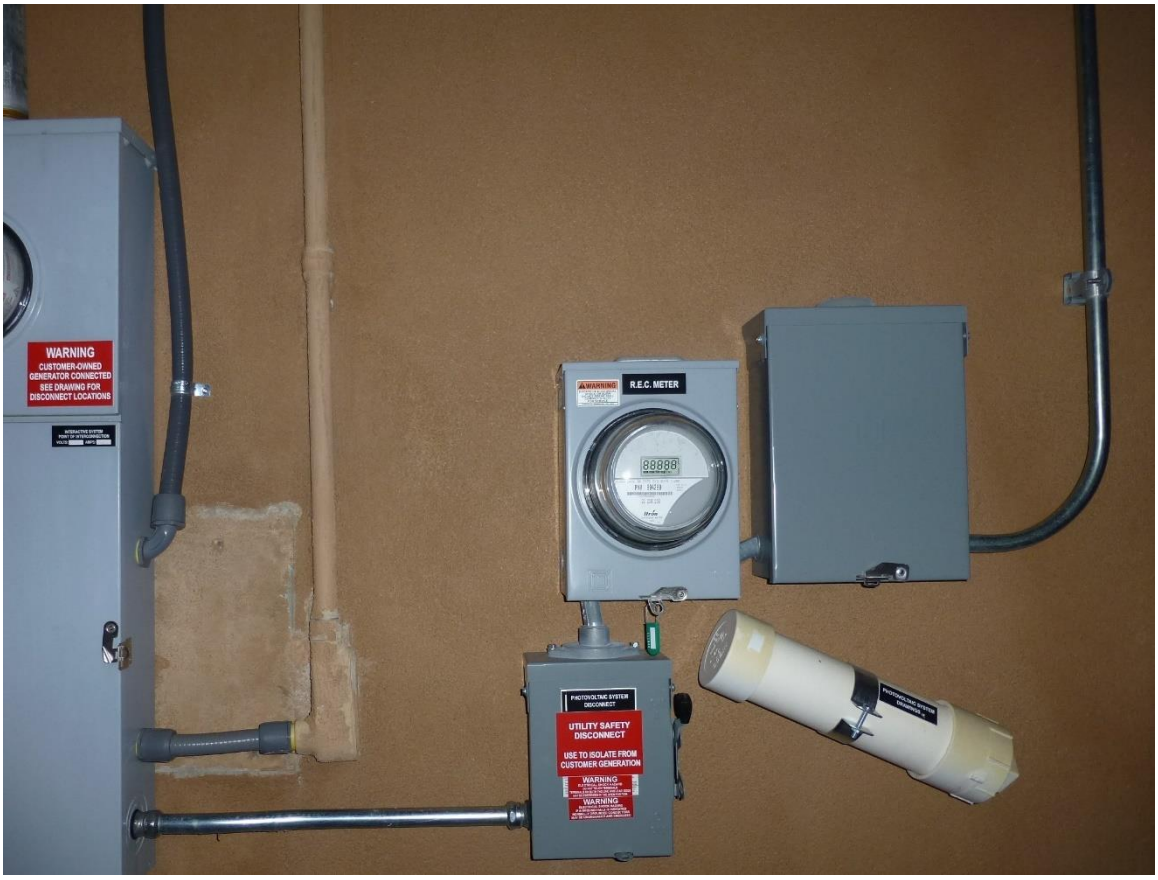


Figure 2-4. Point of Common Coupling (PCC) of a Residential PV system.

In a residence or business with grid connected PV, this presents a scenario when an electrician disconnects power from the grid at the PCC, but the PV continues to energize the building internally.

With such safety issues a concern for electricians, federal regulators have adopted an extremely conservative stance through the regulation of inverter sales for grid connected PV and batteries. IEEE Std 1547 governs PV to grid connection protocols and IEEE Std 2030 governs battery to grid connection protocols [66], [67]. Both protocols mandate disconnection of any inverter (within seconds) from the grid when the grid loses power [68]. This sort of operational mismatch of regulatory mandates versus implied intent will have suppressing effects on the implementation

of SIMF at the residential level [69]. It should be noted that at the time of the implementation of the above-mentioned standards, SIMF technology was not developed.

## 2.3. Smart Grid Operations with SIMF Integrateable Legacy Technology

A "Smart Grid" is a term that has emerged recently as description of a power grid that communicates with both the load as well as generation [70], [71], [72], [73]. In most market operations, the power company must react to frequency, voltage and reactive power problems. With smart grids there is a symbiotic relationship between load and generation with preexisting contracts that are executed automatically [74] [75]. The load and generation resources are actively in contact with each other constantly to ensure matched generation with the load.

The scope of any smart grid operation is extensive and involves a large amount of communications infrastructure. However, the scope of the following analysis is limited to operations that integrate well with SIMF and are legacy technologies proven in use. These categories are listed below.

1. Distributed Generation Dispatch
2. Grid-Tied Battery Dispatch
3. Demand Response Operations

### 2.3.1. SIMF Integration with Distributed Generation Resources

Distributed Generation (DG) resources are the first of three SIMF integrable technologies. DG is primarily producer initiated as is highlighted in Figure 2-5.

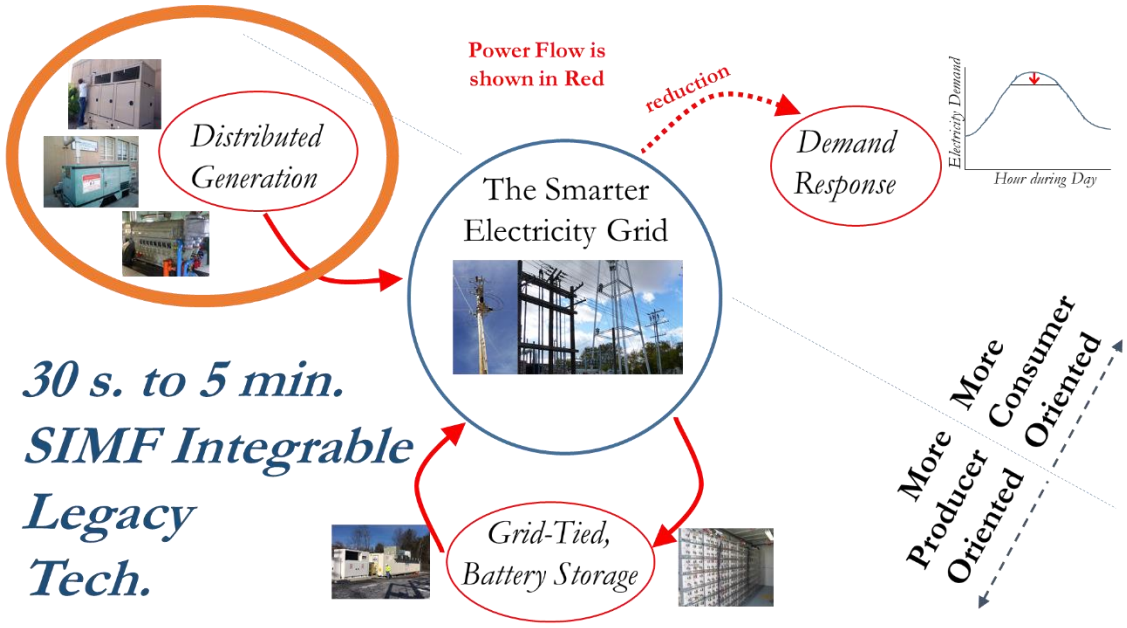


Figure 2-5. Distributed Generation as the first of three SIMF Integratable Technologies.

DG is the placement of many generation resources throughout a geographical region. These can include gas turbines and diesel generators, but there is an increasing amount of solar without storage that is also DG. [76], [77] Diesel generators that produce reliable power, on demand, are the limit of this analysis, as they integrate the best with SIMF. Most commercial DG diesel generators take less 30 seconds to ramp up and down to full generation capacity. Smaller home, and specialty commercial generators for uninterruptable power applications can react within seconds to provide uninterrupted power through power outages.

Two such commercial DG resources that provide voltage regulation for the University of New Mexico are shown in Figure 2-6.


Figure 2-6. Distributed Generation Resources at UNM; Left: 150 KVA diesel generator with author for scale, located at the Architecture building at UNM; Right: 50 KVA generator at Northrop Hall UNM.

Currently, diesel powered generators like those in Figure 2-6, operate sporadically, on the order of a few times per year and possibly only for a few minutes. This presents a scenario where DG is underutilized from a maintenance standpoint. [78], [79] This underutilization is due to maintenance being required on a resource that is not needed. One example is that diesel fuel in DG has a finite lifetime while sitting in a storage tank. If the DG does not utilize the fuel within the fuel's lifespan, the resource must operate to maintain the equipment simply to burn the old fuel and replace it with new.

These fast-acting DG resources have been considered by the Department of Energy and Department of Defense to provide firm power in the event of a terrorist attack. [80], [81], [82] The connecting technical specifications that unite SIMF and DOE/DOD reliability studies follows:

1. DG is often underutilized as a generation resource. There are known costs associated the with normal use of fossil fueled DG. However, the ongoing costs of maintenance, can be utilized to provide an economic value of the marginal cost of DG, when the resource is underutilized. This cost could of utilization is less if the resource is already installed.
2. Fast acting power fluctuation from PV without storage could be mitigated by SIMF and DG. For example, if a PV field is about to lose power due to a cloud passing over, SIMF could be integrated with DG to automatically call for the DG to supply power to the grid.

### 2.3.2. SIMF Integration with Grid-Connected Battery Technology

The second well integrable technology is grid connected battery storage as highlighted in Figure 2-7.

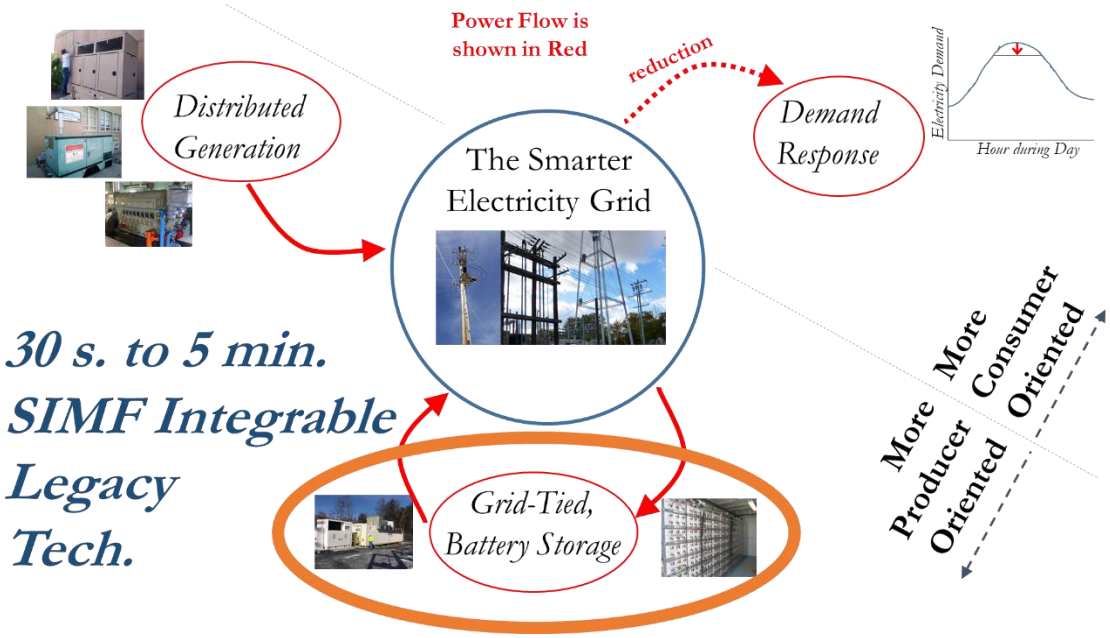


Figure 2-7. Grid tied battery storage is the second SIMF integrable legacy technology.

Lead acid and Li-Ion battery technology is fast enough to interact with SIMF to provide grid smoothing from PV cloud occlusions [83]. Typical configurations are highlighted in Figure 2-8. The ones highlighted are sold by GS Battery USA [84] and NEC Energy Solutions [85], but there are different types and configurations for sale by many companies.

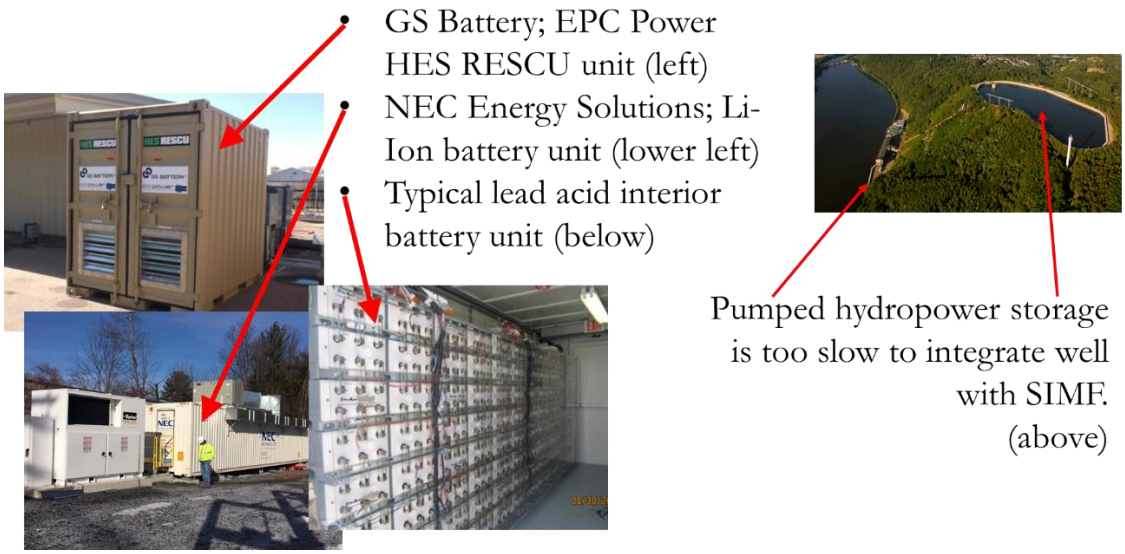


Figure 2-8. GS Battery USA and NEC Energy Solutions (left); and Genex Power's Kidston Pumped Storage Hydro Project (right) [86].

Pumped hydropower is a common energy storage solution employed by nuclear power plants for daily load shifting, but it is too slow to integrate with SIMF to smooth PV intermittencies. Such longer-term energy storage solutions are utilized for daily load shifting and have proven useful in combination with hour and day-ahead forecasts [87], [88], [89]. Pumped hydropower storage is one of grid sized power-storage legacy technologies with a proven record of reliability and cost-effectiveness.

Batteries that operate at partial capacity can both discharge and charge with electricity from the grid [90]. This utilization makes them a more valuable resource than one that can only generate electricity such as DG [91]. As was highlighted in Figure 1-10, partially charged grid tied batteries in combination with modern power electronics, can provide ancillary services to the grid by both absorbing and discharging real and reactive power [92], [93].

It is known that battery life and degradation is a function of total lifetime energy discharged and charged [92], [6]. Thus, when utilizing batteries for smoothing operations the amount of energy delivered or discharged can be lessened by utilization of a centered window of PV power output prediction as opposed to a trailing window. A trailing window is equivalent to reacting to a power disturbance after you know about it. A centered window utilizes prediction from SIMF. The following experimental data is from the Prosperity PV site located in Albuquerque, New Mexico [94]. Its 500 kW PV field also has a 1.5 MWh total load shifting/smoothing batterie attached [95]. The battery is providing smoothing operations. When utilizing a 2-minute SIMF prediction, energy drawn or stored in the battery was significantly reduced [6]. The engineering goal in the experimental simulation of battery operations, was to set a limit of the rate at which excess electricity from variable PV goes onto or off the grid. Batteries must discharge more energy, faster, when no SIMF is available.

Since all batterie have a lifespan that correlates to the total amount of energy charged or discharged over their lifetime, SIMF can greatly increase the lifespan of all grid connected batteries. This leads to longer uptime of grid connected storage for PV smoothing, better reliability, a longer overall lifespan and reduced maintenance costs. These are all problems that cause many grid-connected storage projects to be too expensive. Reliable SIMF could help with this problem and enable grid connected battery storage.

### 2.3.3. SIMF Integration with Demand Response

The final power mitigation strategy that integrates well with legacy technology is Demand Response (DR) events.

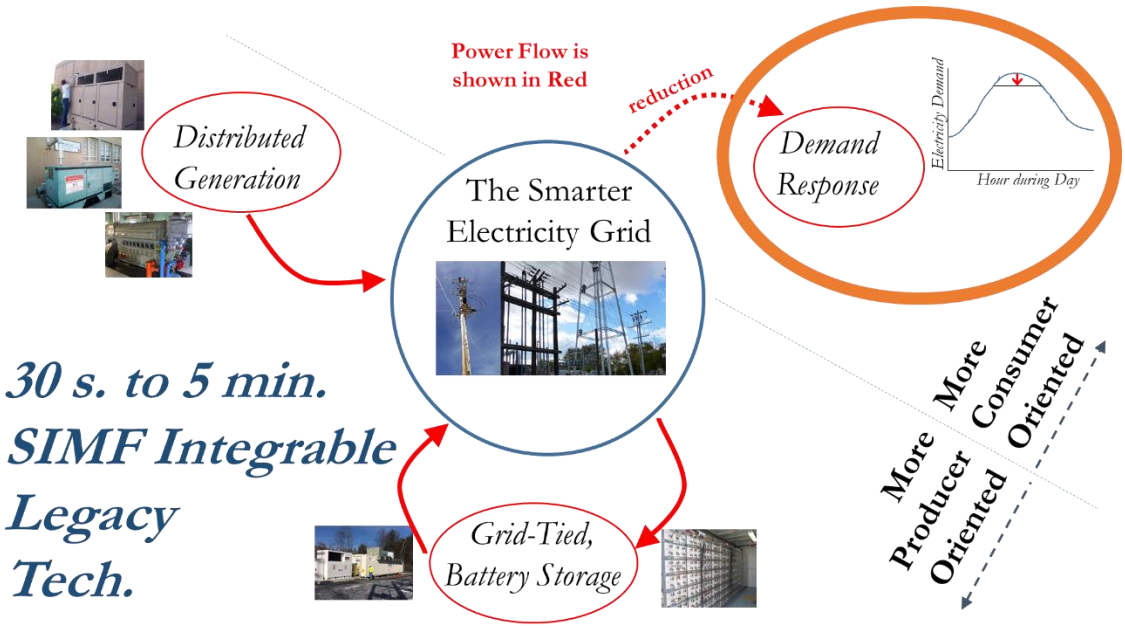


Figure 2-9. Automated Demand Response is the third SIMF integrable legacy technology.

Unlike batteries that charge and discharge, demand response (DR) can only reduce loads by momentarily turning off power uses like HVAC compressors or fans. Several simulations and experiments have confirmed the feasibility of current HVAC building components, among others, for such use [96], [97]. These outages are temporary and only last minutes. To integrate with intermittent PV, DR can only reduce customer loads. When the sun emerges from behind a cloud and begins to produce more electricity, a DR event would by definition not be useful.

The Federal Energy Regulatory Commission (FERC) issued final Order 745, *Demand Response Compensation in Organized Wholesale Energy Markets* that regulates DR

compensation in wholesale markets. This order mandates that any power saved from calling of a DR event, must be compensated by the power company to the customer at spot-market prices. These prices are high during a DR event because there is a shortage of electricity to be delivered immediately (within a few tens of seconds or the supplier is in violation of the contract.

Sandia National Laboratories recently studied demand response events on their campus and concluded; "Due to the recent Federal Energy Regulatory Commission (FERC) Order 745, *Demand Response Compensation in Organized Wholesale Energy Markets*, the potential annual compensation to Sandia National Laboratories (SNL) from performing DR ranges from $200K to $1,800K" [98]. As stated above, FERC order 745 ensures that reduction of power during a DR events is compensated at the current and higher spot-market rate. This is also how Sandia calculated its possible monetary benefits to reducing its electricity loads during high rate times of the day.

Though DR is typically integrated with load reductions, SIMF technology in combination with DR could be a large untapped market. In the case of SIMF with PV, DR events could be utilized to stabilize the grid during daylight hours, instead of only high during high electricity demand hours [97], [99].

SIMF integrates well with DR events when coupled with PV. When a cloud is about to pass over a PV field an integrated DR event could be called. Unlike high electricity demand times, which are probably hot and possibly humid thus increasing the latent air conditioning electricity load, a cloud occlusion event reduces the air conditioning

load. When clouds occlude an area, there is typically less need for air conditioning electrical power due to cooler temperatures and reduced cooling load. Thus, DR events to smooth PV can be longer without affecting the comfort of the building occupants. With spot price fluctuations becoming even more pronounced, this may become more significant in the future.

Current testing and implementation of DR events is in the wholesale market, but residential DR in combination with SIMF could be yet another large, untapped and newly enabled market. The major impediment to implementation of DR events in the markets in general, is lack of communications infrastructure for real-time prices.

# 3. Literature Review

Literature reviews of forecasting methods are extensive and encompass multiple technologies for multiple prediction time-frames. [100], [41] Figure 3-1 illustrates these three sets of technologies and the time-frame prediction lengths that are generally accompany by them.

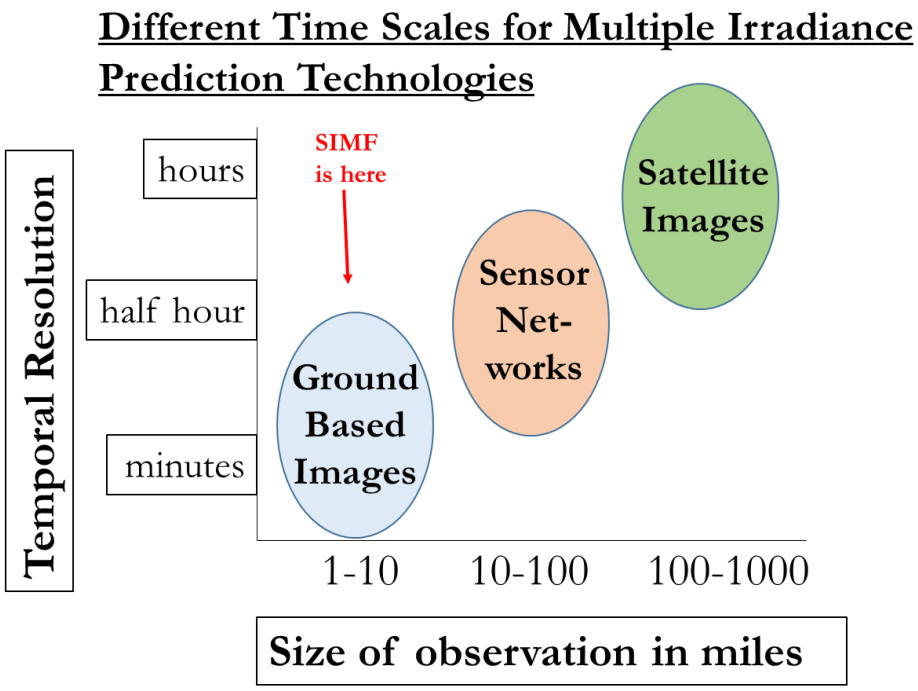


Figure 3-1. Time frame for three main categories of solar irradiance forecasting techniques based on technology category, relative to time horizon of prediction and observation area in miles.

Ground based image systems used photonic based sensors to make prediction of irradiance up to 15 minutes into the future. Sensor networks use a variety of ground-based sensors to make irradiance predictions of 10 minutes to one hour, based on sensor location. One such example of a sensor in a sensor network would be home and business, roof and ground-based PV collector generation capacity as a percentage

of maximum output. Satellite systems are self-explanatory in data acquisition function and are useful for one hour or longer irradiance forecasts. Though this literature review focuses on short term forecasting methods of less than 30 minutes, some technologies for longer forecasting are also reviewed due to their similarities with SIMF. Some processing and preprocessing methods for SIMF are similar for longer term irradiance forecasts. A list of relevant search terms for SIMF and irradiance forecasting in general, is listed in Appendix A.

## 3.1. Statistical Methods, Machine Learning Algorithms and Neural Networks in SIMF Prediction Systems

For each data input technology, the forecasting technology can be broken down into two models, Statistical and Machine Learning models. Figure 3-2 highlights this division of these prediction types.

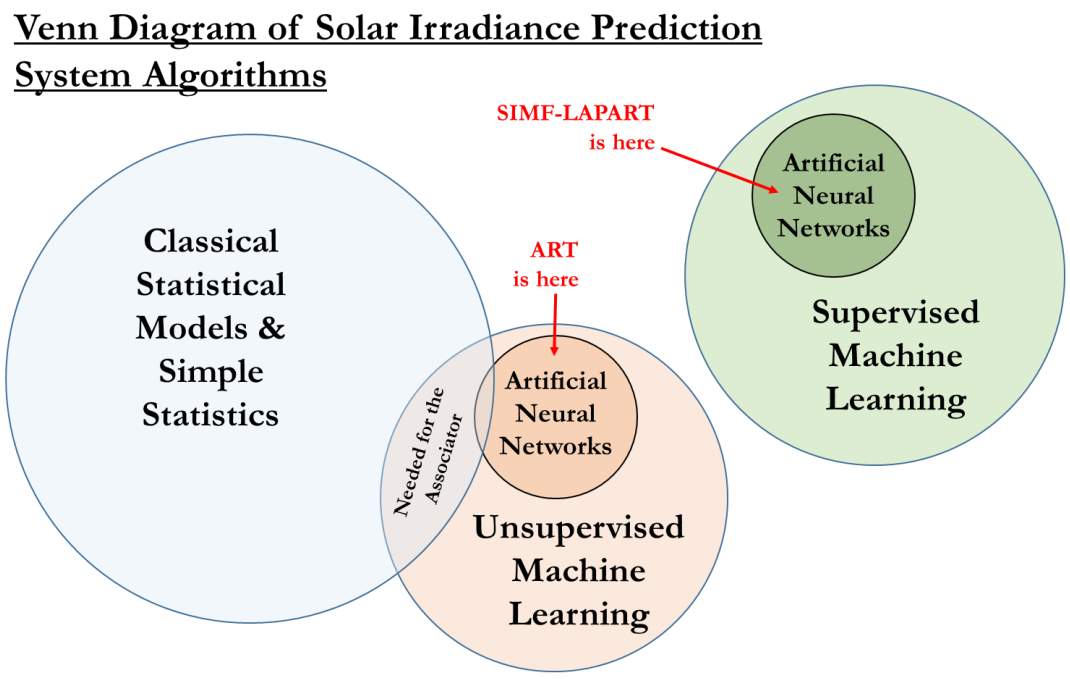


Figure 3-2. Diagram of different types of prediction algorithms used for solar irradiance forecasts.

This review follows the same basic structure.

## 3.2. Overview and Definition of Types of Statistical Methods and Machine Learning Algorithms as Applied to Solar Irradiance Forecasting

From a mathematical standpoint, the formulation of many statistical models can be the same as machine learning models. However, machine learning models are distinct in two specific ways.

1. As Phani Srikanth, editor of Data Science Analytics puts it; "*Statistical learning involves forming a hypothesis before we proceed with building a model. The hypothesis could*

*involve making certain assumptions which we validate after building the models.*" [101] He goes on to note the assumptions embedded in, for example, the linear regression model. The three assumptions are: A. All residuals follow a normal distribution around the mean. B. The data follow an independent relationship. C. Lastly, the variance of the residuals for random data is constant. (homoscedasticity). Under the above framework, a linear regression model could be constructed. If the hypothesis was wrong, the model would ostensibly, also be wrong.

However, even machine learning can contain some hypothesis about the data structure. For example, the unsupervised machine learning model K-Means Clustering contains an initial hypothesis about how many K categories to look for in the data. Though even in this example, machine learning remains different in that there is no hypothesis about where in the data to go about looking for these K number of categories. Indeed, using random initial conditions, could lead to different clusters.

2. The second, distinctive feature of Machine Learning comes in the subcategory of Artificial Neural Networks (ANNs). Whereas Machine Learning that is not an ANN, has a hypothesis about network structure but not the mathematical formulation; ANNs need not be constrained by such hypothesis. Obviously, the network has rules by which it is governed to work. However, ANNs can extract un-hypothesized features in network layers. They then can alter themselves, both physically in size and spatiotemporally based on those un-

hypothesized features and/or also other network inputs. These are examples of recursive and adaptive neural networks.

ANNs are specifically modeled after the neuro synaptic responses in the brains of all mammals and many other species [102]. Of course, they contain simplifications in operation relative to mammalian brains, but the structure of ANNs is biologically inspired. There are several other distinctive features that ANNs have, but a rigorous mathematical derivation of the most common architectures used for SIMF and in general analysis are reviewed.

It should be noted that the simplest ANN could be formulated almost identically to a statistical model. However, machine learning and specifically ANNs shed more and more hypotheses about how the model is supposed to work, while still maintaining a framework of network actions and interactions. From a mathematical perspective, ANNs could violate the independent variable hypothesis noted for a linear regression, by giving two distinct and valid answers to one distinct input variable, depending on when and how you query the network.

In current SIMF research, statistical models are typically used to preprocess or smooth parameters. That input is then used for other models or ANNs. When used to predict irradiance, a multivariate problem is usually preprocessed and reduced to one independent and one assumed-dependent variable space. When multiple variables are included in a formulation, the result is usually stacked statistical network

like a Markov chain process or a Bayesian network. Statistical models are particularly appropriate for longer term forecasts, greater than one hour.

Machine Learning Models use irradiance and other inputs, along with statistics to construct probability spaces for irradiance predictions. When referring to systems using ANNs to predict outcomes, there are associators and there are predictors. Associators in this context, use unsupervised machine learning to associate future irradiance with input features. That unsupervised correlation of feature spaces is mapped statistically to a future irradiance level with what is referred to as a Relationship Map. Predictors in this context, use machine learning algorithms and supervised learning to predict future irradiances from past learned data. Thus, predictors directly predict irradiance where associators must use a statistical relationship map to construct a quasi-dependent relationship between inputs and outputs.

### 3.2.1. Statistical Methods

The most common statistical models utilized in SIMF research are show below in Figure 3-3.

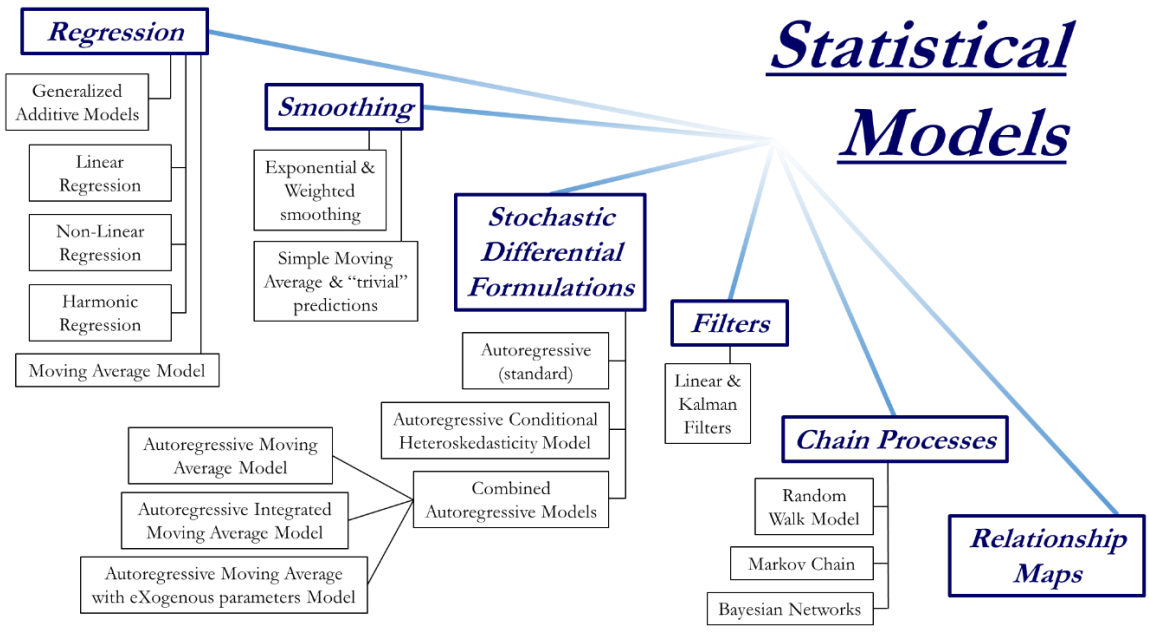


Figure 3-3. Diagram of classical statistical methods used in solar irradiance forecasting.

A discussion of the most common statistical tools as they are applied to irradiance forecasting, below.

#### 3.2.1.1. Regression Analysis

Regression analysis assumes a mathematical relationship between dependent and independent variables. The techniques for solving this relationship is the estimation of various parameters of these functions that fit past data. Regression analysis is split into multidimensional and one-dimensional data.

- Generalized Additive Models: attempt to reconstruct a signal, like irradiance, by assuming a linear relationship between smoothing functions and discrete signal values in order to fit the data. They are the multifunctional form of a regression analysis. The formulation is shown below for irradiance I.

$$g\big(I(y)\big) = \alpha + f_1(x_1) + f_2(x_2) + \cdots + f_i(x_i) \tag{3-1}$$

Where α is a constant and $\mathrm{f_i(x_i)}$ are functions of a parametric form, ie. polynomial or linear functions

A notable example of the use of a generalized additive model is from M. Brabec, M. et al. who used latitude, time of day, day of year and other variables to produce a single nowcasted irradiance [103].

Linear Regression: assumes a linear relationship between the independent and dependent variables. It has the form:

$$\vec{Y} = \vec{m}X + \vec{\beta} \tag{3-2}$$

$$X = \begin{bmatrix} 1 & x_{11} & \cdots & x_{1n} \\ 1 & x_{21} & \cdots & x_{2n} \\ \vdots & \vdots & \ddots & \vdots \\ 1 & x_{n1} & \cdots & x_{mn} \end{bmatrix}$$

Where $\vec{\mathrm{Y}}, \vec{\mathrm{m}}$ and $\vec{\beta}$ are vectors and X is a matrix or a vector.

β is vector representation of the error between the regression and the data.

Linear regression has been used for irradiance forecasting techniques, from extracting features from images of the sky to quantifying systematic drift error in irradiance measurements, among others [104], [105], [106], [107], [108].

- Non-linear and Harmonic Regression: use basis functions that do not assume a linear relationship between the independent and dependent variables. Harmonic regression models a functional relationship between the variables as a combination of sinusoidal functions.

- Moving Average Model: The moving average model is mathematically a linear regression, but it also contains a stochastic term. It assumes a linear relationship between the output and current plus previous stochastic terms. The moving average model of order *q* is defined below:

$$Y_t = \mu + \varepsilon_t + \alpha_1 \varepsilon_{t-1} + \cdots + \alpha_q \varepsilon_{t-q} \quad (3\text{-}3)$$

Where $\mu$ is the mean, $\varepsilon_q$ is white noise and $\alpha_q$ are the parameters to find.

The moving average model is used extensively with the Autoregressive model and is revisited later in Stochastic Differential Formulations.

#### 3.2.1.2. Smoothing

Smoothing is the least computationally intensive of all the irradiance forecasting techniques. The "trivial" case is the baseline by which all models must outperform for a forecasting technique to be considered valid. It involves using the current irradiance forecast as the predicted irradiance.

#### 3.2.1.3. Stochastic Differential Formulations

Stochastic Differential Formulations are a set of mathematical equations that take the form of a stochastic differential equation. Implicitly, the formulation relies on past data to predict future irradiance. They also contain a stochastic term.

Attempts have been made to formulate continuous irradiance models based on a stochastic differential equation (SDE) framework and irradiance only [109]. A list of the most common discrete forms follows:

- Autoregressive model: The autoregressive model assumes a linear relationship between its output and a its previous values plus a stochastic term. The formulation is shown below for irradiance I and model order *p*:

$$I_t = \alpha + \sum_{i=1}^{p} \varphi_i I_{t-1} + \epsilon_t \tag{3-4}$$

Where $\alpha$ is a constant and $\varphi_i$ are parameters of the system. The autoregressive model is rarely used by itself. Instead it is usually combined with the moving average model and/or other parameters for predictions.

However, the autoregressive model can be used as a filter when the stochastic terms are calculated from previous data. The autoregressive filter has the advantage of being more responsive to the direction of movement of the signal as opposed to a linear moving average. V. Bone et al. [110] of the University of Queensland used an autoregressive filter to preprocess sky images to obtain a better velocity profile of the cloud motion. This is noted for future reference, as smoothing velocities from a particle image velocimetry algorithm is a problem that has arisen with the current research.

- Autoregressive Moving Average Model (ARMA) and the Autoregressive Integrated Moving Average Model (ARIMA): These two models are extensively used as a benchmark of older technique for which machine learning and neural networks have become the dominant analysis tool for irradiance forecasting [111], [112], [113], [114]. The formulation of the

autoregressive moving average model for irradiance I and order *p, q* is listed below:

$$I_t = \alpha + \varepsilon_t + \sum_{i=1}^{p} \varphi_i I_{t-1} + \sum_{j=1}^{q} \theta_j \epsilon_{t-j} \quad (3\text{-}5)$$

Where $\alpha + \varepsilon_t$ is the expected mean and $\varphi_i$ & $\theta_j$ are the parameters of the system.

The autoregressive integrated moving average model (ARIMA) attempt to keep the mean of the data constant or zero by doing a transformation on the mean before the ARMA process. The data transformation is accomplished by calculating the data as a difference from the mean. The new transformed data has a mean of zero. The ARMA model is then applied to the data.

Reikard and Hansen of Sandia National Laboratories and US Cellular used frequency domain model based on a Fourier transformation of the ARIMA [115] They had several models that tested time horizon irradiance forecasts from 15 minutes to three hours.

- Autoregressive Moving Average with exogenous parameters: This formulation is almost identical to the ARMA model, but it adds another parameter. Its formulation is listed below. It utilizes the same parameters as (3-5) but also adds the parameter τ.

$$I_t = \alpha + \varepsilon_t + \sum_{i=1}^{p} \varphi_i I_{t-1} + \sum_{j=1}^{q} \theta_j \epsilon_{t-j} + \sum_{k=1}^{k} \theta_k \tau_{t-k} \quad (3\text{-}6)$$

#### 3.2.1.4. Filters and Chain Processes

Chain Processing is a simple model that assumes current conditions have a strong effect on the future.

- Random Walk: The simplest chain process is a random walk process. For example, if the sky is uniformly hazy, then it is likely that future irradiance will be impacted by current irradiance conditions. Thus, when predicting future irradiance, it does not matter what the irradiance was five hours ago. It only matters what the irradiance was a few minutes ago. This random walk process works well for uniform conditions.
- Markov Chain Networks: attempts to predict future irradiance by linking probabilities. The process incorporates a probability map of future irradiances given that certain occurrences already happened. For example, given that today was sunny, the probability tomorrow will be sunny can be predicted with better accuracy given that today is sunny. Markov chains are useful in predicting day-ahead irradiances [116], [117].
- Kalman and linear filters operate in the same manner as a Markov chain, but the probabilities are updated as time and new data progress forward. When forecasting irradiance, the Kalman filter has proved useful for longer term

forecasts of irradiance (1-3 hours) by smoothing weather forecasts of wind direction among other variables [118], [119], [120], [121].

- Bayesian Networks: are like a Markov chain except they assume a Bayesian relationship among the inputs. For example, if a distributed sensor network of irradiance sensors is used to predict irradiance at a given area, a Bayesian network can be constructed. Suppose that every time a particular sensor is occluded, the solar field gets occluded. However, occasionally, the occlusion is due to a bird. During migratory season this chance goes up to 1% false positive from a bird. The sensor is 99% sensitive. However, 1% of the time the sensor returns a low value almost at zero. The sensor is 99% specific. The sensor test will produce 99% true positive results and 99% true negative results of actual irradiance. The operator attempts to ask the question posed mathematically in (3-7). What is the probability of a cloud occlusion scenario we shall call "A" being correct, given the known sensor failure probability we shall call "B".

$$P(A|B) = \frac{P(B|A) * P(A)}{P(B)} \tag{3-7}$$

Where $P(A|B) =$ the probability of A, given B is true and where $P(A) =$ probability of A.

A Bayesian network would quantify all the probabilities for all the sensors to construct a network. Unlike a Markov chain, a Bayesian network can produce

a certainty about the accuracy of the prediction given the inaccuracies within the data collection sensor network.

#### 3.2.1.5. Relationship Maps

Relationship maps are included for completeness. When unsupervised learning is expounded upon below, it is shown that a relationship map is needed to make meaningful predictions. Unsupervised learning techniques are categorizers. They can give information about a state of the system, but they require another categorizer network and a relationship map between the two categories. Thus, relationship maps in this context are usually, but not always, binary maps that connect categories of operational states with future irradiance categories.

The type of mathematics from which relationships maps are derived is called category Theory. Adaptive Resonance Theory (ART), which will be elaborated on later, is a prime example of the utilization of category theory mathematics with multiple ANNs [122], [123], [124]. With LAPART, which will be elaborated on later, two unsupervised learning ART networks are coupled to form a unit map between inputs and outputs. Though other operators exist in category theory mathematics, the unit operator is the extent of the currently useful operators. When restricted to the unit operator with two networks, a binary relationship map can be constructed as a matrix.

### 3.2.2. Machine Learning and Artificial Intelligence Methods

The most common Machine Learning and Artificial Neural Networks that are utilized in SIMF research are shown below in Figure 3-4.

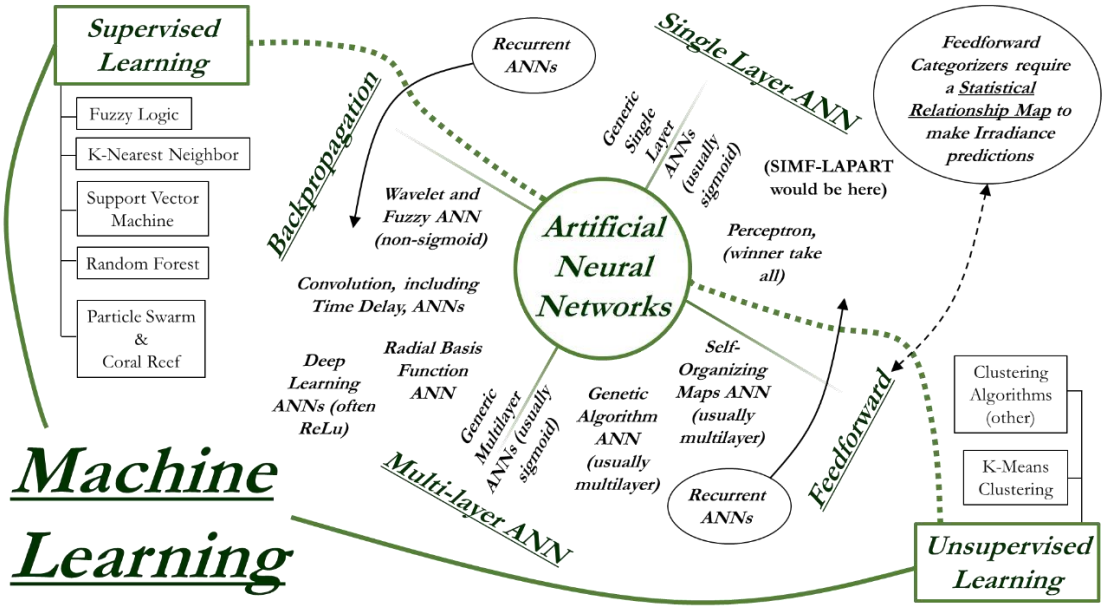


Figure 3-4. Diagram of machine learning models used in solar irradiance forecasting.

Since artificial neural networks comprise a large part of current techniques in forecasting SIMFs of less than 15 minutes, they are discussed first.

#### 3.2.2.1. Artificial Neural Network Architecture

The Rosenblatt Perceptron (1958, 1962) was the first neural model to formulate a convergence theorem for linearly separable inputs. Rosenblatt proved that given the linearity condition of the inputs, the perceptron would converge. This convergence manifests itself in the form of a hyperplane between the two classes [102]. This breakthrough facilitated the first neural models by which a "learning" (parameter

update from a statistical model standpoint) can occur. This convergence theorem is known as the *Rosenblatt Convergence Theorem*.

The simplest neuron is a single layer nonlinear neuron shown in Figure 3-5.

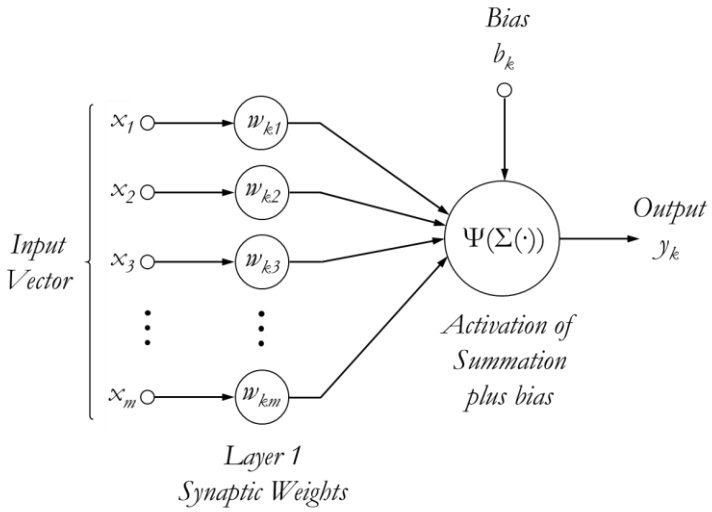


Figure 3-5. Nonlinear single neuron, single layer model.

The neuron output $y_k$ can be written as follows:

$$y_k = \varphi(u_k + b_k)$$

$$u_k = \sum_{j=1}^{m} w_{kj} x_j \tag{3-8}$$

The bias $b_k$ has the effect of moving the activation function so it's centered over the summation of the range of the synaptic weights. Depending on network type, the activation function can take many forms. However, it usually is constrained on the interval [0,1] or [-1,1]. The input is also normalized on the interval [0,1] or [-1,1]. In order to match the neuron output to the appropriate interval, the bias needs to be selected correctly.

The number of types of activation functions are one level of classification of Neural Networks. They are listed below.

- Winner Take All (WTA): The WTA activation function is a binary all or nothing function. It is shown in Graph 3-1

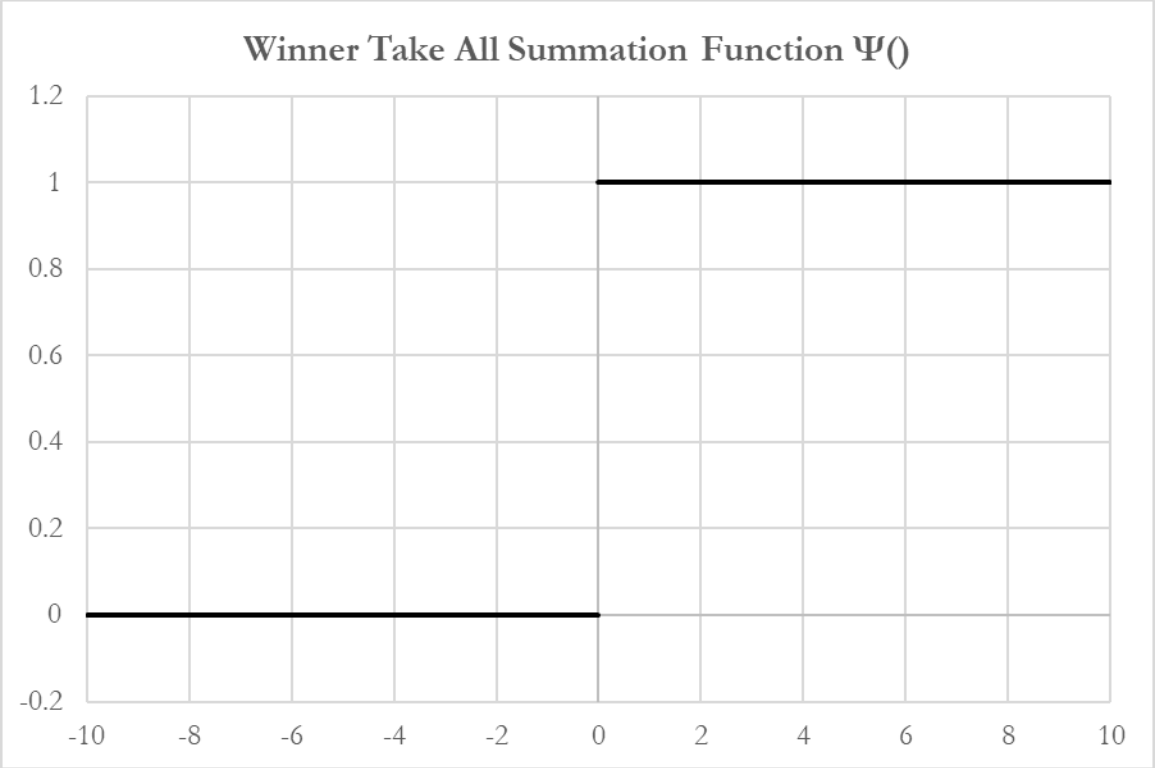


Graph 3-1. Winner Take All (WTA) summation function for neuron output

The WTA perceptron was the basis for neural networks, however it is typically not used in practice, and is only included for completeness.

- Sigmoid and Tanh: A more common activation function for a neuron is the sigmoid and tanh. They are graphed below.

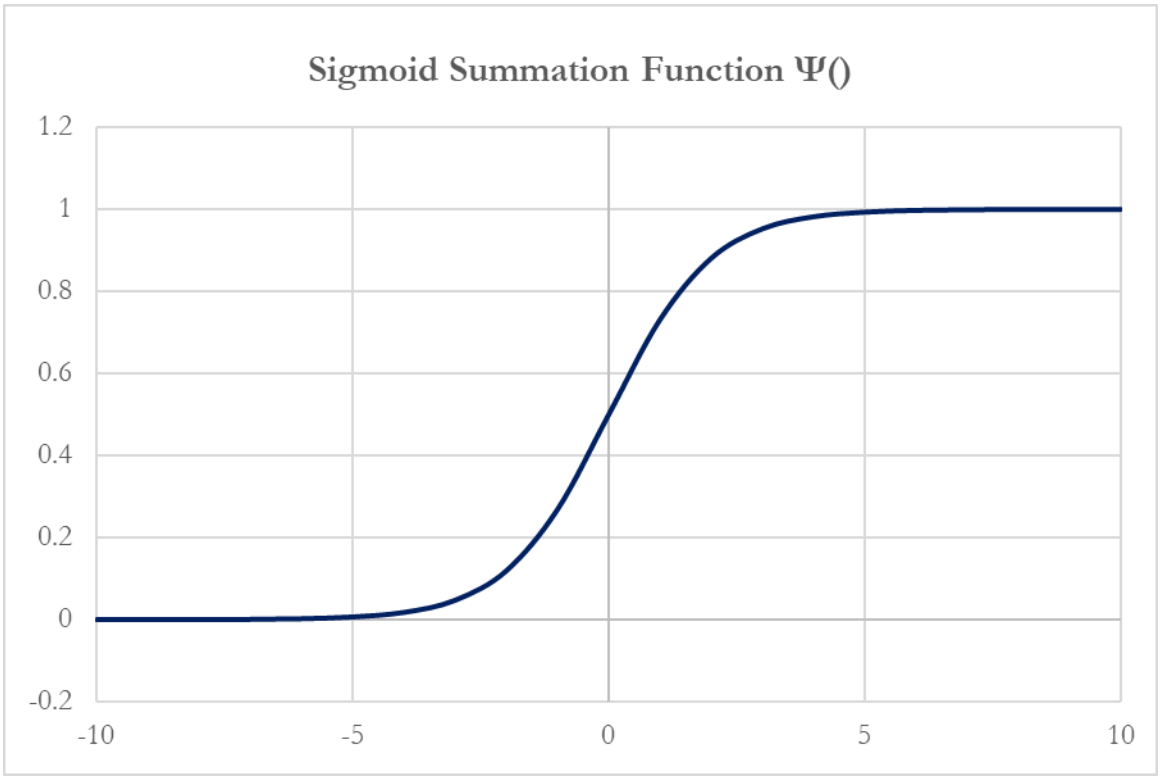


Graph 3-2. Sigmoid neuron activation function.

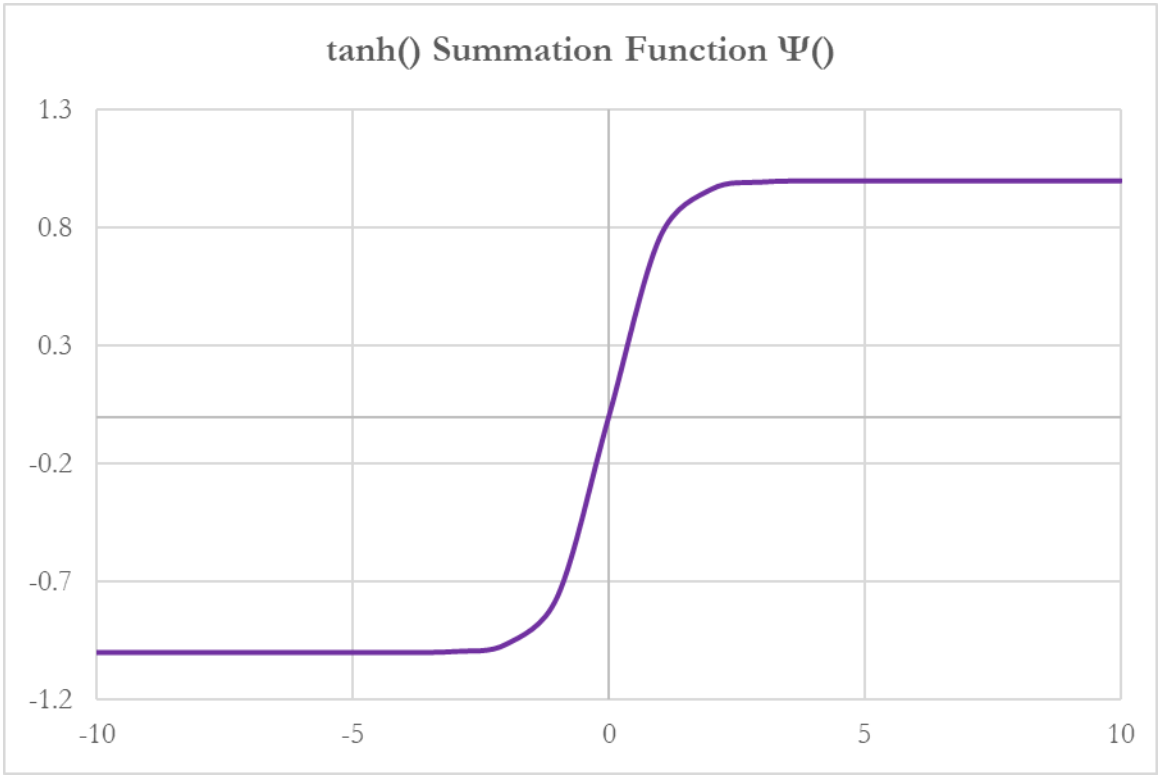


Graph 3-3. Hyperbolic tangent neuron activation function.

C. Combria and H. Pedro, among others, have extensively used single layer perceptron networks with sigmoid activation functions [125], [126], [127], [128], [129]. The main inputs are sky images, but they have also extensively used other weather data as inputs to the network to make irradiance predictions [130].

The hyperbolic tangent function is nearly the same as the sigmoid function, but the range is different. As was stated earlier, the inputs should be scaled accordingly, and a correct bias needs to be selected when using either activation function.

- ReLu and Wavelet Functions: The ReLu neuron activation function is useful for so called "deep learning" neural networks, in that it converges faster than the sigmoid and tanh functions. In this context, "convergence" means the weights "converge" and stop updating. "Deep Learning" implies among other metrics, a very large data set. In operation with the sigmoid and tanh functions, the weights will continue to update until a parameter is set that declares weight-convergence because the update is very small. Lastly, learning and the weight update process, will be explained below. Several papers have used this function to help converge with large deep learning data sets [131], [132].

  Wavelet Neural Networks are included for completeness as another form of activation function. The two types of neuron activation functions are graphed below.

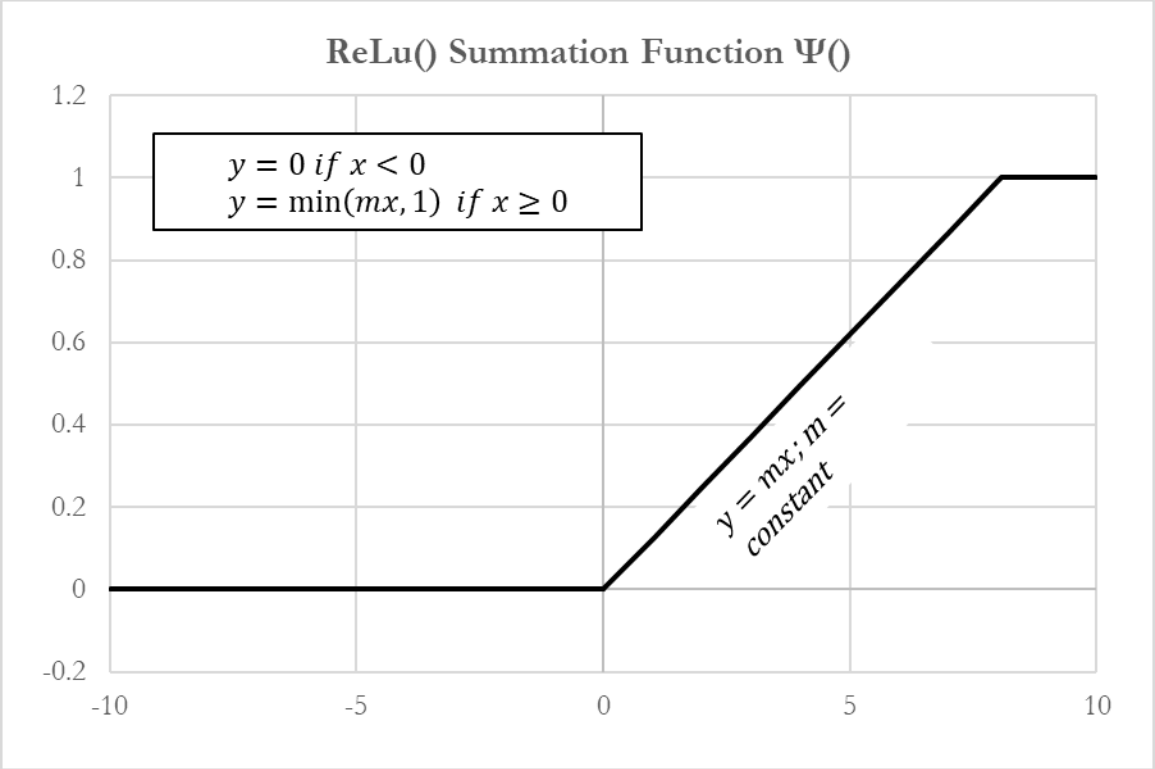


Graph 3-4. ReLu neuron activation function.

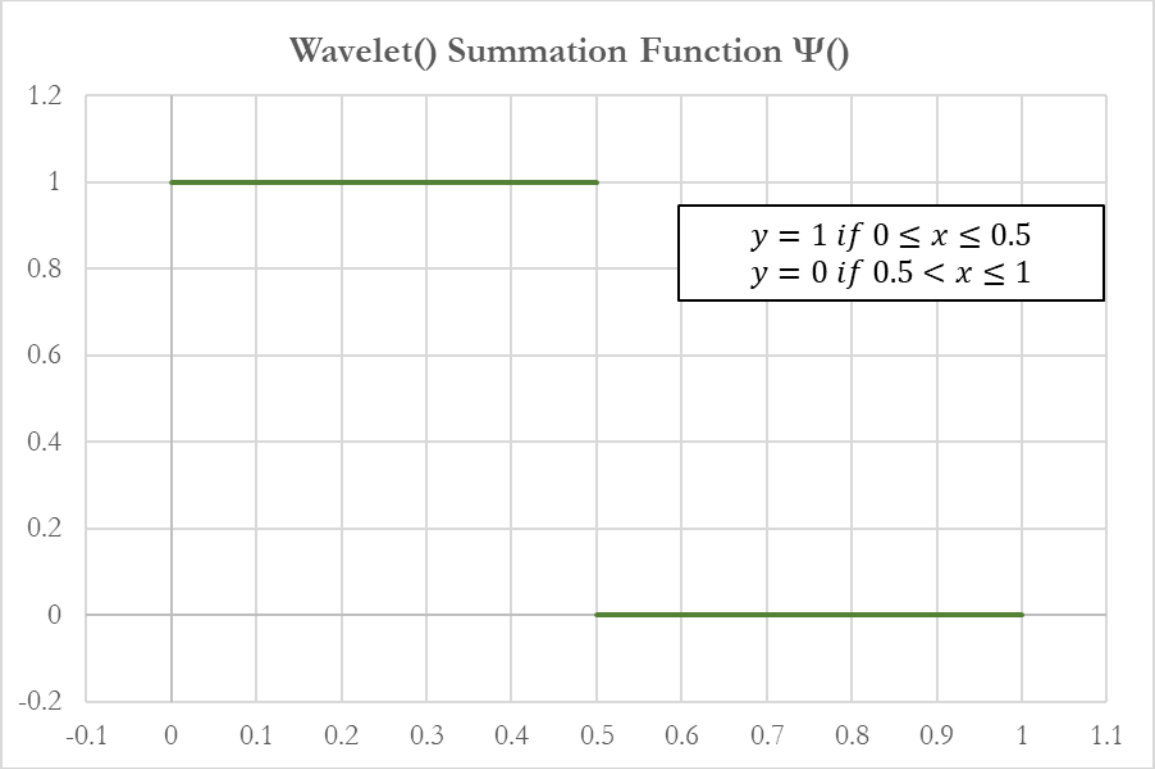


Graph 3-5. Wavelet neuron activation function.

- Gaussian: The Gaussian activation function is utilized in Fuzzy Logic and Fuzzy neural networks. These concepts will be discussed later but the Gaussian curve is shown in Graph 3-6 below, with multiple centers.

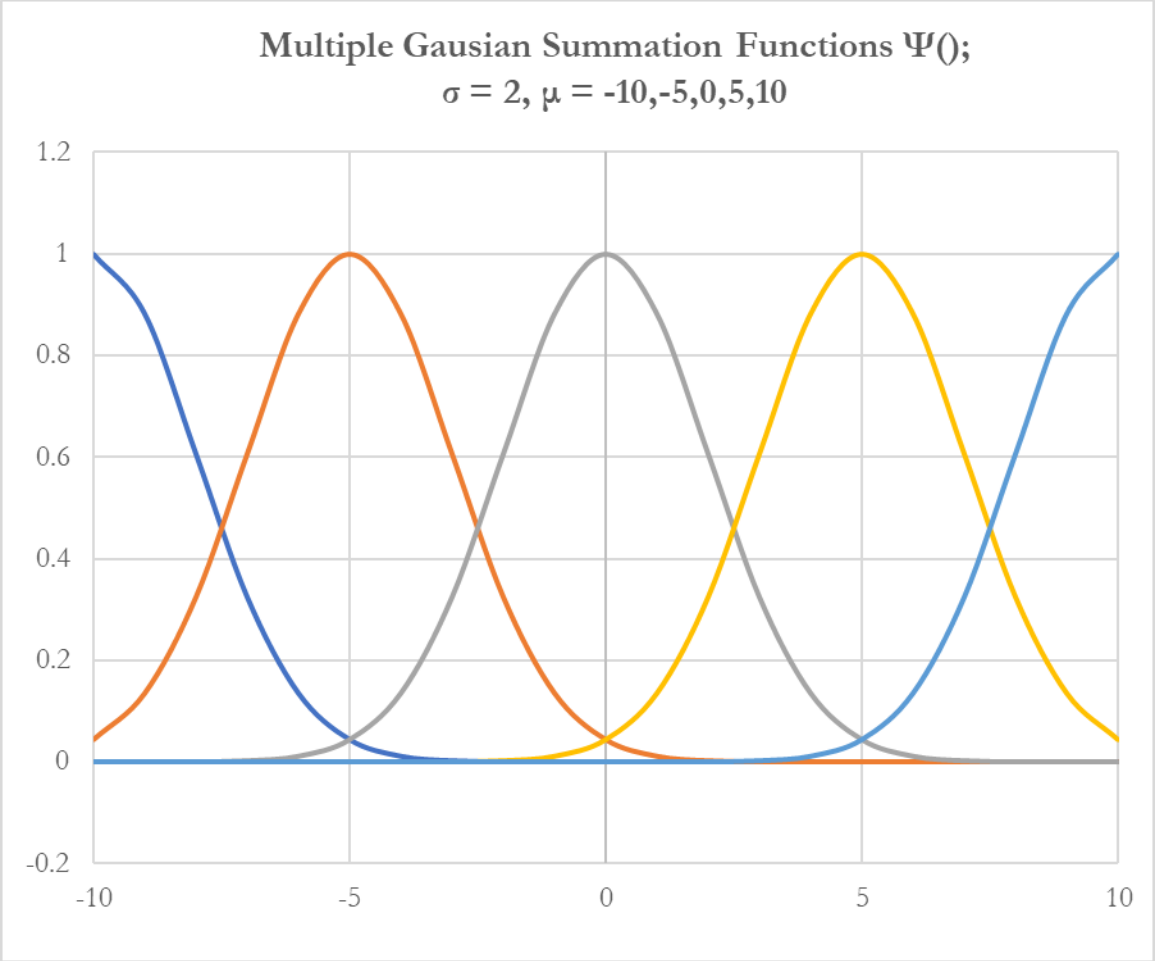


Graph 3-6. Gaussian neuron activation functions utilized in fuzzy neural networks.

- Radial Basis Functions (RBF): RBF ANNs use the weight of the activation of a neuron as the distance from a cluster center in the data. They must be initialized with the centers of the data. Often, a clustering algorithm is utilized as a basis for the initial weights. In other case, random values are utilized. Though not as common, RBF ANNs have been utilized for irradiance forecasting [133], [134], [135].
- Fuzzy Logic: Fuzzy Logic has been implemented in several forecasting papers both in the form of a map and as a multilayer ANN [136], [137]. Fuzzy logic

is a form of "if and" logic, where membership categories assign a truth value to each contribution of each statement. What results is a truth value of predicted outcome between zero and one, as opposed to a binary true or false. For example, take the fuzzy system with three membership functions shown below in Graph 3-7. It represents the three states of human comfort in a fuzzy system.

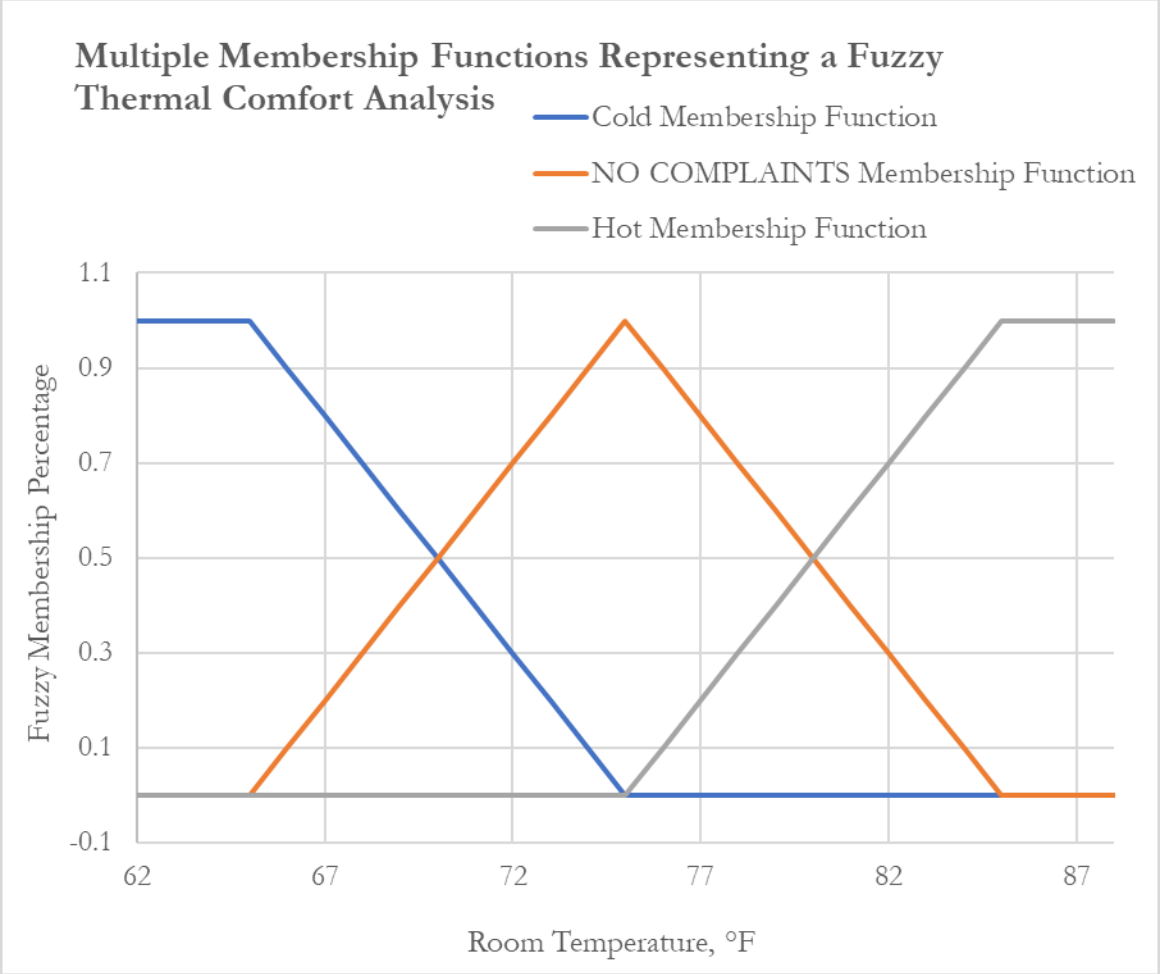


Graph 3-7. Fuzzy system representing the thermal comfort of a room by most people.

When taking a temperature reading at 69° F, fuzzy logic uses the aggregation of membership function to construct several fuzzy truth statements shown below.

- T=69; **if** cold is 0.6 **&** no-complaints is 0.4 **&** hot is null; then **fuzzy logic truth value between 0 and 1 (example, raise temperature 0.6° F)**
- T=70; **if** cold is 0.5 **&** no-complaints is 0.5 **&** hot is null; then **fuzzy logic truth value between 0 and 1 (example, raise temperature 0.5° F)**

These fuzzy truth statements can be aggregated to make a multilayer neural network or fuzzy control system [138] to make irradiance predictions. To convert back to crisp logic, a maximum or minimum function is employed to select a binary true or false output.

In order to highlight the multiple concepts that comprise a multilayer fuzzy ANN, an example of how this is implemented is highlighted in the Supervised Learning of fuzzy Neural Networks section below.

#### 3.2.2.2. Multilayer Neural Network Architecture

The concept of a single layer ANN was shown in Figure 3-5, above. The multilayer model is shown below in Figure 3-6.

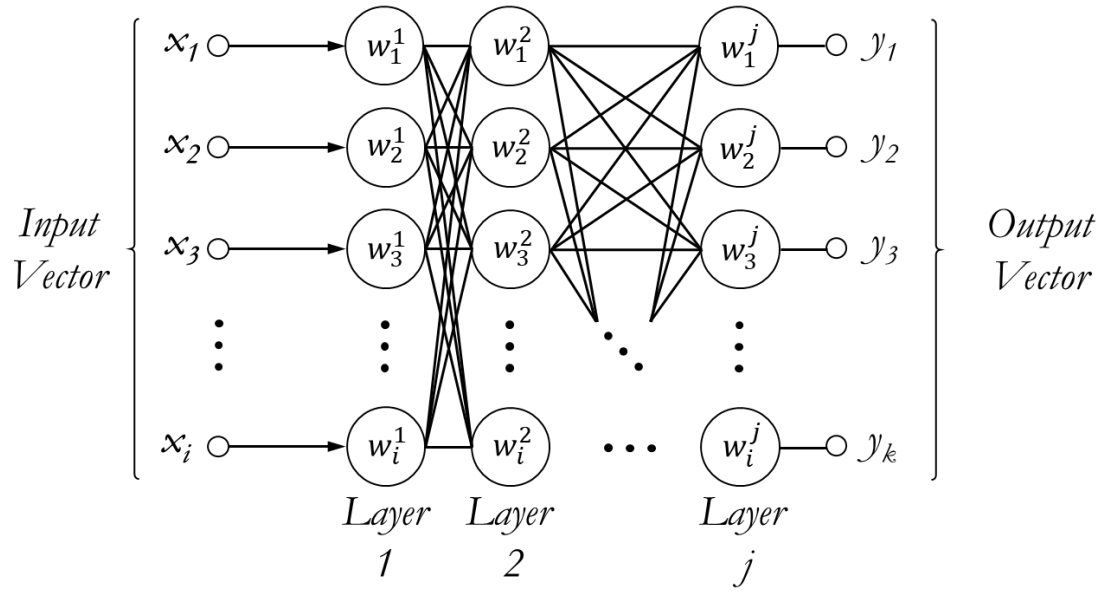


Figure 3-6. Multilayer Neural Network with the same number of outputs as inputs and the same number of weights per layer.

This network has the same number of inputs as outputs and the same number of weights per layer. In use, the number of layers and weights in each individual layer can vary. In another application of deep learning that did not included explicitly utilize ReLu() functions, Ahmed and Chen used a general multilayer neural network along with environmental parameters among others, to forecast up to week ahead grid level energy consumption [139].

Methods for the adaptation of weights, known as ANN learning is highlighted below in Backpropagation and Supervised Learning of General Neural Networks.

### 3.2.2.3. Supervised Learning of Fuzzy Neural Networks

A fuzzy ANN model is shown below

The mathematics of a multilayer ANN will be highlighted with the construction of the T-S fuzzy ANN used by Kaiju, Xuefeng, Chaoxu and Dan to make same day irradiance predictions. The T-S Fuzzy ANN is highlighted in Figure 3-6 with Layer one as the Fuzzification layer, layer two as the fuzzy reasoning layer and layer j corresponding to the third layer known as the defuzzification layer.

The fuzzification layer obtains a membership value μ with (3-9) below.

$$\mu_i^j(x_i) = e^{-\left(\frac{x_i - c_i^j}{b_i^j}\right)^2} \tag{3-9}$$

Where $c_i^j$ and $b_i^j$ are constants to update.

The second layer calculates the weights with (3-10).

$$w^j = \prod_{i=1}^{n} \mu_i^j(x_i) = e^{-\sum_{i=1}^{n} -\left(\frac{x_i - c_i^j}{b_i^j}\right)^2} \; ; j = 2 \tag{3-10}$$

This fuzzy reasoning layer is the only operational difference between a fuzzy ANN and the more generic ANNs. After this step, a fuzzy ANN operates with learning in the same manner as other ANNs utilizing an energy minimization function.

The fourth layer calculates the proportion of each weight that is applicable in the fuzzy reasoning layer. It is calculated with (3-11).

$$p_i^j = \frac{w^j}{\sum_{j=1}^{n} w^j} \tag{3-11}$$

In order to obtain the output, one must convert from the fuzzy response to a crisp output. This is done with (3-12).

$$y_i = \frac{\sum_{i=1}^{n} w_i * \left(\sum_{j=1}^{n} p_i^j\right)}{\sum_{i=1}^{n} w_i} \tag{3-12}$$

The process of supervised learning is constructed with an error calculation shown in (3-13).

$$e = \frac{1}{2}(y - y_c)^2 \tag{3-13}$$

Where $\mathbf{y}$ and $\mathbf{y_c}$ are the actual and expected outputs.

The TS fuzzy ANN was highlighted above. The concept of backpropagation and weight updates is not highlighted for a fuzzy ANNs. Instead, this concept is mathematically shown below for general ANNs, continuing from the cost function.

#### 3.2.2.4. Backpropagation and Supervised Learning of General Neural Networks

With general ANNs, the output function of layer *j* and row *i* is defined in (3-14). It is like (3-8) for a single neuron.

$$a_i^j = \sigma\left(\sum_{i=1}^{n} w_i^j * x_i^{j-1} - b^j\right) \tag{3-14}$$

Where $\sigma$ is the activation function j is the layer.

To illustrate the backpropagation algorithm, the cost function is derived to obtain the direction of descent in our gradient descent algorithm. We wish to vary the weights

of the network to better approximate the input to output mapping that exists in the data. Since the bias is a constant, we wish to take the derivative of the cost function relative to the weights. For this operation, we employ the chain rule as is illustrated in (3-16) while also slightly tweaking the cost function from its earlier version in (3-13), known as the error function.

$$c_i^j = \left(a_i^j - y_i^j\right)^2 \tag{3-15}$$

Where $a_i^j$ is the output activation from the previous layer and $y_i^j$ is the expected output.

The analysis proceeds with one row of activation in order to drop the subscript *i* and simplify the math. The cost function derivative follows

$$\frac{\delta c^j}{\delta w^j} = \frac{\delta z^j}{\delta w^j}\frac{\delta a^j}{\delta z^j}\frac{\delta c^j}{\delta a^j} \tag{3-16}$$

It is now easier to define the output in terms of the weights.

$$z^j = w^j * a^{j-1} + b^j \tag{3-17}$$

Where $a^{j-1}$ is the activation of the j-1 layer and $b^j$ is the bias.

$$a^j = \sigma(z^j) \tag{3-18}$$

Where $\sigma(z^j)$ is the activation output of neuron j.

The following definitions pertain to the chain rule derivatives of the cost function.

$$\frac{\delta c^j}{\delta a^j} = 2(a^j - y) \tag{3-19}$$

$$\frac{\delta a^j}{\delta z^j} = \sigma'(z^j) \tag{3-20}$$

$$\frac{\delta z^j}{\delta w^j} = a^{j-1} \tag{3-21}$$

Finally, we define the backpropagation update with a gradient descent formulation shown below.

$$\Delta w = -\eta \frac{\delta c^j}{\delta w^j} \tag{3-22}$$

Where $\eta$ is a learning rate between 0 and 1.

Note that this backpropagation technique was highlighted for a single neuron. In a multilayer application there is a summation of effects from each neuron's output. Thus, when backpropagating the algorithm, there involves another or multiple other rows. The gradient in (3-22) is utilized in cost function energy minimization technique, known as gradient descent iterative solvers.

The backpropagation algorithm feeds forward the input and then backpropagates an update many times. It is said to converge when the weights have sufficiently stabilized and stopped changing within a certain threshold and/or the answer becomes close enough to tolerance threshold. These thresholds can be calculated in several ways including utilizing a mathematical normalization algorithm such as Euclidian distance.

In the solar irradiance forecasting paper reviewed, whenever an ANN was used, unless otherwise stated as a different architecture, it utilized a backpropagation learning algorithm based on a gradient descent methodology. This was to be expected as backpropagation networks are most widely known.

#### 3.2.2.5. Unsupervised Learning

Unsupervised learning is mentioned in the context of irradiance forecasting because from a mathematical standpoint of the prediction system, there is no such thing as unsupervised learning. As was mentioned in the Relationship Maps section above, two or more ANNs can extract features from data, but it is the association of features of the input space to the features of the output space with a relationship map, that makes an irradiance prediction possible. The prediction comes in the form of a recognized input feature space that has a learned association to a mapped output. One concept of unsupervised learning will be highlighted in the Literature Review of Adaptive Resonance Theory and LAPART Architecture section. Unsupervised learning is also visited in the clustering section.

#### 3.2.2.6. Recurrent Neural Networks

Recurrent ANNs have a layer that feeds back on themselves with the output of one input presentation as the input to the next input set. A model is shown below as an example.

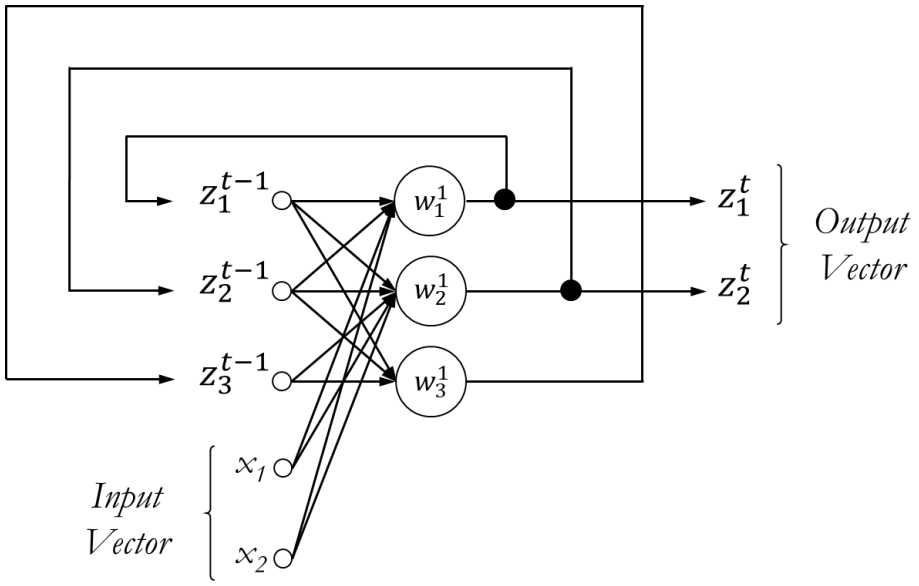


Figure 3-7, Recurrent artificial neural network with one hidden neuron layer.

Though not as common, recurrent ANNs have been used to predict intraday irradiance [140]. Weather models utilizing recurrent ANNs were also utilized to predict energy production of PV plants for microgrid planning at the day ahead timeframe [141].

#### 3.2.2.7. Convolutional Neural Networks and Time Delay Neural Networks

Convolution ANNs are a multilayer formulation where each layer of the network extracts features of the inputs. When using a convolution network with two-dimensional data, the network is designed to be invariant to scaling, translation and skewing among other forms of distortion. An example of a convolution ANN processing a 24 by 24 pixel image is shown below in Figure 3-8.

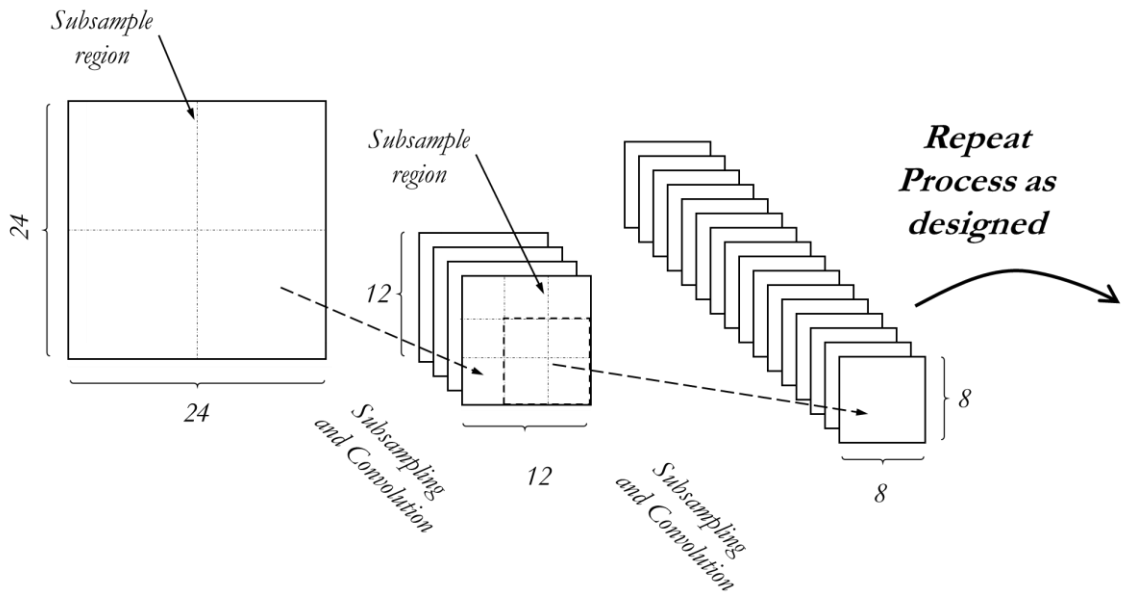


Figure 3-8, Convolution artificial neural network showing the first two layers.

Convolution ANNs have been utilized by Siddiqui, Bharadwaj et.al. to make nowcasting predictions of solar irradiance [140]. They combine the nowcast with real time images of the sky to produce one to four-hour irradiance predictions.

Time delay networks are added for completeness despite there being no examples of this network in use for irradiance forecasting in the papers reviewed. Time delay ANNs perform a similar task as a convolution ANN but on the input side instead of in the network. For time delay ANNs, the input is time delayed and aggregated instead of using a single data vector as one input. This is highlighted below.

$$I_t = S_{t-2} + S_{t-1} + S_t \tag{3-23}$$

Where I is the input vector and the ANN at time t, and S are the sample vectors at previous time intervals.

#### 3.2.2.8. Self-Organizing Maps

Self-organizing maps (SOMs) are typically organized in a two-dimensional map where the weights of the ANN are based on the distance from other activated weights. Higher dimensional self-organizing maps also exist. SOMs have been used to produce irradiance predictions to prevent overfitting of the data [142].

#### 3.2.2.9. K-Nearest Neighbor

The K nearest neighbor methodology is a form of unsupervised learning. The algorithm utilizes a single data point and a preset "K" number of neighbors. The data point calculates a distance from itself relative to all other data points. It then selects the highest number of reclassified points. For example, if the data point in question is based on K equal to three, and two of the three classes of nearest neighbors are close to (arbitrarily chosen) class "4", the classification of the data point would be class 4. If there is an equal number of classes for each nearest neighbor, the algorithm fails, or the algorithm could return the closest class of the nearest neighbor of other data points.

Chu, Coimbra and Pedro have utilized this algorithm along with global horizontal irradiance, direct normal incidence and sky images to make 5-30 minute irradiance predictions for PV farms [143], [144], [145]. They achieved forecasts improvements of 10% to 25% over persistence models utilizing global horizontal irradiance and direct normal irradiance.

#### 3.2.2.10. Clustering Algorithms and Support Vector Machines

Other clustering algorithms have been utilized as a preprocessing to further algorithms. Due to the low dynamic range of visual images utilizing clustering algorithms and support vector machines as prediction methodologies, clouds often appear brighter than the corresponding insolation values at the time of the prediction. Several methodologies for intrahour irradiance predictions utilize a clustering algorithm to correlate current cloud thickness to irradiance values. Then a separate methodology is employed to make irradiance predictions base on ground or satellite images [146], [147], [148].

Support Vector Machines (SVMs) are included for completeness as a separate form of bifurcation of data. SVMs can classify nonlinear data by processing it with multiple mathematical transformation in order to better find a binary linear classifier. In two dimensions, the data is separated by a line. In three and higher dimensions the processed data is bifurcated with planes and hyperplanes.

## 3.3. Short-term and SIMF Methods in Literature by Collection Technology Type and Forecasting Length

A review of the relevant literature about the mathematical models used to make irradiance predictions was highlighted above. A review of the technologies used to make irradiance predictions follows.

### 3.3.1. Single Sensors Ground Based Camera Systems

There are two main categories of apparatuses that obtain images of the sky form the ground. The first category is like that of a telescope, where light is reflected off a curved mirror. The second category is direct observation with a fisheye lens. In both cases, a physical and/or electronic shutter was sometimes employed to produce higher dynamic range pictures. This was often done by combining multiple pictures taken sequentially.

#### 3.3.1.1. Total Sky Imager

One of most common technology for irradiance forecasting is the use of a Total Sky Imager (TSI) [149], [150], [151], [152], [153]. The TSI is a visible spectrum reflected imaging system to capture images of the sky and surrounding clouds. A picture is shown below in Figure 3-9 highlighting a TSI 440B from the manufacture's brochure [154].

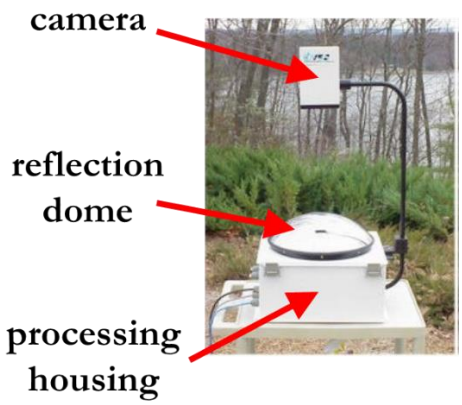


Figure 3-9, Total Sky Imager 440B.

The apparatus has a CCD camera (640 x 480 pixels) that looks down at a curved mirror. The near hemispherical dome allows for the reflection of almost all the sky and clouds.

Along with taking pictures the TSI has an algorithm that parses out clouds from the sky. An example is shown below.

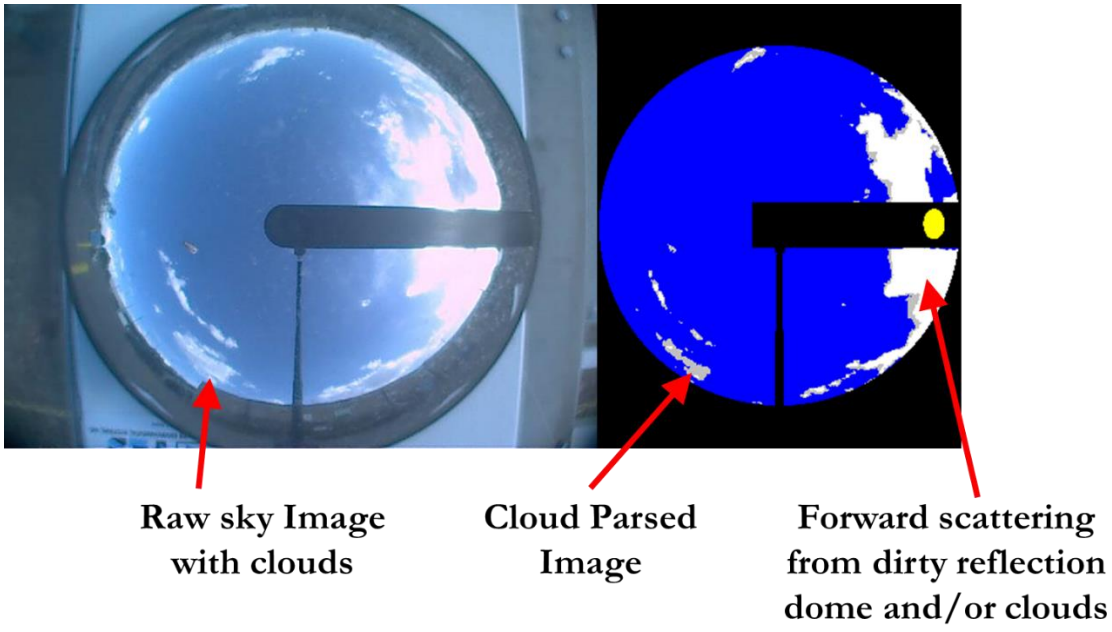


Figure 3-10. Cloud parser example with the TSI 440b identifying clouds. The shadowband is highlighted with the black overlay.

To minimize the forward scattering from the sun a shadowband is painted onto the reflective surface of the TSI. The round reflective mirror rotates with the sun throughout the day so the shadowband is always in the line with the ecliptic longitude of the sun, blocking it in the image.

Sample images taken from Sandia National Laboratories Total Sky Imager are shown below to highlight a cleanliness problem associated with the robustness of the

technology. One should note the red arrow pointing to bird poop that has been classified as a cloud.

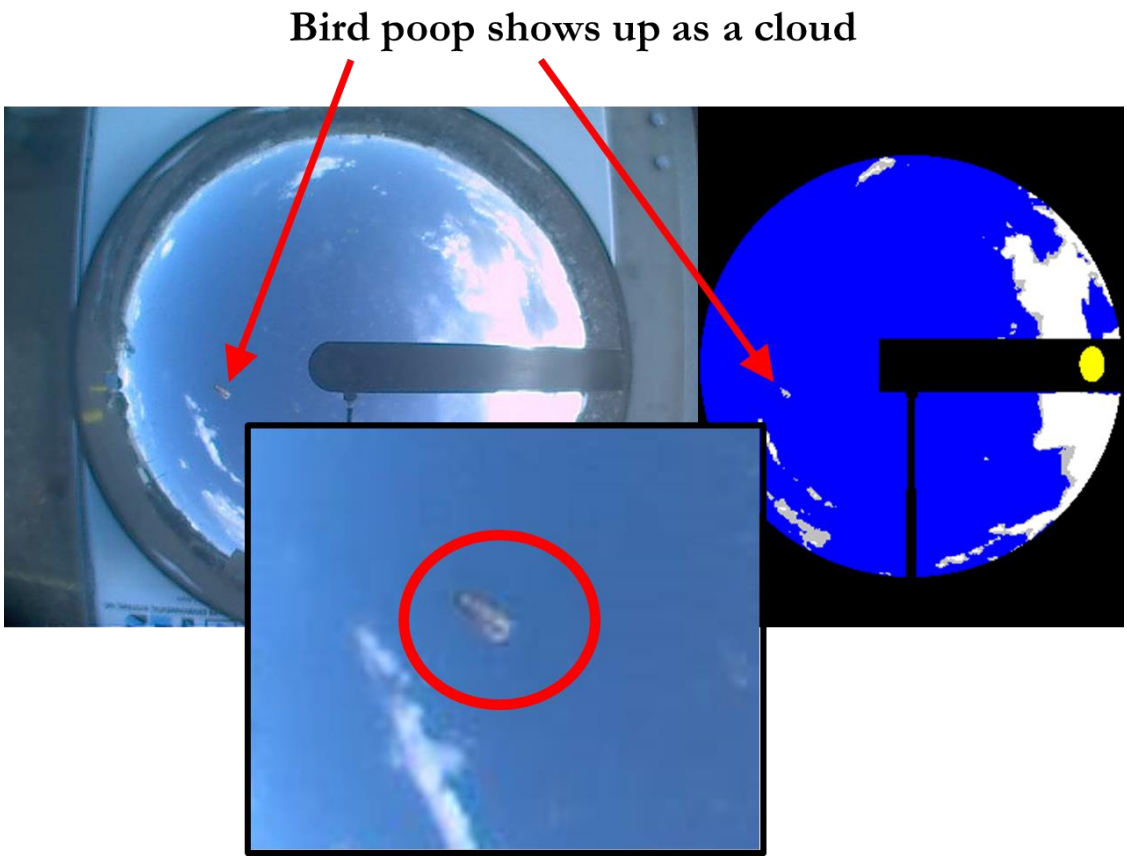


Figure 3-11. Total Sky Imager (TSI) pictures from Sandia National Laboratories. The picture on the right is the automated cloud detection algorithm built into the TSI system. The bottom TSI also mistakes the bird poop as a cloud.

In addition, Mie scattering around both the sun and near the horizon are producing artificial cloud images. This is due to the small water spots from past rain.

The main drawbacks of the TSI apparatus are listed below.

1. The shadowband occludes clouds near the sun and thus removes some potentially significant information.

2. The reflective surface needs constant maintenance by keeping it clean from rain spotting and bird excrement among other debris. Birds are a particular problem because the camera apparatus on top makes an ideal landing area.
3. Cosine distortion of the picture near the horizon is amplified by the round reflective mirror geometry.

#### 3.3.1.2. All Sky Imager and Generic devices

Another popular technology used for irradiance forecasting is the All Sky Imager and similar wide field-of-view camera imagers encased in a weather enclosure [155], [156], [157], [158], [159], [160]. The All Sky Imager made by EKO Instruments B.V and is shown below in Figure 3-12 from their brochure [161].

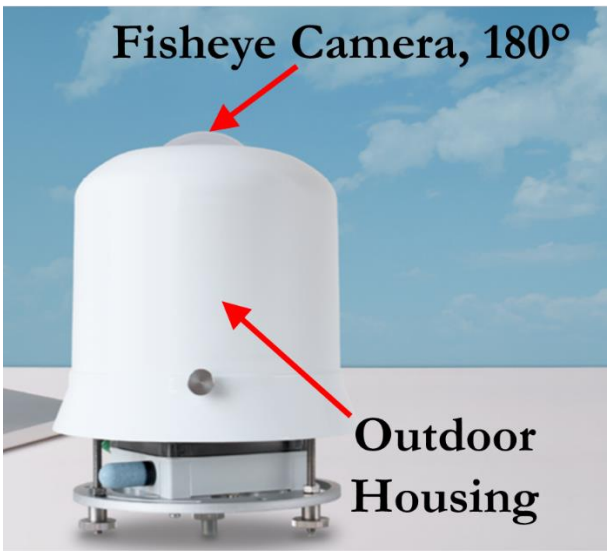


Figure 3-12. All Sky imager, ASI-16.

Unlike the TSI, the All Sky Imager (ASI) directly looks at the sun and does not have a shadowband to prevent or limit forward scattering. The TSI has a 180° field of view.

Though similar in lens distortion the ASI has similar main drawbacks. They are listed below.

1. Cosine distortion of the image still occurs near the horizon.
2. The ASI has no sun occlusion to limit forward scattering.

Lastly, the ASI has an algorithm for estimating cloud height that is built in. To obtain cloud heights, however, multiple ASIs must be utilized.

#### 3.3.1.3. Cloud Base Height Estimations with the TSI and ASI

Several articles pertaining to irradiance forecasting have utilized multiple TSIs and/or multiple ASIs to estimate the cloud ceiling height [162], [163], [164], [165], [166]. It is advantageous to estimates of cloud heights to enhance prediction accuracy near the horizon. This is because the effects of the cosine error near the horizon can be directly calculated when the cloud ceiling height is known. Cosine error occurs when the angle normal to the plane is non-zero. When a pixel is projected onto a plane, the new area it occupies is proportional the size of the pixel divided by the cosine of the angle relative to the normal. Cosine error is of course zero when the sun is directly overhead.

Knowing the cloud height is also advantageous due to transmission through higher level clouds being different from lower heights. Intuitively, this would make sense as clouds above 50,000 ft. are light and wispy, whereas lower height clouds can be much denser and allow less irradiance through them. This is important because, in the

visible spectrum, clouds of different irradiance transmission levels often have disproportionately similar pixel values.

### 3.3.2. Multiple Sensor Networks

Multiple sensors are often used to produce irradiance forecasting for a given area. This methodology shifts the costs associated with irradiance predictions from a single expensive sensor at the forecasting site to multiple low-cost sensors across a large geographic area, like a city. The disadvantage is that a communications infrastructure must be in place and operational for the system to work. In a smart grid context or at a commercial level where communications infrastructure is operational, this is a more feasible goal.

Using small scale PV installation infrastructure is a methodology that that has the advantage of not needing additional sensors [167], [168]. However, a communications infrastructure must be installed and operational for the system to operate.

Other methodologies for irradiance forecasting with multiple sensor networks rely on embracing the infrastructure challenge by installing specific sensors for irradiance measurements. One model has been studied to install small, portable, PV powered cellular connected radiation measurement sensors [169]. Another methodology is to use the already installed, smart-grid connected irradiance measurements at reliable locations, like a substation [170].

A third methodology does not require any additional sensors. Bessa, Trindade, Silva, and Miranda used feeder information and smart-grid enabled PV sites to make irradiance predictions for six hour-ahead forecasts [171].

The distance of the sensors relative to each other and the distance to the forecast site have a large effect on the timeframe of prediction for multiple sensor network irradiance forecasting methodologies. These parameters can be controlled by adding more sensors, but that comes at a cost.

### 3.3.3. Weather Data Models

Weather models are included for completeness. However, weather models for irradiance forecasting are almost exclusively for longer predictions of greater than one hour. They typically take weather variable like winds speed, ambient temperature and current irradiance among others as the inputs to their models [172], [173], [174], [175], [176]. Spatial data about surrounding sites as well as site elevation, latitude and panel tilt have also been investigated as parameters of investigation for weather data models in the literature [177], [178]. Helioclim maps have been investigate for 30-min. to 6-hour irradiance forecasting [42]. Helioclim maps are daily average irradiance maps of a given area. In another use of weather data Huang and Thatcher investigated using the Conformal Cubic Atmospheric Model (CCAM) and the Global Forecast System (GFS) weather data models for future irradiance forecasts at a resolution of 4-km [179].

### 3.3.4. Satellite Data Models

Satellite data models are included for completeness; however, their models are best suited for a 30-minutes to 3-hour ahead forecasting [180]. Satellite data is used to observe surrounding clouds and project the cloud path and shadows onto the ground. They are useful to longer term predictions of large cloud masses.

### 3.3.5. Irradiance Input Models

Irradiance input models are more akin to signal processing than forecasting in that they are highly dependent if not solely dependent on irradiance only as the input. Triple exponential smoothing and autoregressive methods are popular employments of utilizing past irradiance data as a prediction of the future [181], [182]. Other models preprocess irradiance data first and then input that result to an ANN [183].

### 3.3.6. Simulations

Simulations are included because it is often useful to validate a model on a varied data set, especially when that data does not exist. Jamaly and Kleissel generated virtual clouds and irradiances using a large eddy, fluid dynamics code [184]. In another simulated data set, Kurtz, Mejia and Kleissl used a large eddy simulation and a 3D radiative model to produce synthetic sky images and irradiance measurements [185]. Simulations are useful in predicting day ahead irradiance predictions.

# 4. Literature Review of Adaptive Resonance Theory and LAPART Architecture

The ANNs reviewed thus far have always used a cost function along with some sort of gradient method. However, a relevant question to ask is: *Is the network simply memorizing when deep learning, or is there an inherent structure to the data that enables learning in the traditional sense?* An attempt to answer this important question came out of a paper titled, 'A Closer Look at Memorization in Deep Networks' [186]. Their research compared multilayer ANN backpropagation learning of randomly labeled data sets to that of properly labeled data sets. When comparing the learning accuracy of random labeled data to that of proper data they found comparable results. The structured data did provide better absolute but not statistically significantly better results. However, when they compared the rate at which the weights updated and the network eventually stabilized via the weights no longer changing significantly, they found that the properly labeled data converged non-linearly fast as measured by the number of epochs needed. The random data converged at a linear rate, showing no such non-linear learning behavior. This could imply that structured data has inherent features and ANNs are learning a structure as opposed to memorizing answers.

Since ANNs have some other structure to learning aside from simple memorization, a second question arises; *If a local minimum on the surface of the cost function is found, do all local minima provide similar accuracy answers?* This question was investigated by a team of researchers who found, assuming the data is structured, all local minima do provide

roughly equivalent answers [187]. Thus, it is not essential to find the absolute maximum to learn structured data. The same was not true for unstructured or random data.

It was shown that ANNs are doing more than simple memorization. This motivates two new questions. *How fast does the network learn and how, or does, the network forget?* The stability-plasticity dilemma highlights this forgetfulness question which Adaptive Resonance Theory (ART) attempts to provide an answer to.

## 4.1. Adaptive Resonance Theory Stability and Plasticity

The stability-plasticity dilemma is highlighted by the following example. Imagine the sitting in Plato's Allegory of the Cave [188] as a captive person watching the shadows on the wall. The stability of the captor's brain is well established to recognize shadows on the wall. However, when the captor breaks out of their mental prison and they wander out of the cave, the novelty of seeing the full beauty of all the colors, they recoil and do not want to accept this new stimulus. They recoil because their brain is "stable" and has been trained only on shadows. Comprehending colors would require a degree of neural "plasticity" to learn novel situations of which they cannot.

The Allegory of the Cave highlights the in-plasticity of the human brain. The whole point of the allegory of the cave is a comment on humanities stability of thought to accept the shackles of propaganda and the extreme hardship of plastically adapting one's own neuro-kinetics to a new form of thinking. The same problem occurs with

ANNs, where the ANN may be very good at recalling situations of the past from a stable learning process, but then fail plastically when they encounter a novel situation.

Gail Carpenter and Stephen Grossberg highlighted this tradeoff in their 1987 introducing Adaptive Resonance theory. "*The properties of plasticity and stability are intimately related. An adequate system must be able to adaptively switch between its stable and plastic modes. It must be capable of plasticity in order to learn about significant new events, yet it must also remain stable in response to irrelevant or often repeated events.*" [189] Adaptive Resonance Theory (ART) attempts to address this dilemma by adapting the networks size to learn novelty yet maintain memory [190], [191].

ART 1 and ART 2 are both forms of an unsupervised feedforward ANN used for categorization of binary input patterns [192], [193], [194]. Where ART 1 will directly categorize a binary input pattern, ART 2 adds another layer to quantify a binary pattern. This input pattern is then fed-forward where its category membership is subject to (4-3). A fuzzification process was introduced for the input as highlighted in (4-1). This allowed floating point numbers so long as each component of the input was normalized between zero and one.

## 4.2. ART Maps and LAPART

Fuzzy ARTMAP and ARTMAP utilize a combination of two feedforward fuzzy ART and general binary ART networks to create a relationship map between them [195] [196]. To illustrate this mapping process, the Laterally Primed Adaptive Resonance Theory network (LAPART) is introduced below. LAPART highlights the ARTMAP

process while adding an additional lateral priming pre-search algorithm [197], [198], [199], [200].

In the fuzzy form, the normalized input must be complement-coded as follows:

$$I = (a, a^c) = (a_1, a_2, 1 - a_1, 1 - a_2) \tag{4-1}$$

The weight update follows the equation:

$$W_J^{new} = \beta\left(I \wedge W_J^{old}\right) + (1 - \beta)\left(W_J^{old}\right) \tag{4-2}$$

Fast learning occurs when $\beta = 1$.

Fuzzy ART then solves these two equations to find a category:

$$T_J = \frac{\|I \wedge W_J\|}{\alpha + \|W_J\|}$$

$$\|D\| = \sum_{g=1}^{m} |D_i| \tag{4-3}$$

$$\alpha \leq \frac{1}{n-1}$$

Subject to vigilance:

$$\rho \leqq \frac{\|I \wedge W_J\|}{\|I\|} \tag{4-4}$$

When Fuzzy LAPART is presented a new input if both (4-3) and (4-4), then the preferred category is the max choice from (4-3).

Fuzzy LAPART is a connection of two Fuzzy ART networks, with the ability to create new categories. A diagram of the Fuzzy LAPART network is shown below.

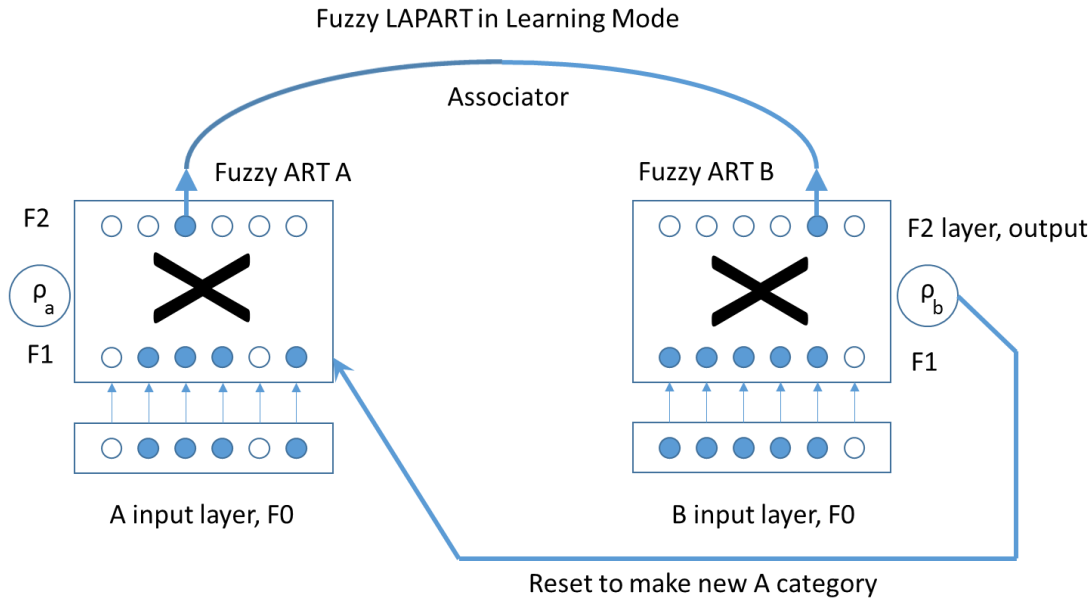


Figure 4-1. Fuzzy LAPART in Learning Mode.

When learning is not occurring, the B side reverses and a prediction is made based on the associator. This prediction mode is shown below.

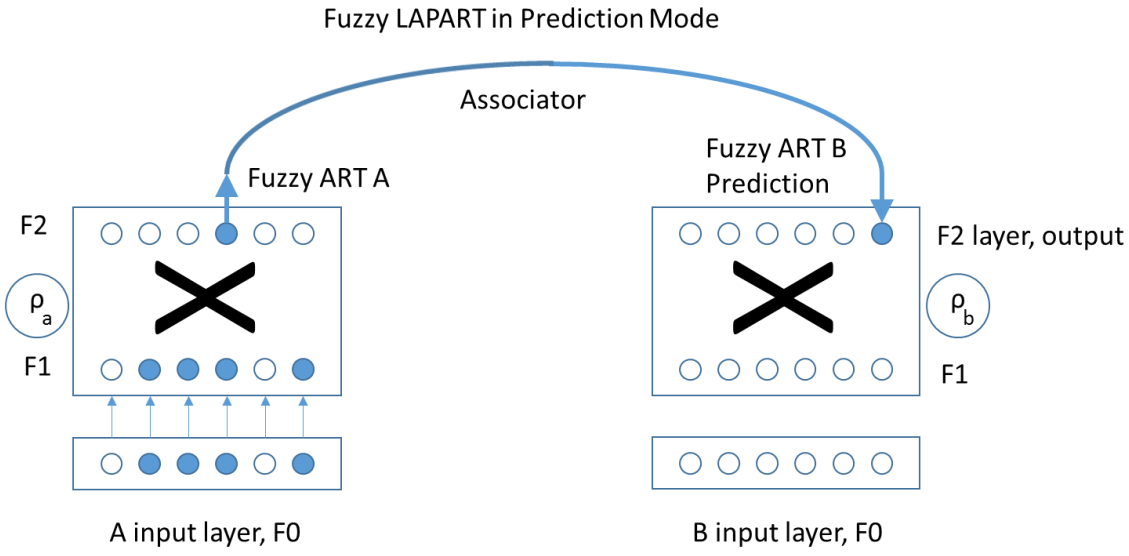


Figure 4-2. Fuzzy LAPART in Prediction Mode.

Four scenarios arise when the network is active. They are listed below:

1. New A and New B categories; Make new A and B categories. Update the associator and weight matrix.
2. New A and Old B categories; Create new A category and select the max choice for the B category. Update the associator and weight matrix
3. Old A and New B categories; This cannot exist because the associator already has an association to an existing B category. Proceed as normal in step 1 by making a new A category.
4. Old A and Old B categories; Find the A category and see if it corresponds to a B category that also passes vigilance. Proceed to the next passing A category and repeat. If no category in B can be found that passes vigilance and is associated to a passing A category, proceed to step 1 by creating a new A and B category.

The process then repeats for a new input or (4-2 is utilized for learning.

## 4.3. Advantages of LAPART for SIMF

A main advantage of LAPART for microforecasting is speed at which it converges. LAPART has no mathematical proof of stability as old input could theoretically continue to jump around in different categories. LAPART 2 is a modified version of LAPART. It creates a new A category during the second training input if the previously found A category is no longer the maximum choice and/or it no longer passes vigilance.

When utilizing LAPART2 the ANN provides a guaranteed two pass input representation convergence [201]. LAPART typically converges in two if not three passes, though as stated before, there is no convergence proof. The speed at which LAPART learns is an incredible advantage to training in low power computational environments. Often the number of backpropagation representations of other traditional supervised networks can reach into the thousands or more for relatively simple multilayer ANNs.

When making output predictions, LAPART has the advantage of providing a max choice return always, weather it passes vigilance or not. Even if LAPART does not have an officially converged answer, it can still provide an output prediction.

Anomaly detection is another major advantage of LAPART and ART in general. It was discussed earlier and is mentioned here to emphasize its importance. It relates to the robustness of the network to be able to return an answer even if no official convergence is found. LAPART can return an answer and utilizing the vigilance parameter, it also can quantify the degree of novelty of that solution. This is a huge advantage over other ANNs.

# 5. Design Goals and SIMF Technology Solution Iterations from Visual to Far Infrared Photon Sensors

It is important to have a concise and logical design goal before starting any project. The design goals for this SIMF project are listed below:

1. An accurate prediction of a PV array output 30 seconds to 10 minutes into the future.
2. A small (around one cubic foot) apparatus that is located at the PV site and looks at the sky and can see both the sun and surrounding clouds.
3. An apparatus cheap enough to be adopted by utilities and as a secondary goal, cheap enough to be adopted by residential consumers for utility use. At a minimum, the cost must be able to offset the operational values of the data it provides. This is more likely to occur with utilities first.
4. An apparatus that is highly reliable, will last 10 years, has minimal if any moving parts and requires little or no maintenance at all.
5. An apparatus adaptable enough to be used anywhere in the world.
6. An apparatus that learns and predicts better as more learning occurs.

The design goals are presented in four sections to illustrate the temporal progression of the multiple hardware options that were utilized in each proof of concept. Every

progression utilizes progressively lower energy photon sensors. This progression is summarized in Figure 5-1.

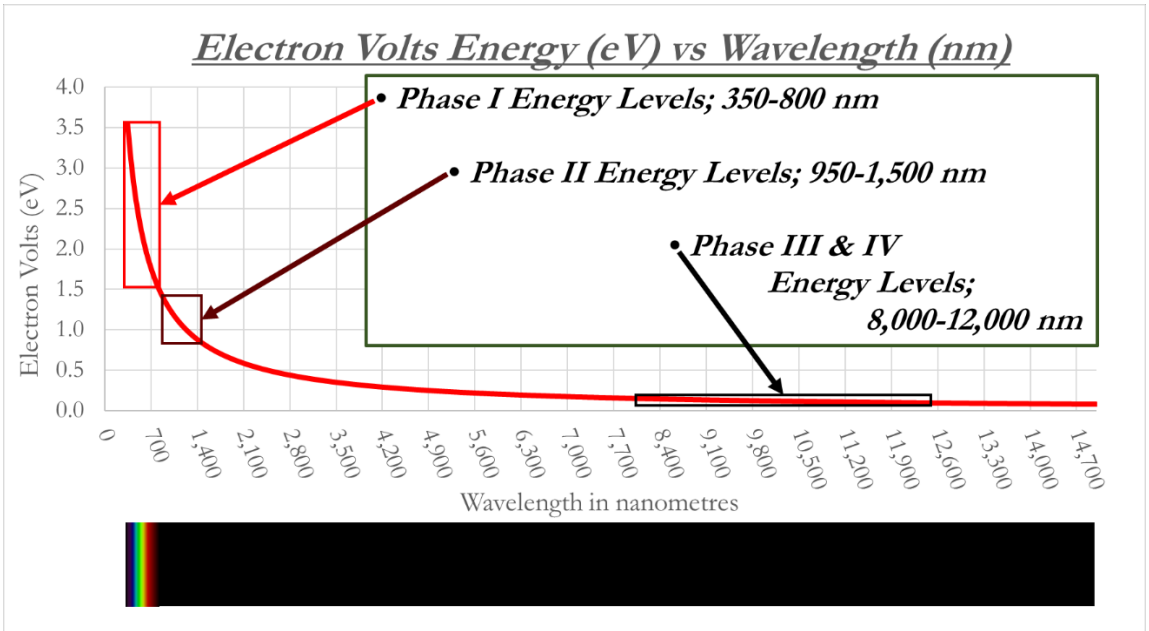


Figure 5-1, Technological progression summary by phase and working energies.

The motivation for this progression toward lower energy wavelength sensors becomes clear when the entire range of the spectrum is utilized for an image. This is especially apparent when image captures are needed near the sun.

## Review of Optical Problems Associated With Photographing Near the Sun as a Driving Technological Motivation

Pixel saturation occurs when a photon detector is over activated by photons (typically of the sun) and the activated pixels begin to activate neighboring pixels also. With older film cameras, the film was prevented from over exposing by restricting the light

input via an iris which constricted the radius of the lens. Newer DSLR cameras sometimes utilize a physical iris but often they do not.

In order to save money CCD or CMOS detector utilize a electronic shutter and no iris [202]. An electronic shutter is a sensor, typically CCD or CMOS for visual, with a filter in front of it to deaden the burden of the incoming photons. The sensor acts with a quasi-photoelectric effect to generate a current. Before the picture is made, the electronic shutter can turn up or down the sensitivity of all of the sensors. This ensures that not too many pixels are too dark and not too many pixels are too bright. This methodology works well assuming the pixels will not be overloaded by an overwhelming signal, like the bright sun.

If the sensor or film were only overloaded by one isolated signal, that may be fine as a strategy for image acquisitions. Since the sun is only approximately 0.5° as viewed from earth, the sensor should only have a few overloaded pixels, in hypothesis. In fact, pixel bleed over has an effect also, but the overwhelming problem that occurs when photographing the sun occurs with Rayleigh scattering. Because direct radiation from the sun is so extremely intense, the scattering of light from particulate matter and molecules of air in the sky also saturates surrounding pixels. However, Rayleigh scattering, depending on how far in angle it is from the sun can often be attenuated with the automatic shutter, physical shutter and/or iris.

The problem of extreme dynamic range photographing near the sun was highlighted. Possible solutions to this photon energy dynamic range problem could include

filtering the images or taking multiple pictures from multiple cameras. Or another idea would be to take multiple pictures with the same camera but with different automatic shutter settings. This multiple high dynamic range picture acquisition is a feature of the Total Sky Imager. [154] They also attempted to mitigate pixel saturation by painting the shadowband on the mirror. However, we decided to move technologically to lower energy sensors. This enabling technology was made possible around the year of 2017, by the introduction of the Flir Lepton© and the subsequent development of the breakout/interface hardware boards. The temporal progression of the technology selection follows.

## 5.1. Hardware and Apparatus Proof of Concept I, Visible Spectrum Sensors; 350-800 nm, 3.5-1.5 eV

A main advantage to using simple CMOS cameras for SIMF is the cost of the technology. Cell phone cameras are very cheap. If costs were a main factor in this technological goal, cheap cameras may have been a better technology source. However, the functionality and inconsistency make them a sub optimal technology choice.

Lens flare is another problem encountered with imaging the sun. When multiple lenses are present and the camera is capturing a very bright object, the lens will often reflect a small amount of light. This will appear in the form of a single dot for every reflection or large rings around the bright object. An advantage to simple cameras is

the lack of multiple lenses, but all cameras with any lens suffer from lens flare problems.

When investigation the use of cheap CMOS cameras, a cross spectral neutral density welding filter was applied to multiple pictures of the sun with surrounding clouds. A sample of four pictures and the surrounding clouds taken with an inexpensive CMOS camera is shown below in Figure 5-2.

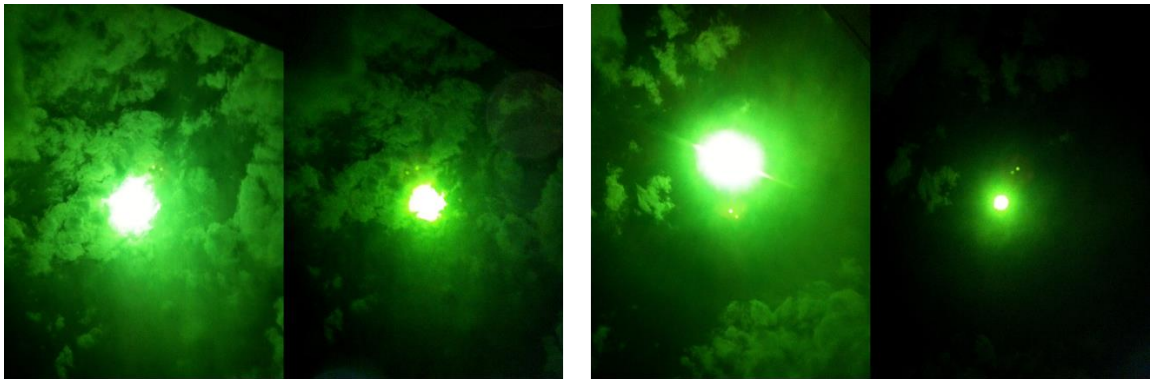


Figure 5-2. Complementary metal–oxide–semiconductor (CMOS) pictures with neutral density filter welding filter #10 and #12 & #10 and #13.

A methodology was to be utilized where two cheap shutter-less cameras take pictures through different opacity filters. The two pictures would then be combined to create a high dynamic range picture. From visual inspection, many cases it appeared that more than two pictures may have to be acquired. One camera with a minimal filter could acquire images of the clouds away from the sun and one with a heavier filter would acquire images near the sun. The decision was made to move to lower energy wavelengths.

## 5.2. Hardware and Apparatus Proof of Concept II, Near Infrared Sensors; 950-1,500 nm, 0.15-0.10 eV 1.3-0.8 eV

The visible spectrum has wavelengths from 350 to 800 nm. However, CCD and CMOS sensors are sensitive to light outside of the visible range. Though all sensors are different, Figure 5-3 below illustrates that the relative response of a Charged Coupled Device (CCD) camera slightly protrudes into the near infrared range.

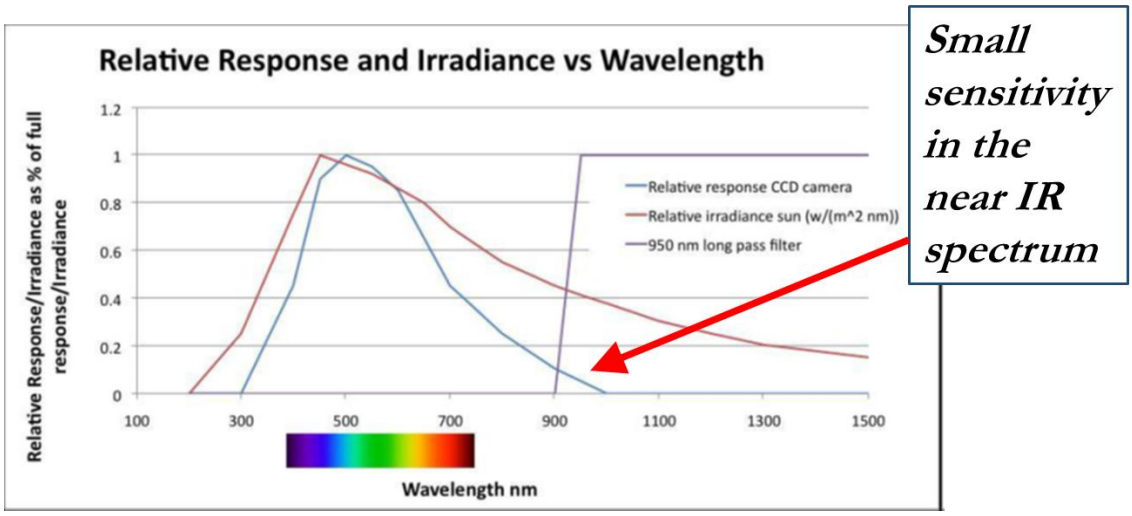


Figure 5-3. Charged Coupled Device (CCD) near-infrared relative response.

The next step was to utilize a camera that was sensitive to near-infrared wavelengths.

### 5.2.1. Near IR Experimental Apparatus, A

The first experimental apparatus is show below in Figure 5-4.

Figure 5-4. A. Top Left/Right; Nikon D40 charged coupled device camera utilizing a 950 nm long pass filter. Facing directly at the sun, is a LI-200R Pyranometer for irradiance measurements. B. Bottom right; shows an Eppley Laboratory solar tracker to track the sun. C. Bottom left, shows UNMs National Instruments NI-CompactDAQ chassis activation system to automatically take pictures of the sun and irradiance measurements at the same time at 10 second intervals.

The experiment was located on the roof of the mechanical engineering building in Albuquerque, NM. A Nikon D40 digital CCD camera with mechanical iris and mechanical shutter along with a 950 nm long pass filter was utilized. Irradiance measurements were made with a LI-200R Pyranometer, which always pointed directly at the sun. The tracking apparatus utilized was a repurposed Eppley Laboratory dual axis resetting solar tracker. Lastly, the electronics and control module were in an IP66 waterproof metal housing. The control module was built on a National

Instruments NI-CompactDAQ chassis with various modules. It took pictures and logged irradiance consecutively in ten second intervals.

The use of complex imaging equipment and continued lens flare problems made this technology impractical. Though this experiment did not meet any of the design goals, it was utilized as a proof of concept for the utilization of near IR photographs for SIMF.

Results obtained utilizing this data and the processing methods mentioned in the chapter Motivation for Accurate 2D Cloud Geometry; below were published as a proof of concept at the 2013 IEEE Conference on Technologies for Sustainability (SusTech 2013) [6].

### 5.2.2. Near IR Experimental Apparatus, B

Shortly after the construction of the first experiment, more research was done on the specifics of CCD and CMOS sensors. Almost all common digital cameras contain a neutral density visible band-pass filter. This filter significantly reduces the sensitivity of sensor outside of the visible range. Specific camera modification options can be implemented on cameras, whereby that filter is removed replaced with a different optical material. These filters typically come in two modifications, near IR sensitive and ultraviolet sensitive. Each conversion replaces the bandpass visible filter with a long or short-pass filter, while still allowing some visible spectrum. To highlight this conversion process visually, various photos are highlighted below in Figure 5-5. Photographers Andrew Steele and David (below) highlight photos taken with an

ultraviolet sensitive and near IR sensitive conversion, respectively. Anthony Menicucci took the picture with the visible spectrum bandpass filter completely removed on a Sony Cyber-shot DSC-H2.

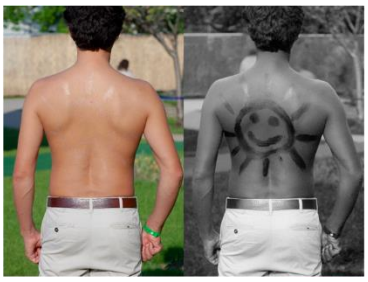

***Images above, taken by Andrew Steele, ultraviolet (UV) sensitive conversion (right) VS regular (left); File: Sunscreen on back under normal and UV light.jpg***

***Note: The different camera conversions affect the red, green and blue pixels differently.***

***Image By Anthony Menicucci, Band-pass filter removed, raw sensor; Name: Majestic Meadow Alumni Field***

***Image above taken by David; near-IR sensitive, Infrared converted Canon Rebel Xti; File: Infrared HDR Palmer Park Colorado Springs.jpg***

Figure 5-5. Ultraviolet, near IR and raw sensor digital photography examples [203], [204].

Note, when the filter is removed the sensor appears to be most sensitive to red. The second part of this near-IR sensitive experimental apparatus utilized a Nikon D-70 converted to near IR sensitive by the Life Pixel Infrared company [205]. A 950 nm long pass filter was also utilized. Dual camera sensitivity is illustrated in Figure 5-7 below.

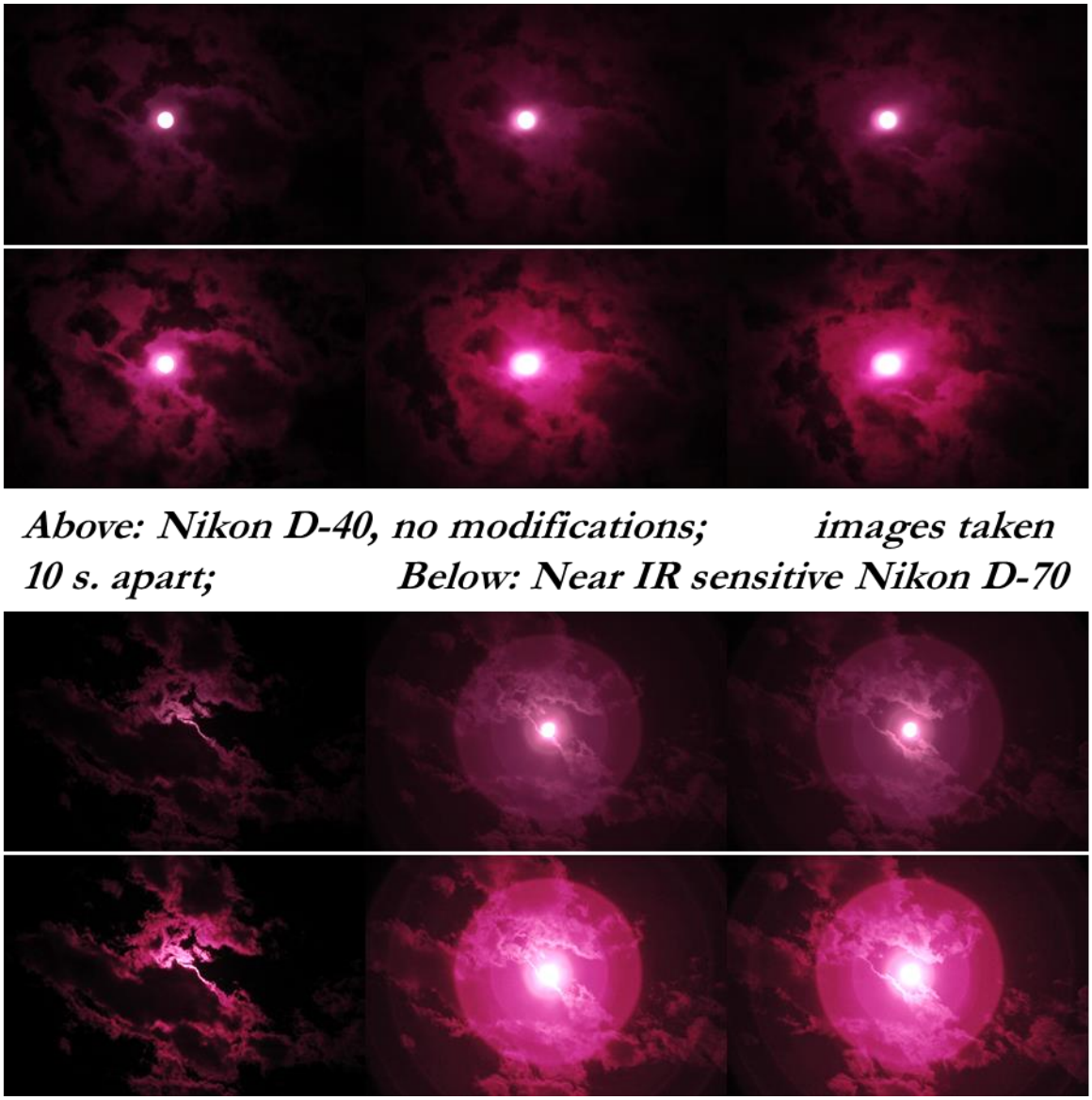


Figure 5-6. Different images of the sun and surrounding clouds. A. Above, Nikon D40 images. B. Below, Nikon D-70 near IR sensitive conversion. Both utilize a 950 nm bandpass filter and are contrast, brightness and sharpness enhanced.

The problem of taking photos near the sun is apparent when they are contrast, brightness and sharpness enhanced. Clouds near the sun are nonlinearly bright when compared to clouds radially further away. When utilizing the near-IR sensitive Nikon D-70 camera the problem of lens flare is also apparent. Lens flare occurs when a

small amount of light reflects onto the camera sensor from one of the many lenses. These artifacts are shown with green arrows in Figure 5-7.

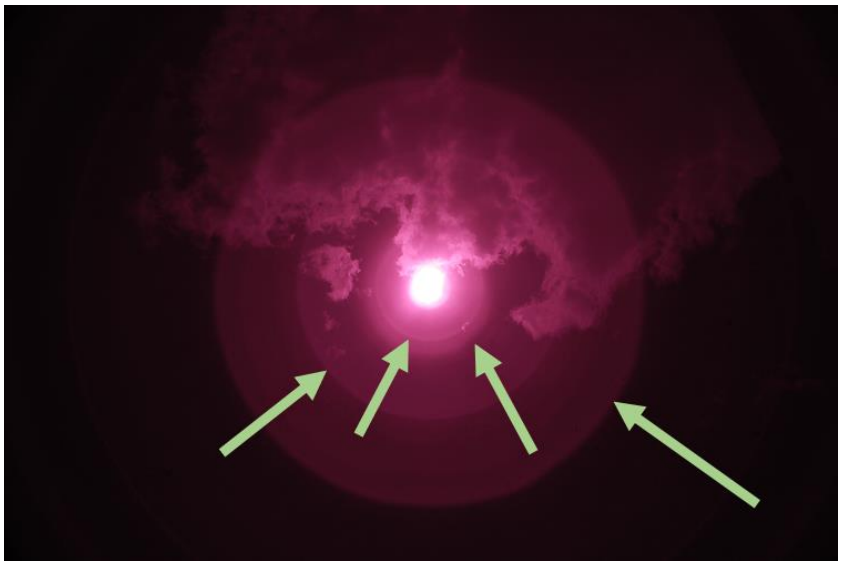

Figure 5-7. 950 nm Long Pass, near IR pictures taken with Nikon D70 on Feb. 7th, 2014. The green arrows point to lens flare artifacts that form in the optics.

If the sky conditions were the same every day at every time, a mitigation strategy could include subtracting a reference photo. However, all days and times do not present similar pictures, which makes implementation of a subtraction algorithm to reduce lens flare complex.

One variable affecting the size and shape of the artifacts is exposure time. Note the progressively larger flares as a function of exposure time in Figure 5-8.

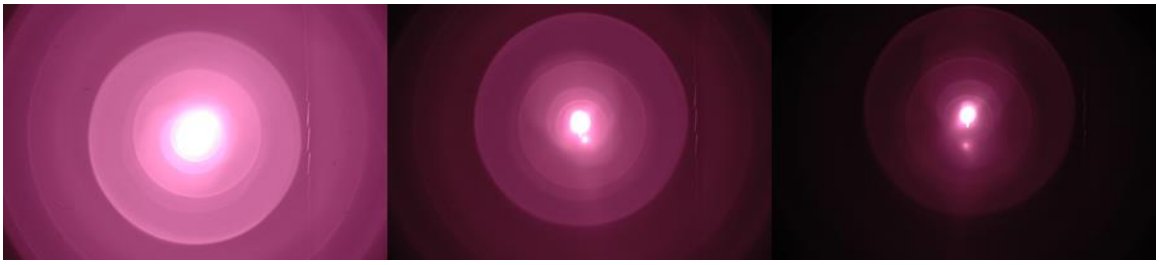

Figure 5-8. Lens flare artifacts as a function of exposure time. Nikon D-70, f/4 exposure time left to right; 1/100, 1/400 and 1/1250 s.

There are new artifacts that appear when the exposure time is extended. They were always there, but the extended exposure and near IR sensitive conversion, they then show up. Note that the flare is not exactly in the center of the sun when the sun is not perfectly in the middle of the picture frame. This would also affect a subtraction algorithm to filter out the lens flare artifacts.

A proof of concept was analyzed with this data and published at the 2013 IEEE Conference on Technologies for Sustainability (SusTech 2013) [6]. Accurate particle image velocimetry measurements were needed for cloud fluid flow analysis. This was almost impossible with lens flare distortion. Pictures were acquired every 10 seconds and a subtraction algorithm was implemented with the following attributes:

1. If both sequential images have irradiance above 800 W/m^2 proceed to step 2.
2. Subtract the images with the following equation.

$$I_s(\mathrm{x},\mathrm{y},\mathrm{z}) = abs(I_2(x,y,z) - I_1(x,y,z)) \tag{5-1}$$

Where x and y are the location coordinates and z is the R,G,B red green and blue channels.

3. Lastly, the image pixel was thresholded to a maximum red, green and blue if all the channels exceeded a certain value.

Below are three thresholded pictures that were utilized with a cross-correlation particle image velocimetry method to obtain average cloud velocities. The subtracted images are shown in Figure 5-9. The data-flag shown as a transparent green rectangle will be highlighted in the Motivation for Accurate 2D Cloud Geometry; chapter.

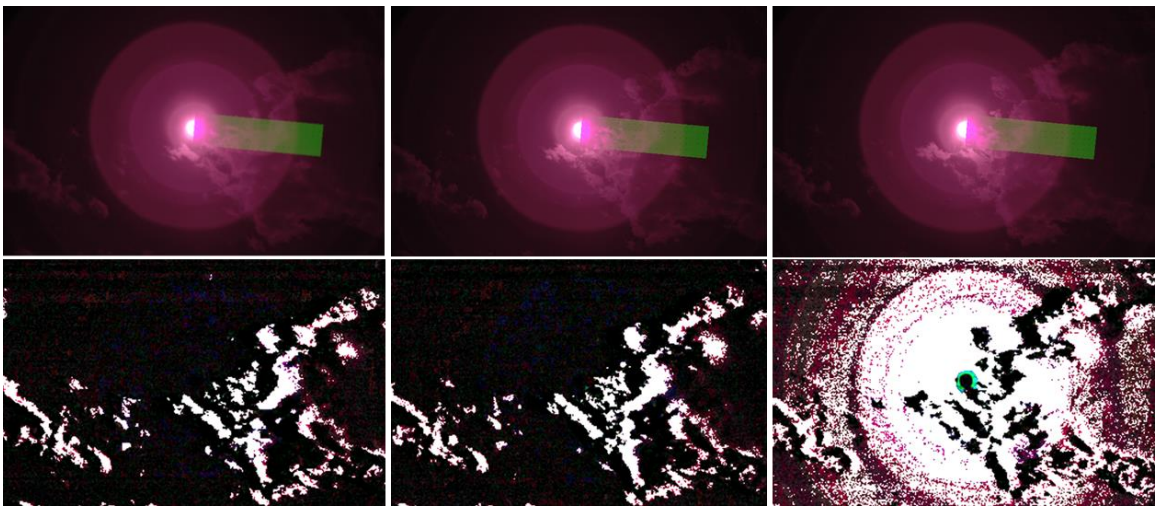

Figure 5-9. Particle velocimetry used on subtracted and thresholded pictures. Each image is taken at a 10 second interval.

The pictures in the top row are the originals and the bottom row contains the subtracted and thresholded images. They were obtained 10 seconds apart. Note that the last thresholded picture to the right fails in its algorithm. Though both pictures making the subtracted image had current irradiances above 800 $W/m^2$, the sun was occluded enough in the second one that the lens flare was not present in its average value. Thus, the thresholding produced a large amount of noise. These problems

and setbacks highlight a needed to move to a different technology for image acquisition.

## 5.3. Hardware and Apparatus Proof of Concept III, Far Infrared Sensors; 8,000-12,000 nm, 0.15-0.10 eV

In recent years, FLIR Systems has released the FLIR Lepton I and II modules. It is a 60 x 80 resolution long wave sensor sensitive from 8 to 12 μm that only costs around $200 per module. This breakthrough in technology has provided the ability to make a cheap SIMF system using a long wave infrared sensor. Since long wave infrared has a lower energy than visible or near infrared and therefore interacts less with particulates and air molecules, forward scattering around the sun is minimized. Examples of the Lepton module taken with the FLIR One and the raw sensor are shown below in Figure 5-10.

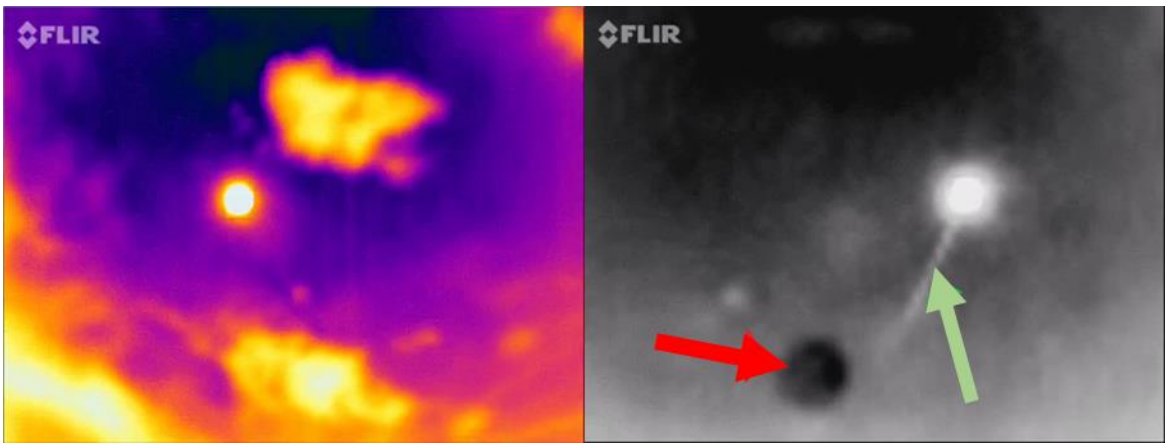


Figure 5-10. Far IR pictures taken with the FLIR ONE on April 27th, 2015 (left) and May 26th, 2015 (right).

The raw sensor modules shown in Figure 5-10 to the right is mounted to a stationary tripod shown in Figure 5-11.

Figure 5-11. Stationary FLIR Lepton with breakout on tripod.

The picture in Figure 5-10 on the left clearly shows the surrounding clouds with the sun as the white dot in the middle. The picture on the right colored, in grey scale, shows an overcast sky. The green arrow indicates a pronounced overheating in the sensor where the sun heated the pixels to a high temperature, and it remained hot after the sun moved. This burn was mitigated later using a germanium external window. The green arrow shows a spot on the camera where the pixels are not as sensitive as they should be. It is not a dead spot but rather a less sensitive spot.

Knowing that the dynamic range of far IR pictures is far smaller than that of the visible images, it was hypothesized that far IR pictures will yield better cloud

occlusion results due to better discernment of clouds from the sky with minimal forward scattering. Also, clouds show up through a different mechanism. Visible light in clouds is reflected, where IR light is mostly emitted by clouds. Initial results confirm this.

### 5.3.1. Far IR Tracking Experimental Apparatus, "The Dog House"

The first experimental apparatus that was constructed to investigate far IR methodologies was colloquially named "The Dog House". This is because it looked like a dog house located on top of the UNM Mechanical Engineering building. A CAD rendering is shown below with its various components.

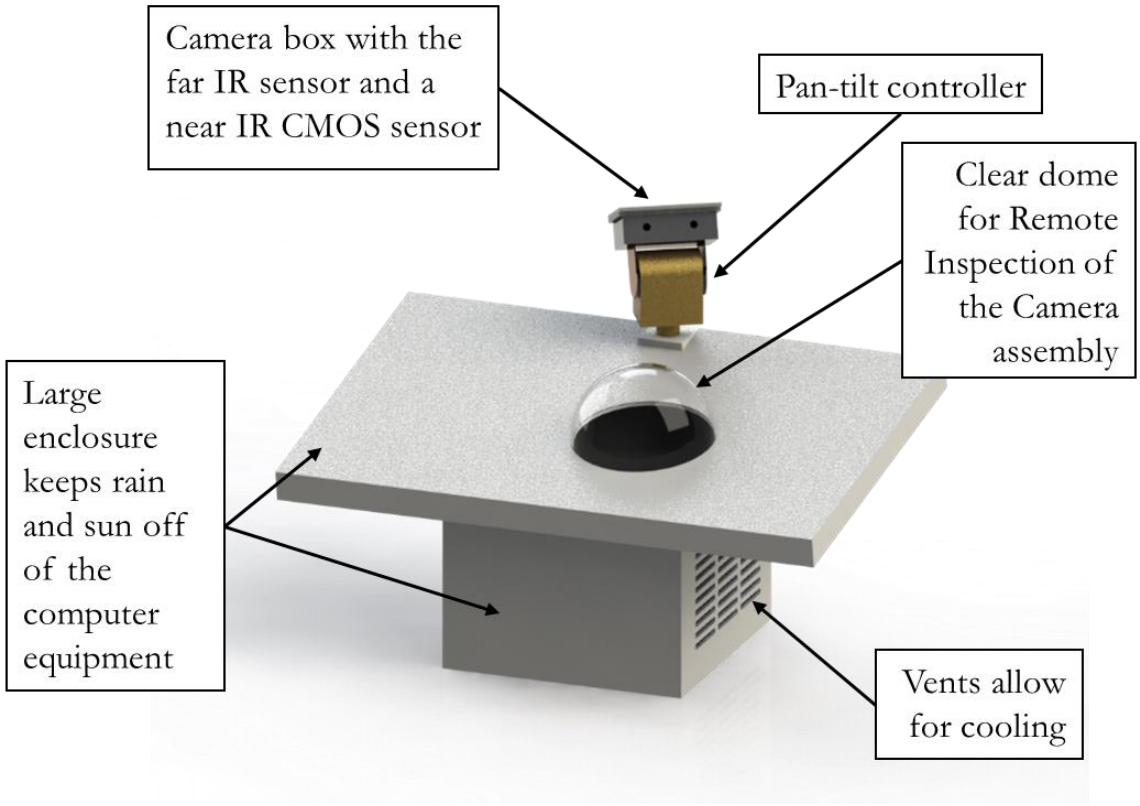


Figure 5-12. CAD rendering of the Dog House experiment at UNM.

It is approximately 3' x 3' x 6' and made out of ¾" pressed particle board that is painted with a highly reflective weather resistant white paint. A look inside is shown in Figure 5-13 below.

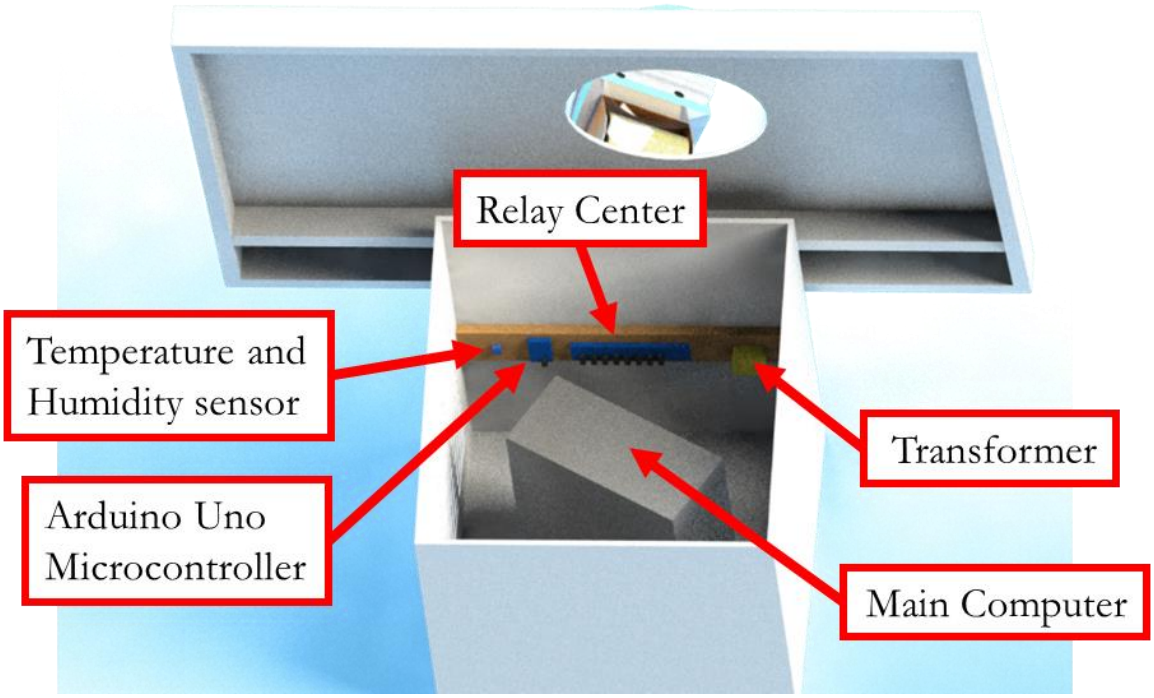


Figure 5-13. Internal components of the experimental apparatus.

The purpose for the large size of the experimental apparatus was to facilitate other experiments into the future. The dog house has the advantage of centrally locating all computer processing equipment physically close to the experiment. This is advantageous because one can develop end-use product technologies with the native data transfer protocols while simultaneously harnessing the more powerful computing of a desktop or cluster computer. SATA or Serial AT Attachment is one such protocol that degrades with cable lengths longer than three feet but is useful in end use programing. The dog house offered the ideal testing environment for high computational power, large cheap computer memory availability and a dual end-use harsh external environment for testing product design temperature resistance and waterproofness abilities.

The far-IR experiment pan-tilt controller was controlled via a rugged version of an Arduino UNO microcontroller and a solid-state relay board. All visual inputs from the sensors in the camera box were sent to the main desktop computer via a Raspberry Pi controller and temperature measurements were sent to the Arduino Uno inside of the dog house. An externally mounted Li-Cor global irradiance sensor was also sent into the Arduino UNO. At various times, it was advantageous to see if the camera box is moving when it is required to do so. A clear 12" dome was installed revealing a tilted halfsphere viewing window shown in Figure 5-14.

Figure 5-14. External Enclosure with the clear dome.

The Li-Cor used was used for irradiance measurements. It is shown below.

Figure 5-15. Externally Mounted Li-Cor global irradiance sensor.

Matlab was the central controller for the Arduino UNO and Raspberry Pi. Matlab also was utilized for all data processing.

As the months progressed into June, it became clear that indoor desktop computers, located on black roofs, on sunny days, were computationally powerful, but needed active cooling.

### 5.3.2. Far IR Tracking Experimental Apparatus, "The Cool Dog House"

A 5,000 BTU 115-Volt window air conditioner was installed on the east side of the unit. The cooling modification of course automatically renamed the experimental apparatus to, "The Cool Dog House", as an actual dog would be quite happy living in its consistently cool 55° F environment. The modification is shown in Figure 5-16 below.


Figure 5-16. Modified experimental apparatus with 5,000 BTU cooling unit.

Thought the air cooling unit cycled often, a temperature of 55° to 65°. F was maintained internally with no further complications. A vent on the west side reduced the number of cooling cycles that the air conditioner would require per hour.

#### 5.3.2.1. Near and Far-IR Camera Box

The camera box is a custom-built aluminum and 1" thick PVC enclosure with a removable top. It is show below in Figure 5-17 and was designed to stay outside.

Figure 5-17. Camera Box containing the far and near-IR cameras.

The apparatus uses a Pelco PT280 pan tilt unit with cylindrical coordinates. The internal components are shown in Figure 5-18 below.

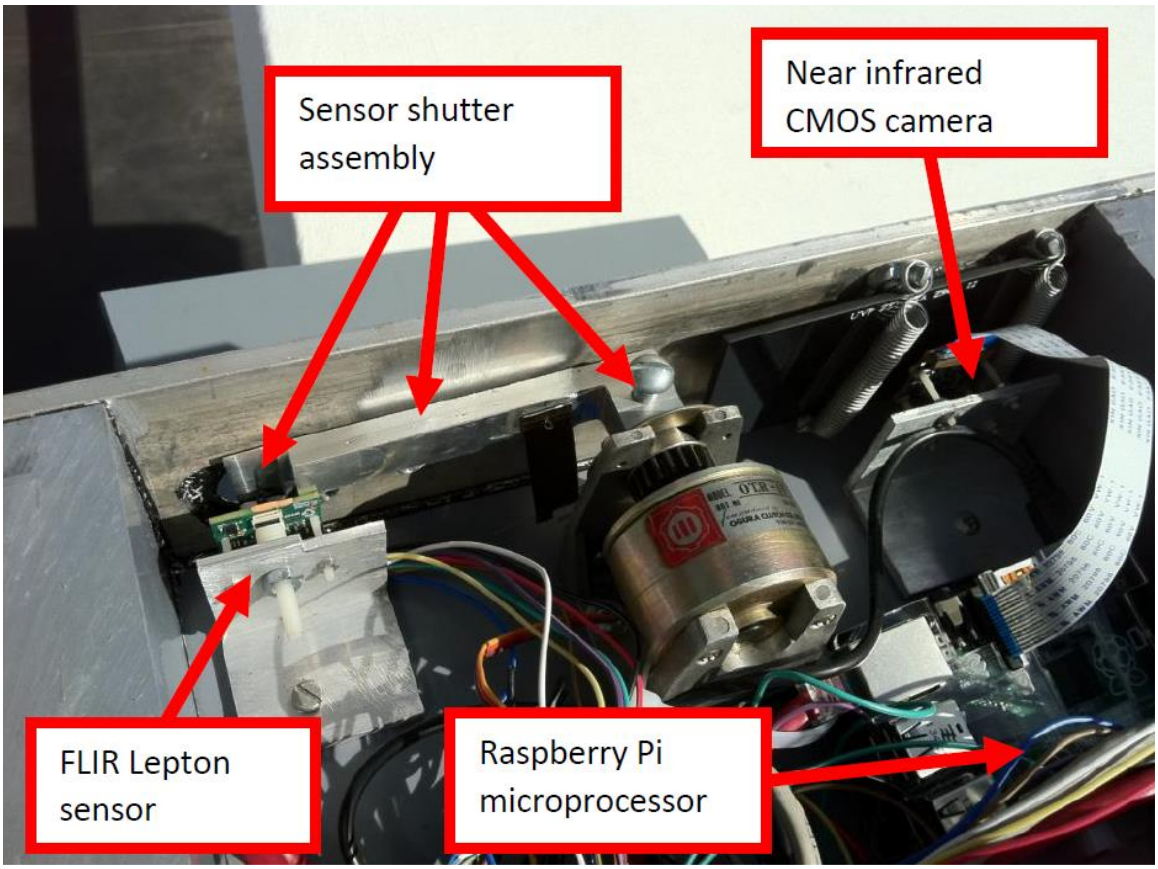


Figure 5-18. Internal components of the Camera Box.

In trying to mitigate sensor heating effects and because of the sensor burn that was highlighted in Figure 5-10, this apparatus was equipped with a manual shutter and the germanium window was also removed to assess the raw sensor values unobstructed. The shutter was opened and then a capture was obtained from the far IR sensor. After, the shutter was closed to prevent the sensor from heating up. A near IR CMOS sensor image was also obtained and installed to compare images. Samples of these images are shown below in Figure 5-19.

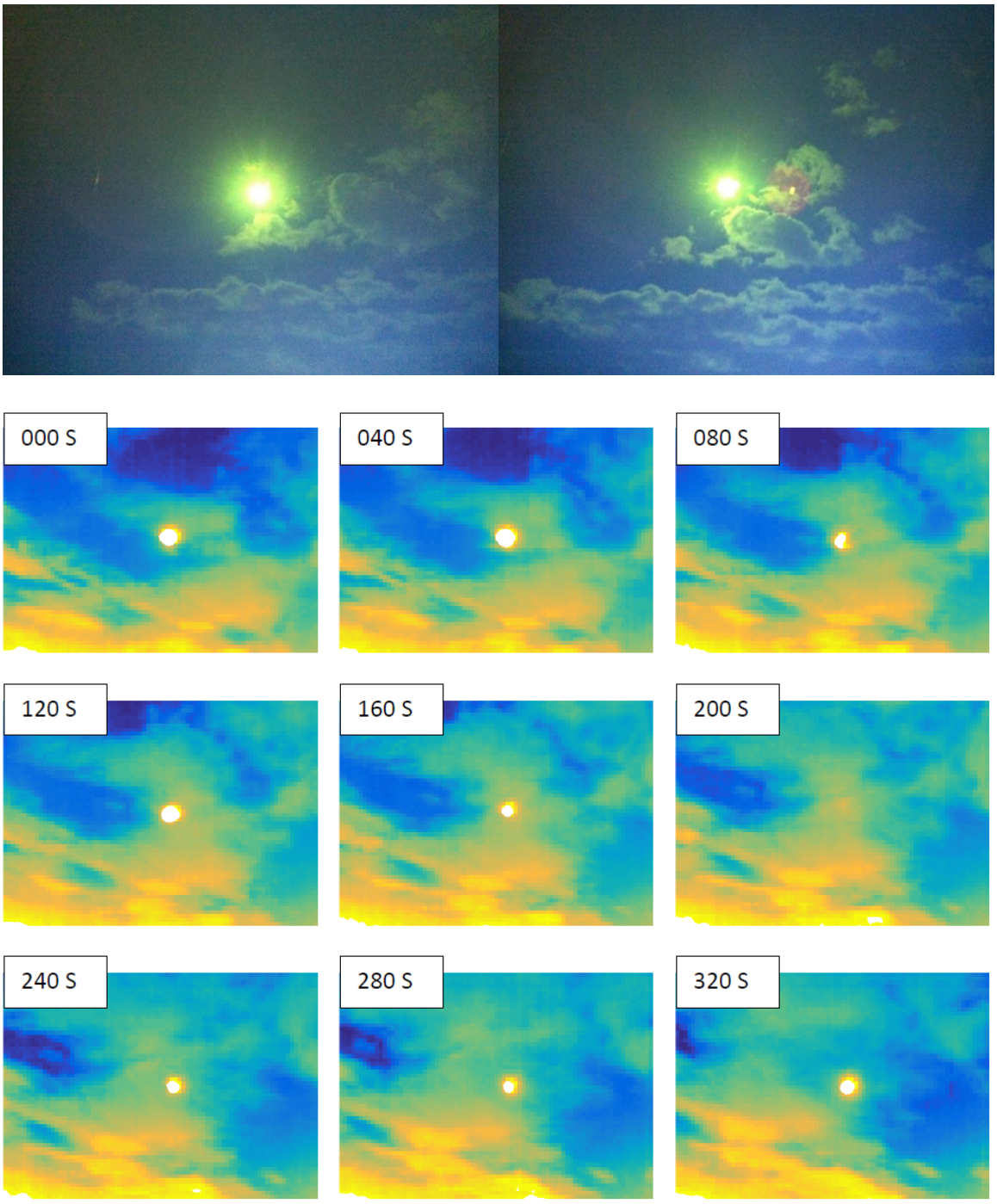


Figure 5-19. A. Two, near infrared Complementary metal–oxide–semiconductor image (above) & B. series of nine far infrared images taken 10 seconds apart (below).

This work proved that an effective solution for stopping sensor burn and confirmed the hypothesis that far IR wavelengths are preferable in reducing lens flare. A new

apparatus that incorporated a full field sky view was hypothesized and created as a proposed deployable product.

## 5.4. The Eight Sensor System, a Deployable Product, Proof of Concept IV

With success utilizing the Dog House to obtain far IR images of the sun and surrounding clouds with minimal saturation and no lens flare, an eight sensors system was proposed. By utilizing multiple views and stitching them together into one image, the pan tilt unit was removed. This accomplished the goal of removing nearly all moving parts.

By reducing overall mechanical movement, it was hypothesized that the system would increase in reliability. The views were set in three equatorial planes instead of utilizing spherical, cylindrical or cartesian coordinates. The mathematics of these transformations is in section 6.4 Mathematics of the Alignment of Flat Views Projected Onto a Flat Sky Plane. Figure 5-20 shows the location of the eight sensors.


Figure 5-20. Outer shell location and labeling of all eight views in three equatorial planes labeled L0 through L7.

The first equatorial plane contains the sensors L4 and L5. It is closest to horizontal.

The next two planes contain L6, L0 and L3 as well as L7, L1 and L2, respectively.

The L7, L1 and L2 plane had each sensor rotated 90°. The sensors are shown in Figure 5-21.

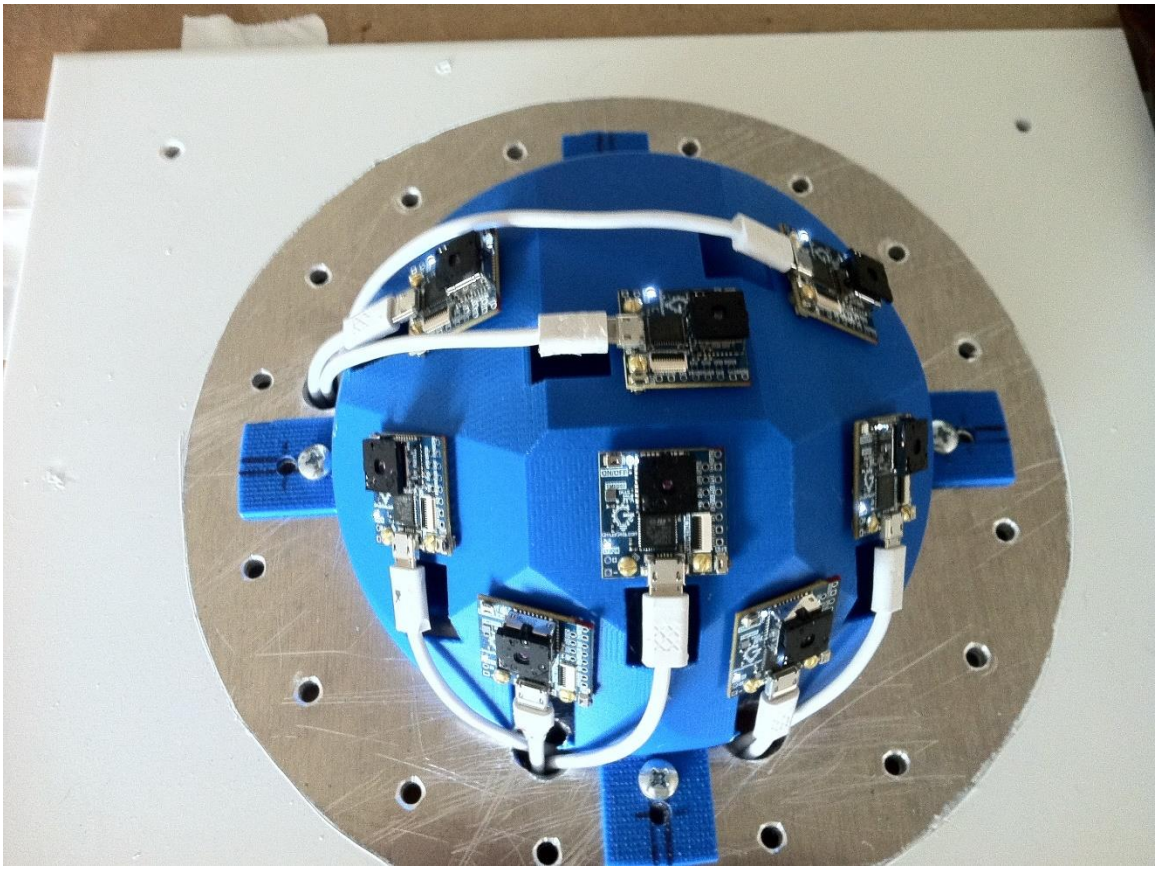

Figure 5-21. Location of each of the eight sensors, underneath the outer shell.

The outer shell provided protection from the weather and germanium lens cavities were incorporated to provide an IR transmissible window. The system was nicknamed "Ladybug" because of the spots the germanium windows created on the white outer shell, shown in Figure 5-22.

Figure 5-22. Initial fielded trials of the Ladybug upper apparatus system in the field.

A 1/8" oring seal was added to the bottom of the outer shell on the next version of the Ladybug. Window locks that encase the germanium windows with waterproof Loctite's Marine Adhesive Sealant ensured waterproof operations for testing in intermittent rainy conditions. Figure 5-23 and Figure 5-24 highlight the second version of the Ladybug in CAD.

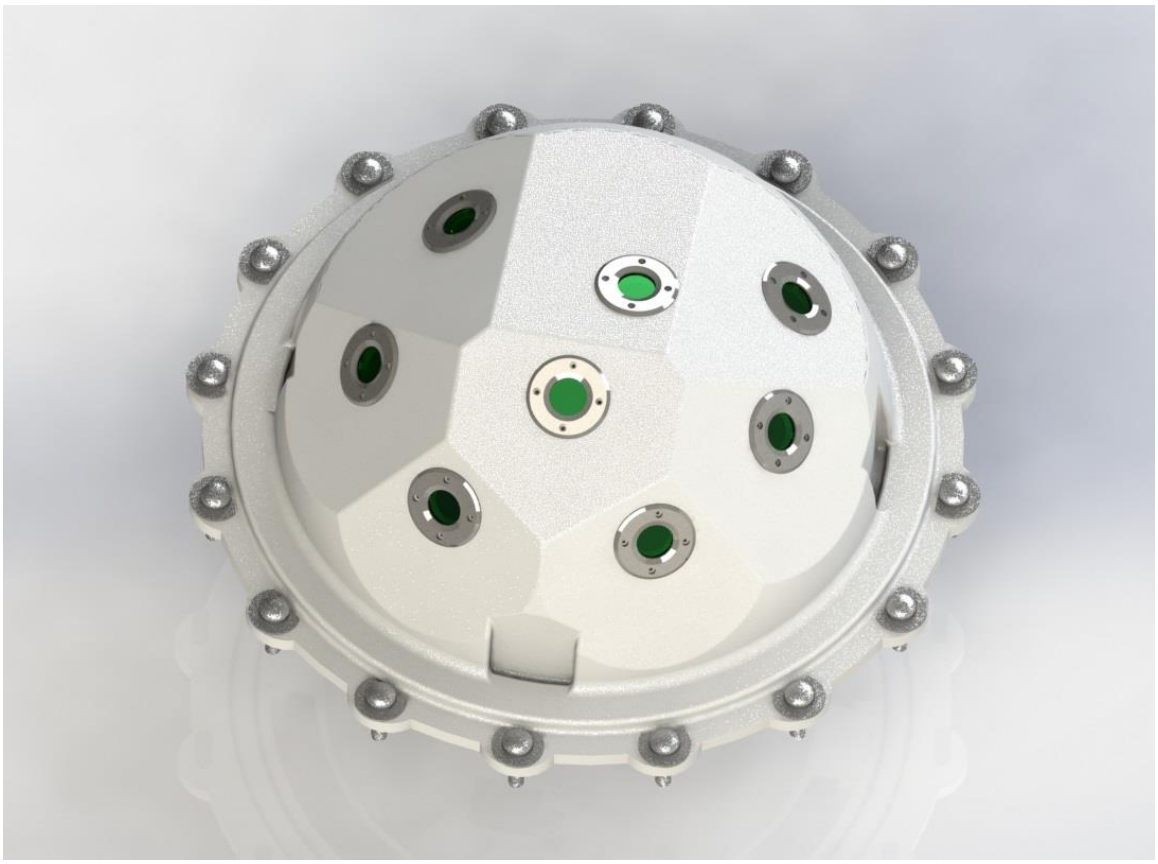

Figure 5-23. Version 2 of the Ladybug system highlighting the window covers in silver.

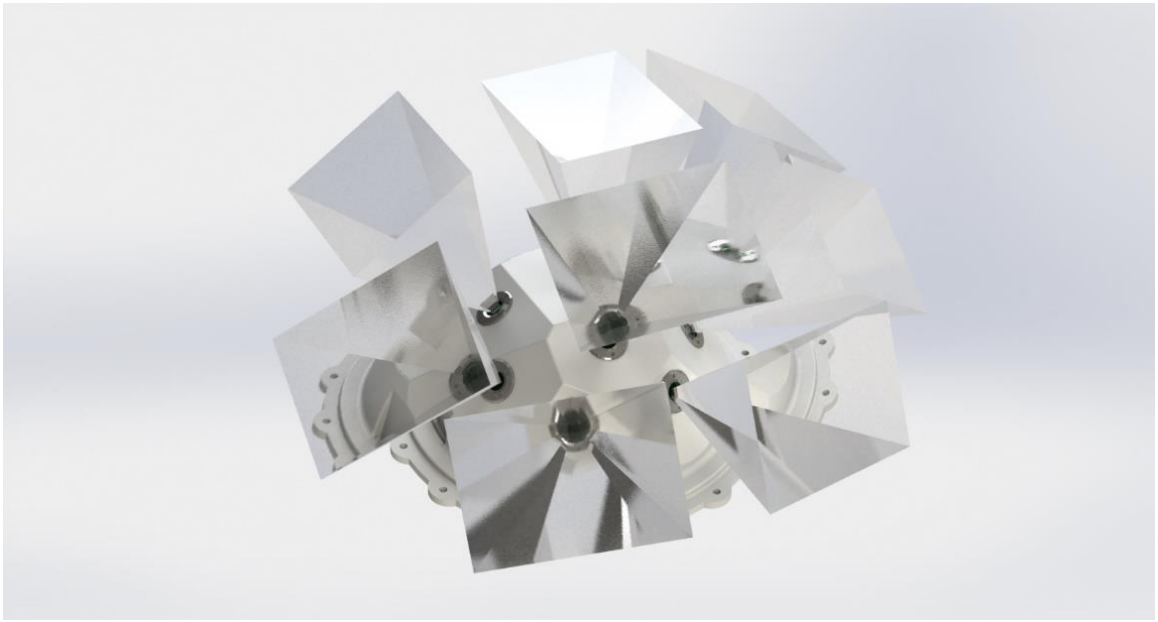

Figure 5-24. Rendered Ladybug Version 2 view of the apparatus with the views emerging from the individual windows shown as transparent glass.

It was assumed that the distance between far IR sensors was trivial compared to the distance to the cloud ceiling. A minimum of a five degree overlap with all views was calculated. Therefore, the views of the IR sensors do overlap at approximately the height of the cloud ceiling and exactly match a five degree overlap at infinity.

The fielded version of the Ladybug is shown below in Figure 5-25, Figure 5-26 and Figure 5-27.

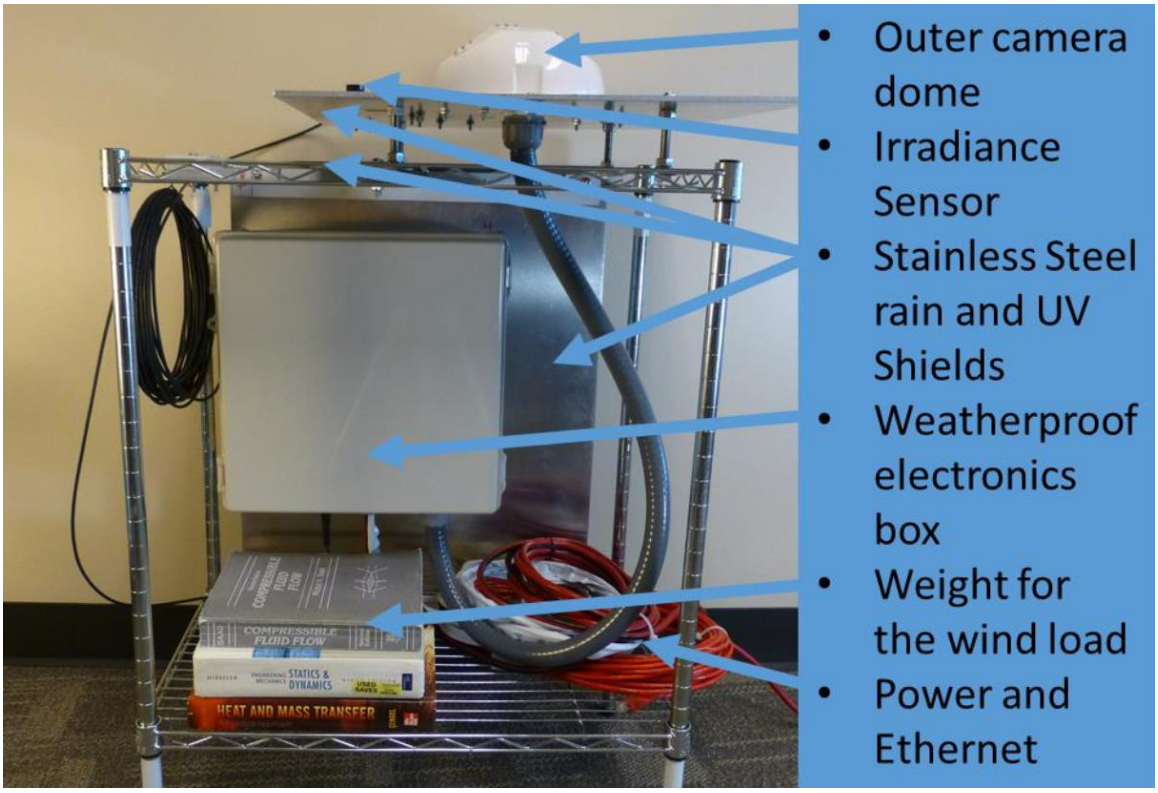


Figure 5-25. V2 of the fielded Ladybug SIMF apparatus, View 1.

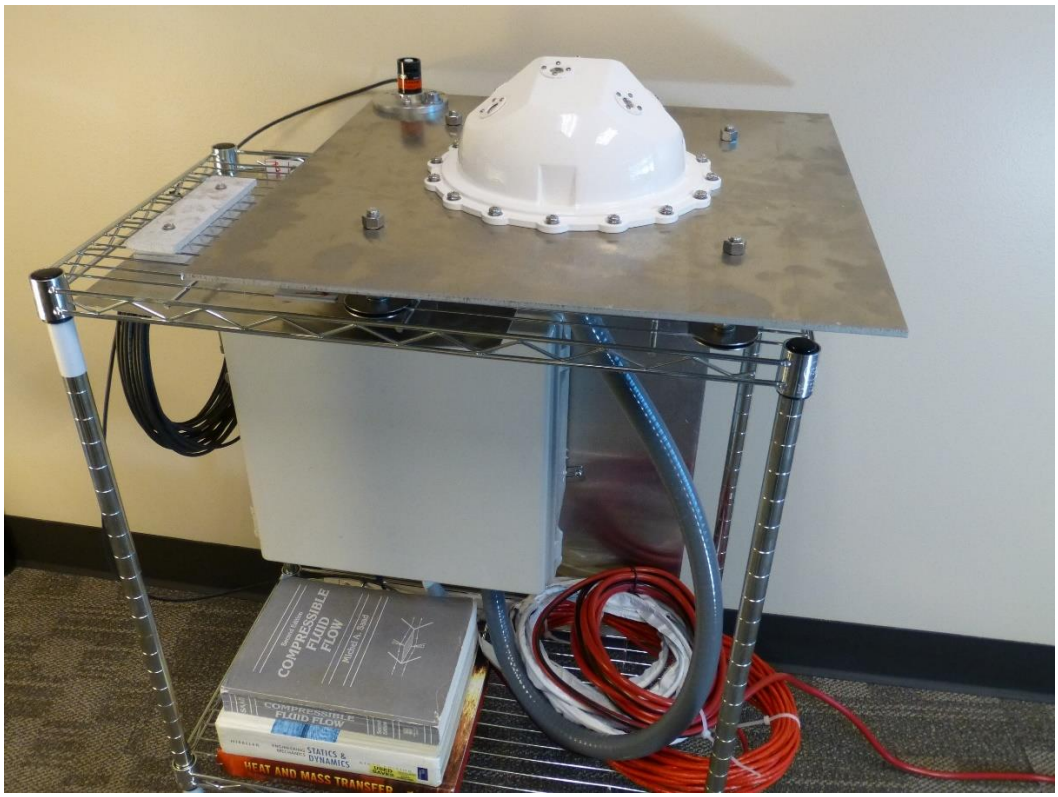


Figure 5-26. V2 of the fielded Ladybug SIMF apparatus, View 2.

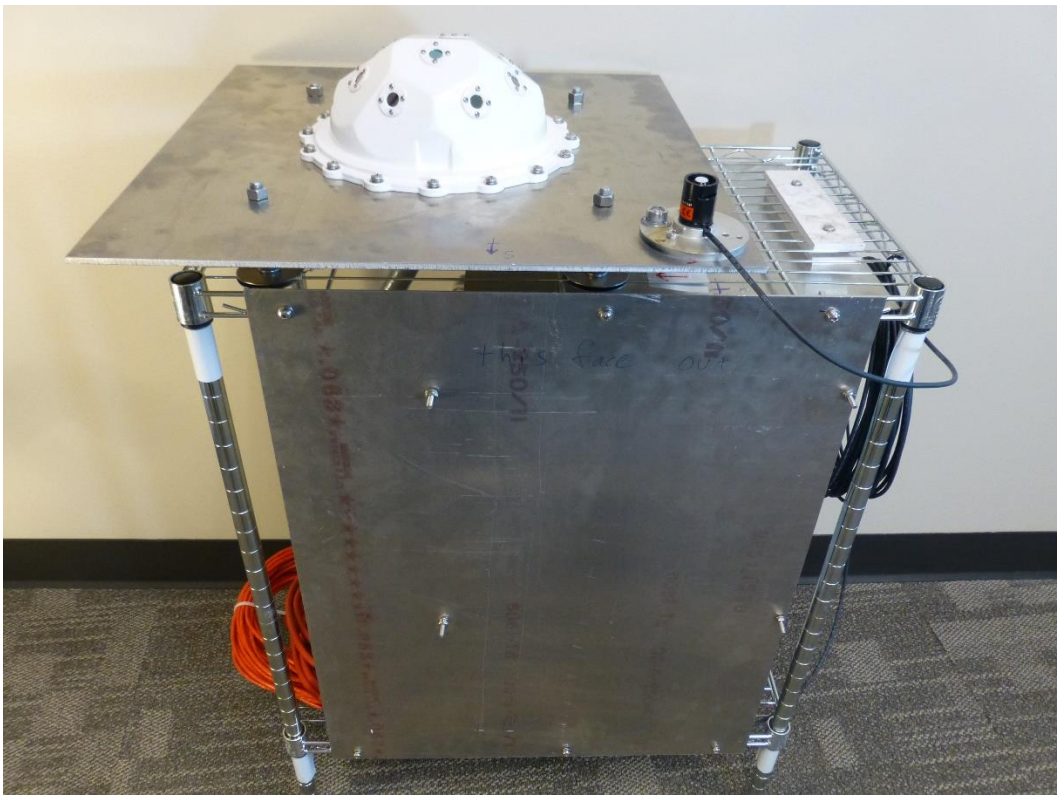

Figure 5-27. V2 of the fielded Ladybug SIMF apparatus, View 3.

Three units of the final V2 of the Ladybug were constructed and utilized for testing as part of a Small Business Innovation Research grant (SBIR, NSF 16-555). All testing was done in Boulder Co. and is highlighted in the '8 Fielded System Results with Multiple Data Extraction Methodologies for the Neural Network' section.

This research has resulted in two US patents issued through STC, formerly known as the Science & Technology Corporation at UNM, US Patent 9,921,339 [206] and US Patent 10,345,486 [207].

# 6. Data Aggregation and Pre-Processing on the Eight Sensor System, "The Ladybug"

One of the design goals for a SIMF system is the placement of the apparatus in the middle of a PV field to obtain the best prediction results. A Computer Aided Drafted (CAD) model of a PV field containing a SIMF system is highlighted in Figure 6-1, below. The upper graphic highlights the unit in a sunny PV filed and the lower graphic shows the apparatus as a decision maker for alternative power generation resources.

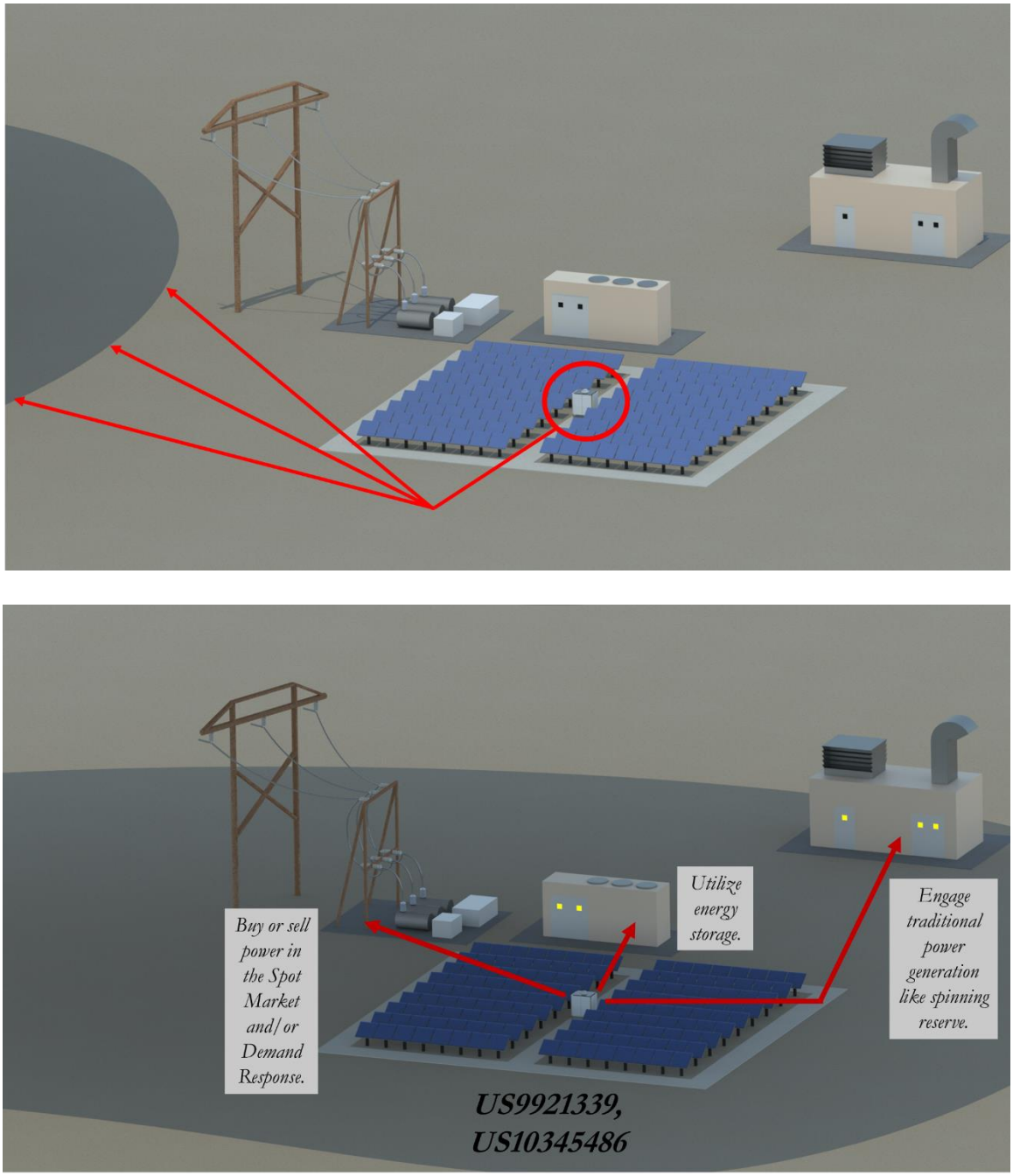


Figure 6-1. SIMF Unit in the middle of a Sunny PV field (above) and shown as a decision-making flow diagram (below).

It is useful to show a perspective of the SIMF unit in the field as the unit views the sky and its surroundings.

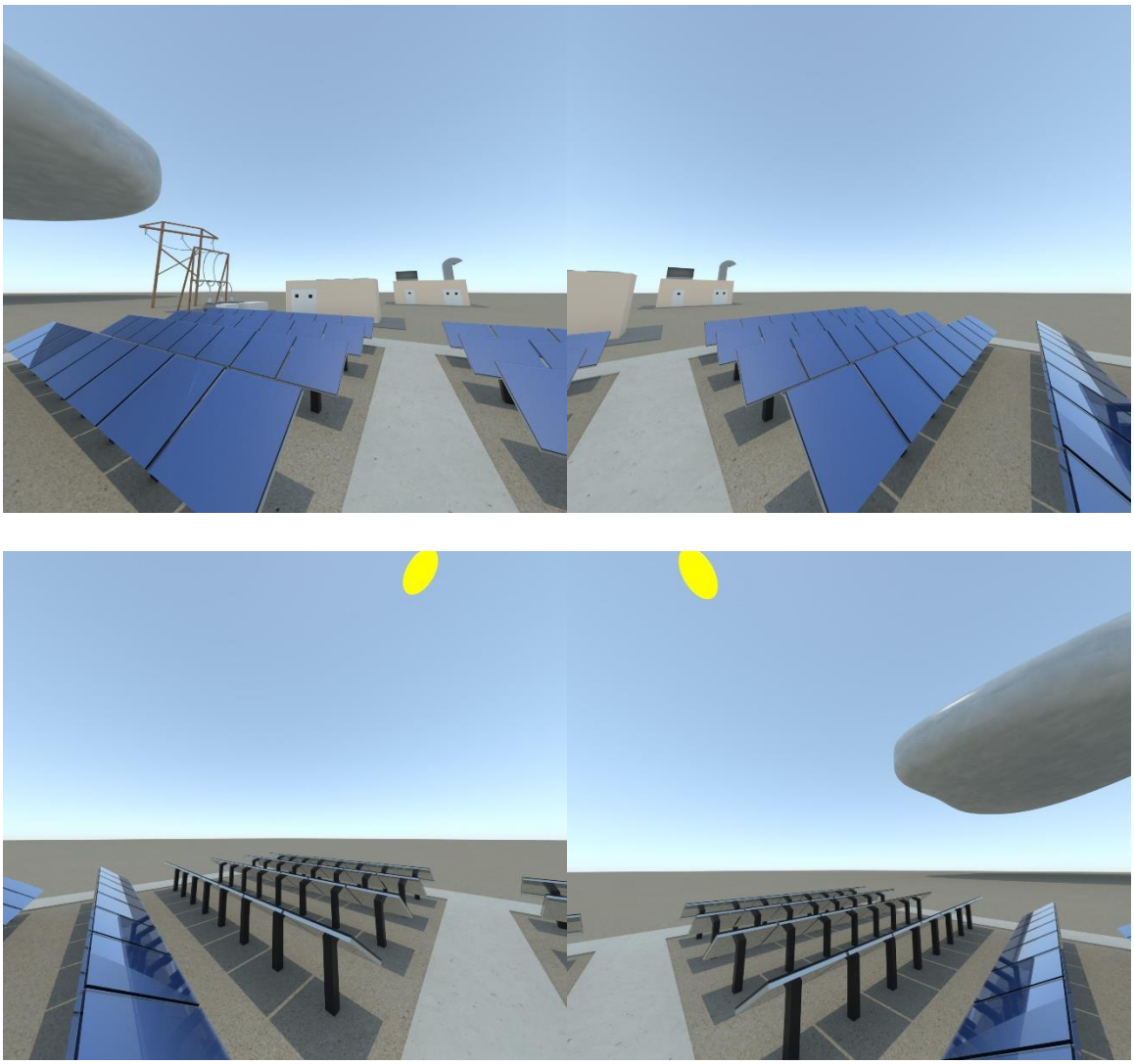

Figure 6-2. On the ground SIMF perspective views in clockwise order from top left; A. NNW view, going left to right, showing the grey cloud, transmission infrastructure, onsite battery storage and onsite gas turbine generation (far right); B. NE view with same onsite gas generation; C. SE view (lower left); and D. SW view of PV field and cloud (lower right).

These views will help locate aspects of the following discussion.

## 6.1. Cloud Ceiling Geometry

The geometry of the views in the system relies on the assumption that the sky ceiling and cloud-cover are flat. Therefore, the projection of the views of the Ladybug system onto the sky was assumed to be a flat plane projected onto a flat plane. To

illustrate this projection a render of the Ladybug IR sensor apparatus is shown in the middle of a solar field with the L6 view turned on. This is shown in Figure 6-3.

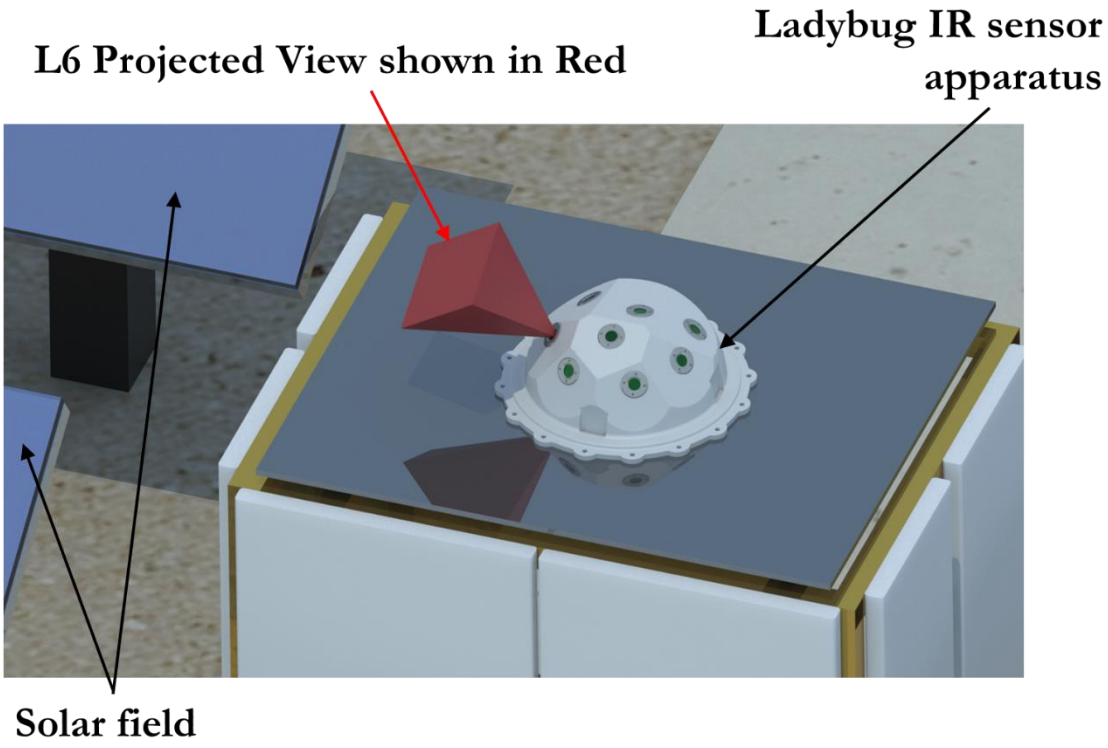


Figure 6-3. Ladybug IR sensor apparatus with the L6 view shown for reference.

The first flat plane mentioned was the flat plane projection of the camera view. It is the only view shown in red in Figure 6-3. The second flat plane is an assumption of cloud ceiling as a flat plane even though it is spherical. Both are highlighted in Figure 6-4.

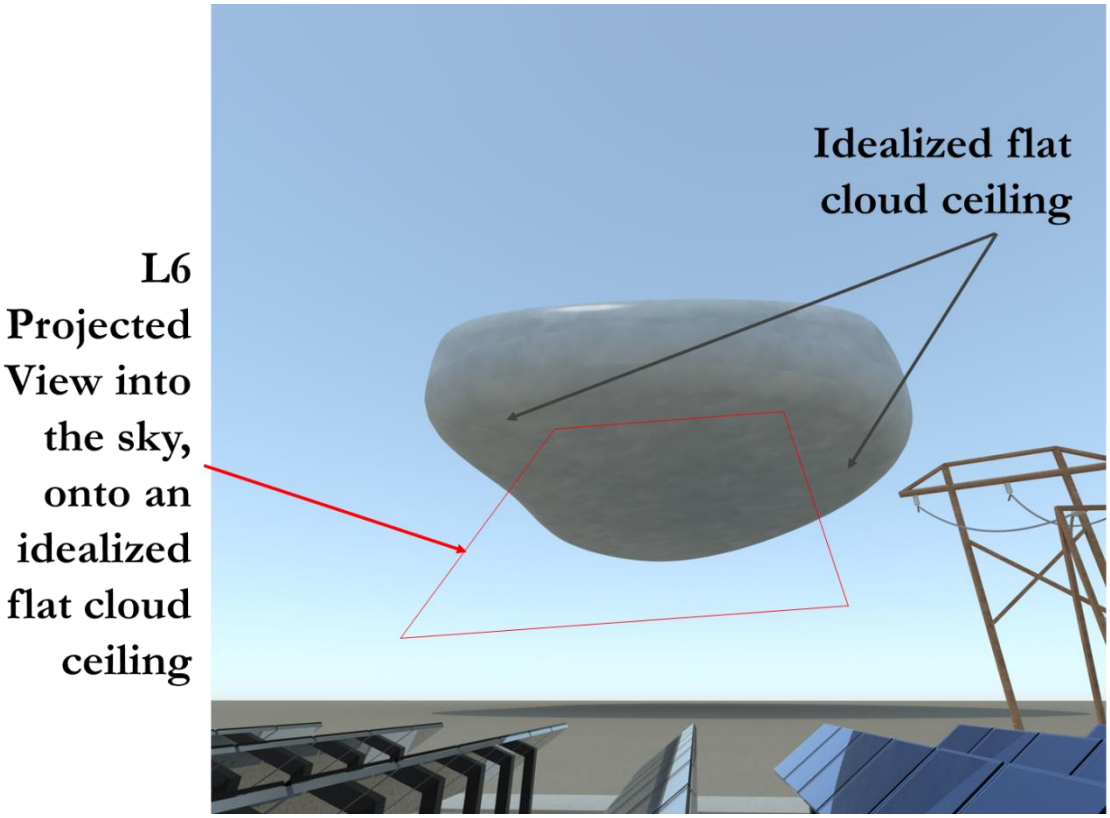


Figure 6-4. Projection of the L6 view as seen from the Ladybug IR sensor apparatus.

When all of the views are projected onto an assumed flat cloud plane, a montage of each view is assembled with overlapping regions. A diagram of this view is shown in Figure 6-5.

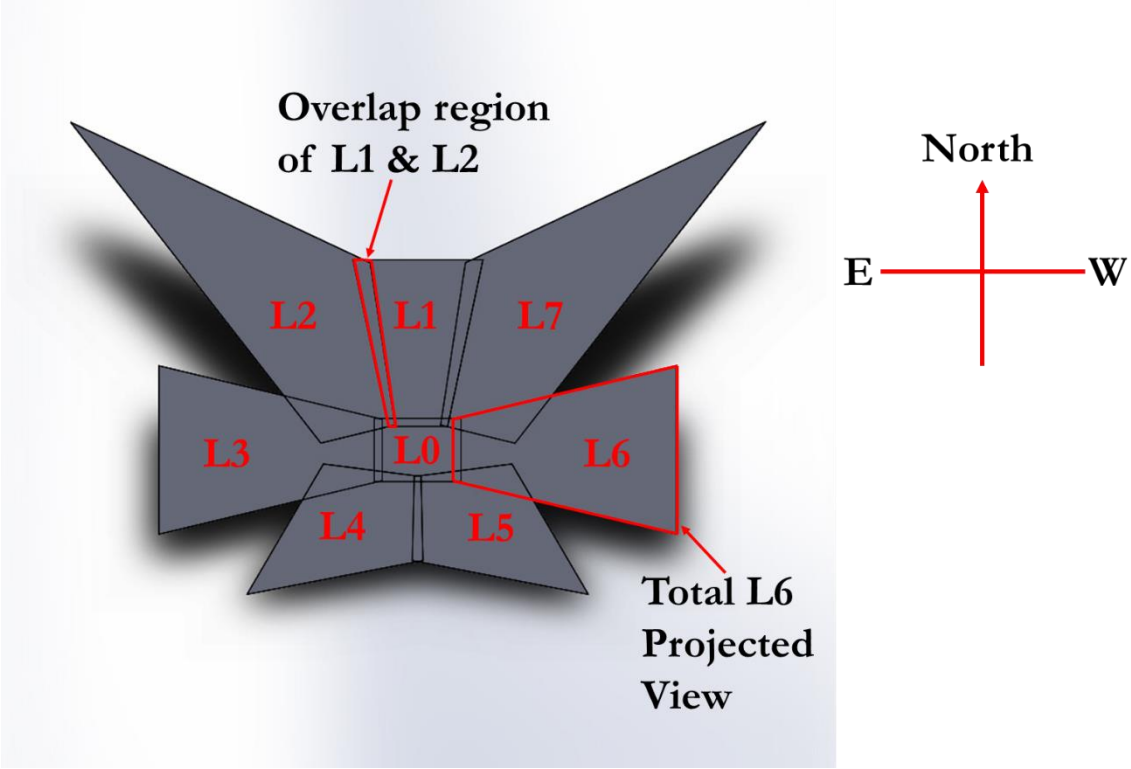


Figure 6-5. Montage of each of the eight views from the Ladybug and their labels as seen projected onto a flat cloud ceiling.

Several preprocessing steps were required including barrel distortion correction in the view itself and alignment of the system to the sky and the other sensors.

## 6.2. Motivation for Accurate 2D Cloud Geometry; Data Selection with Velocity Gate (VG) Method

Data selection was accomplished by making a series of progressive assumptions about the input space. The first assumption that was highlighted before, was that the cloud ceiling was assumed to be flat. It was also assumed the cloud vector field was relatively constant in the near term and can be extracted from a series of past sky

images taken at set intervals like every ten seconds. A diagram of a hypothetical sky image with the cloud vector field is shown below.

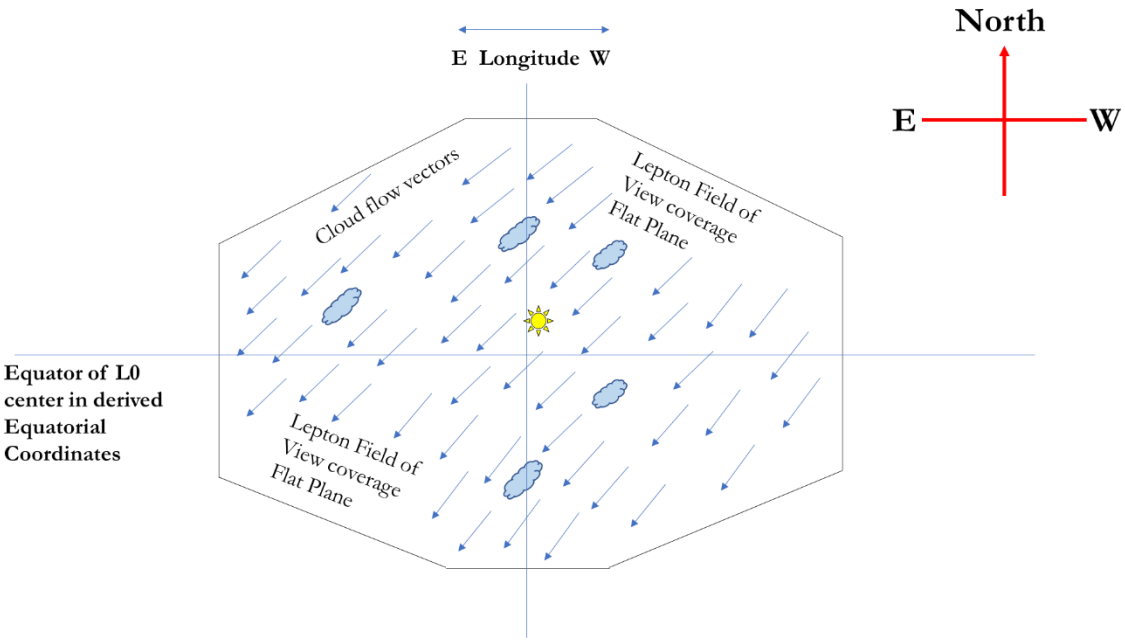


Figure 6-6. Sky image with cloud velocity vector field.

Since the vector field and surrounding clouds near the sun are more relevant data for SIMF, it is assumed than an average velocity can be extracted from the flow field near the sun. This extraction of data highlighted in Figure 6-7.

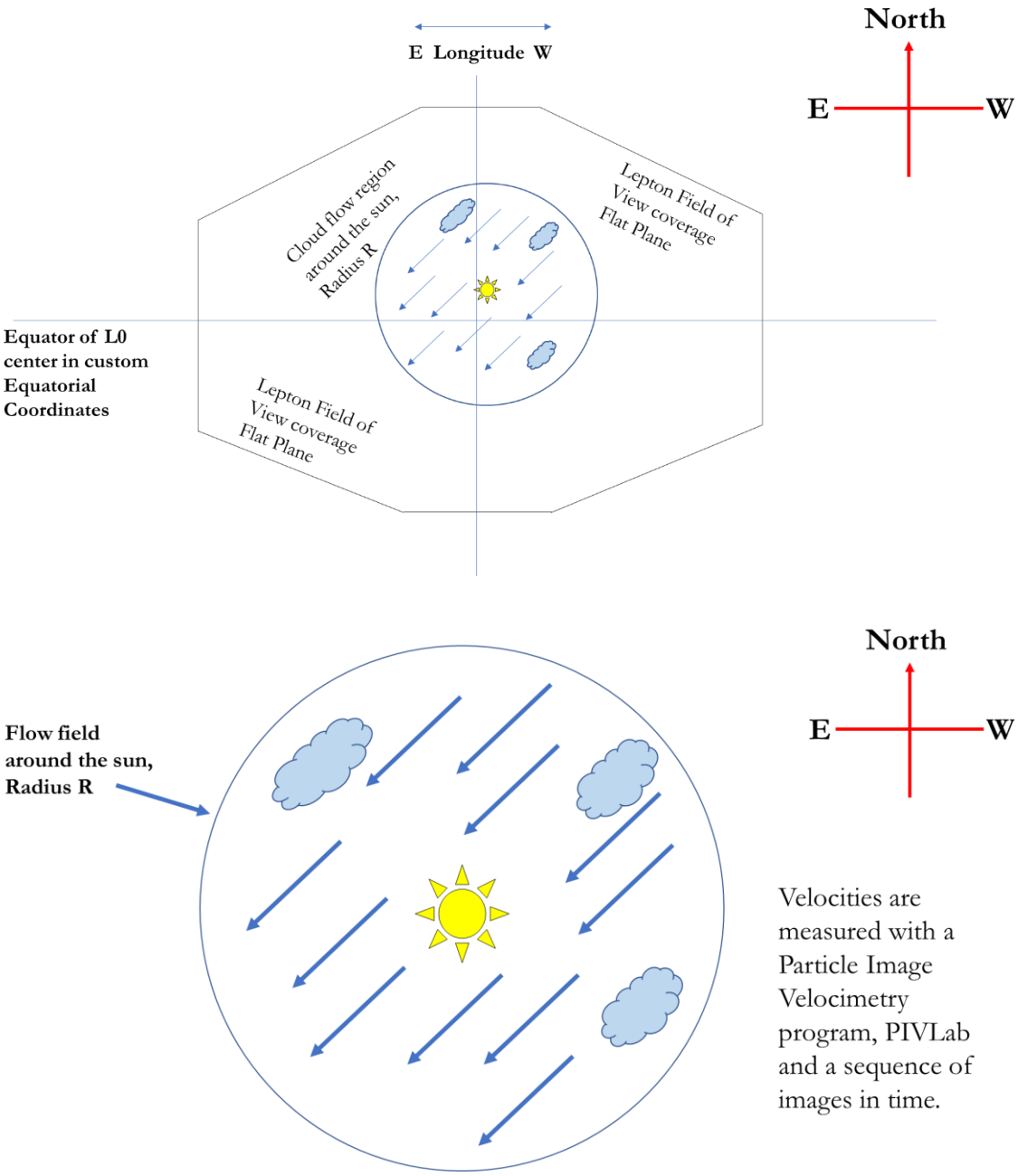


Figure 6-7. Radius of assumed relevant cloud vector flow data near the sun.

A radius is drawn around the sun, and velocity vectors within that region are used to estimate an average velocity. This is shown in Figure 6-8.

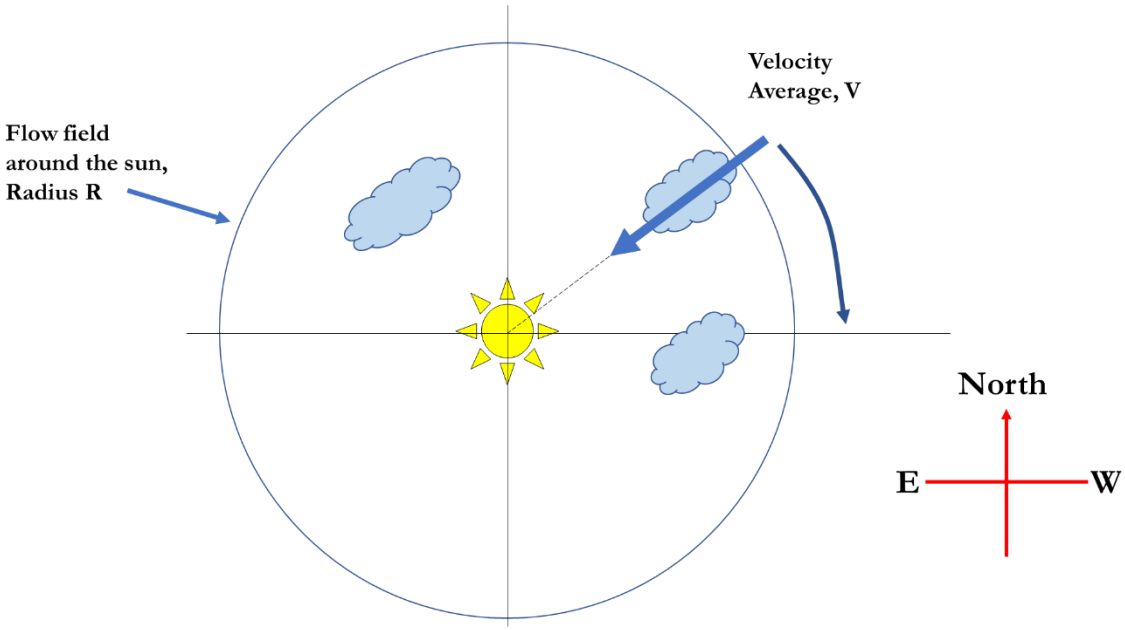


Figure 6-8. Average cloud flow field velocity near the sun.

It was assumed that the average cloud flow field velocity was a representative measure of expected cloud movement and future PV field occlusion events. It was further assumed that clouds are geometrically invariant in the near term, within the flow radius around the sun. For ease of calculation and for visualization purposes, the sky image is rotated about the sun center, so the average velocity is in line with the positive x axis, as is shown in Figure 6-9.

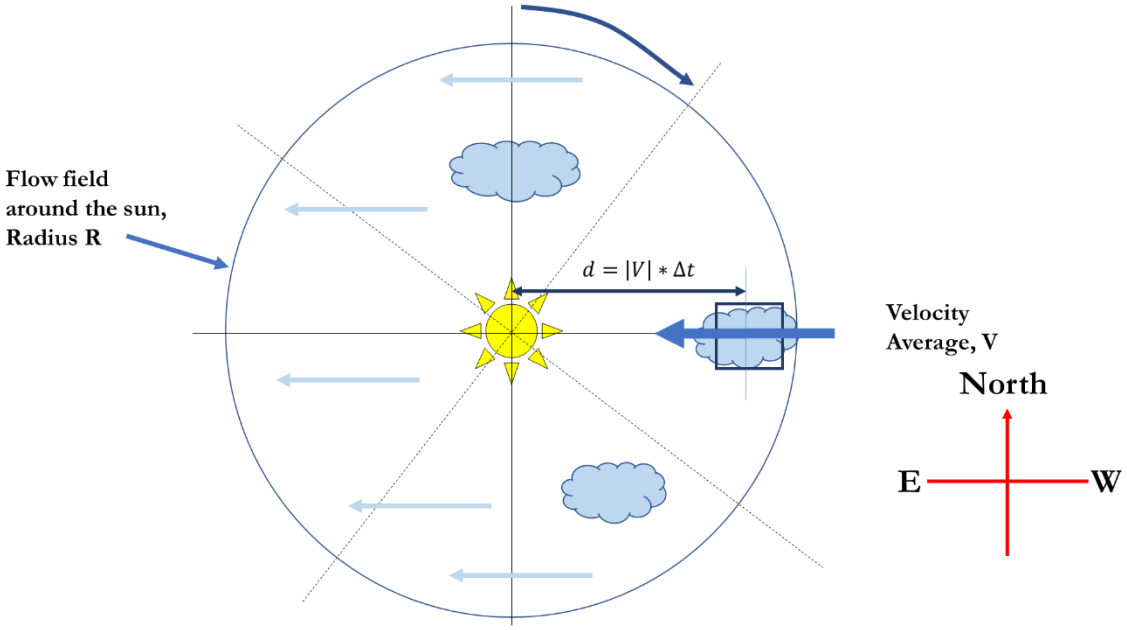


Figure 6-9. Data rotated about the sun center.

Once the average velocity is known and the image is rotated in line with the flow field, a region of interest called a Velocity Gate (VG) can be formed also. The VG is a section of sky, evenly spaced about the X axis, that is a distance equivalent to the velocity of clouds in pixels/frame multiplied by the number of frames equivalent to a prediction of future irradiance. If frames are acquired every ten seconds, the number of frames for a five-minute prediction would be 30, or five minutes times 6 frames per minute. The resulting distance gives the center location of the VG on the X axis. This concept is shown in Figure 6-9, above.

As general principle, any reduction of the number of superfluous inputs in any data set is useful to obtaining better outcomes. The VG methodology was employed to reduce the data for LAPART from the entire sky, to a small and systematic region, know as the VG. When referring to the VG, the region of influence along the X-axis was termed the data flag and is shown in Figure 6-10, below.

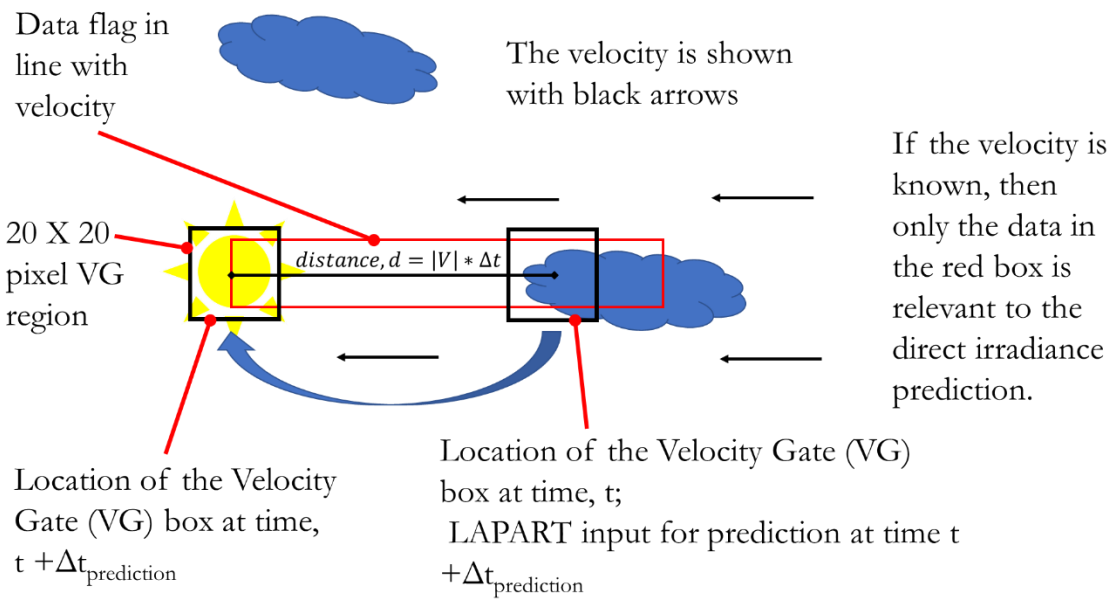


Figure 6-10. Projected path of the clouds across the sun in the direction of velocity.

The data flag width is the size of the VG. The data for LAPART has been first reduced form the entire image of the sky which contain tens of thousands of pixels to only the image of the that falls under the 20 by 20 pixel VG region.

The motivation for accurate cloud geometry was highlighted in the need for accurate velocity vectors. By projecting the clouds into the sky onto an idealized flat plane accurate cloud motion can be obtained. This was the basis for our preprocessing algorithm known as the VG method.

## 6.3. Barrel Distortion Correction

Barrel distortion was reported from the manufacture data as 7.5%. Barrel distortion is the image distortion that occurs from a spherical lens projecting light onto a flat sensor plane. An example of this distortion is shown in Figure 6-11 below. The

original image contained parallel and perpendicular lines, but when the light enters the conical lens it is distorted, making parallel vectors bowed, resembling a barrel.

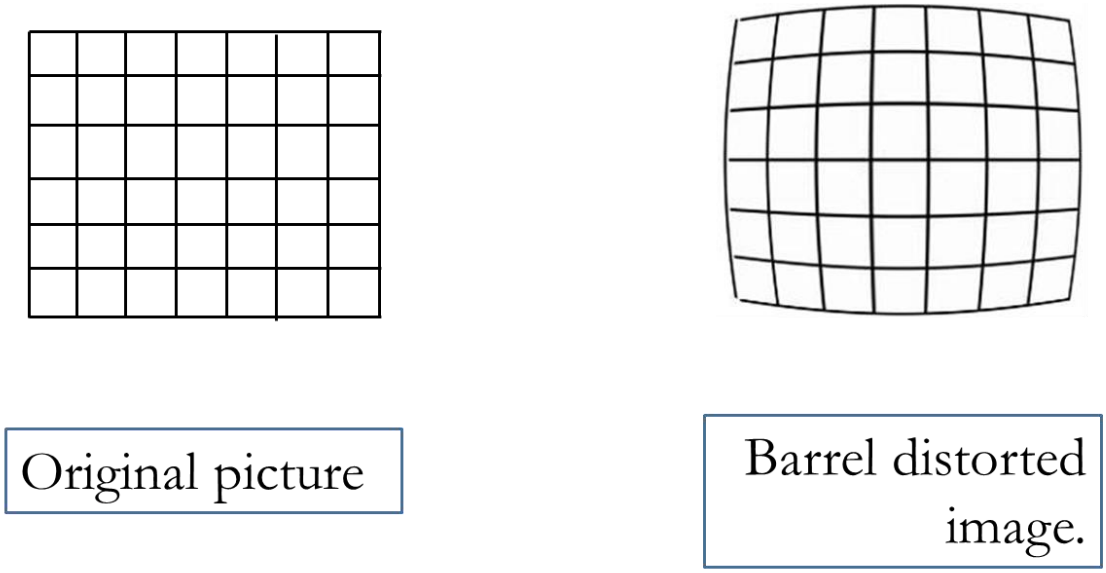


Figure 6-11. Barrel distorted picture of a parallel lines in an original image.

Matlab was employed with the equation LENSDISTORT on all eight views before they were aligned to the sky. LENSDISTORT was not validated or verified for accuracy.

After the barrel distortion was removed from each view, the views were then ready to be projected onto the idealized flat cloud ceiling in the sky. At this stage, they are also ready to be aligned to the sun position and each other. An example of the distortion correction is shown in Figure 6-20, below.

## 6.4. Mathematics of the Alignment of Flat Views Projected Onto a Flat Sky Plane

Since the sun moves in an equatorial pattern, an equatorial coordinate system was employed. This simplified the mathematics by enabling only rotations about axes of unit vectors and precluded the need for any additional projections. I.e. no projection of the unit vector was required when rotating each of the coordinates into each other as would be required with spherical or cylindrical coordinates.

A sextuple rotation with local and global coordinates was employed. The main reason this was done was so pre-written Matlab algorithms could be employed, easing the programing required. The mathematics of the projections is shown below.

The coordinate transformation starts by aligning the X-axis in red, to North by rotating the Y-axis in green, straight up. The rotation is about the Y axis shown in Figure 6-12, below. When talking about the X,Y,Z axis, these are shown in red, green and blue, respectively.

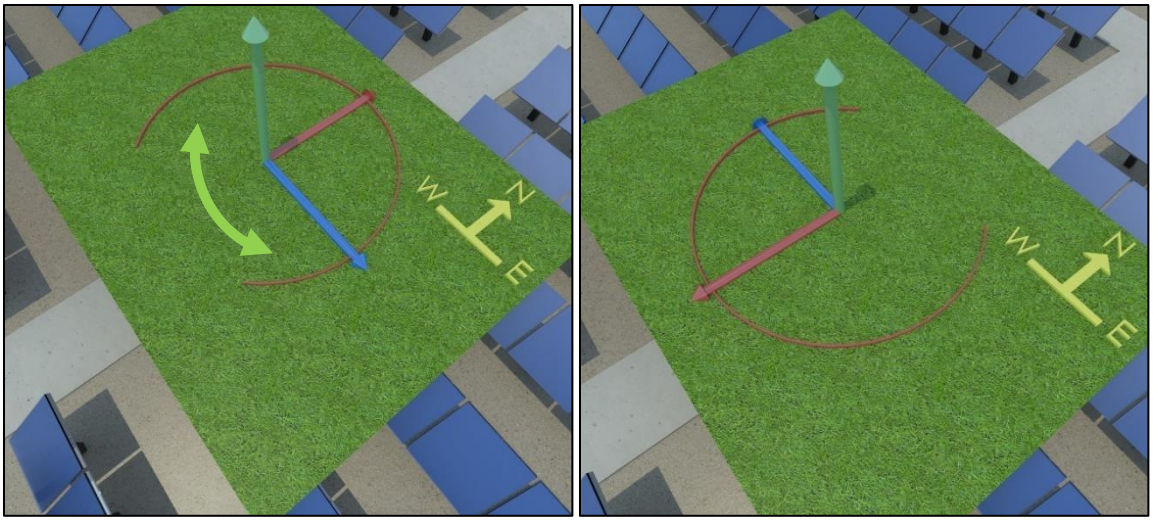


Figure 6-12. T1 rotation in Y to align the coordinate system South.

$$T_1 = \begin{bmatrix} \cos(\theta_1) & 0 & -\sin(\theta_1) \\ 0 & 1 & 0 \\ \sin(\theta_1) & 0 & \cos(\theta_1) \end{bmatrix} \tag{6-1}$$

Where $\theta_1$, ideally $= 180°$. A rotation was then employed to tilt up into the sky looking up from the ground. The X-Z plane, in red-blue, forms an equatorial plane. When the tilt angle up from the ground is set to the sun elevation a rotation about the Y axis again points directly at the sun. These two rotations are shown in (6-1) and (6-2) as well as Figure 6-13 and Figure 6-14.

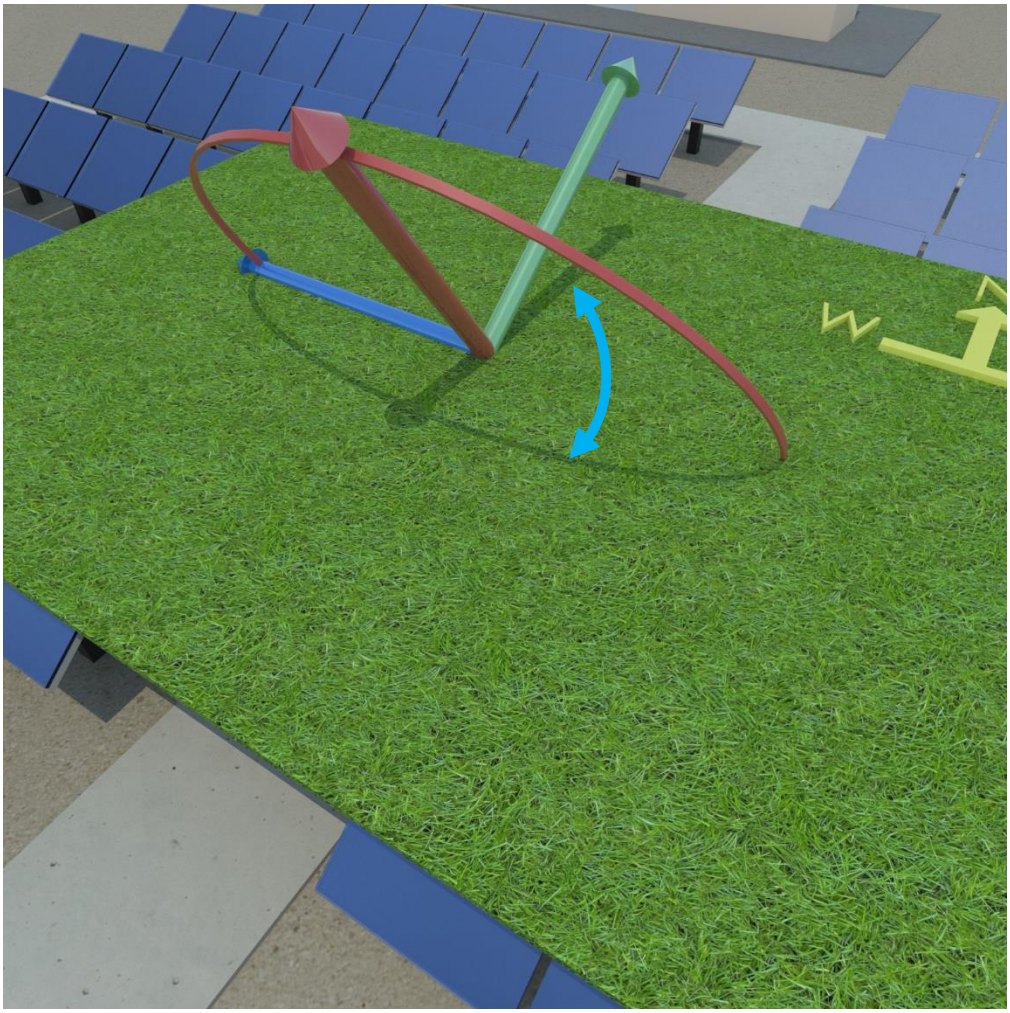

Figure 6-13. T2 rotation about the Z axis.

$$T_2 = \begin{bmatrix} \cos(\theta_2) & \sin(\theta_2) & 0 \\ -\sin(\theta_2) & \cos(\theta_2) & 0 \\ 0 & 0 & 1 \end{bmatrix} \tag{6-2}$$

The rotation about the Y axis is shown below.

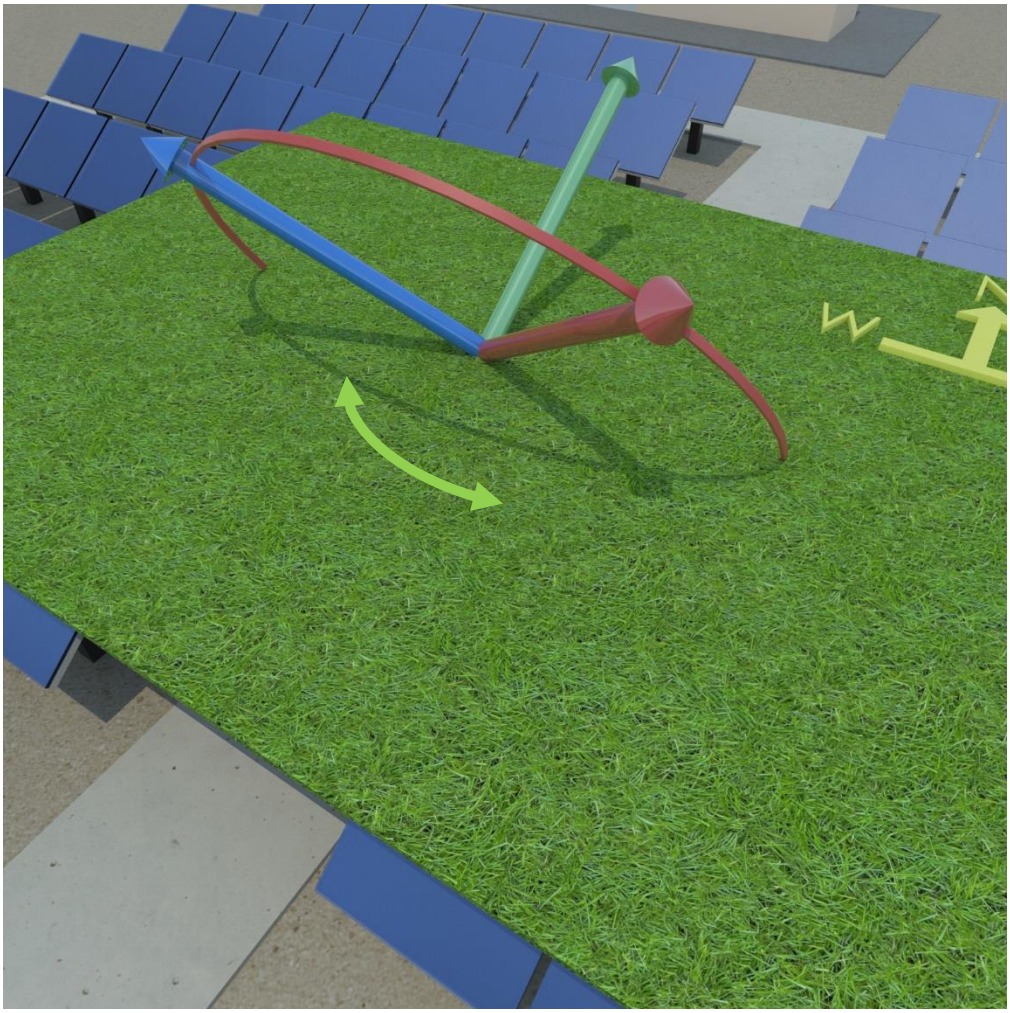

Figure 6-14. T3 rotation About the Y axis pointing to the center of the views.

$$T_3 = \begin{bmatrix} \cos(\theta_3) & 0 & -\sin(\theta_3) \\ 0 & 1 & 0 \\ \sin(\theta_3) & 0 & \cos(\theta_3) \end{bmatrix} \tag{6-3}$$

A view is placed on the coordinate system to illustrate the center as shown in Figure 6-15. Another local coordinate system is used to rotate the view locally also shown in Figure 6-15.

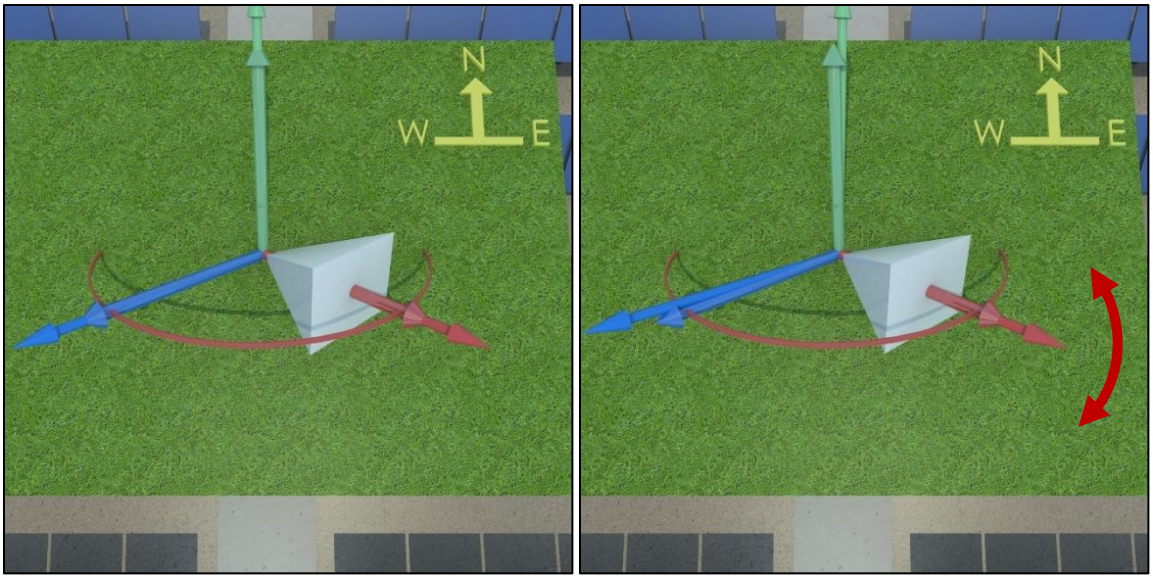


Figure 6-15. Local coordinate system placed on the global system.

The view to the left shows the local coordinate system in line with the global coordinate system. If the sensor is not seated properly, it may be rotated about the view normal as shown to the right.

It was assumed that each view is uniform when they were manufactured. It was then assumed that the location of the window can be rotated in all three axes and the view from the sensor would remain constant from the manufacture. Figure 6-15 shows a fourth rotation, that represent the sensor being rotated in line with the normal.

The mathematics are shown in (6-4).

$$T_4 = \begin{bmatrix} 1 & 0 & 0 \\ 0 & \cos(\theta_4) & \sin(\theta_4) \\ 0 & -\sin(\theta_4) & \cos(\theta_4) \end{bmatrix} \tag{6-4}$$

Where $\theta_4$ ideally = 0. Use of the Matlab function, projective2D, performed the projection of the view onto a theoretically flat cloud-plane. The function rotates the

four corners of a picture to four geospatial locations on the sky. Therefore, the last two rotations needed are to find the corners of the view.

The vertical rotation of the local coordinate system is about the Z-local axis and is shown below in Figure 6-16.

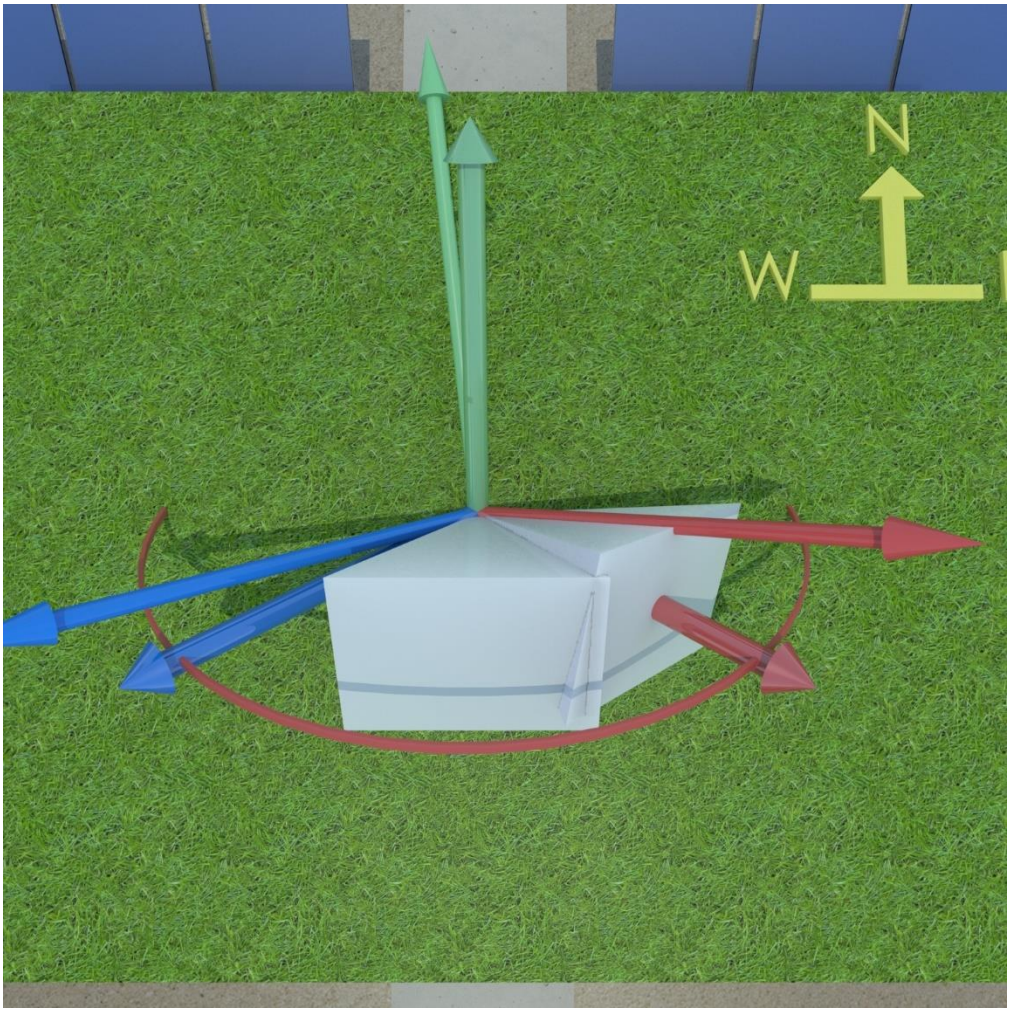


Figure 6-16. Vertical rotation of the local coordinate system about the local Z-axis. L0 is also shown.

$$T_5 = \begin{bmatrix} \cos(\theta_5) & \sin(\theta_5) & 0 \\ -\sin(\theta_5) & \cos(\theta_5) & 0 \\ 0 & 0 & 1 \end{bmatrix} \tag{6-5}$$

$\theta_5$ ideally = +,-; half of the vertical view angle. This locates the left and right edges of the view. The last rotation is about the local Y-axis. It is shown below.

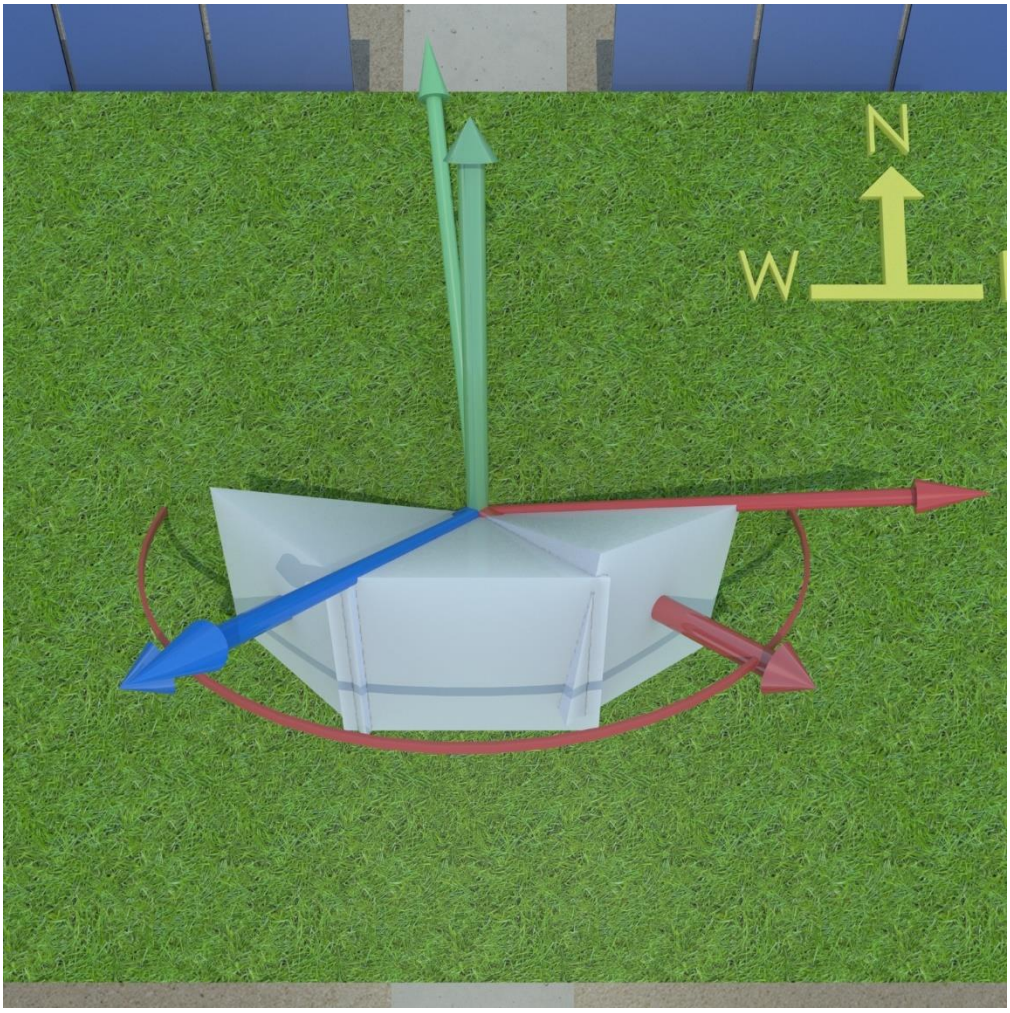


Figure 6-17. Horizontal rotation of the local coordinate system about the local Z-axis. L0, L3 and L6 are shown.

$$T_6 = \begin{bmatrix} \cos(\theta_6) & 0 & -\sin(\theta_6) \\ 0 & 1 & 0 \\ \sin(\theta_6) & 0 & \cos(\theta_6) \end{bmatrix} \tag{6-6}$$

Where $\theta_6$ = +,-; half of the horizontal view angle. The final projections of the corners are shown in Figure 6-17. Note that L0, L3 and L6 are all shown.

A final rendering of all eight views located in the middle of a PV field is shown in Figure 6-18, below.

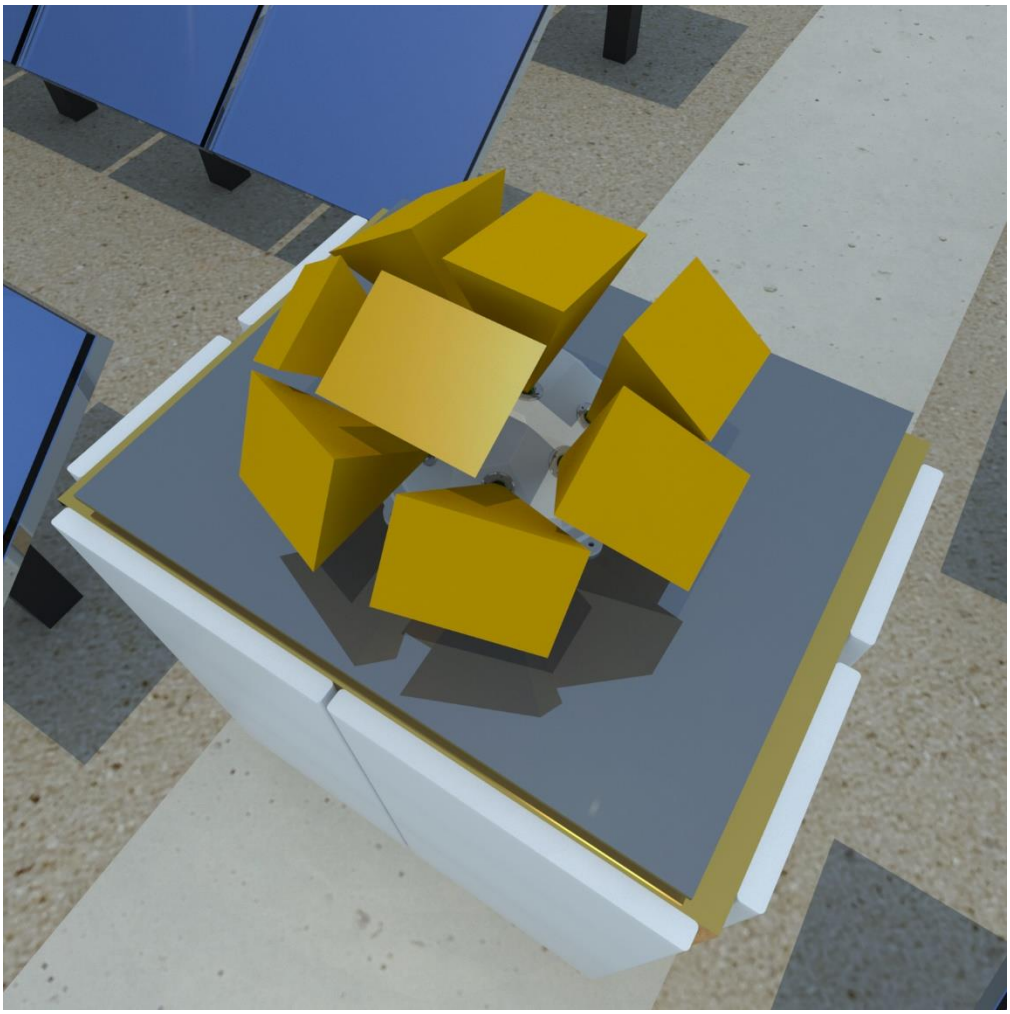

Figure 6-18. Final rendering of all eight views shown in yellow.

The final corners of each view were calculated with (6-7).

$$R_{projected} = T_6\left[T_5\left[T_4\left[T_3\left[T_2\left[T_1\left[R_{original}\right]\right]\right]\right]\right]\right] \tag{6-7}$$

To summarize, the first three rotations project the view into the sky at the appropriate equatorial level. When these rotations are applied, the view is centered

directly normal to the flat surface plane of the ladybug shown in Figure 5-24 and Figure 6-3. $\theta_4$ rotates the sensor about the normal axis to account for rotational errors of the sensor when it is installed onto the ladybug frame. $\theta_5$ and $\theta_6$ rotate left/right and up/down, respectively, to locate individual pixels in each view.

The sun position is directly calculated in the picture from elevation and azimuth, which are both functions of time of day, day of year, latitude and longitude.

## 6.5. Alignment of the System to the Sky

To align the system to the sky, the L0 center view's T1 rotation to that apparatus is assumed to be exactly 180°. It is noted that T1 and T3 are both rotated about the Y-Axis. Since combinations of the X, Y, and Z axis rotations can reconstruct any projection into a 3-Dimensional space, T4 is used as the third coordinate in space to initially align the system to the sky. What results is a calculated projection of where the sun should be in the L0 view versus the actual sun. The sun location is found during high irradiance times from the pixels that are fully saturated.

With the above assumptions, the alignment process of the L0 view, which is assumed to be the structural apparatus alignment to the sky, requires the following parameters.

1. A minimum of three sample of the sun located in the L0 view are required.
2. Alignment accuracy improves when samples of the sun are as far away from each other, while still located within the L0 view.

3. A distance is calculated, in number of pixels, that locate the actual sun relative to the calculated sun center.
4. Alignment errors from geospatial differences in assuming the cloud plane is flat as opposed to spherical are minimized by picking times equally on both sides of solar noon.

A Visual example of this process are shown in the figure below.

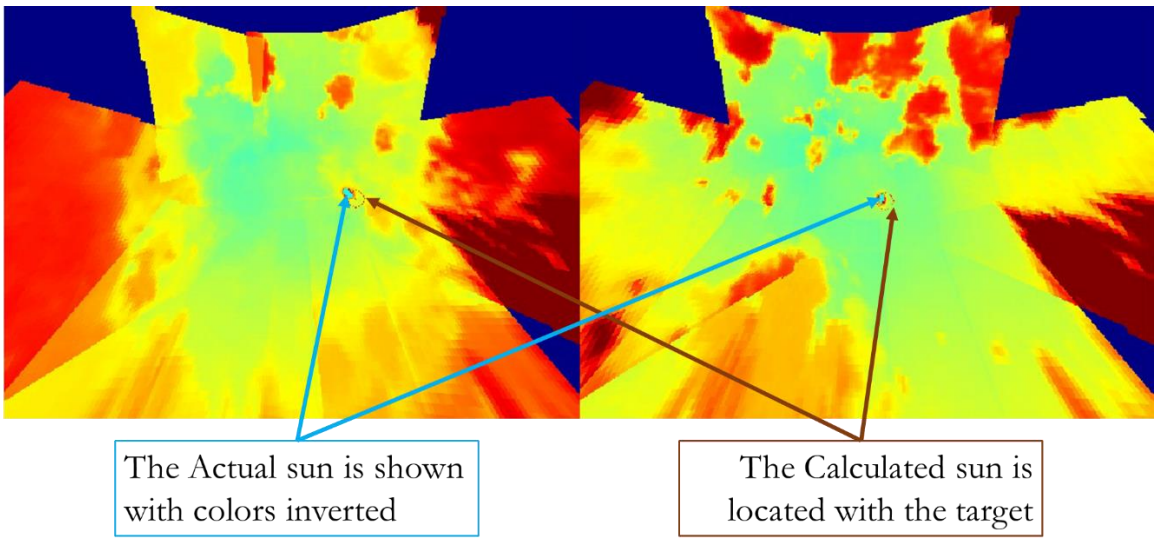


Figure 6-19. Two times of the day highlighting the actual sun shown in blue and the calculated sun highlighted with the circular target.

The sun actual position was calculated with a thresholding process where pixels above a threshold were considered to calculate the sun. The alignment process is as follows:

1. θ1, θ2 and θ4 are slightly varied from their ideal angles in a random order during each alignment step.
2. The distance between the two sun positions is calculated and averaged.

3. If the distance decreases, the new θ1, θ2 and θ4 values are set as the updated alignment values.
4. Processes 1-3 repeated until the distance is minimized.

After this process, L0 and the structural apparatus is considered aligned to the sky. The stitching of L1-L7 with L0 and their subsequent alignment to the sky, follows.

## 6.6. Stitching of Eight Sensors Together and Alignment of Other Sensors to the Sun

Figure 6-20 shows the raw output of the views in reverse, i.e. the views look up from the ground and not from an astronaut's view, looking down from orbit.

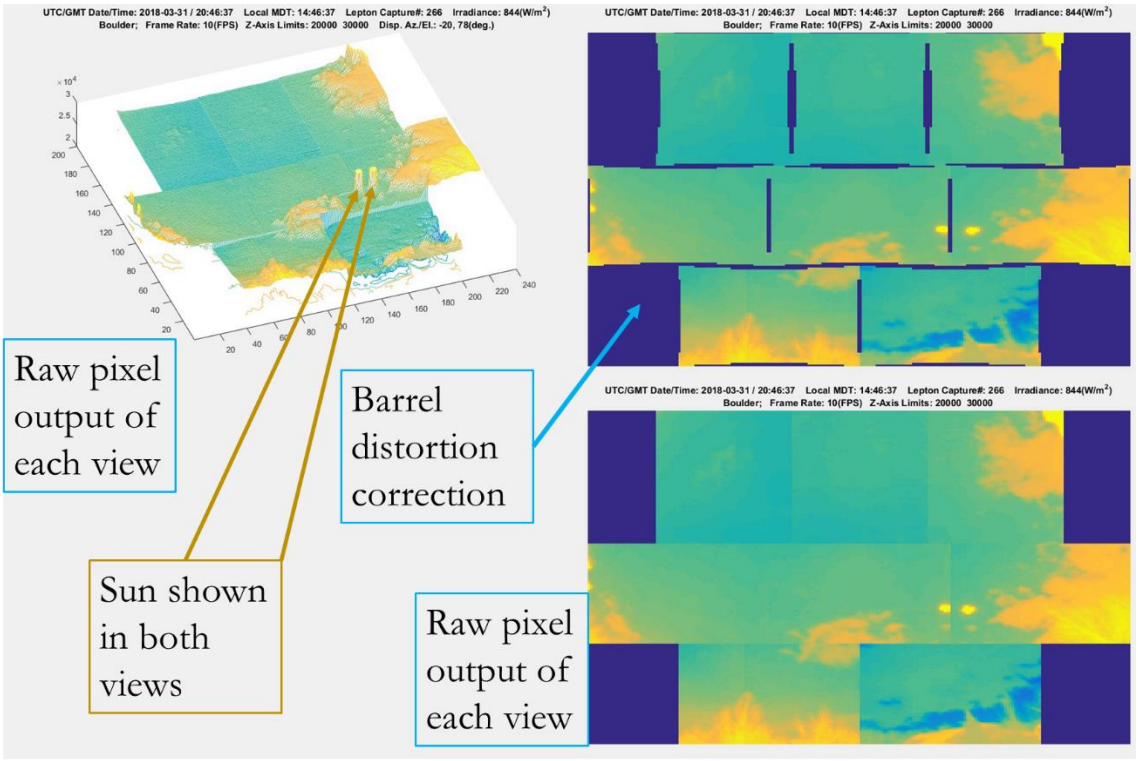


Figure 6-20, Raw output of the views in approximate orientation.

In Figure 6-19. all the views are shown in their equatorial transformations.

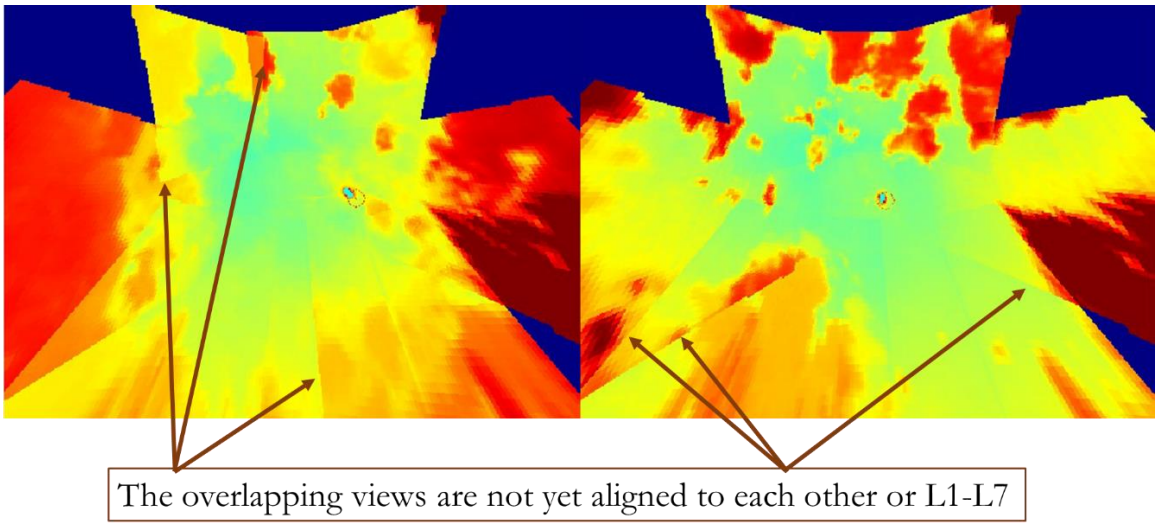


Figure 6-21, A reproduction of Figure 6-19 highlighting the inaccuracies of the aligned L1-L7 views.

The total alignment process is highlighted in the two methods highlighted above.

### 6.6.1. Alignment process of Sensors with each other

Overlapped regions are shown in Figure 6-21. These regions are used to calculate a stitching algorithm with the following assumptions.

1. Individual sensors have their own manufacturing defects that systematically alter individual pixel responses. A function called the Far Field Correction on the sensor itself normalizes all pixels to a closed shutter. Though the offset of each pixel is now uniform relative to the sensor, the total offset of the sensor itself is mainly temperature skewed and varies between sensors. It was assumed that the offset of each sensor, once corrected with the Far Field

Correction, is an offset that can be calculated by comparing pixel values of different sensors viewing the same object.

2. It is assumed that the range of pixel response of each sensor is different from sensor to sensor but uniform across individual sensors.

With the above assumptions, a similar process was employed to align the views with each other as was the process to align the sun to the view. The process is the following:

1. L1 and L3 were already calculated and their offsets are incorporated into the projection calculations of all views.
2. L3 was known and used to set the theoretical overlap region of each sensor with $\theta 3 = 0$ for L0.
3. $\theta 4 - \theta 6$ were then varied randomly around their current values for views L1-L7.
4. The standard deviation and average of each overlap region relative to L0 was used to normalize the non L0 view to the L0 view. This was accomplished by utilizing L0 as the reference average and reference standard deviation. The other view was systematically offset and then multiplied by a percentage so that standard deviations of the overlap region match to the L0 region.
5. The average error between the different overlap regions was calculated by taking the absolute value of the difference in pixel intensities that overlap each other and dividing by the number of pixels. This average difference was used

to update the θ4 – θ6 values of the L1-L7 sensors if #6 and #7 also passes. If the average error value with the different random rotations of each overlap region is lower than before, the new values were used as the new random offsets for each sensor individually, again assuming #6 and #7 holds.

6. The difference between the overlap regions with each other sensor not including L0 was calculate. For example, L4 overlaps with L5. If the average error between views L1-L7 and their overlap regions reduces, #7 proceeds.
7. If the sun is in one of the L1-L7 views, an additional step is required before the determination is made to update the values. This step is highlighted in the chapter 'Alignment of Non-L0 Sensors', below.

If each sensor had the same range, average pixel response and their geometries aligned with each other, the theoretical error should drop to zero. If the total error between all sensors slows to a threshold, the new values are accepted

### 6.6.2. Alignment of Non-L0 Sensors

The alignment process of non L0 sensors that also incorporate the sun is listed below:

1. Since the variation in angles is already made, the distance between the two sun positions is calculated and averaged.
2. If the distance lowers, this process is considered complete and fulfills the requirements of the alignment of the L1-L7 sensors.

This alignment process is like the alignment of L0 with the sun, where the view angles are varied to match the sun position.

Figure 6-22 shows two fully stitched images of the sky.

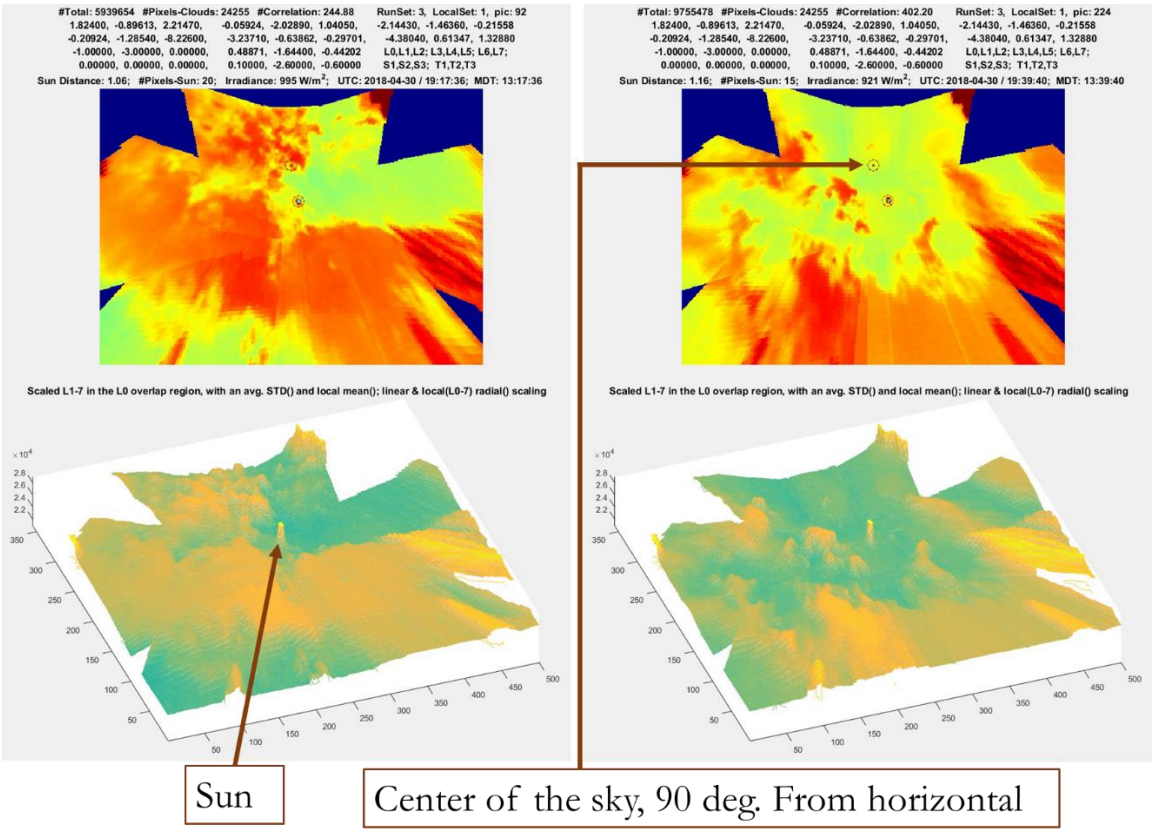


Figure 6-22. Two full sky-views highlighting fully stitched images with mean pixel intensity adjustment and normalization to the standard deviations in the overlap regions of L0.

Note the lower half of the stitched images shows the raw pixel values. Though there are still some discrepancies between views, the stitching algorithm produces data that is nearly seamless. The sun is also shown, highlighting the pixel values that can be used above a threshold value to locate the sun center.

The importance of accurate cloud velocities was highlighted as the motivation for precise image stitching.

# 7. Verification and Validation of LAPART

The Defense Advanced Research Projects Agency (DARPA) set two benchmarks for the validation of a similar form of LAPART know as Fuzzy ARTMAP. [196] [208] The benchmarks were to identify both a circle in a box and a more complex benchmark, identification of two interwoven black and white spirals. The methodology of identification of the two spirals was to provide a non-linear and non-systematic problem for the parsing of distinct categories of the neural network. A similar methodology to validate LAPART was formed and explained below.

## Verification and Validation of LAPART with a Non-Systematic and Non-Linear Dataset

To validate LAPART was functioning correctly, an image [209] of a microscopic skin cell was processed through LAPART to reconstruct the original picture. The A and B-side input space are shown in Figure 7-1 and Figure 7-2 below. In the cartesian preprocessing method the A-side inputs were the x and y normalized location of the red, green and blue pixels. The origin was the upper left-hand corner. The A-side inputs of the cylindrical preprocessing method was the normalized radius and angle of the red, green and blue pixels. The origin is the center of the image.

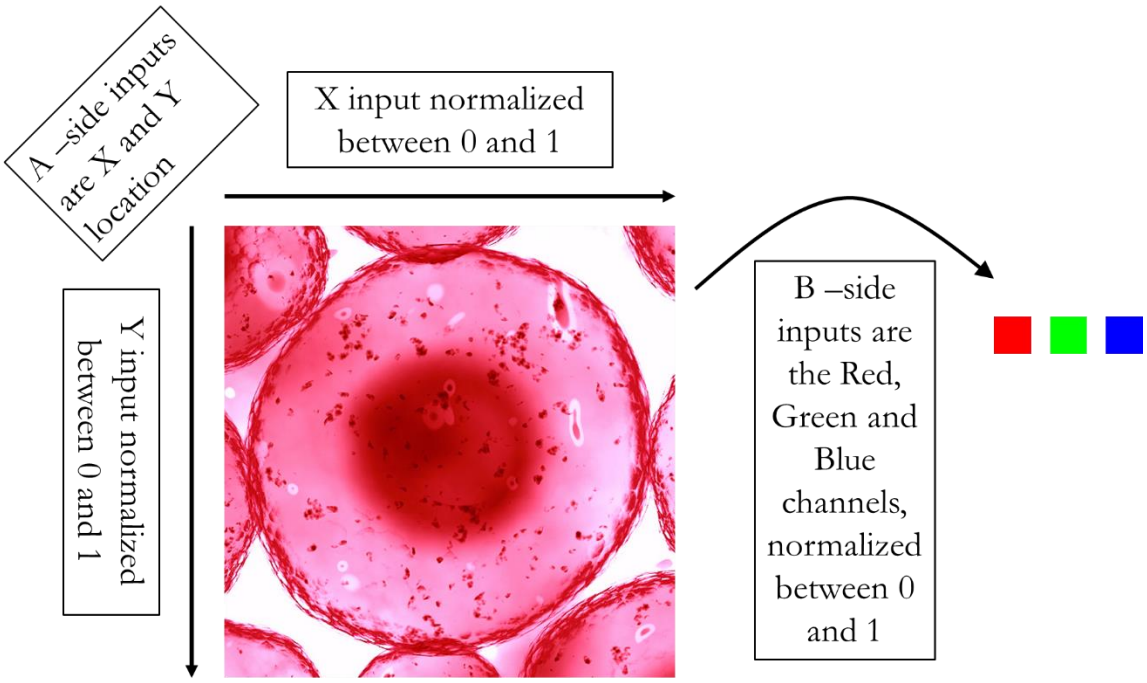


Figure 7-1. Non-systematic input space for Verification and Validation of LAPART, inspired by biology, processed in cartesian coordinates.

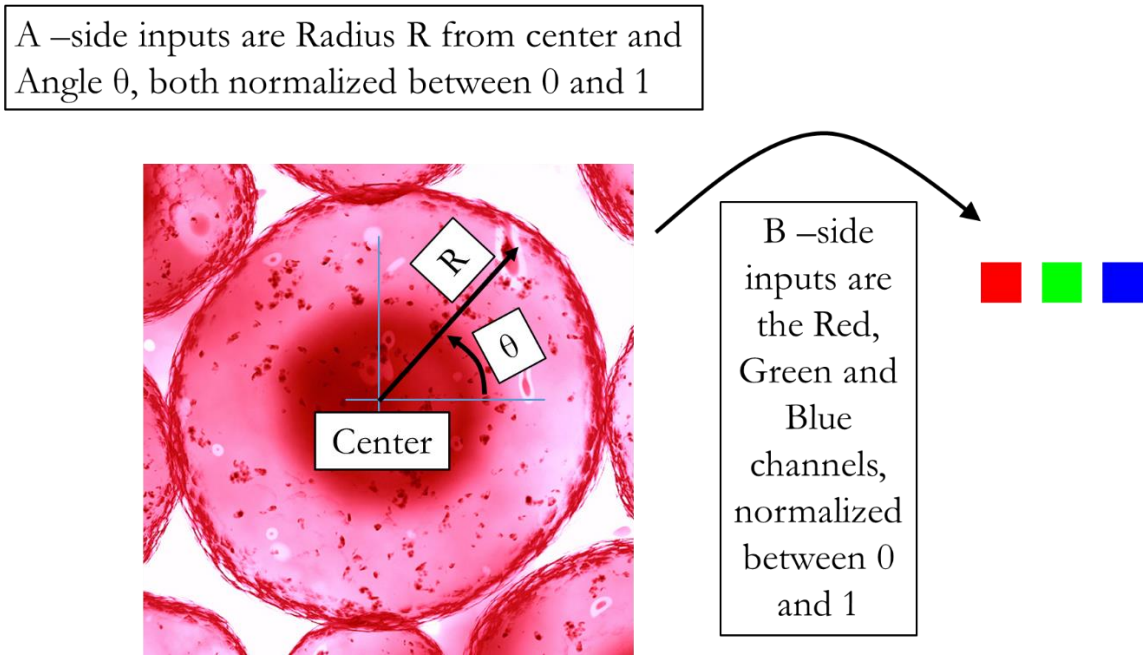


Figure 7-2. Non-systematic input space for Verification and Validation of LAPART, inspired by biology, processed in cylindrical coordinates.

In order to validate LAPART was classifying correctly, the Root Mean Squared (RMS) error, as defined in (8-1) for a single input, was utilized in the multidimensional space as a measure of accuracy. Both $\rho_A$ and $\rho_B$ were varied together from 0.5 to 0.9 and 0.95. The number of categories on the A and B side were recorded and the RMS error of the color reconstruction was also recorded and is shown in Table 7-1 and Table 7-2 below.

| **Cartesian Coordinates; LAPART Classification and Accuracy as a function of Parameters** | | | | |
|---|---|---|---|---|
| **Rho A** | **Rho B** | **Num. A categories** | **Num. B categories** | **Average RMS Error** |
| 0.5 | 0.5 | 45 | 12 | 73.25 |
| 0.6 | 0.6 | 73 | 15 | 70.44 |
| 0.7 | 0.7 | 145 | 22 | 72.82 |
| 0.8 | 0.8 | 467 | 42 | 72.43 |
| 0.9 | 0.9 | 2743 | 128 | 64.06 |
| 0.95 | 0.95 | 13665 | 508 | 37.07 |

Table 7-1. Accuracy and classification error of LAPART as a function of A&B ρ inputs in Cartesian coordinates.

| **Cylindrical Coordinates; LAPART Classification and Accuracy as a function of Parameters** | | | | |
|---|---|---|---|---|
| **Rho A** | **Rho B** | **Num. A categories** | **Num. B categories** | **Average RMS Error** |
| 0.5 | 0.5 | 27 | 8 | 63.89 |
| 0.6 | 0.6 | 59 | 15 | 64.05 |
| 0.7 | 0.7 | 115 | 22 | 70.21 |
| 0.8 | 0.8 | 365 | 39 | 77.07 |
| 0.9 | 0.9 | 2050 | 145 | 68.38 |
| 0.95 | 0.95 | 10921 | 515 | 44.98 |

Table 7-2. Accuracy and classification error of LAPART as a function of A&B ρ inputs in Cylindrical coordinates.

"Robust Returns" was a function written to modify the Fuzzy LAPART to ensure a prediction was made. Instead of failing when a category is not found, the function returns the max choice whether it passed vigilance or not. This function was employed to ensure a B-side prediction was always returned.

In both cylindrical and cartesian coordinates, the RMS error was reduced when the A and B rho parameters were increased. This was expected of LAPRT and of other neural networks that are functioning correctly. Since the accuracy of LAPART was the parameter analyzed, the time to run and train each of the scenarios was not analyzed. In both preprocessing methods, there was a local minimum of error around A and B rho of 0.6 and 0.7 even though the overall error went down. This would suggest the ability of LAPART to classify well before it overclassifies by memorizing.

Of note are the input pre-processing parameters that construct the A-side input space. Since a cell is a relatively round object and the image was constructed with the main features centered, the expected output would result in a larger number of A side categories in the cartesian input relative to the cylindrical coordinate system preprocessing. This was shown as the number of A-side categories formed for the cartesian coordinate system preprocessing was consistently 50% to 20% higher than the number of A-side categories formed for the cylindrical coordinate system. Consistent with the formation of the B-side color pallet, the number of categories formed for both the cartesian and cylindrical coordinate systems preprocessing was

relatively the same. Both the increased number of A-side categories in the cartesian preprocessing system and the relatively similar number of B-side categories for the color pallet for both preprocessing methodologies was consistent with a functioning and operative neural network.

Lastly, the human brain inclusive of the visual perception system should be able to perceive an increase in the accuracy of the images reproduced by LAPART. These reproductions are shown below in Figure 7-3 and Figure 7-4 for human visual observation.

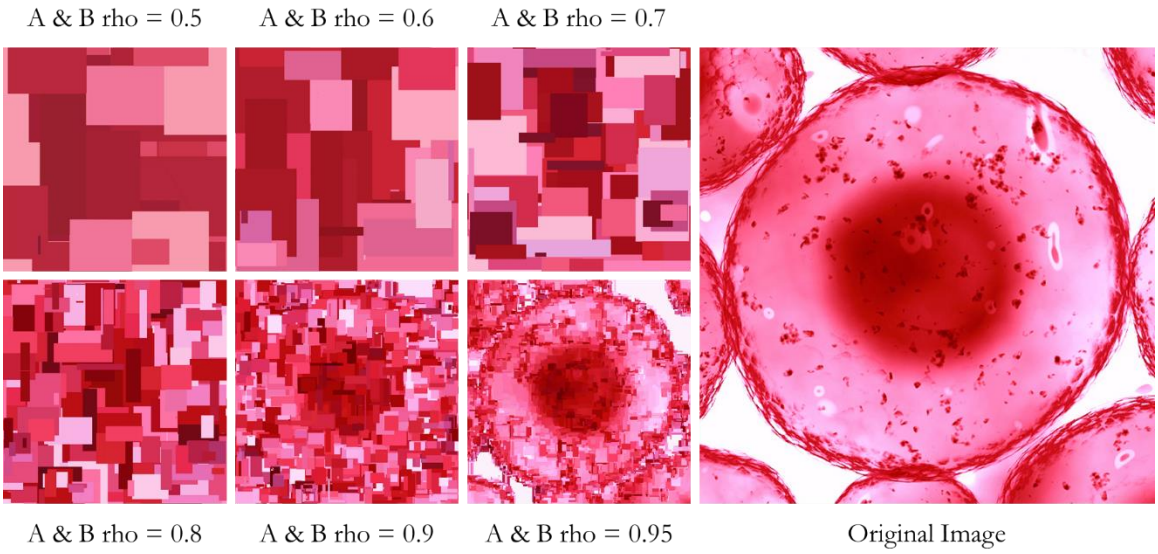


Figure 7-3. B-side image reconstruction of the original LAPART A-side inputs in cartesian coordinates by rho value.

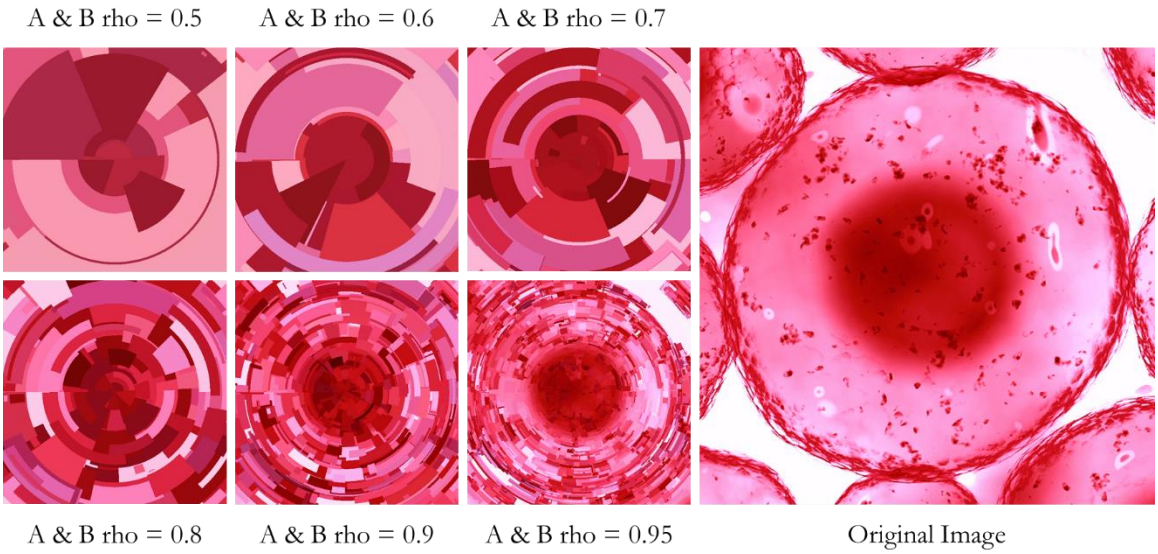


Figure 7-4. B-side image reconstruction of the original LAPART A-side inputs in cylindrical coordinates by rho value.

Persistent to a neural network that learns and becomes more accurate, LAPART has shown that both images were reconstructed closer to the original image as both $\rho_A$ and $\rho_B$ were increased closer to unity, despite the local minimums.

# 8. Fielded System Results with Multiple Data Extraction Methodologies for the Neural Network

A Small Business Technology Transfer Grant (STTR I NSF 16-555) was submitted in collaboration with Micro Grid Labs (MGL) and the University of New Mexico (UNM) to develop a forecasting methodology based on the aforementioned algorithms and technology. Fielded trials were conducted in Boulder Co. and at the University of New Mexico's Center for Emerging Energy Technologies (CEET) microgrid in Albuquerque. A table of all the days and times used from Boulder, Co. is listed in Appendix C.

## 8.1. LAPART Inputs

An outline of LAPART and the inputs and outputs during the training and testing methodologies follows. During the training stage of LAPART, the A-side input was the VG data pixel intensity at time t and the B-side input is the irradiance at time t + Δt, where Δt is the prediction time horizon. Therefore, training is delayed until the actual irradiance in the future is known. This process is shown in Figure 8-1 below.

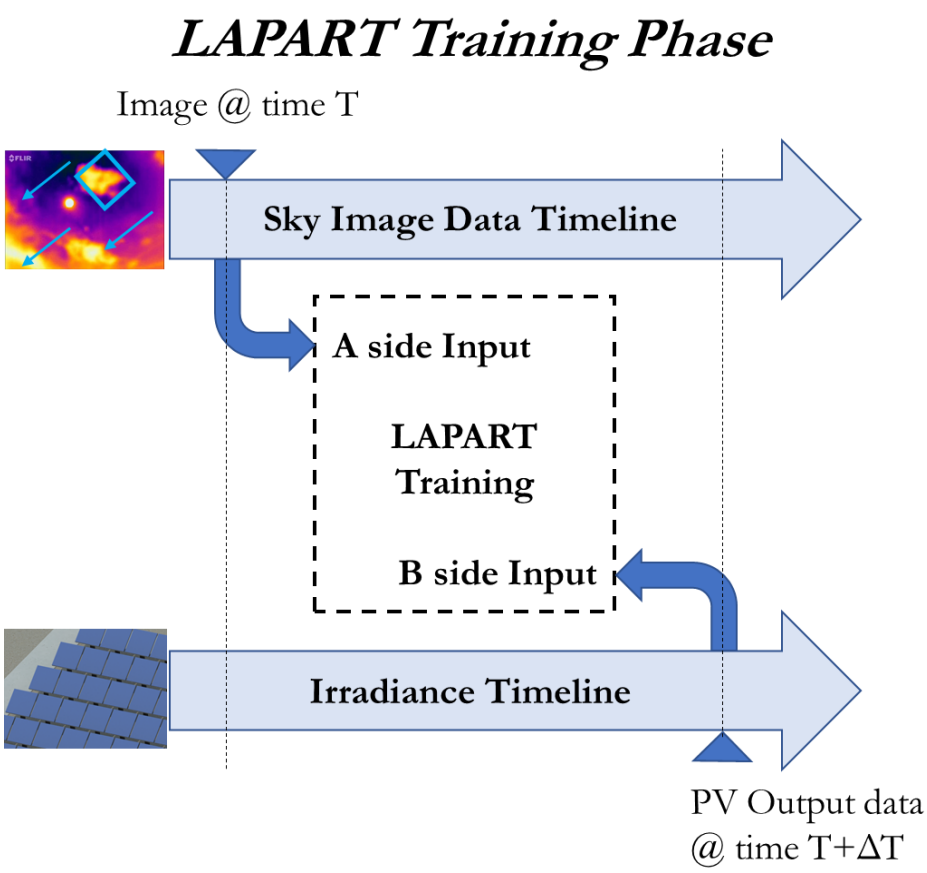


Figure 8-1. Training in LAPART for SIMF.

When LAPART is in testing or prediciton mode the same VG input are fed into the A-side of the network. However, the B-side of LAPART predicts the irradiance output at time Δt from the association of the hyperbox linked to the A-side input. This process is shown in Figure 8-2 below.

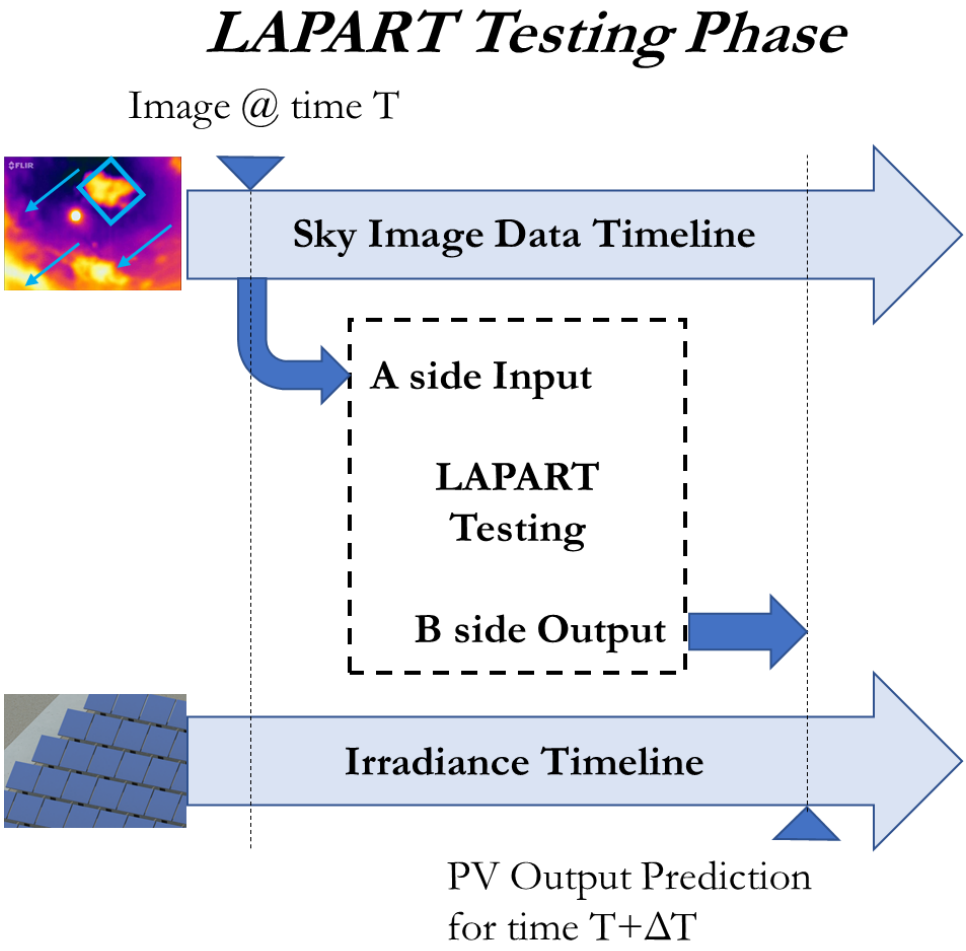


Figure 8-2. Testing (prediction) in LAPART for SIMF

In the testing scenario, the associator is not updated with the learning implementation until after the irradiance is known and or there is enough computation time for the learning process.

## 8.2. LAPART Error Definitions

LAPART is an associatorf that connects hyperboxes of A-side inputs to B-side inputs with laterally weighted connections. This is shown in Figure 8-3 below.

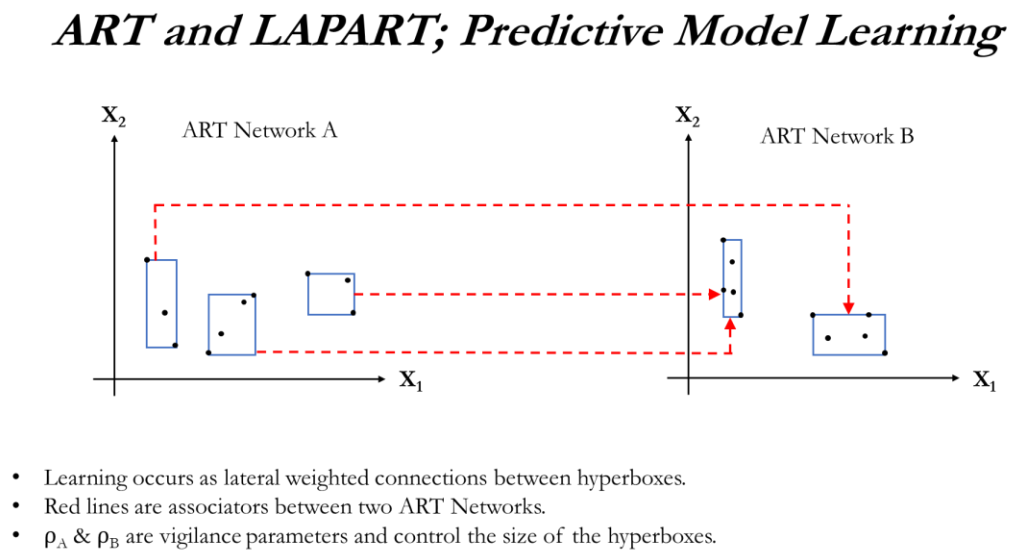


Figure 8-3. LAPART predictive model learning of lateral weighted connections between hyperboxes.

In the example above, the A side network has two inputs and so does the B-side. However, when applied to SIMF, the A side inputs are four hundred long and the B-side is only 1 inut long. This is shown in Figure 8-4 below.

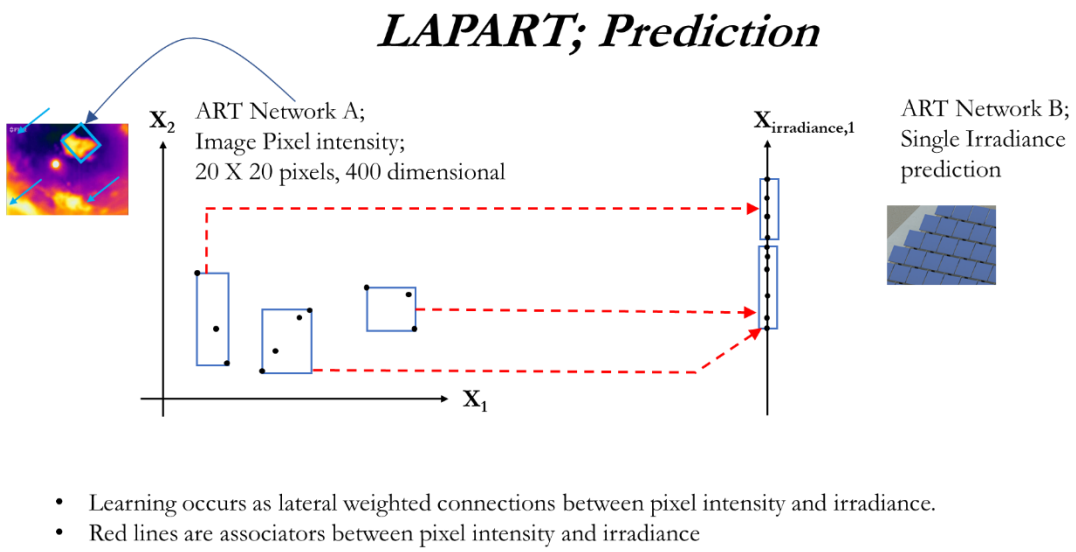


Figure 8-4. SIMF A and B-side inputs for LAPART.

The pixel intensities are associated on the A-side of LAPART and the irradiance is associated on the B-side. In the example above, the B-side irradiance hyperbox contains a range of irradiance values in which the associator might link to. When LAPART is in testing and an association is found that links to a known hyperbox, the prediction is considered a succes. This is shown in Figure 8-5, below.

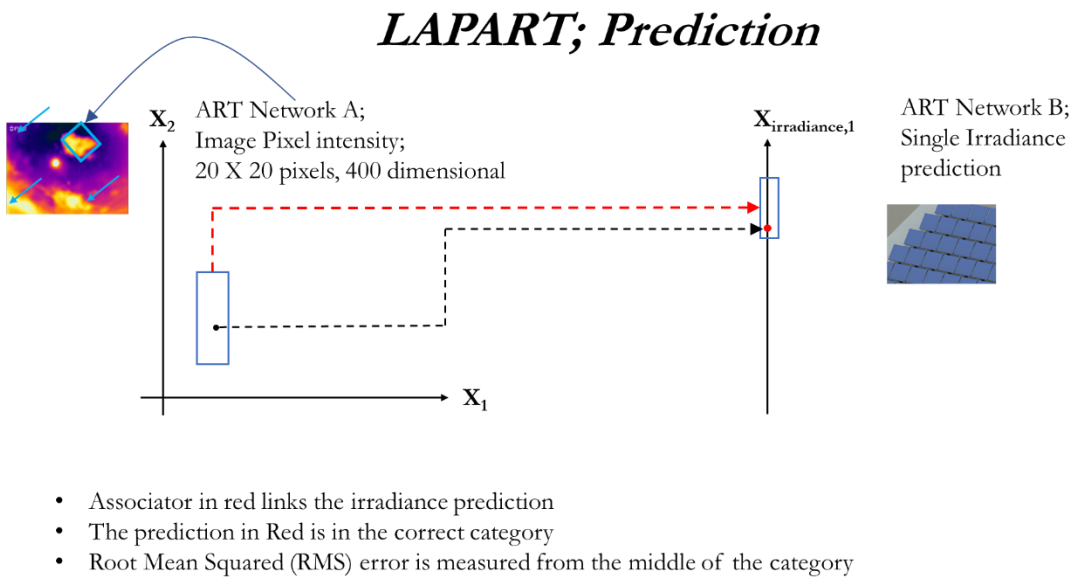


Figure 8-5. Successful LAPART prediction to know irradiance category.

Since the B-side category is known and the irradiance is within the bounds of the category, the prediction error can be considered to be the size of the category itself. In practice, the RMS error was always calculated from the center of the category no matter what the irradiance actually was. This error analysis is shown in Figure 8-6, below.

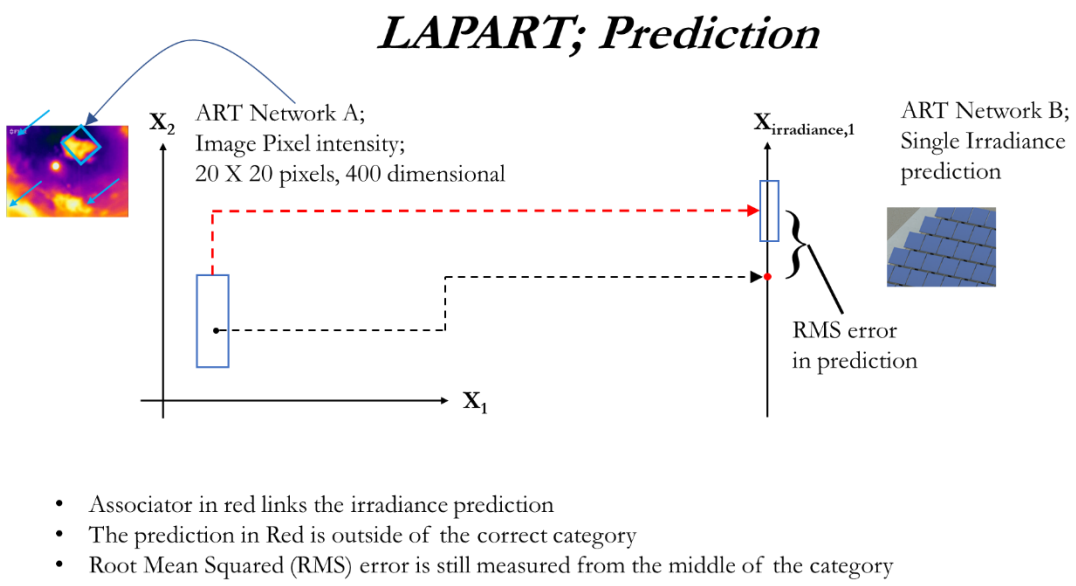


Figure 8-6. Incorrect irradiance prediction by LAPART.

In all cases, an RMS error was constructed from the center of the B-Side irradiance prediction category to the actual irradiance in the future.

## 8.3. Data Flag Methodology

Data extraction for any neural network relies on limiting the input space to the minimum necessary information. This is done for two reasons:

1. LAPART and any neural network will learn faster when the input is limited in size to the essential information necessary to form a correlation relationship between the A-Side and B-side inputs.
2. LAPART and any neural network will form less association between A-side data that may be correlated but provides no cause and effect relationship to B-side data. Learning any superfluous A-side data can confuse the network by

overlearning associations that are not present in a cause and effect relationship to B-side inputs.

This principal was adopted, and the data flag was formulated to limit the input space. Take for example Figure 8-7, shown below.

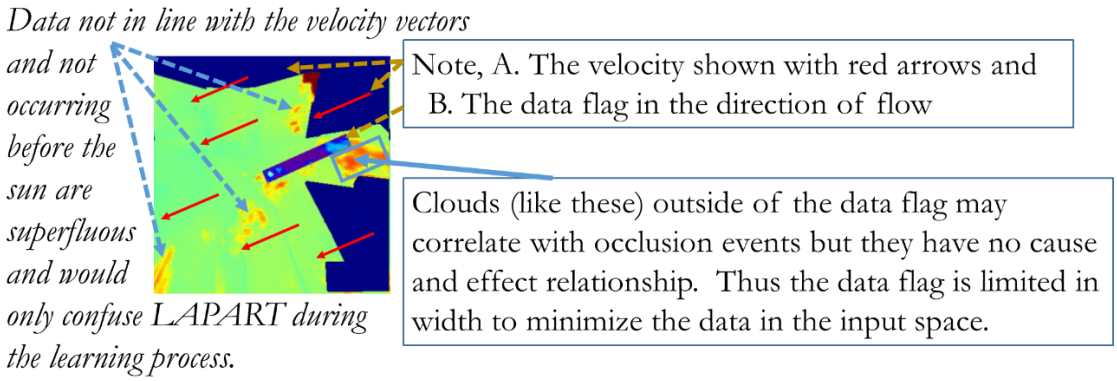


Figure 8-7. Data Flag example to limit the input space.

It contains cloud data, but only the clouds that are under the data flag will intersect the sun. Note that the picture is large compared to the data flag that contains the relevant data. The VG method was formulated as an initial means to further reduce the input space and is explained below.

## 8.4. Velocity Gate Method Error Analysis

The VG method utilizes the current cloud velocity in pixels/frame to construct a window of A-Side inputs over the data flag. Figure 8-8 shows an example of this calculation. This method experiences error when accurate cloud velocity measurements are not utilized. The VG location is calculated by multiplying the velocity of the clouds in pixels/frame by the number of frames, thus if inaccurate

velocity measurements are used, the VG will not accurately contain the proper sky patch. A padding could them be applied on both sides typically equal to half of the width of the Data Flag to account for inaccuracies in the velocity measurements.

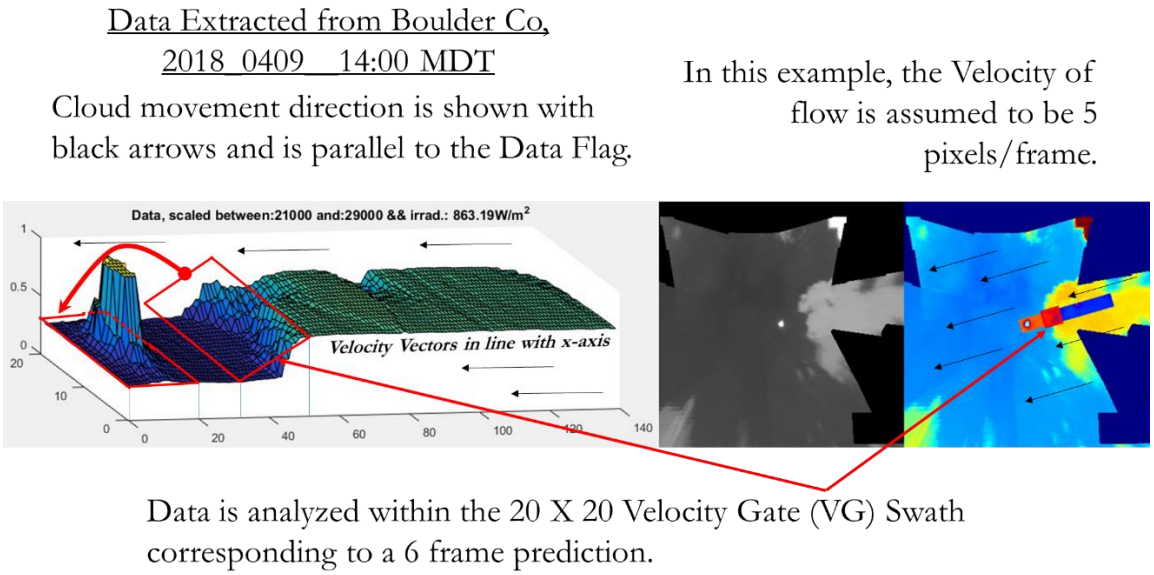


Figure 8-8. Velocity Gate Example shown for Boulder Colorado. The velocity for this example is assumed to be 4 pixels per frame predicting 6 frames into the future. The Data graph show the normalized value of each pixel.

As is the case in Figure 8-8, the sun is centered at coordinated (10,10) in the Data Flag. Assuming a 6-frame prediction and a velocity of 5 pixels/frame the left and right coordinates of the VG are 30 and 50 pixels. The VG then contains a 20 x 20 swath of date.

The input to LAPART was a 1X400 swath as shown in Figure 8-9.

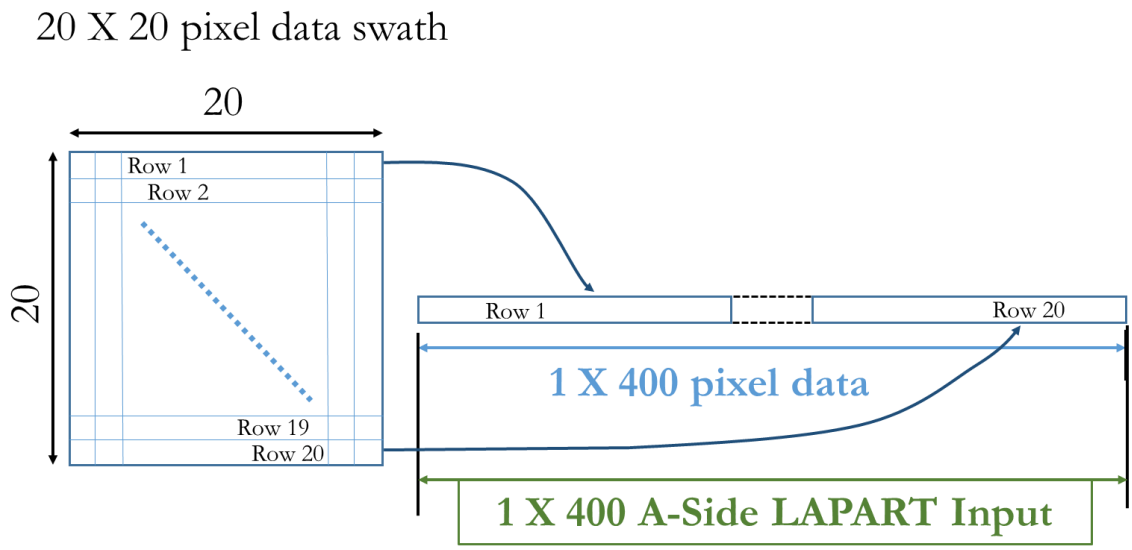


Figure 8-9. Data processing example for a 1x400 total swath of data for the A-Side input to LAPART.

Error analysis for the VG method comes in the form of heuristic observations of inaccurate average cloud velocity measurements. If the velocity is not correct, then the VG will not be placed in the correct location in the data flag area.

## 8.5. Correlation of VG Pixel Intensity and Future Irradiance

In ideal circumstances the pixel intensity should be directly correlated to irradiance. However, in practice it was not. This was likely due to internal functions on the firmware of the sensor itself that systematically altered its output higher or lower based on several known outside factors. This was also the reasoning behind the stitching algorithm that was employed. An example of this problem is highlighted in Figure 8-10 below. It illustrates how similar irradiances correlate to different sensor

output ranges. In all data collection scenarios, data was obtained in 10 second intervals.

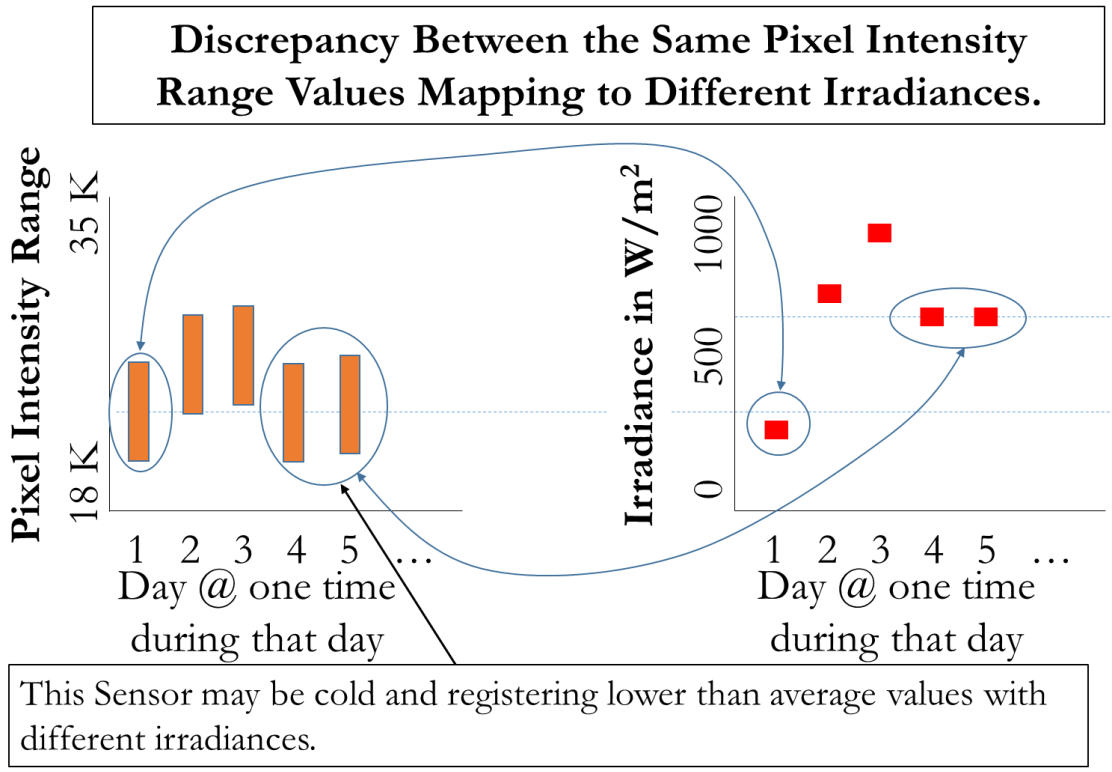


Figure 8-10. Visualization of date sensors mapping to artificially higher or lower irradiance predictions.

To quantify this problem, the averaged and normalized pixel intensity for the VG was plotted against the normalized future irradiance for a 120 second prediction. The first seven days of the fielded trials were plotted in Graph 8-1, with different colors for each day, for Boulder, Co.

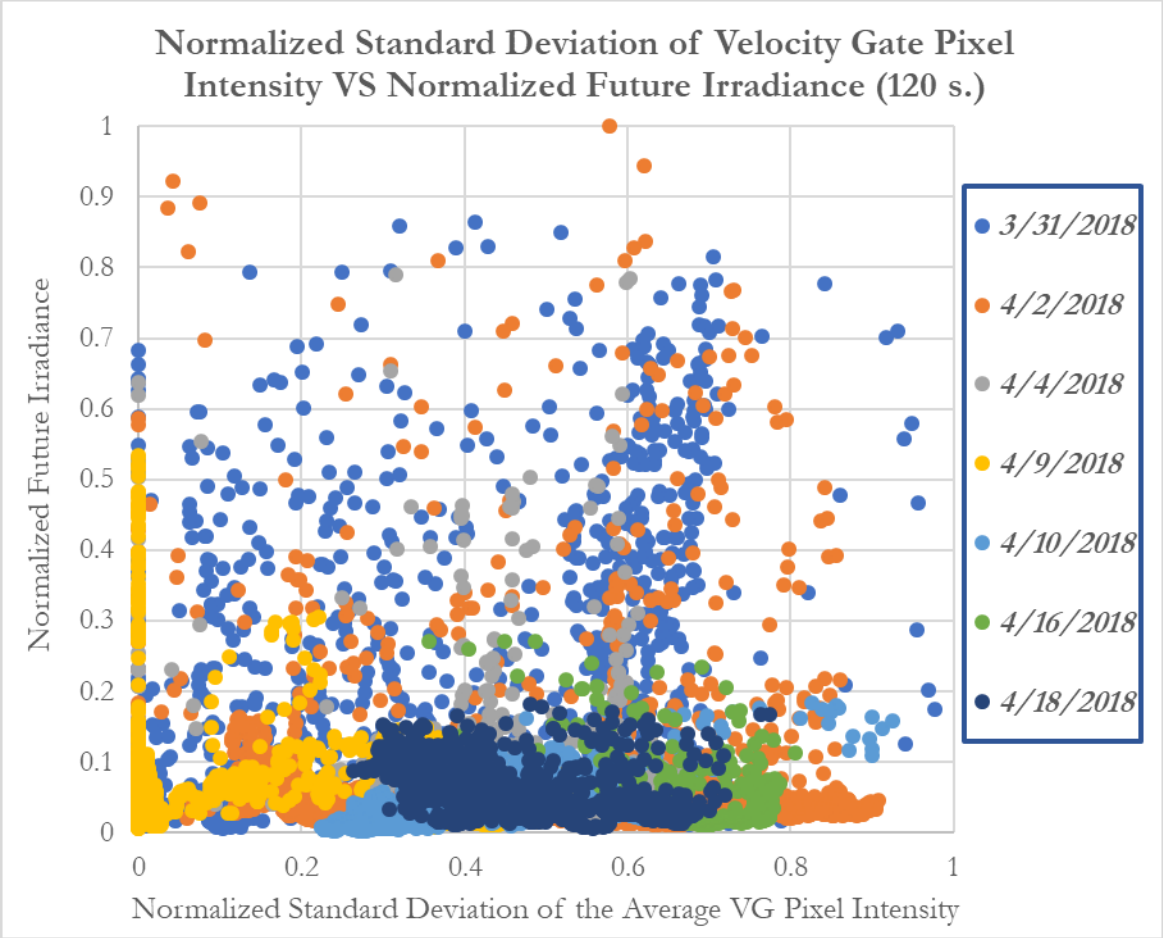


Graph 8-1, Normalized and averaged velocity gate pixel intensity vs 120 second normalized irradiance.

Graph 8-1 illustrates there is no multi-day correlation between VG pixel intensity and future irradiance. It is hypothesized from the observation of Figure 8-10, that the temperature of the sensor may have some effect on the output reading. Due to visual inspection of data variability between days, no correlation analysis was completed on Graph 8-1, as none exists.

The VG A-Side pixel data inputs were then scaled from 15,000 to 45,000 the irradiance was scaled between 200 and 1200 W/m$^2$.

## 8.6. Examination of the Correlation Between Uniform Velocity Gate Conditions and Future Irradiance

Since the total VG was averaged in Graph 8-1, it was assumed that nonuniformly cloudy conditions could exist. For example, a cloud could be located half in the VG and the other half could be clear sky as is illustrated in Figure 8-8. To examine a relationship where only clouds or only clear sky exists in the VG, the standard deviation (SD) was calculated for all of the VG data points. In all scenarios, the VG consisted of 20*20 = 400 total pixel data points.

In all data collection scenarios, larger VG values correspond to lower irradiance values. This was highlighted in Figure 8-8. The lower the value of the VG pixels the higher was the projected irradiance. This assumes ideal conditions, uniform sensor firmware data acquisitions and constant environmental conditions. This correlation was opposite from the older style sensors that correlate larger pixel values with lower irradiance values. The following scenarios limited the normalized VG SD to less than 0.02 when specified. This was done to investigate different correlations between VG pixel values and future irradiance, on individual days, with fixed firmware initializations.

Graph 8-1 was replotted as Graph 8-2 with the restricted normalized VG SD parameter being set to less than 0.02.

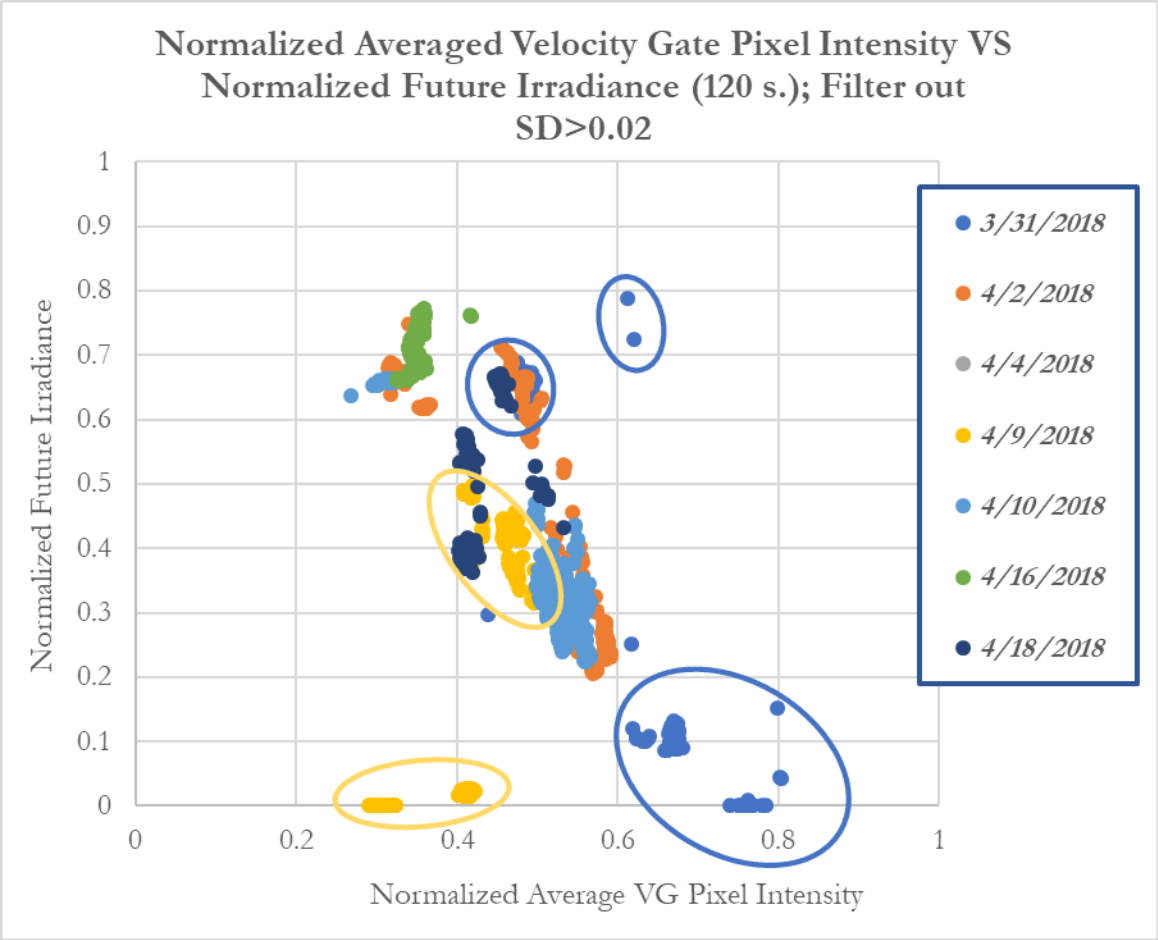


Graph 8-2. Normalized Averaged Velocity Gate Pixel Intensity vs. Normalized Future Irradiance (120 s.); Filter out SD>0.02.

The dates of 3/31/2018 and 4/9/2018 highlighted again the nonlinearity of the correlation between pixel intensity and future irradiance. On date 4/9/2018 normalized future irradiance is bifurcated into two ranges. The first group is shown with normalized future irradiance near zero. The second group is in the middle with normalized future irradiance values between 0.3 and 0.5. These two groups were encircled in gold. The date of 3/31/2018 exhibits multiple outliers in four clusters, all of which were encircled with blue. The outliers for that date, both above and below, showed that the correlation does not hold.

Analysis of the remaining dates provided more favorable results. In general, the correlation is negative and showed that as the average VG values decrease, the irradiance increases.

To investigate the overall correlation of normalized future irradiance and normalized average velocity gate values the first seven days of data were plotted in Graph 8-3.

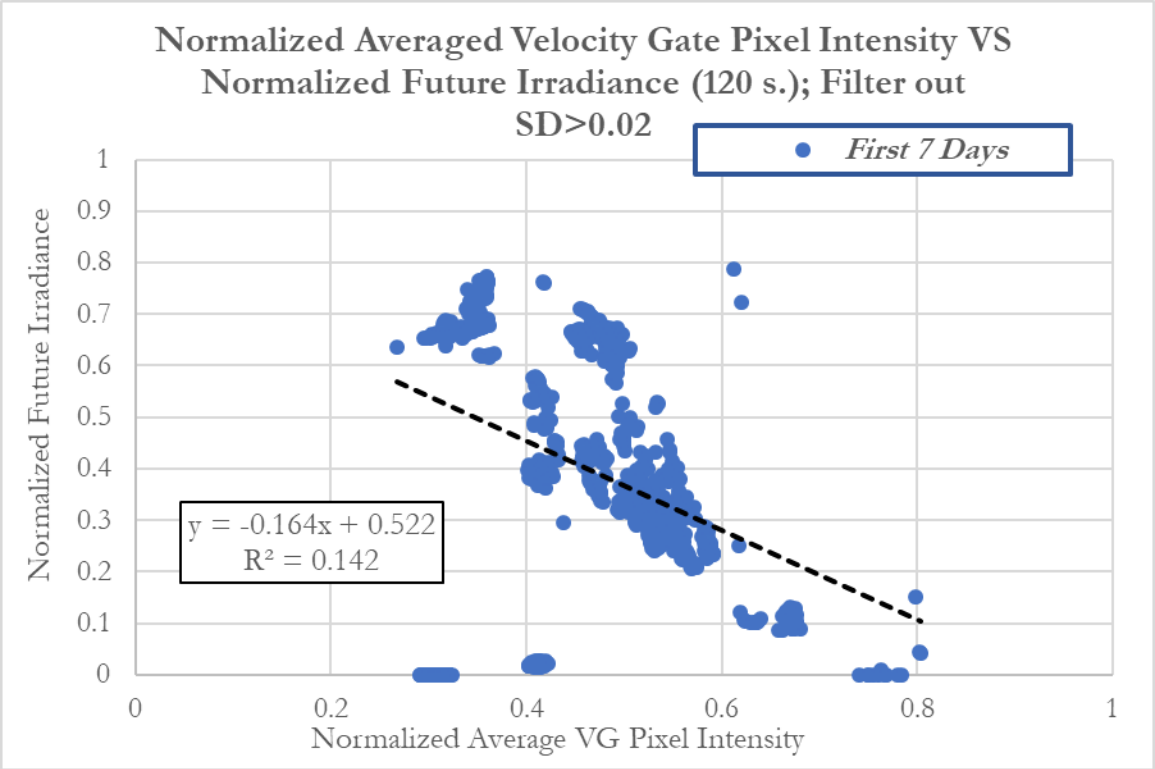


Graph 8-3. Normalized Averaged Velocity Gate Pixel Intensity vs. Normalized Future Irradiance (120 s.); Filter out SD>0.02.

A linear interpolation was applied and an R-squared value of 0.142 was obtained. Thought the trend was generally linearly decreasing, as was to be expected, the R-squared value proves little correlation between normalized future irradiance and average VG pixel intensity.

It was hypothesized that as the sun crosses the sky and passes into the view of different sensors, errors may occur due to the different firmware settings in the individual sensors. To investigate this hypothesis, two days were plotted individually. The data set was further restricted to a timeframe when the sun was in only one sensor. These are shown in Graph 8-4 and Graph 8-5 below.

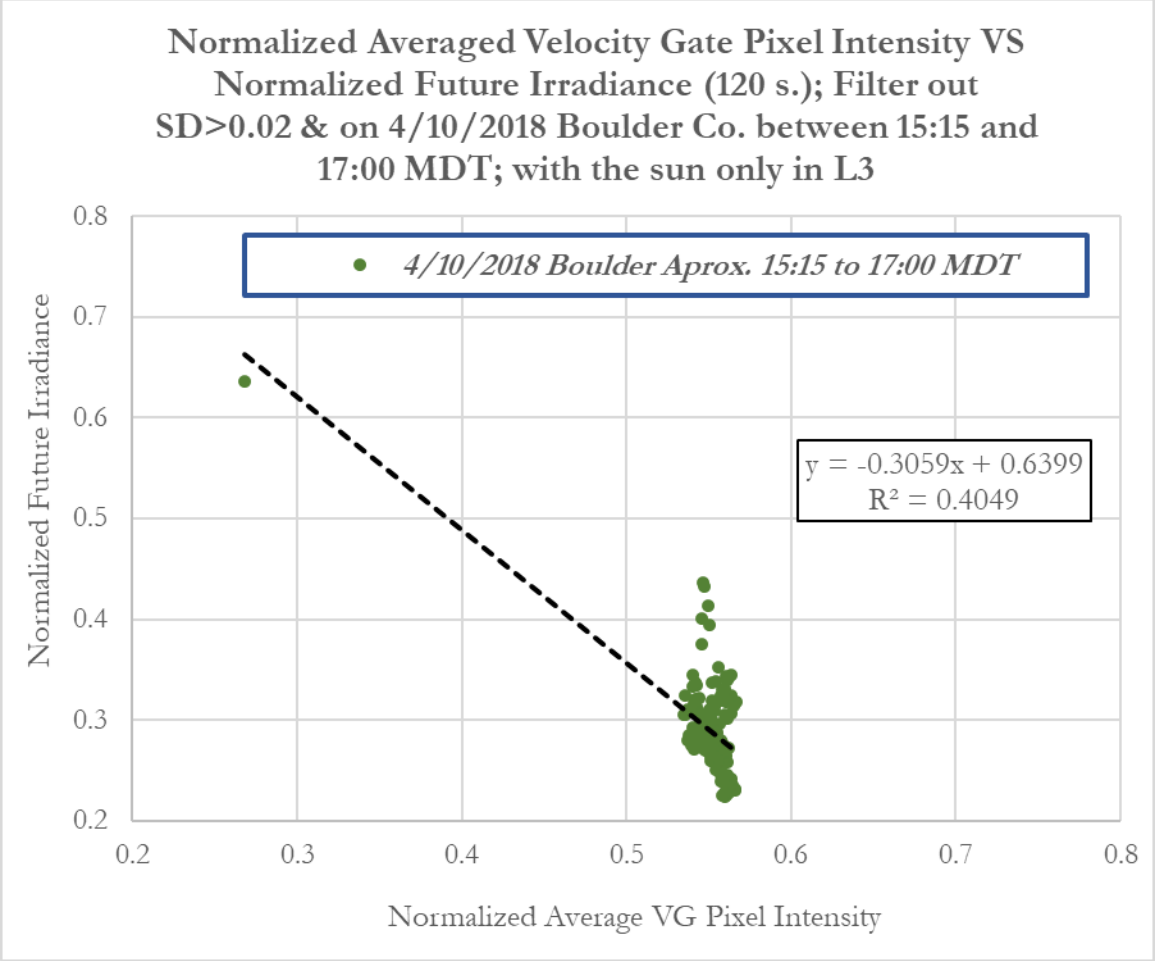


Graph 8-4. Normalized Averaged Velocity Gate Pixel Intensity vs. Normalized Future Irradiance (120 s.); Filter out SD>0.02 & on 4/10/2018 Boulder Co. between 15:15 and 17:00 MDT; with the sun only in L3.

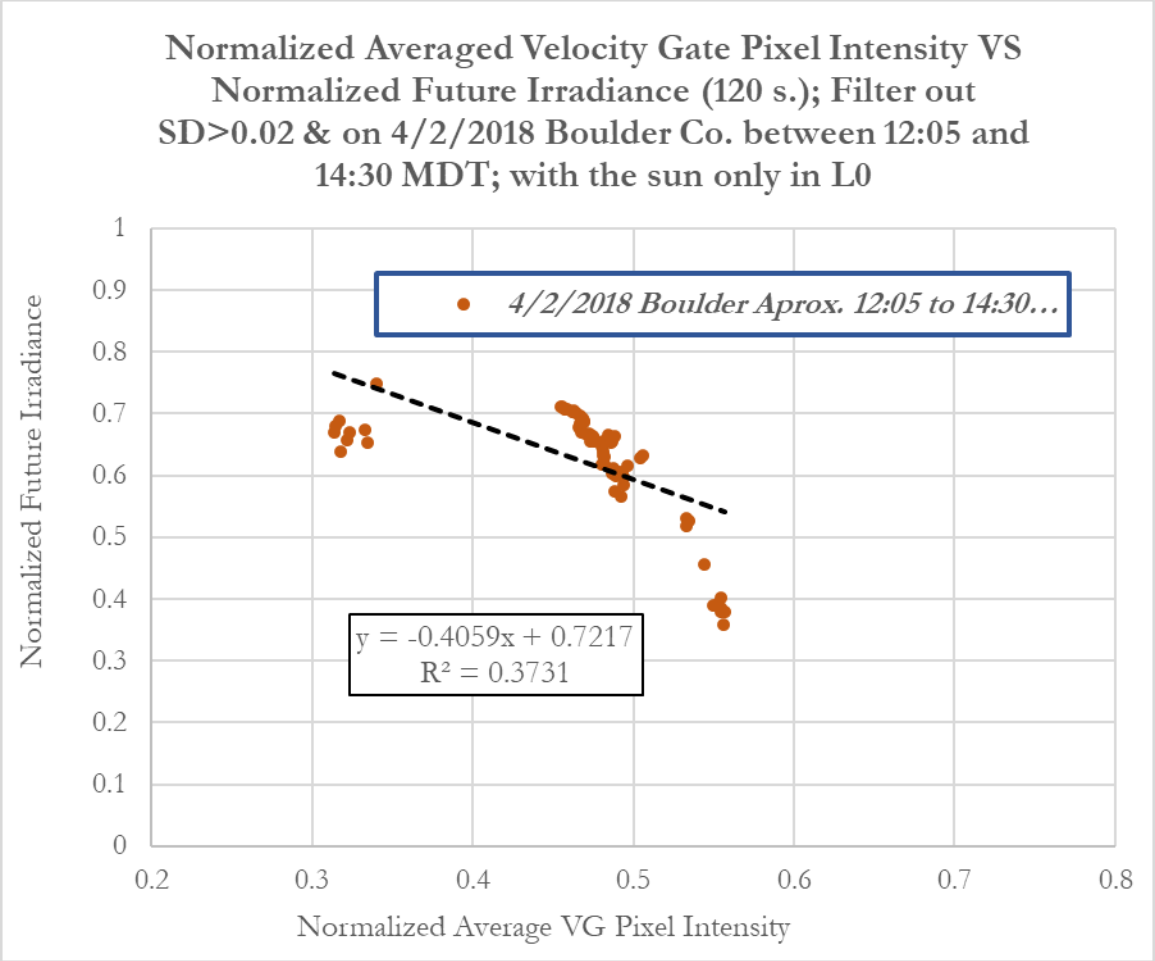


Graph 8-5. Normalized Averaged Velocity Gate Pixel Intensity vs. Normalized Future Irradiance (120 s.); Filter out SD>0.02 & on 4/2/2018 Boulder Co. between 12:05 and 14:30 MDT; with the sun only in L0.

The R-squared values greatly improved but remained suboptimal.

To furthered highlight these disjoint correlations, the normalized average VG pixel intensity was plotted with the normalized future irradiance. They are shown below in Graph 8-6 and Graph 8-7 for specific dates and times when the sun is only in one of the sensors.

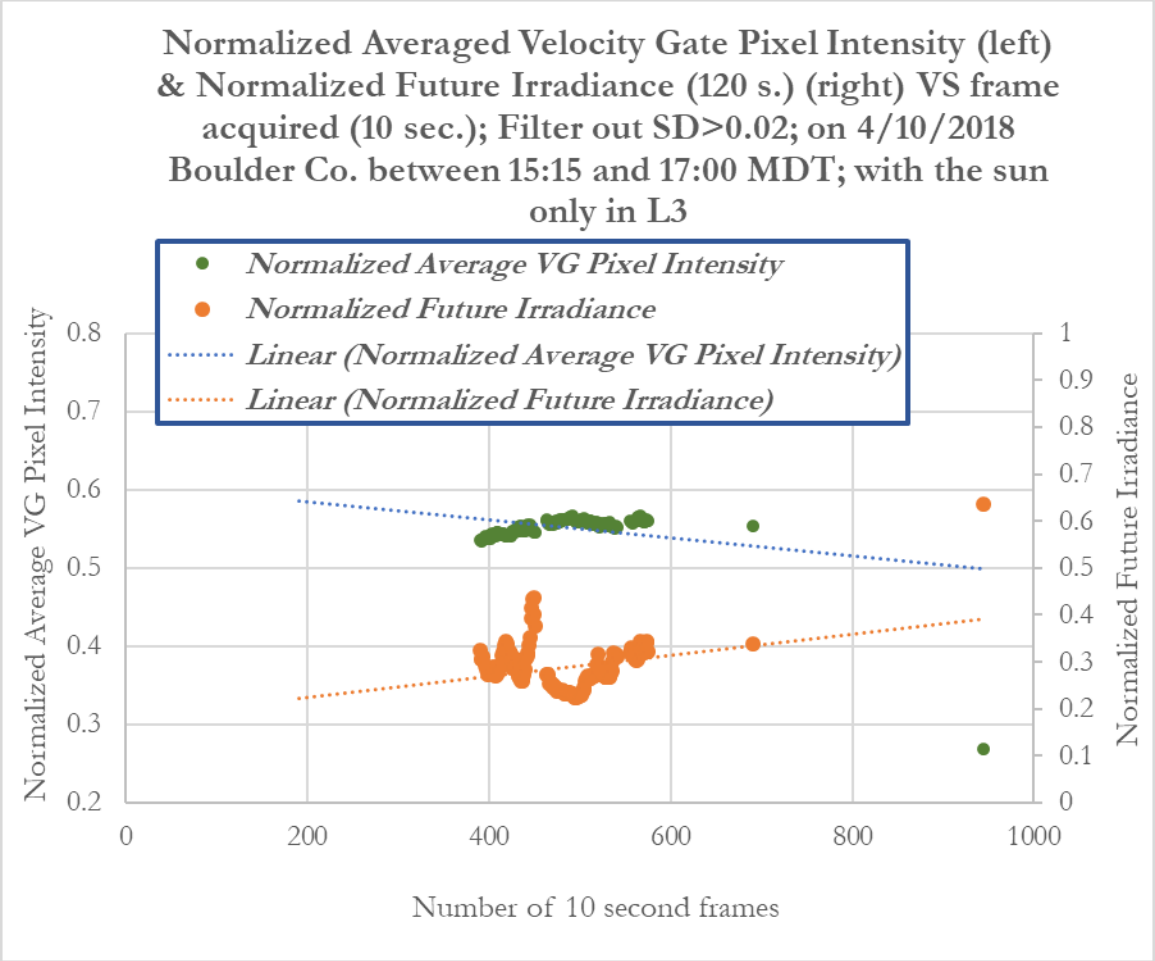


Graph 8-6. Normalized Averaged Velocity Gate Pixel Intensity (left) & Normalized Future Irradiance (120 s.) (right) vs. frame acquired (10 sec.); Filter out SD>0.02; on 4/10/2018 Boulder Co. between 15:15 and 17:00 MDT; with the sun only in L3.

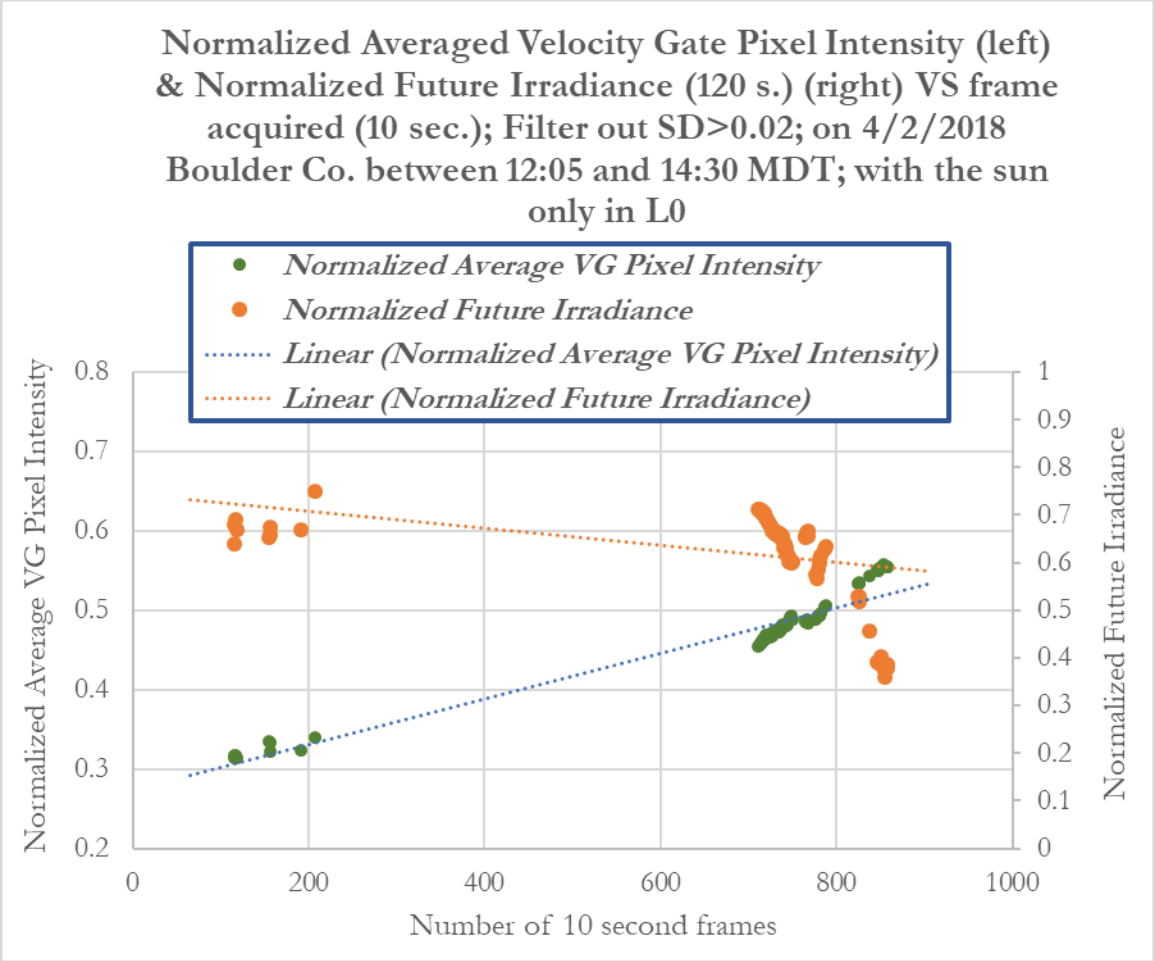


Graph 8-7. Normalized Averaged Velocity Gate Pixel Intensity (left) & Normalized Future Irradiance (120 s.) (right) vs. frame acquired (10 sec.); Filter out SD>0.02; on 4/2/2018 Boulder Co. between 12:05 and 14:30 MDT; with the sun only in L0.

In two scenarios with different days, the correlation between normalized VG pixel intensity and normalized irradiance can be opposite or at a minimum actively changing throughout the day.

## 8.7. Error Analysis Definitions

Root Mean Square (RMS) error was calculated by taking the average of the B-Side irradiance prediction output and comparing it to the actual irradiance realized in the future. The RMS error is defined as follows:

$$E_{RMS} = \sqrt{\frac{1}{n}(x_1^2 + x_2^2 + \cdots + x_n^2)} \tag{8-1}$$

However, the B-Side data is one dimensional. With SIMF average B-side categories from LAPART being one dimensional, the formula reduces to the absolute value of the error from mid category, derived below.

$$E_{RMS} = \sqrt{\frac{1}{n}(I_B - I_{t+P.T.H.})^2} = |I_B - I_{t+P.T.H.}| \tag{8-2}$$

Where $I_B = \text{Irradiance}_{\text{LAPART B-Side Prediction}}$ and $I_{t+P.T.H.} = \text{Irradiance}_{\text{time+ Prediction Time Horizon}}$

## 8.8. Velocity Estimation for the Velocity Gate Placement on the Data Flag

PIV-Lab [210] was utilized to make a map of velocities of clouds relative to position. A search radius of 140 pixels around the sun was specified and only velocities in that radius were averaged for the data flag and VG. This is illustrated in Figure 8-11 below.

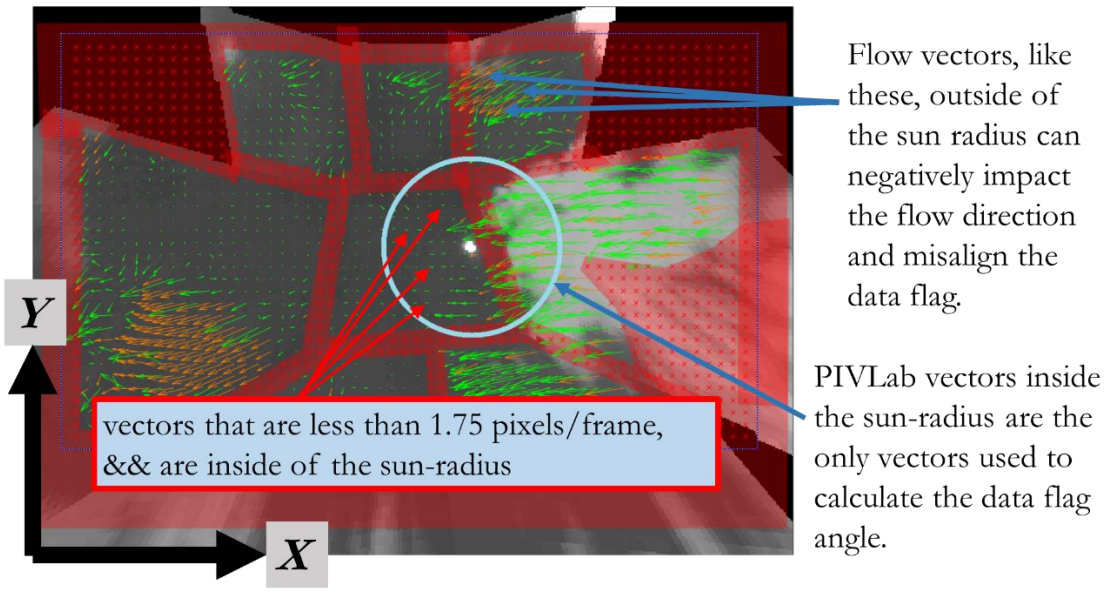


Figure 8-11. PIVLab velocities as calculated near the sun.

All velocities that were not a minimum of 1.75 pixels/frame were discarded.

In order to parse better velocity vectors, a strategy was derived to grade the cloud movement vectors. The steps are as follows:

1. A list of all vectors inside of the sun-radius was compiled for every frame.
2. The percentage of vectors that have pixel lengths greater than 1.75 was obtained.
3. A grade was assigned to all frames based on the number of vectors longer than the 1.75 pixels per frame value. Some of the small, non-passing vectors, can be seen on the left side of the sun, within the sun-radius, shown in Figure 8-11.
4. The X and Y components of vectors that pass and are in the sun-radius are averaged utilizing a running average. The value of the running average was

taken from the grade assessed previously. These grades and corresponding running averages are shown in Table 8-1. For example, if 55% of the vectors inside of the sun-circle are longer than 1.75 pixels/frame, the running average of the X and Y components would include the current averages inside of the sun-circle plus 19 previous averages. If a grade of D was received, the X and Y component averages would be repeated from the last frame. An average angle for the frame was calculated.

5. Once a minimum of 20 average sun-circle average angles was obtained, the data-flag angle was calculated with a 20-frame running average.

The entire process is highlighted in Figure 8-12.

| Grade from within sun-radius | Percentage of PIVLab Vectors in the sun-radius that are greater than 1.75 pixels/frame | Running Average of the X and Y Components of Average Velocity Vector for one Frame | # Frames for Running-Average for the Date-Flag Angle |
|---|---|---|---|
| A | between 100% and more than 65% | 10 frames | 20 frames |
| B | less than 65% and more than 35% | 20 frames | 20 frames |
| C | less than 35% and more than 10% | 30 frames | 20 frames |
| D | less than 10% | NONE, repeat last frame | 20 frames |

Table 8-1. PIVLab vectors grading table for vectors inside of the sun-radius and the subsequent number of past X and Y vector components to average.

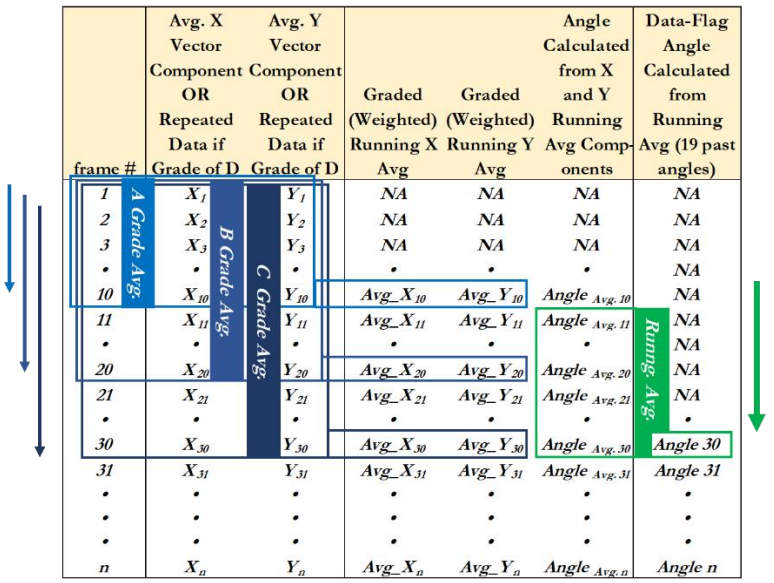


Figure 8-12, Example of graded PIVLab values for the Data-Flag in a double averaging process. This example assumes "A" quality data is available.

When throwing out small vectors from the sun-circle, an arbitrary angle of 20° was set as the maximum error allowed for any given velocity vector calculated by PIVLab. Assuming a purely X and Y coordinate vector movement, the maximum error per pixel is less than 0.5 pixels/vector. This is assumed because an extremely small cloud movement near the edge of one pixel could result in a neighboring pixel being activated. Likewise, a pixel could be half activated prematurely when instead it should read nothing. Assuming:

A. A 0.5 pixels/unit-vector error in both X and Y is the maximum error for one vector.

B. The vector is purely in the X direction and has only a Y error component.

The minimum vector to obtain approximately 20° of error or less per vector is shown in (8-3).

$$\tan(20°) = \frac{0.5_{Max\ Pixel\ Resolution\ Error}}{X_{Vector\ Max\ Length}}$$

$$\frac{0.5_{Max\ Pixel\ Resolution\ Error}}{\tan(20°)} = X_{Vector\ Max\ Length}$$

$$X_{Vector\ Max\ Length} \cong 1.37 \tag{8-3}$$

Adding the Max Pixel Resolution Error to the X length

$$X_{Vector\ Max\ Length} \cong 1.37 + 0.5_{Max\ Pixel\ Resolution\ Error} \cong 1.87$$

$$V_{Max\ Pixel\ Length\ Cutoff\ PIVLab} =$$

$$\sqrt{X_{Vector\ Max\ Length}{}^2 + 0.5_{Max\ Pixel\ Resolution\ Error}{}^2} \cong \sqrt{1.87^2 + 0.5^2} \cong 1.93$$

Assuming a Max Pixel Resolution Error in the Y direction of 0.5 pixels, the total length of the vector is calculated for a maximum angle error of 20°.

The maximum error vector length was rounded down to the nearest 0.25 pixels and was selected as 1.75 pixels.

If all grades returned grad-D due to the small amount of uniform cloud movement, or no movement at all, the direction angle was used as purely Y in direction. The velocity was set to 2 pixels/frame. This occurred when it was sunny or uniformly overcast.

### 8.8.1. Preprocessing; Heuristic Correction vs. PIV-Lab Average Velocities

Visual observations from the author of clouds moving across the data swath were noted. In many cases that involve non-trivial cloud velocity movements, the visual observation of the cloud velocity is higher than what is aggregated from PIVLab. For example, in Figure 8-13 below from Boulder Co., velocities of this cloud are about 152% of normal.

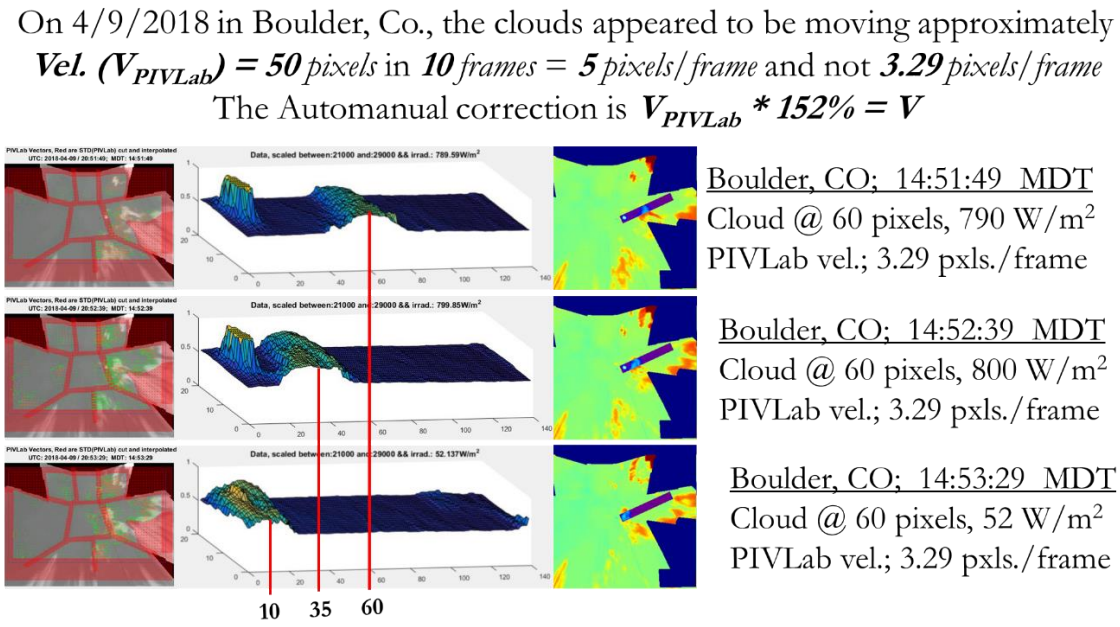


Figure 8-13. Heuristic correction from visual observations on 4/9/18 in Boulder Colorado.

When observing the entire data set, a correlation was formed and reported in Graph 8-8.

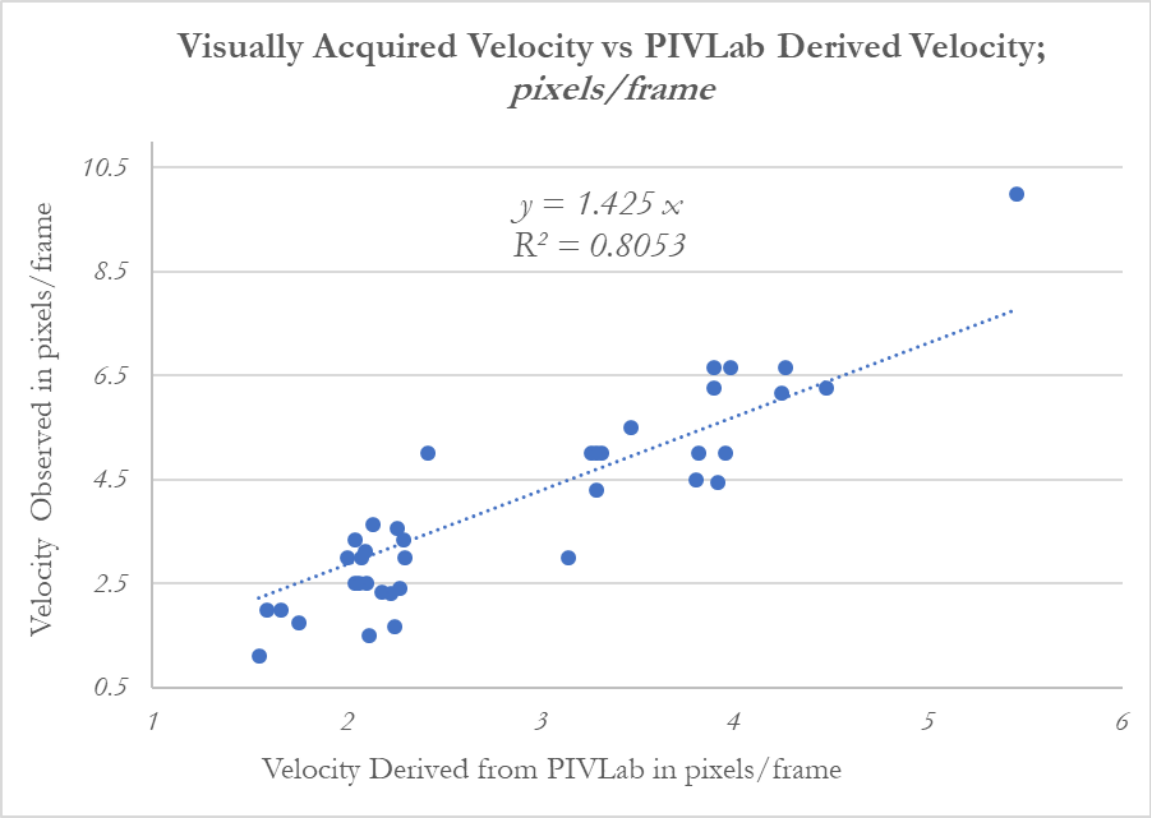


Graph 8-8. Heuristic correlation of all observable cloud velocities.

This correction was used as a parameter to analyze the accuracy of the prediction space. The heuristic correlation was linearly fitted to intersect the origin and has a subsequent correction of 142.5% of normal. When referring to an heuristic correction in Table 8-2, Table 8-3 and Table 8-4, the PIVLab derived velocity is multiplied by 142.5%, and that number is used for the VG with an heuristic correction. Later, the heuristic velocity was varied to include a range of values to confirm that a correction of 142.5% minimizes error with the VG method.

## 8.9. Persistence Method, UsingCurrent Irradiance as the Future Irradiance Prediction

As a base case of prediction, it is easy to use the current irradiance as a prediction for the future. From a mathematical standpoint, this "trivial" case is utilized as a minimum performance standard since it requires no computation to produce a systematic answer. Other publications may refer to this testing method as the "persistence method". However, the word "trivial" conveys a better sense of uselessness when considering that a processing method must "process" data in some meaningful way, rather than just duplicate the input as the output. Thus, if no processing occurs, the process is trivial.

## 8.10. High Variability Data Analysis

When making a prediction of irradiance, Figure 1-1 highlights the ability to predict both purely cloudy and completely sunny days. When the sky background is uniformly clear or overcast, the trivial case functions well as a valid prediction, because there is no irradiance variability over time. As a result, a High Variability (HV) metric was used to limit data to future irradiance differences of 250 $W/m^2$ or greater. This is highlighted in Figure 8-14.

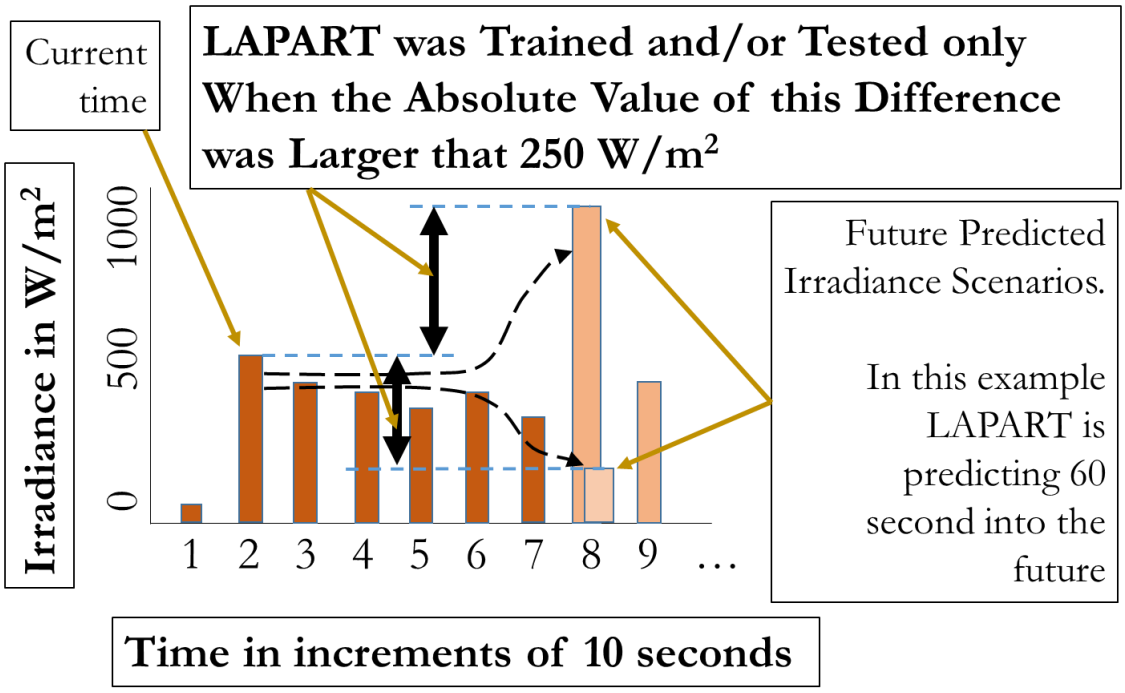


Figure 8-14. High Variability data example.

A HV testing set was made that contains exclusively HV data for multiple time. In addition, LAPART was trained on both exclusively HV data as well as all data and then compared to exclusively HV testing data respectively.

## 8.11. LAPART Testing Scenarios

Two LAPART testing scenarios were employed to test the accuracy of SIMF predictions. They are shown in Figure 8-15, below.

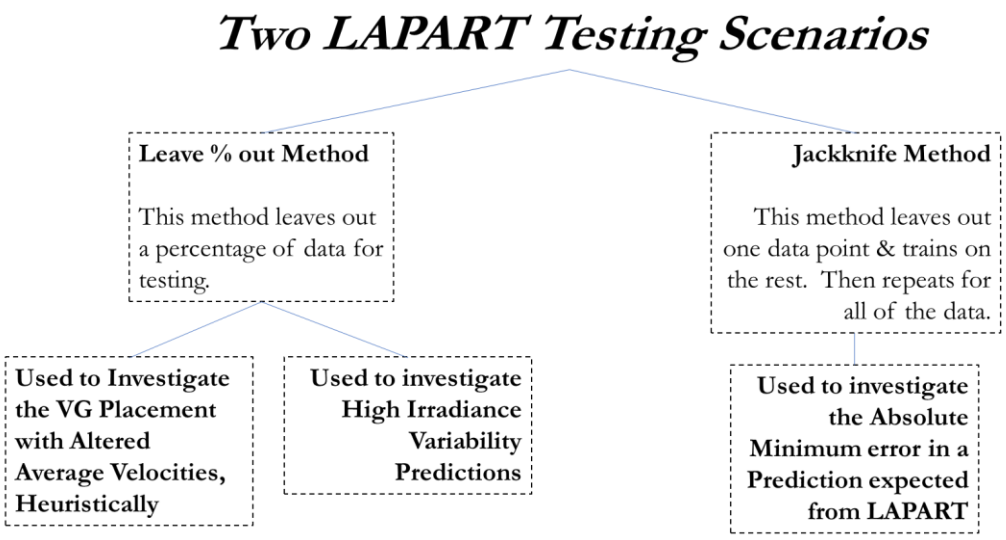


Figure 8-15. LAPART testing scenarios.

Section 8.11.1 employed a method of leaving out a percentage of data for testing. In most scenarios 25% of the data were randomly left out for testing prediction accuracy. The other 75% was used for testing. Section 8.11.2 utilized a jackknife testing scenario where LAPART was trained on all but one of the data and tested on the one left out. The process was repeated with another set of data left out for testing where the rest of the days were used for training. The method repeats with one set of data left out until the entire set has been tested.

A variety of issues from the hardware was examined above, including the lack of correlation between VG pixel intensity and irradiance. Other issues affecting the pre-processing of data include the Heuristic velocity corrections to the VG location along the data flag. A number of these scenarios and the accuracy of each trial follows.

### 8.11.1. LAPART Testing Scenario; Comparison of Heuristic Corrections, High Variability Data and the Trivial Case

To begin an analysis with LAPART, ρA and ρB were both set to 0.98. In each case a random 25% of the data was reserved for testing and the remainder was utilized for training. When the HV data was specified as a parameter, the remainder of the data that did not match the HV criteria was not utilized for both testing and/or training. A summary of the RMS error in W/m² along with other statistics are shown in Table 8-2, below. Table 8-3 and Table 8-4, highlight a 60 s, 90 s and 120 s prediction.

| Prediction Time: 60 s | time interval between pictures: 10 s |
|---|---|
| ρA: 98% | Perc. For Testing: 25% |
| ρB: 98% | Always predict best choice ?: YES |

| Trivial Case | Heuristic Velocity Correction | High Variability Training > \|250\| W/m² | High Variability Testing > \|250\| W/m² | RMS Error from mid cat. W/m² | # A-Templates | # N Inputs | % # A-Templates / # N Inputs | % passing vigilance |
|---|---|---|---|---|---|---|---|---|
| | YES | | YES | 272.0 | 4,009 | 20,610 | 19.5% | 96.9% |
| | YES | YES | YES | 136.1 | 750 | 1,127 | 66.5% | 95.5% |
| | YES | | | 53.4 | 4,057 | 20,709 | 19.6% | 99.6% |
| YES | YES | | YES | 314.3 | 4,049 | 20,633 | 19.6% | 96.6% |
| YES | YES | YES | YES | 464.8 | 746 | 1,137 | 65.6% | 95.6% |
| YES | YES | | | 61.4 | 4,017 | 20,667 | 19.4% | 99.6% |
| | | | YES | 206.8 | 5,310 | 20,723 | 25.6% | 94.1% |
| | | YES | YES | 130.1 | 855 | 1,154 | 74.1% | 88.5% |
| | | | | 46.1 | 5,302 | 20,719 | 25.6% | 98.5% |

Table 8-2. One-minute prediction statistics comparing heuristic velocity corrections, HV data and the trivial case.

| Prediction Time: 90 s | time interval between pictures: | 10 s |
|---|---|---|
| ϱA: 98% | Perc. For Testing: | 25% |
| ϱB: 98% | Always predict best choice ?: | YES |

| Trivial Case | Heuristic Velocity Correction | High Variability Training > \|250\| W/m$^2$ | High Variability Testing > \|250\| W/m$^2$ | RMS Error from mid cat. W/m$^2$ | # A-Templates | # N Inputs | % # A-Templates / # N Inputs | % passing vigilance |
|---|---|---|---|---|---|---|---|---|
| | YES | | YES | 271.0 | 3,037 | 20,552 | 14.8% | 98.7% |
| | YES | YES | YES | 153.3 | 804 | 1,449 | 55.5% | 97.9% |
| | YES | | | 70.1 | 3,047 | 20,525 | 14.8% | 99.9% |
| YES | YES | | YES | 281.8 | 3,066 | 20,532 | 14.9% | 99.4% |
| YES | YES | YES | YES | 480.0 | 793 | 1,400 | 56.6% | 99.4% |
| YES | YES | | | 70.3 | 3,071 | 20,453 | 15.0% | 99.8% |
| | | | YES | 259.7 | 4,078 | 20,648 | 19.8% | 99.0% |
| | | YES | YES | 150.3 | 881 | 1,440 | 61.2% | 95.7% |
| | | | | 63.8 | 4,034 | 20,502 | 19.7% | 99.6% |

Table 8-3. One-and-a-half-minute prediction statistics comparing heuristic velocity corrections, HV data and the trivial case.

| Prediction Time: 120 s | time interval between pictures: | 10 s |
|---|---|---|
| ϱA: 98% | Perc. For Testing: | 25% |
| ϱB: 98% | Always predict best choice ?: | YES |

| Trivial Case | Heuristic Velocity Correction | High Variability Training > \|250\| W/m$^2$ | High Variability Testing > \|250\| W/m$^2$ | RMS Error from mid cat. W/m$^2$ | # A-Templates | # N Inputs | % # A-Templates / # N Inputs | % passing vigilance |
|---|---|---|---|---|---|---|---|---|
| | YES | | YES | 277.2 | 2,883 | 20,289 | 14.2% | 99.3% |
| | YES | YES | YES | 156.8 | 829 | 1,642 | 50.5% | 97.7% |
| | YES | | | 90.3 | 2,897 | 20,397 | 14.2% | 99.9% |
| YES | YES | | YES | 281.8 | 2,890 | 20,377 | 14.2% | 99.1% |
| YES | YES | YES | YES | 470.6 | 829 | 1,628 | 50.9% | 98.8% |
| YES | YES | | | 86.2 | 2,919 | 20,305 | 14.4% | 99.9% |
| | | | YES | 274.5 | 3,180 | 20,585 | 15.4% | 99.5% |
| | | YES | YES | 171.1 | 850 | 1,627 | 52.2% | 98.8% |
| | | | | 78.0 | 3,218 | 20,551 | 15.7% | 99.9% |

Table 8-4. Two-minute prediction statistics comparing heuristic velocity corrections, HV data and the trivial case.

When comparing the RMS error of the heuristic velocity correction vs. no correction (using PIVLab velocities as calculated), graphing these values reveals contradictory results, as indicated in Graph 8-9 below.

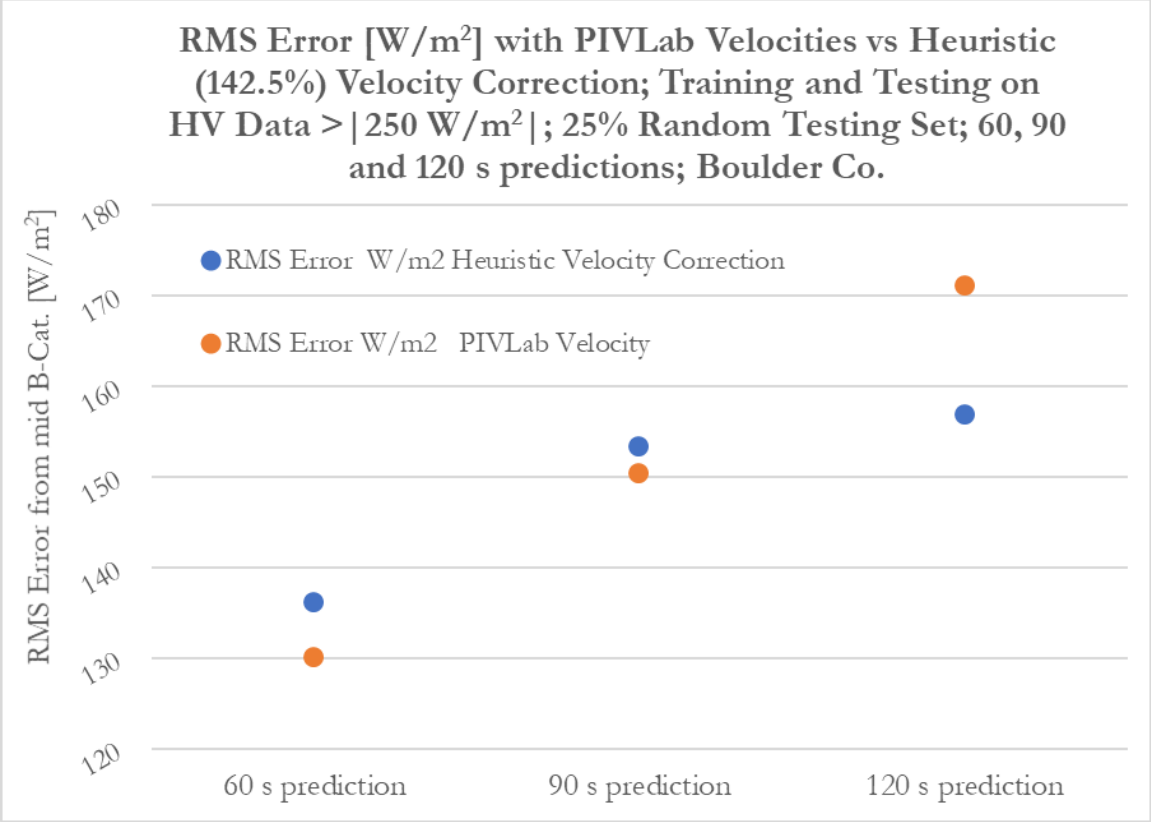


Graph 8-9. RMS error of predictions, testing and training on high variability data using PIVLab and heuristic velocities.

It is shown that the RMS error steadily increases as the prediction time increases. What is not consistent, is why the error of the heuristic velocity correction decreases with a two-minute prediction. This motivated an analysis to vary the heuristic velocity correction percentage versus the RMS error for the prediction. Since a two-minute prediction would affect the velocity gate the most compared to a 90 s and 60 s prediction, two minutes was chosen as the prediction horizon.

#### 8.11.1.1. Heuristic Velocity Correction Comparison vs. Observed Scenarios

An analysis was done to compare the error of multiple heuristic velocity corrections with a 120 second prediction. The results are shown below in Table 8-5 and Graph 8-10.

| | | | |
|---|---|---|---|
| Prediction Time: | 120 s | time interval between pictures: | 10 s |
| ϱA: | 98% | Perc. For Testing: | 25% |
| ϱB: | 98% | Always predict best choice ?: | YES |
| High Variability Data Training: | YES | Time restriction on Testing ?: | NO |
| High Variability Data Testing: | YES | Time restriction Times (24 hrs.): | NA |

| Auto-manual Velocity Correction | RMS Error from mid cat. $W/m^2$ | # A-Templates | # N Inputs | Percentage (%) # A-Templates / # N Inputs | Percentage (%) passing vigilance |
|---|---|---|---|---|---|
| 100% | 171.1 | 850 | 1,627 | 52.2% | 98.8% |
| 110% | 159.4 | 827 | 1,668 | 49.6% | 99.2% |
| 120% | 167.0 | 821 | 1,621 | 50.6% | 99.6% |
| 130% | 166.1 | 800 | 1,604 | 49.9% | 99.6% |
| 140% | 165.9 | 775 | 1,590 | 48.7% | 99.8% |
| 142.5% | 156.8 | 829 | 1,642 | 50.5% | 97.7% |
| 150% | 163.6 | 769 | 1601 | 48.0% | 98.9% |
| 160% | 172.0 | 792 | 1581 | 50.1% | 99.4% |
| 170% | 166.4 | 741 | 1528 | 48.5% | 99.3% |
| 180% | 169.6 | 731 | 1550 | 47.2% | 99.8% |
| 190% | 167.2 | 715 | 1487 | 48.1% | 99.3% |
| 200% | 157.5 | 709 | 1488 | 47.6% | 99.6% |

Table 8-5. RMS error based on multiple heuristic velocity corrections.

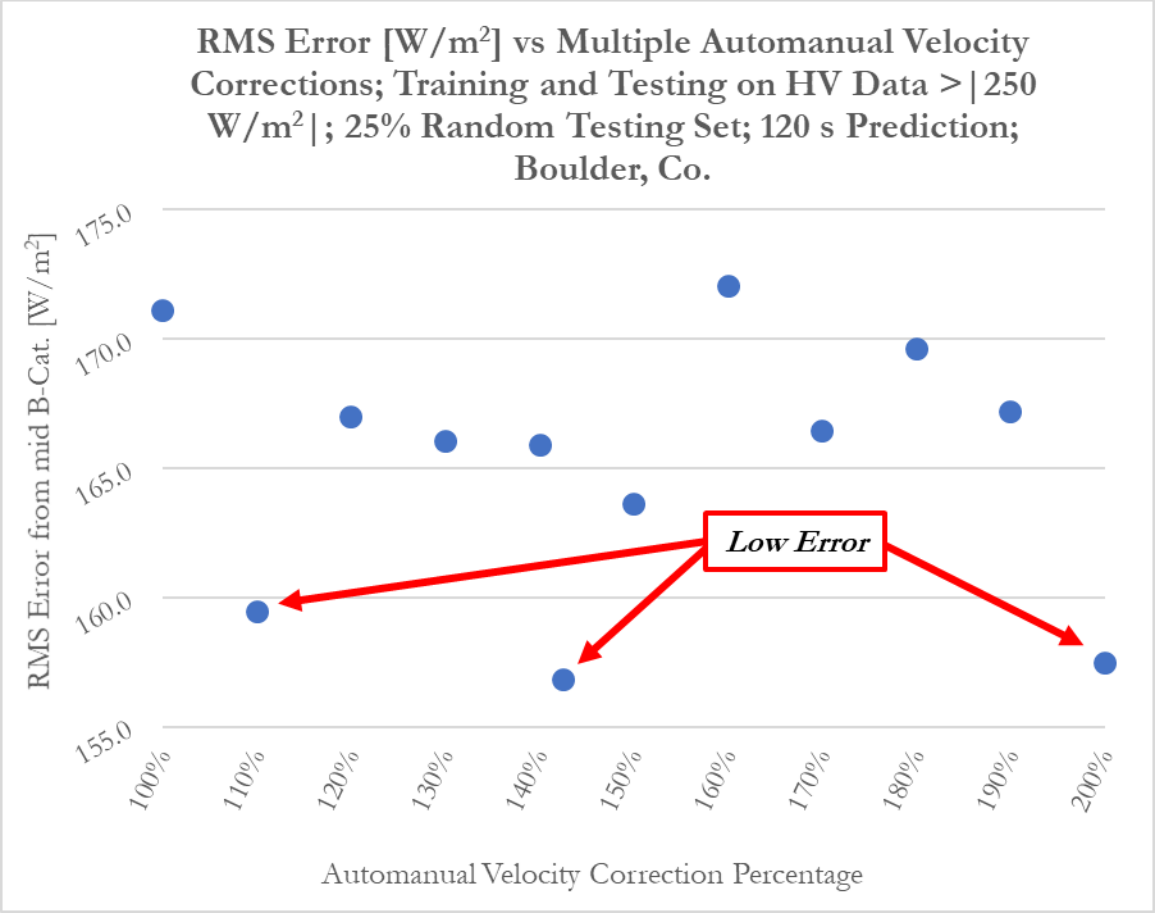


Graph 8-10. Graph of the RMS error based on multiple heuristic velocity corrections.

Since the original heuristic velocity correction was 142.5% and no correction is 100%, these data were added into the analysis. New LAPART tests were compared with heuristic velocity corrections between 110% and 200%, in increments of 10%. Graph 8-10, would indicate that a heuristic correction of 142.5%, as was verified by linear regression of Graph 8-8. However, subsequent corrections of 110% and 200% present similar error results. This observation was derived from HV data only while testing and training.

Though the data input was simplified via a projection of multiple cameras onto flat sky, there could be visual effects at low angles that cause false or distorted inputs. As

a result, a analysis was re-run to restrict the time of day to approximately two hours before and after solar noon and without consideration of longitudinal or analemma effects. Since this data set is from Boulder, Co. during daylight savings time, solar noon was calculated as approximately 13:00. RMS errors are shown below in Table 8-5 and Table 8-6, with all data for both training and testing restricted between times of 11:00 to 15:00. This is about two hours on both sides of solar noon.

| Prediction Time: | 120 s | time interval between pictures: | 10 s |
|---|---|---|---|
| ϱA: | 98% | Perc. For Testing: | 25% |
| ϱB: | 98% | Always predict best choice ?: | YES |
| High Variability Data Training: | YES | Time restriction on Testing ?: | YES |
| High Variability Data Testing: | YES | Time restriction Times (24 hrs.): | 11:00 to 15:00 MDT |

| Heuristic Velocity Correction | RMS Error from mid cat. $W/m^2$ | # A-Templates | # N Inputs | Percentage (%) # A-Templates / # N Inputs | Percentage (%) passing vigilance |
|---|---|---|---|---|---|
| 100% | 175.8 | 841 | 1,645 | 51.1% | 99.3% |
| 105% | 167.3 | 817 | 1,599 | 51.1% | 99.1% |
| 110% | 174.3 | 808 | 1,632 | 49.5% | 98.9% |
| 115% | 159.3 | 832 | 1,611 | 51.6% | 98.6% |
| 120% | 166.5 | 835 | 1,646 | 50.7% | 99.4% |
| 125% | 170.4 | 805 | 1,607 | 50.1% | 99.6% |
| 130% | 163.5 | 800 | 1627 | 49.2% | 99.4% |
| 135% | 173.4 | 796 | 1591 | 50.0% | 99.8% |
| 140% | 150.5 | 791 | 1597 | 49.5% | 99.8% |
| 142.5% | 142.9 | 788 | 1606 | 49.1% | 99.2% |
| 145% | 159.5 | 770 | 1573 | 49.0% | 99.8% |
| 150% | 161.7 | 781 | 1629 | 47.9% | 99.4% |
| 155% | 158.6 | 766 | 1576 | 48.6% | 99.5% |
| 160% | 168.5 | 784 | 1611 | 48.7% | 99.2% |
| 165% | 165.0 | 746 | 1565 | 47.7% | 99.6% |
| 170% | 161.2 | 759 | 1579 | 48.1% | 99.4% |
| 175% | 160.0 | 740 | 1558 | 47.5% | 99.8% |

Table 8-6. RMS error based on multiple heuristic velocity corrections restricted to two hours before and after solar noon.

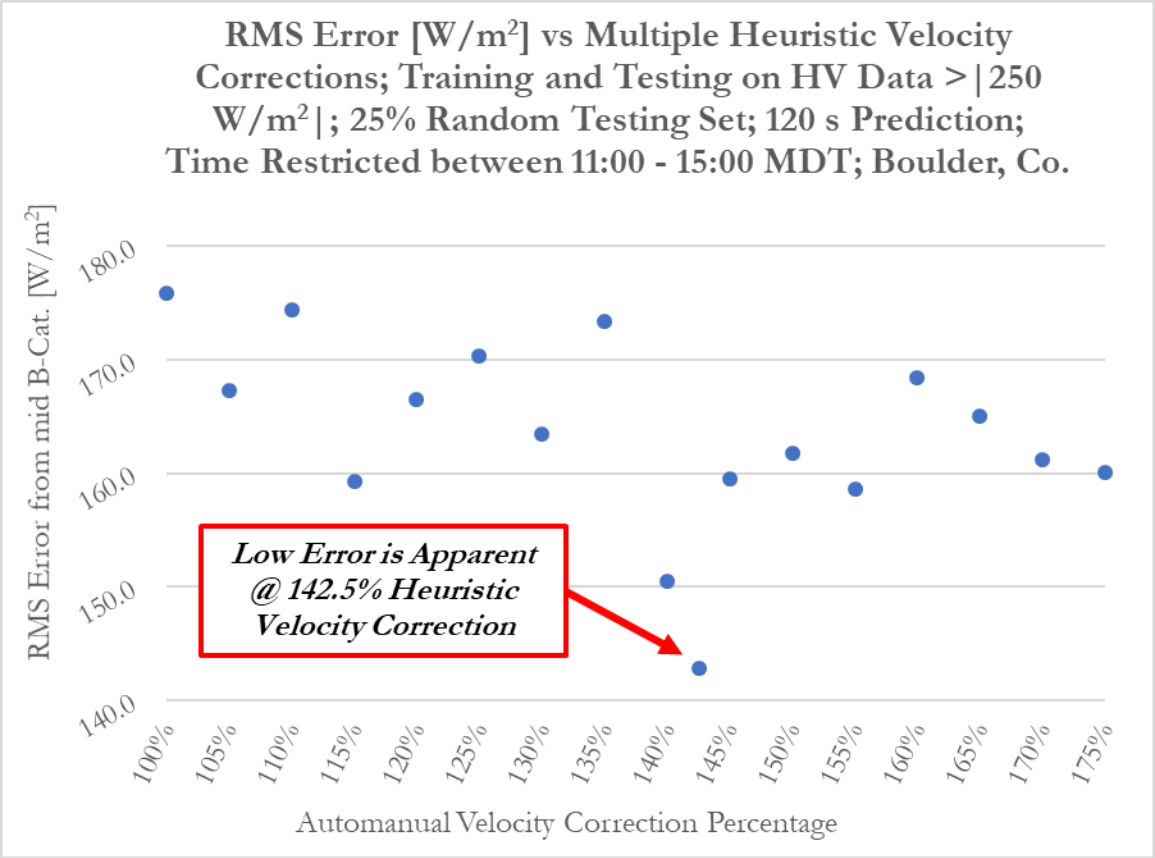


Graph 8-11. Graph of the RMS error based on multiple heuristic velocity corrections restricted to two hours before and after solar noon.

When the data were restricted to scenarios with the sun's lowest incidence angle which was two hours on each side of solar noon, the heuristic correction consistent with Graph 8-8, 142.5%, produced a two-minute prediction with the lowest RMS error.

Though no mathematical convergence theorem exists for LAPART at the neuron level, the statistical metric of *the number of A-Categories formed* relative to *the number of training inputs*, reveals useful information. In all testing scenarios that alter the heuristic velocities, it is important to note the number of A-Categories relative to the number of training inputs were always between 40%-50%. This implies that

LAPART may be returning accurate predictions, but it is not done learning. With 50% of A-Categories relative to the number of inputs formed, one could expect a non-passing vigilance choice on approximately 50% of the prediction inputs.

In all subsequent training scenarios, when specifying a heuristic correction, the value used was 142.5% of normal. This value was calculated in Graph 8-8 with a linear regression and an R-squared linear correlation of 0.81. It was also confirmed to be the best experimentally in Graph 8-10 and Graph 8-11.

### 8.11.2. LAPART Testing Scenario; Jackknife Training

Jackknife training was employed as a LAPART training scenario. With this training method, LAPART was randomly trained on all but one of the data inputs. Testing was then performed on the one input that was left out and its prediction metrics were recorded. The entire process was repeated, progressively leaving out individual inputs and training on the rest, until all the inputs were tested. The jackknife process was particularly useful in acquiring the minimum possible error that can be expected from the network.

The normalized VG standard deviation was also restricted at various levels while utilizing the jackknife process. The number of A and B-side categories was also recorded. Since there were as many training scenarios as there were data inputs, the standard deviation and average number of A and B-side categories found was also recorded.

A summary of the findings from this testing scenario is shown in Table 8-7 below.

| **Jacknife training, leave one out, train on all others; 120 s. prediction Restricting the VG Standard Deviation a/b rho = 0.98/0.98; 25,409 total data** | | | | | | | |
|---|---|---|---|---|---|---|---|
| VG Normalized StDev. Restriction (less than) | Avg. # A Cats. | Avg. # B Cats. | stdev # A Cats. | stdev # B Cats. | RMS Error in $W/m^2$ | # of data | % of Total Data |
| 0.01 | 79 | 24 | 3.9 | 1.5 | 8.33 | 3011 | 11.9% |
| 0.02 | 109 | 26 | 4.6 | 1.6 | 8.33 | 3722 | 14.6% |
| 0.03 | 130 | 28 | 5.3 | 1.7 | 8.61 | 4147 | 16.3% |
| 0.10 | 347 | 34 | 8.0 | 2.0 | 12.45 | 5870 | 23.1% |

Table 8-7. Jackknife training scenarios limited by the standard deviation of the normalized velocity gate.

By progressively relaxing the VG standard deviation restrictions, the data sets contain less and less uniform data. With less uniform data in the VG and a higher number of training inputs, the number of A and B side categories as well as the standard deviations of the number of categories, progressively raised.

Graphs of LAPART's high and low predictions from the B side category are shown below in Graph 8-12, Graph 8-13, Graph 8-14 and Graph 8-15. They were restricted by normalized VG standard deviation cutoff and the residual error of the predictions was also plotted versus the 10 second data input in linear order.

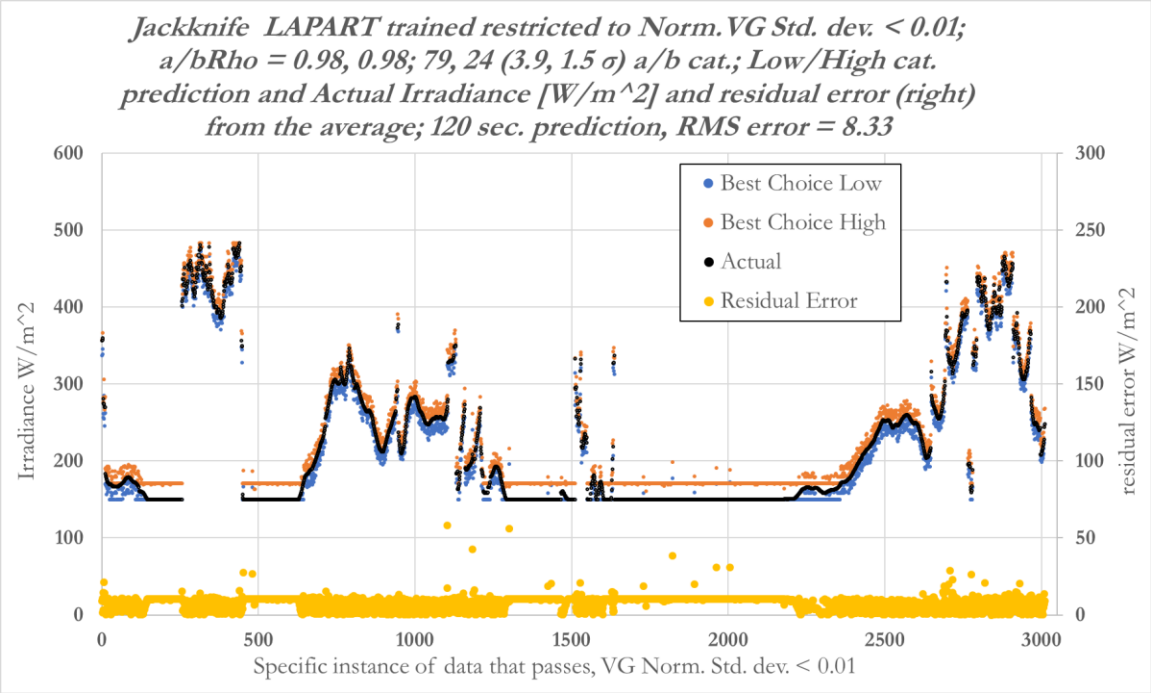


Graph 8-12. Jackknife LAPART trained restricted to Norm.VG Std. dev. < 0.01; 120 sec. prediction.

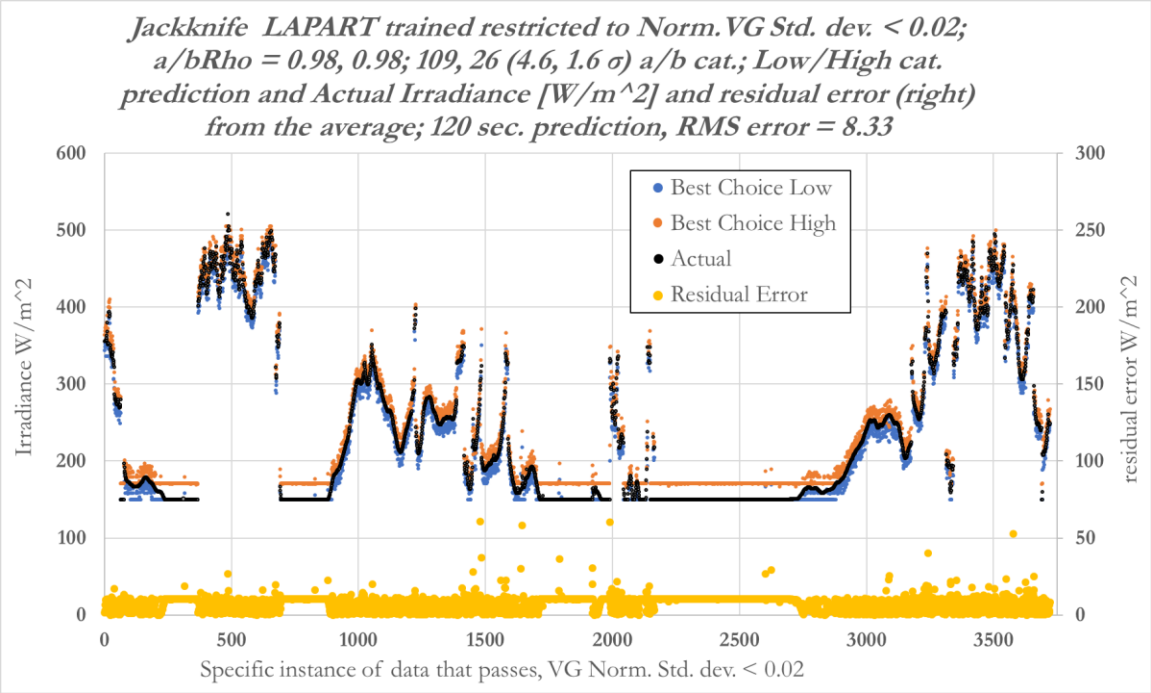


Graph 8-13. Jackknife LAPART trained restricted to Norm.VG Std. dev. < 0.02; 120 sec. prediction.

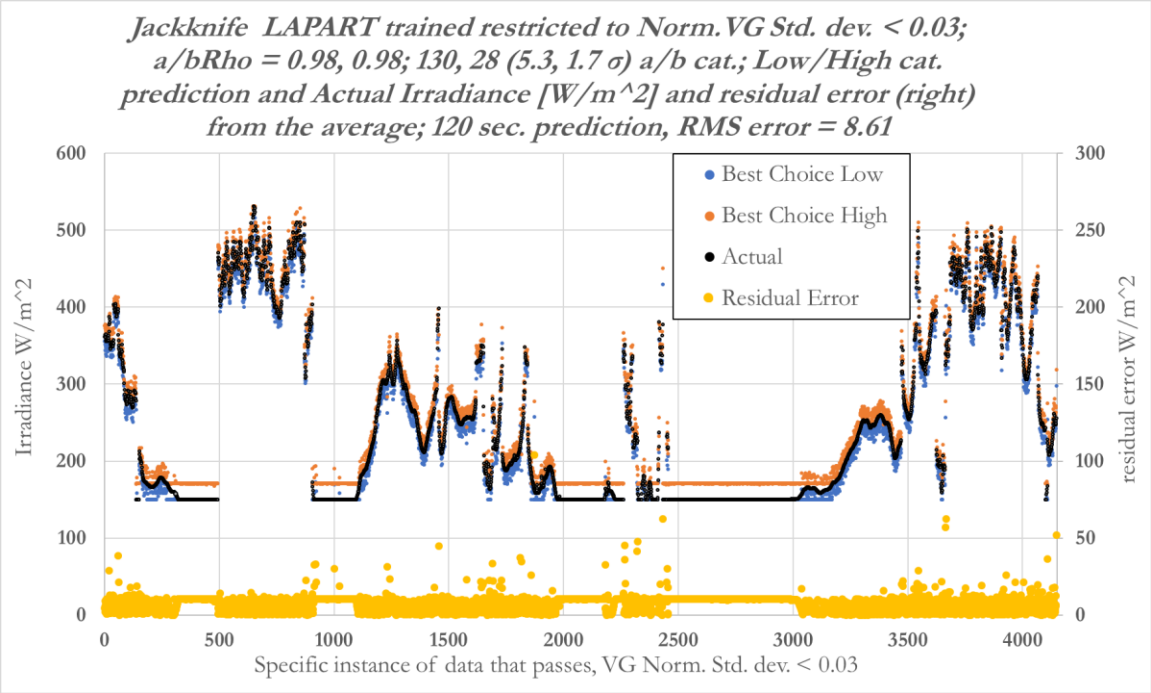


Graph 8-14. Jackknife LAPART trained restricted to Norm.VG Std. dev. < 0.03; 120 sec. prediction.

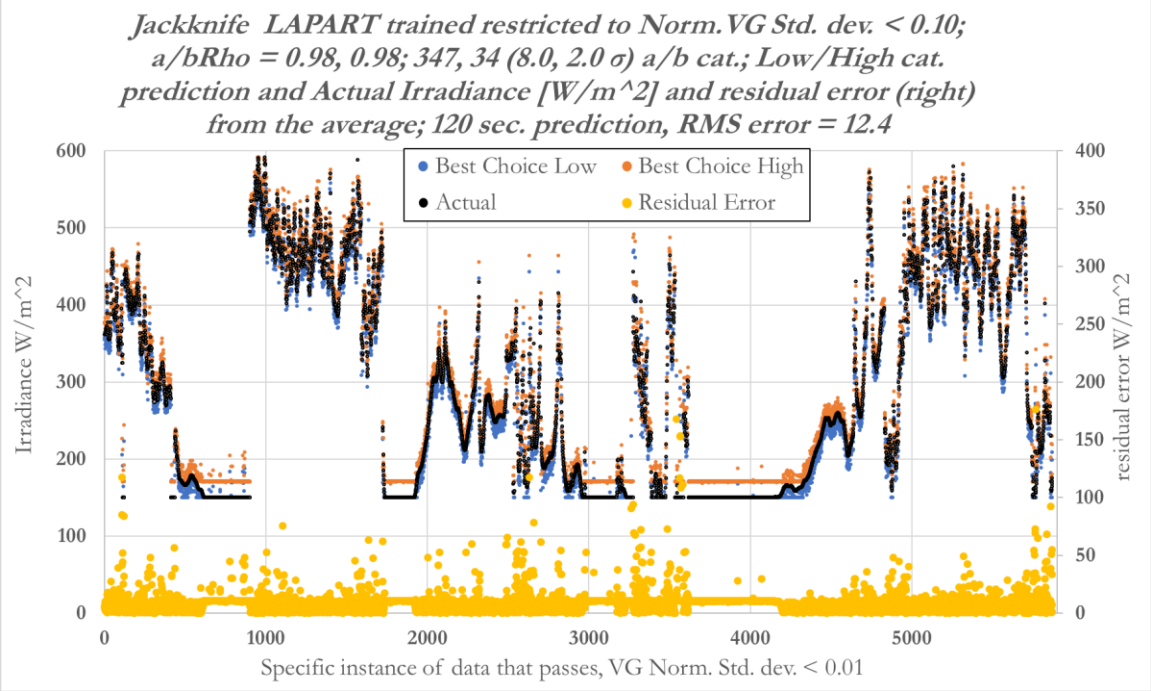


Graph 8-15. Jackknife LAPART trained restricted to Norm.VG Std. dev. < 0.10; 120 sec. prediction.

In all jackknife training scenarios, the expected RMS error was less than the variation caused by the size of the B side category. Since ρB was set to 0.98 and the single input irradiance was normalized to a range of 1000 W/m², the size of the B category was expected to be 2% of the range or approximately 20 W/m². In all jackknife testing scenarios, the average prediction error was less than the size of the category. This was consistent with what would be expected from LAPART if it was learning correctly. Though an RMS error of 20 W/m² cannot be expected for every prediction case, the data from the jackknife training scenarios has shown the forecasting methodology to be valid.

Analysis of individual RMS errors in Graph 8-15 shows that they often occur in single incidents. This could be explained by the VG misplacement on the data flag, which was highlighted above. However, it could also be explained by the extremely sensitive nature of a single irradiance sensor having not been occluded yet but was about to be. Since measurements occur at intervals of ten seconds and the response time of the irradiance sensor is about one tenth of a second, it would be entirely plausible for a measurement error to occur within a ten second period due only to the sample rate. What would be indicative of a non-systematic problem in the physical hardware or LAPART would be a sustained RMS prediction error of the irradiance. Jackknife training has shown that this was not typically the case as large prediction errors usually occurred in single cases as opposed to reoccurring multiple times sequentially.

# 9. Conclusions and Observations of Importance

It has been shown, when utilizing new sensor technology, the velocity gate preprocessing method and LAPART, that two and a half minute predictions of irradiance measurements over solar fields are possible. When relatively uniformly cloudy conditions occur LAPART was able to predict an RMS error less than half of the size of the B-side category. In all cases LAPART's average RMS error was less than the B-side category. This would indicate that LAPART can learn and adapt to changing cloud patterns while maintaining accurate predictions. Jackknife testing has shown, when predictions occur with irradiance over large PV fields, the actual RMS error of the field prediction may less due to the smoothing effect that the field has on the output of electricity to the grid. When a PV field is large, the accuracy of the prediction of the field will increase as it will take longer for the field to be occluded by clouds relative to a single sensor.

## 9.1. Multiple Cloud Layers

The largest motivation for accurate cloud mappings was that the VG method required accurate velocity vectors for both the data flag direction and correct location of the VG on the data flag.

This observation was confirmed in an example by retrieving the Aviation Weather Center published by the National Oceanic and Atmospheric Administration for Denver Airport on a cloudy day, shown in Figure 9-1 below.

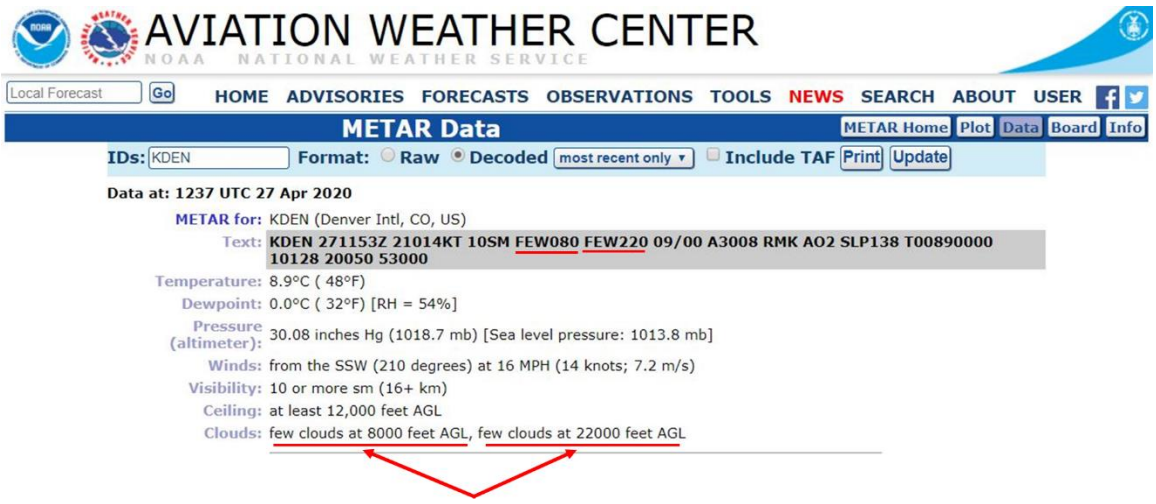


Figure 9-1. Multiple cloud layers shown at the Denver airport [211].

Multiple cloud layers have an impact on the velocity vectors that control the data flag direction. In many observed cases, the upper layer of clouds is more uniform and systematic involving clouds like cirrocumulus, cirrostratus, cirrus, altocumulus and altostratus, as shown in Figure 9-2 below. These upper layers can have a different velocity vector and affect the data flag. However, when high level clouds are present, they typically are already occluding the sun and reducing irradiance in a uniform manner. This means that irradiance predictions are not as crucial to PV fields. When these clouds are present only minimally and irradiance predictions are more important, their effects are diminished.

## 9.2. Limitations on the Input Space

A discussion of various cloud heights and the problems they entail was highlighted. Thick, dense, cotton ball looking clouds that are not rain generating are now analyzed. These clouds typically include cumulus, stratocumulus and stratus clouds, shown in Figure 9-2 below.

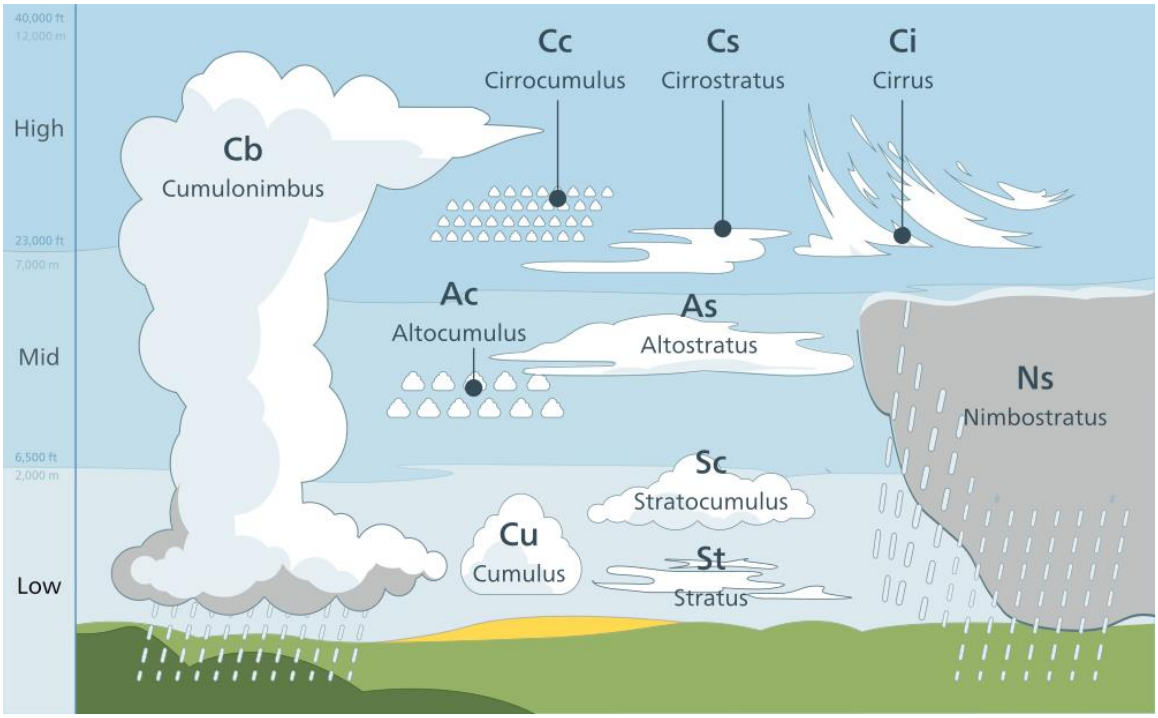


Figure 9-2. Cloud types and general heights [212].

These clouds are the main source of large PV field instabilities because they are dense, reoccurring and non-indicative of a permanently changing weather pattern for the day. Rain producing clouds like cumulonimbus and nimbostratus formations also occlude solar panels, but they also indicate a relatively constant change in the daily weather pattern. Rain producing clouds occlude PV farms, but then usually stay in one place and do not cause many more short-term occlusions events. Cumulus, stratocumulus and stratus cloud formations can persist all day turning on and off PV farms many times without indicating any systematic change in irradiance. These are the cloud formations that should be the continued focus of SIMF.

Because these cloud formations are small compared to rain producing formations, they are highly suspectable to changing size due to atmospheric conditions to which

they change move into or out of. This includes growing as well as disappearing in size as they move from one part of the sky to another. It is hypothesized that LIDAR could be utilized to identify the specific sections of the atmosphere that affect these cloud's densities to better improve SIMF accuracies.

## 9.3. Improvements in PIV Pre-Processing Using the Gradient Map (Streamlines)

In many cases, cloud formations do not move in linear patter. However, the data flag requires a linear direction for its construction. For short time periods this is sufficient. For longer time frames where the VG is far from the sun, it is hypothesized that a gradient map of vectors be utilized to make a curved data flag that follows a streamline intersecting the sun. How necessary this advanced geometric construction is, depends on both the curl of the velocity map and the timeframe of the prediction.

## 9.4. Overcast and sunny use of Now-Cast like input

When the cloud input is overcast and uniform or completely sunny, it was often hard for PIVLab to obtain enough cloud features to find a direction. When these conditions occurred, the default value was set to the predominant wind direction of the earth. In the case of testing in Boulder, Co. that direction was pointing straight west as that location is in the westerlies. If weather data were available via wi-fi or a cellular data hotspot, the algorithm could simply query the closest NOAA Aviation

Weather Center data and utilize the wind direction they report. Weather this is necessary for SIMF when the sky is uniformly cloudy or completely sunny, was not investigated.

# Works Cited


[1] Clean Edge Inc., "U.S. Homeowners on Clean Energy: A National Survey, 2014 Poll Results & Clean Energy Growth Trends," SolarCity and Clean Edge, 2015.

[2] U. S. Energy Information Administration Office of Integrated and International Energy Analysis, "Annual Energy Outlook 2013 with Projections to 2040," U.S. Department of Energy, Washington, DC 20585, April 2013.

[3] Edison Electric Institute, by Peter Kind, Energy Infrastructure Advocates, "Disruptive Challenges: Financial Implications and Strategic Responses to a Changing Retail Electric Business," Edison Electric institute, Washington, D.C. 20004-2696, January 2013.

[4] Industry Dive Inc., "The State of the Electric Utility," 2014. [Online]. Available: https://www.utilitydive.com/news/state-of-the-electric-utility-2020/572374/.

[5] Biparticsan Policy Center, "National Commission On Energy Policy's,Task Force On America's Future Energy Jobs," National Commission On Energy Policy, WASHINGTON, D.C. 20005.

[6] A. Mammoli, A. Menicucci, A. Ellis, T. Caudell, S. Willard, and J. Simmins, "Low-cost Solar Micro-Forecasts for Improving the Efficiency of PV Farm Output Smoothing," in *IEEE-SUSTECH 2013 CONFERENCE*, Portland, 2013.

[7] P. Denholm and R. Margolis, "Very Large-Scale Deployment of Grid-Connected Solar Photovoltaics in the United States: Challenges and Opportunities," National Renewable Energy Laboratory, Boulder, Co, 2014.

[8] X. Chen, Y. Du, and H. When, "Forecasting Based Power Ramp-Rate Control For PV Systems Without Energy Storage," Department of Electrical and Electronic Engineering, Xi'an Jiaotong-Liverpool University, China, Jiaotong-Liverpool University, 2014.

[9] W. D. Grossman, I. Grossman, and K. W. Steininger, "Distributed solar electricity generation across large geographic areas, Part I: A method to optimize site selection, generation and storage," *Renewable and Sustainable Energy Reviews,* vol. 25, pp. 831-843, 2013.

[10] D. Lew, M. Milligan, G. Jordan, L. Freeman, N.Miller, K. Clark, and R. Piwko, "How do Wind and Solar Power Affect Grid Operations: The Western Wind and Solar Integration Study," National Renewable Enregy Laboratory, Boulder, 2009.

[11] A. Jay, "The spectrum of power from wind turbines," *Journal of Power Sources 169,* vol. 169, pp. 369-374, 2007.

[12] J. B. Olson, J. S. Kenyon, I. Djalalova, L. Bianco, D. D. Turner, Y. Pichugina, A. Choukulkar, M. D. Toy, J. M. Brown, W. M. Angevine, E. Akish, J. Bao, P. Jimenez, B. Kosovic, K. A. Lundquist, C. Draxl, J. K. Lundquist, J. McCaa, K. McCaffrey, et al., "Improving Wind Energy Forecasting Through Numerical Weather Prediction Model Development," *Bulletin of the American Meteorological Society,* vol. 100, no. 11, p. 2201–2220, 2019.

[13] W. J. Shaw, M. S. Pekour, and R. K. Newsom, "Lidar Buoy Data Analysis: Basic Assessment of Observed Conditions and Instrument Performance Off Virginia and New Jersey," Pacific Northwest National Laboratory, PNNL-28058, 2018-10-12.

[14] Xcel Energy, "What are the parts of a wind turbine?," Xcel Energy, 2019. [Online]. Available: http://energyclassroom.com/ catch-the-wind/. [Accessed 24 06 2019].

[15] Y. Ren, P. N. Suganthan, and N. Srikanth, "Ensemble methods for wind and solar power forecasting—A state-of-the-artreview," *Renewable and Sustainable Energy Reviews,* vol. 50, pp. 82-91, 2015.

[16] S. Salcedo-Sanz, A. M. Perez-Bellido, E. G. Ortiz-Garcıa, A. Portilla-Figueras, L. Prieto, and F. Correoso, "Accurate short-term wind speed prediction by exploiting diversity in input data using banks of artificial neural networks," *Neurocomputing,* vol. 72, pp. 1336-1341, 2009.

[17] J. Mullen and M. A. Osman, "Wind Power Ramping in Bonneville Power Administration area," in *IEEE Confrence on Technologies for Sustainability*, Richland, USA, 2013.

[18] M. H. Albadi and E. F. El-Saadany, "Overview of wind power intermittency impacts on power systems," *Electric Power Systems Research,* vol. 80, pp. 627-632, 2010.

[19] J. D. Freeman, M. Sabu, B. Shankar, and K. Achuthan, "Novel Wireless Performance Monitoring for Small Wind Turbines," in *IEEE Confrence on Technology for Sustainability*, 2013.

[20] T. E. Hoff and R. Perez, "Quantifying PV power Output Variability," *Solar Energy,* vol. 84, pp. 1782-1793, 2010.

[21] Energy Information Administration, "Demand for electricity changes through the day," 2013. [Online]. Available: http://www.eia.gov/todayinenergy/detail.cfm?id=830. [Accessed 05 March 2014].

[22] National Renewable Energy Laboratory, "Flexible Coal: An Example Evolution from Baseload to Peaking Plant," Nashville, 2014.

[23] A. von Jouanne and B. Banerjee, "Assessment of Voltage Unbalance," *IEEE Transactions on Power Delivery,* vol. 16, no. 4, pp. 782-790, Oct. 2001.

[24] T. Luther, "Peaking plant ready for use," New Haven Register, New Haven, CT., 2011.

[25] A. A. Akhil, G. Huff, A. B. Currier, B. C. Kaun, D. M. Rastler, S. B. Chen, A. L. Cotter, D. T. Bradshaw, and W. D. Gauntlett, "DOE/EPRI Electricity Storage Handbook in Collaboration with NRECA, SAND2015-1002," Sandia National Laboratories, Albuquerque, New Mexico and Livermore, California, 2015.

[26] H. Voet, I. C. Garretson, B. Falk, R. H. Schmitt, and B. S. Linke, "Peak Power Load and Energy Costs Using the Example of the Startup and Idling of a Grinding Machine," *Procedia CIRP, CIRP Life Cycle Engineering,* vol. 69, pp. 324-329, 2018.

[27] F. Cheng, S. Willard, J. Hawkins, B. Arellano, O. Lavrova, and A. Mammoli, "Applying Battery Energy Storage to Enhance the Benefits of Photovoltaics," University of New Mexico, Albuquerque, 2012.

[28] D. Lew and G. Brinkman, "The Western Wind and Solar Integration Study (WWSIS-2) PHASE 2," National Renewable Energy Laboratory, Prepared under Task Nos. OE10.3020, SS12.2720, SM12.2010, and WE11.0810, 2013.

[29] J. Cochran, D. Lew, and N. Kumar, "Flexible Coal, Evolution from Baseload to Peaking Plant," National Renewable Energy Laboratory and Intentek, Golden, CO, 2013.

[30] J. Cochran, D. Lew, and N. Kumar, "Making Coal Flexible: Getting From Baseload to Peaking Plan," Inertek / National Renewable Energy Laboratory, 2013.

[31] Cnet, "Flywheel storage maker Beacon Power declares bankruptcy," [Online]. Available: https://www.cnet.com/news/flywheel-storage -maker-beacon-power-declares-bankruptcy/. [Accessed July 2019].

[32] A. Mills, M. Ahlstrom, M. Brower, A. Ellis, R. George, T. Hoff, B. Kroposki, C. Lenox, N. Miller, M. Milligan, J. Stein, and Y. Wan, "Dark Shadows," *IEEE Power and Energy Magazine,* vol. 9, no. 3, pp. 33-41, 2011.

[33] National Electrical Manufacturers Association, *American National Standard for Electric Power Systems and Equipment—Voltage Ratings,* ANSI C84.1-2016.

[34] American National Standard for Electric Power Systems and National Electrical Manufacturers Association, *ANSI C84.1 ELECTRIC POWER SYSTEMS AND EQUIPMENT - VOLTAGE RANGES,* 2018.

[35] Pratt's Energy Law Report, "VOLUME 17, NUMBER 9," A.S. Pratt Publication, New York, NY, OCTOBER 2017.

[36] K. Blunt and R. Gold, "PG&E Knew for Years Its Lines Could Spark Wildfires, and Didn't Fix Them," The Wall Street Journal, 10 July 2019. [Online]. Available: https://www.wsj.com/articles/pg-e-knew-for-years-its-lines-could-spark-wildfires-and-didnt-fix-them-11562768885. [Accessed 19 October 2019].

[37] R. Gold, K. Blunt, and R. Smith, "PG&E Sparked at Least 1,500 California Fires. Now the Utility Faces Collapse," The Wall Street Journal, 13 January 2019. [Online]. Available: https://www.wsj.com/articles/pg-e-sparked-at-least-1-500-california-fires-now-the-utility- faces-collapse-11547410768. [Accessed 13 January 2019].

[38] P. Blumberg and J. Rosenblat, "PG&E Took 8 Months to Prune a Tree at Risk of Catching Fire," Bloomberg Business, 15 August 2019. [Online]. Available: https://www.bloomberg.com/news/articles/2019-08-15/pg-e-

took-8-months-to-prune-a-tree-that-could-have-caught-fire. [Accessed 19 October 2019].

[39] B. Katherine, "PG&E CEO Says It Could Impose Blackouts in California for a Decade," The Wall Street Journal, 18 October 2019. [Online]. Available: https://www.wsj.com/articles/pg-e-ceo-says-it-could -impose-blackouts-in-california-for-a-decade-11571438206. [Accessed 18 October 2019].

[40] S. Stoft, Power System Economics, Designing Markets for Electricity, JOHN WILEY & SONS, INC., WILEY-INTERSCIENCE, IEEE Press, 2002.

[41] F. Barbieri, S. Rajakaruna, and A. Ghosh, "Very short-term photovoltaic power forecasting with cloud modeling: A review," *Renewable and Sustainable Energy Reviews,* vol. 75, pp. 242-263, 2017.

[42] R. Dambreville, P. Blanc, J. Chanussot, D. Boldo, and S. Dubost, "Very short term forecasting of the Global Horizontal Irradiance through Helioclim maps," in *The fifth International Renewable Energy Congress IREC  2014*, Hammamet, TUNISIA, 2014.

[43] New York Independent System Operator, "Energy Market & Operational Data," 2019, [Online]. Available: https://www.nyiso.com/energy-market-operational-data. [Accessed 14 07 2019].

[44] C. Martin and N. S. Malik, "Texas Power Prices Briefly Surpass $9,000 Amid Scorching Heat," Bloomberg, Bloomberg Markets, 12 August 2019. [Online]. Available: https://www.bloomberg.com/news/articles/2019-08-12/searing-texas-heat-pushes-power-prices-to-near-record-levels. [Accessed 19 October 2019].

[45] R. H. Byrne, V. W. Loose, M. K. Donnelly, and D. J. Trudnowski, "Methodology to Determine the Technical Performance and Value Proposition for Grid-Scale Energy Storage Systems," Sandia National Laboratories, SAND2012-10639, Albuquerque, NM, 2012.

[46] W. Hur, Y. Moon, K. Shin, W. Kim, S. Nam, and K. Park, "Economic Value of Li-ion Energy Storage System in Frequency Regulation Application from Utility Firm's Perspective in Korea," *Energies,* vol. 8, pp. 5000-5017, 2015.

[47] T. Cuccia, "Interview: Account Manager, New York Independent System Operator," April 22, 2020.

[48] T. Basso, National Renewable Energy Laboratory, "IEEE 1547 and 2030 Standards for Distributed Energy Resources Interconnection and Interoperability with the Electricity Grid," NREL/TP-5D00-63157, Golden, CO, December 2014.

[49] IEEE Standards Coordinating Committee, "IEEE Application Guide for IEEE Std 1547, IEEE Standard for Interconnecting Distributed Resources with Electric Power Systems," IEEE, New York, NY, 2009.

[50] IEEE Standards Coordinating Committee, "IEEE Standard Conformance Test Procedures for Equipment Interconnecting Distributed Resources with Electric Power Systems," IEEE, New York, NY, 2005.

[51] C. Martin, "Bloomberg Environmental," Bloomberg L.P., 2019. [Online]. Available: https://news.bloombergenvironment.com/ environment-and-energy/californians-learning-that- solar-panels-dont-work-in-blackouts?context=search&index=0. [Accessed 10 October 2019].

[52] K. Hirose, T. Shimakage, J. T. Reilly, and H. Irie, "The Sendai Microgrid Operational Experience in the Aftermath of the Tohoku Earthquake: A Case Study," Tohoku Fukushi University, Tohoku, Japan, 2012.

[53] A. Maitra, B. York, H. Kamath, T. Key, and V. Singhvi, "Microgrids: A Primer," Electric Power Research Institute, Palo Alto, California, 2018.

[54] T. Bialek, "SDG&E Borrego Springs Microgrid Demonstration Project," San Diego Gas and Electric, San Diego, 2012.

[55] Electric Power Research Institute, "The Integrated Grid EPRI Realizing The Full Value Of Central and Distributed Energy," Electri Power Research Institute, Palo Alto, California, 2014.

[56] K. Ravindra, B. Kannan, and N. Ramappa, "Microgrids A Value-Based Paradigm," IEEE Electrification Magazine, 2014.

[57] Harris Williams & Co., "Transmission & Distribution Infrastructure," Harris Williams & Co., Richmond, VA, Summer 2010.

[58] Delmarva Power Inc, "Infrastructure 101, How transmission lines work," Delmarva Power Inc, 2019. [Online]. Available: https://www.delmarva.com/SafetyCommunity/Education/Pages/EnergyBasics/Infrastructure101.aspx. [Accessed 20 April 2019].

[59] U.S. Energy Information Administration, "What is U.S. electricity generation by energy source?," 27 February 2020. [Online]. Available: https://www.eia.gov/tools/faqs/faq.php?id=427&t=3. [Accessed 02 05 2020].

[60] M. E. Khodayar, M. Barati, and M. Shahidehpour, "Integration of High Reliability Distribution System in Microgrid Operation," *IEEE Transactions on Smart Grid,* vol. 3, no. 4, pp. 1997-2006, 2012.

[61] Pike Research and Navigant Consulting, Inc., "Utility Distribution Microgrids," Navigant Consulting, Inc., 2012.

[62] Z. Ye, R. Walling, L. Garces, R. Zhou, L. Li, and T. Wang, "Study and Development of Anti-Islanding Control for Grid-Connected Inverters," National Renewable Energy Laboratory, SR-560-36243, Niskayuna, New York, 2004.

[63] Public Service Company of New Mexico, "Open Transmittion Planning Meeting," PNM, Albuquerque, NM, November, 5 2015.

[64] A. Khodaei, "Microgrid Optimal Scheduling with Multi-Period Islanding Constraints," *IEEE Transactions on Power Systems,* vol. 29, pp. 1383 - 1392, May 2014.

[65] W. C. Edwards Jr., S. Manson, and J. Vico, "Microgrid Islanding and Grid Restoration With Off-the-Shelf Utility Protection Equipment," in *2017 IEEE Canada International Humanitarian Technology Conference (IHTC)*, Toronto, ON, Canada, 21-22 July 2017.

[66] IEEE Standards Association, "IEEE Standard Technical Specifications of a DC Quick Charger for Use with Electric Vehicles," IEEE, New York, NY, 2015.

[67] IEEE Standards Coordinating Committee, "IEEE Guide for Smart Grid Interoperability of Energy Technology and Information Technology Operation with the Electric Power System (EPS), End-Use Applications, and Loads," IEEE, New York, NY, September 2011.

[68] IEEE Standards Association, "IEEE Guide for the Interoperability of Energy Storage Systems Integrated with the Electric Power Infrastructure," IEEE, New York, NY, 2015.

[69] J. Carl, D. Fedor, D. Grueneich, and C. Goldenberg, "Renewable and Distributed Power in California," Stanford University, Hoover Institution.

[70] National Institute of Standards and Technology, "NIST Framework and Roadmap for Smart Grid Interoperability Standards Release 1.0 (Draft)," Office of the National Coordinator for Smart Grid Interoperability, September 2009.

[71] E. Planas, A. Gil-de-Muro, J. Andreu, I. Kortabarria, and I. Martinez deAlegria, "General aspects, hierarchical controls and droop methods in microgrids: A review," *Renewable and Sustainable Energy Reviews,* vol. 17, pp. 147-159, 2013.

[72] M. B. Blarke and B. M. Jenkins, "SuperGrid orSmartGrid: Competing strategies for large-scale integration of intermittent renewables?," *Energy Policy,* vol. 58, pp. 381-390, 2013.

[73] B. Washom, J. Dilliot, D. Weil, J. Kleissl, N. Balac, W. Torre, and C. Richter, *Ivory Tower of Power,* IEEE power & energy magazine, july/august 2013.

[74] J. F. Kelly and D. V. Dollen, *The Illinois Institute of Technology Perfect Power Prototype,* Grid-Interop Forum 2007, 2007.

[75] A. Mammoli, F. Cheng, W. Greenwood, B. Arellano, J. Hawkins, O. Lavrova, and S. Willard, "Real-Time Control of Utility-Scale Storage on a Distribution Feeder," in *Energytech, 2013 IEEE*, 2013.

[76] L. Varnado and M. Sheehan, "CONNECTING TO, A Guide to Distributed Generation, THE Interconnection GRID Issues," Interstate Renewable Energy Council, 2009.

[77] G. Antonova, M. Nardi, A. Scott, and M. Pesin, "Distributed Generation and Its Impact on Power Grids and Microgrids Protection," in *2012 65th Annual Conference for Protective Relay Engineers*, College Station, TX, 2-5 April 2012.

[78] New York Independent System Operator, "Distributed Energy Resources Roadmap for New York's Wholesale Electricity Markets," New York ISO, New York, January 2017.

[79] New York Independent System Operator, "Distributed Energy Resources Market Design Concept Proposal," New York ISO, New York, December 2017.

[80] A. H. Nerad, "Distributed Power Generation to Counter Grid Vulnerability," U.S. Army War College, Strategy Research Project, Carlisle Barracks,Carlisle,PA 17013, 2007.

[81] L. Milford, R. O'Meara-Costello, "Distributed Power Generation for Homeland Security: Proposal for a New Federal and State Partnership," Clean Energy Group Inc., Montpelier, VT, 2003.

[82] U.S. Department of Energy, "The Potential Benefits of Distributed Generation and Rate-Related Issues That May Impede Their Expansion a Study Pursuant to Section 1817 of The Energy Policy Act of 2005," U.S. Department of Energy, February 2007.

[83] T. D. Hund, S. Gonzalez, and K. Barrett, "Grid-Tied PV System Energy Smoothing," IEEE, 2010.

[84] D. M. Rose, B. Schenkman, and D. Borneo, "Test Report: GS Battery, EPC Power HES RESCU, SAND 2013-8849," Sandia National Laboratories, Albuquerque, New Mexico, 2013.

[85] U.S. Department of Energy, Sandia National Labratories, and Clean Energy States Alliance, "State of the U.S. Energy Storage Industry: 2017 Year in Review," in *Energy Storage Technology Advancement Partnership (ESTAP) Webinar:*, online, February 13, 2018.

[86] National Hydropower Association, "2018 Pumped Storage Report," National Hydropower Association, 601 New Jersey Ave NW, Suite 660; Washington, DC 20001, 2018.

[87] O. Lavrova, F. Cheng, S. Abdollahy, H. Barsun, A. Mammoli, D. Dreisigmayer, S. Willard, B. Arellano, and C. van Zeyl,, "Analysis of Battery Storage Utilization for Load Shifting and Peak Smoothing on a Distribution Feeder in New Mexico,," *Innovative Smart Grid Technologies (ISGT), 2012 IEEE PES,* pp. 1-6, 2012.

[88] J. W. Smith, R. Dugan, M. Rylander, and T. Key, "Advanced Distribution Planning Tools for High Penetration PV Deployment," in *2012 IEEE Power and Energy Society General Meeting*, San Diego, CA, USA, 22-26 July 2012.

[89] R. H. Byrne, R. J. Concepcion, and C. A. Silva-Monroy, "Estimating Potential Revenue from Electrical Energy Storage in PJM," in *2016 IEEE Power and Energy Society General Meeting (PESGM)*, Boston, MA, USA, 17-21 July 2016.

[90] T. D. Hund, S. Gonzalez, and K. Barrett, "Grid-Tied PV system energy smoothing," in *Photovoltaic Specialists Conference (PVSC)*, Honolulu, HI, 2010.

[91] F. Cheng, S. Willard, J. Hawkins, B. Arellano, O. Lavrova, A. Mammoli, "Applying Battery Energy Storage to Enhance the Benefits of Photovoltaics," in *2012 IEEE Energytech*, Cleveland, OH, USA, 29-31 May 2012.

[92] F. Cheng, W. Greenwood, B. Arellano, J. Hawking, O. Lavrova, and A. Mammoli, "Real-Time Control of Utility-Scale Storage on a Distribution Feeder," *Energytech, 2013 IEEE,* pp. 1-5, 2013.

[93] A. Ellis, D. Schoenwald, J. Hawkins, S. Willard, and B. Arellano, "SAND2012-6745, PV Power Output Smoothing using Energy Storage," Sandia National Laboratories, Albuquerque, NM, Printed August 2012.

[94] Public Service Company of New Mexico, "PNM Prosperity Energy Storage," PNM Resources, Albuquerque, NM, 2013.

[95] S. Willard, "Smart Grid Demonstration Project; PV Plus Battery for Simultaneous Voltage Smoothing and Peak Shifting," Public Service Company of New Mexico, Albuquerque, NM, 2012.

[96] A. Mammoli, C. Birk Jones, H. Barsun, D. Dreisigmeyer, G. Goddard, and O. Lavrova,, "Distributed control strategies for high-penetration commercial-

building-scale thermal storage," in *IEEE-PES T&D 2012 CONFERENCE*, 2012.

[97] A. Mammoli, H. Barsun, R. Burnett, J. Hawkins and J. Simmins, "Using high-speed demand response of building HVAC systems to smooth cloud-driven intermittency of distributed solar photovoltaic generation," in *IEEE-PES T&D 2012 CONFERENCE*, 2012.

[98] D. Lincoln, C. Evans, "Demand Response Pilot Events, Conducted August 25, 2011 and August 9, 2012, Summary Report," Sandia National Laboratories, SAND2012-10323, Albuquerque, NM, 2012.

[99] B. Sarlati, "Smoothing PV output fluctuation using cooling fan," Thesis, University of New Mexico Digital Repository, Albuquerque, NM, 6-26-2015.

[100] R. Blaga, A. Sabadus, N. Stefu, C. Dughir, M. Paulescu, and V. Badescu, "A current perspective on the accuracy of incoming solar energy forecasting," *Progress in Energy and Combustion Science,* vol. 70, pp. 119-144, 2019.

[101] P. Srikanth, "Statistical Learning vs Machine Learning," [Online]. Available: https://medium.com/data-science-analytics/statistical-learning-vs-machine-learning-f9682fdc339f. [Accessed 24 9 2019].

[102] S. Haykin, Neural Networks and Learning Machines, 3rd edition (ISBN 978-0-13-147139-9), Pearson Education, Inc., 2009.

[103] M. Brabec, M. Paulescu, and V. Badescu, "Generalized additive models for nowcasting cloud shading," *Solar Energy,* vol. 101, p. 272–282, 2014.

[104] R. Chauvin, J. Nou, S. Thil, and S. Grieu, "Generating high dynamic range images using sky images," in *IFAC Confrence*, online, 2017.

[105] J. Nou, R. Chauvin, J. Eynard, S. Thil, and S. Grieu, "Towards the intrahour forecasting of direct normal irradiance using sky-imaging data," *Heliyon 4, e00598,* 2018.

[106] M. Caldas and R. Alonso-Suarez , "Very short-term solar irradiance forecast using all-sky imaging and real-time irradiance measurements," *Renewable Energy,* vol. 143, pp. 1643-1658, December 2019.

[107] B. Elsinga and W. G. J. H. M. van Sark, "Short-term peer-to-peer solar forecasting in a network of photovoltaic Systems," *Applied Energy,* vol. 206, p. 1464–1483, 2017.

[108] C. Fu and H. Cheng, "Predicting solar irradiance with all-sky image features via regression," *Solar Energy,* vol. 97, p. 537–550, 2013.

[109] E. B. Iversen, J. M. Morales, J. K. Møller, and H. Madsen, "Probabilistic Forecasts of Solar Irradiance by Stochastic Differential Equations," *Environmetrics,* no. arXiv:1310.6904v1, September 26, 2018.

[110] V. Bone, J. Pidgeon, M. Kearney, and A. Veeraragavan, "Intra-hour direct normal irradiance forecasting through adaptive clear-sky modelling and cloud tracking," *Solar Energy,* vol. 159, p. 852–867, 2018.

[111] D. Torregrossa, J. L. Boudec, and M. Paolone, "Model-free computation of ultra-short-term prediction intervals of solar irradiance," *Solar Energy,* vol. 124, pp. 57-67, 2016.

[112] Z. Dong, D. Yang, T. Reindl, and W. M. Walsh, "Satellite image analysis and a hybrid ESSS/ANN model to forecast solar irradiance in the tropics," *Energy Conversion and Management,* vol. 79, pp. 66-73, 2014.

[113] D. Yang, Z. Ye, L. H. I. Lim, and Z. Dong, "Very short term irradiance forecasting using the lasso," *Solar Energy,* vol. 114, pp. 314-326, 2015.

[114] Y. Chu, B. Urquhart, S. M. I. Gohari, H. T. C. Pedro, J. Kleissl, and C. F. M. Coimbra, "Short-term reforecasting of power output from a 48 MWe solar PV plant," *Solar Energy,* vol. 112, pp. 68-77, 2015.

[115] G. Reikard and C. Hansen, "Forecasting solar irradiance at short horizons: Frequency and time domain models," *Renewable Energy,* vol. 135, pp. 1270-1290, 2019.

[116] C. Feng, M. Cui, B. Hodge, S. Lu, H. F. Hamann, and J. Zhang, "An Unsupervised Clustering-Based Short-Term Solar Forecasting Methodology

Using Multi-Model Machine Learning Blending," *Transactions on Sustainable Energy,* 2018.

[117] A. K. Barnes, J. C. Balda, and J. K. Hayes, "Storage, Modelling PV Clouding Effects Using a Semi-Markov Process with Application to Energy," in *The 19th World Congress International Federation of Automatic Control*, Cape Town, South Africa, August 24-29, 2014.

[118] D. Bernecker, C. Riess, E. Angelopoulou, and J. Hornegger, "Continuous short-term irradiance forecasts using sky images," *Solar Energy,* vol. 110, pp. 303-315, 2014.

[119] V. P. A. Lonij, A. E. Brooks, A. D. Cronin, M. Leuthold, and K. Koch, "Intra-hour forecasts of solar power production using measurements from a network of irradiance sensors," *Solar Energy,* vol. 97, pp. 58-66, 2013.

[120] A. T. Lorenzo, W. F. Holmgren, A. D. Cronin, "Irradiance forecasts based on an irradiance monitoring network, cloud motion, and spatial averaging," *Solar Energy,* vol. 122, pp. 1158-1169, December 2015.

[121] D. Bernecker, C. Riess, E. Angelopoulou, and J. Hornegger, "Continuous short-term irradiance forecasts using sky images," *Solar Energy,* vol. 110, pp. 303-315, 2014.

[122] T. P. Caudell and S. D. G Smith, "A data compressed ART-1 neural network algorithm (group technology application)," in *International Joint Conference on Neural Networks*, Seattle, WA, USA, 8-12 July 1991.

[123] M. J. Healy and T. P. Caudell, "A categorical semantic analysis of ART architectures," in *Neural Networks, 2001*, Washington, DC, USA, 2001.

[124] M. J. Healy, R. D. Olinger, R. J. Young, T. P. Caudell, and K. W. Larson, "Modification of the ART-1 architecture based on category theoretic design principles," in *2005 IEEE International Joint Conference on Neural Networks*, Montreal, Que., Canada, 31 July-4 Aug. 2005.

[125] H. T. C. Pedro and C. F. M. Coimbra, "Short-term irradiance forecastability for various solar micro-climates," *Solar Energy,* vol. 122, pp. 587-602, 2015.

[126] G. A. Licciardi, R. Dambreville, J. Chanussot, and S. Dubost, "Spatiotemporal Pattern Recognition and Nonlinear PCA for Global Horizontal Irradiance Forecasting," *IEEE Geoscience and Remote Sensing Letters,* vol. 12, no. 2, 2015.

[127] Y. Chu, M. Li, H. Pedro, and C. Coimbra, "Real-time prediction intervals for intra-hour DNI forecasts," *Renewable Energy,* vol. 83, pp. 234-244, 2015.

[128] Y. Chu, M. Li, and C. Coimbra, "Sun-tracking imaging system for intra-hour DNI forecasts," *Renewable Energy,* vol. 96, pp. 792-799, 2016.

[129] Y. Chu, M. Li, H. Pedro, and C. Coimbra, "Real-time forecasting of solar irradiance ramps with smart image processing," *Solar Energy,* vol. 114, pp. 91-104, 2015.

[130] F. Wang, Z. Mi, S. Su, and H. Zhao, "Short-Term Solar Irradiance Forecasting Model Based on Artificial Neural Network Using Statistical Feature Parameters," *Energies,* vol. 5, no. doi:10.3390/en5051355, pp. 1355-1370, 2012.

[131] A. Ryu, M. Ito, H. Ishii, and Y. Hayashi, "Preliminary Analysis of Short-term Solar Irradiance Forecasting by using Total-sky Imager and Convolutional Neural Network," *Proceedings of the 2019 IEEE PES GTD Asia,* no. 978-1-5386-7434-5/19, 2019.

[132] S. Tiwari, R. Sabzehgar, and M. Rasouli, "Short Term Solar Irradiance Forecast based on Image Processing and Cloud Motion Detection," *IEEE,* no. 978-1-5386-9284-4/19, 2019.

[133] H. Cheng and C. Yu, "Multi-model solar irradiance prediction based on automatic cloud classification," *Energy,* vol. 91, pp. 579-587, 2015.

[134] C. Feng, M. Cui, M. Lee, J. Zhang, B. Hodge, S. Lu, and H. F. Hamann, "Short-term Global Horizontal Irradiance Forecasting Based on Sky Imaging and Pattern Recognition," *IEEE,* no. 978-1-5386-2212-4/17, 2017.

[135] J. O. Kamadinata, T. L. Ken, and T. Suwa, "Sky image-based solar irradiance prediction methodologies using artificial neural networks," *Renewable Energy,* vol. 134, pp. 837-845, 2019.

[136] L. Kaiju, L. Xuefeng, M. Chaoxu, and W. Dan, "Short-Term Photovoltaic Power Prediction Based on T-S Fuzzy Neural Network," in *The 33rd Youth Academic Annual Conference of Chinese Association of Automation*, Nanjing, China, May 18-20, 2018.

[137] J. Nou, R. Chauvin, J. Eynard, and S. Grieu, "Towards the short-term forecasting of direct normal irradiance using a sky imager," *International Federation of Automatic Control PapersOnLine 50-1,* vol. 50, no. 1, p. 14137–14142, 2017.

[138] T. J. Ross, Fuzzy Logic With Engineering Applications, Second Ed., John Wiley & Sons Ltd, The Atrium, Southern Gate, Chichester, West Sussex PO19 8SQ, England, 2004.

[139] T. Ahmad and H. Chen, "Deep learning for multi-scale smart energy forecasting," *Energy,* vol. 175, pp. 98-112, 175.

[140] T. A. Siddiqui, S. Bharadwaj, and S. Kalyanaraman, "A deep learning approach to solar-irradiance forecasting in sky-videos," Cornell University, Ithaca, New York, Jan. 2019.

[141] F. Rodríguez, A. Fleetwood, A. Galarza, and L.Fontan, "Predicting solar energy generation through artificial neural networks using weather forecasts for microgrid control," *Renewable Energy,* vol. 126, pp. 855-864, 2018.

[142] D. Oian, D. Shan-Xu, and C. Tao, "Short-term PV generation system fore casting model without irradiation based on weather type clustering.," *Proceedings of the CSEE,* vol. 31, pp. 28-35, 2011.

[143] H. T. C. Pedro and C. F. M. Coimbra, "Nearest-neighbor methodology for prediction of intra-hour global horizontal and direct normal irradiances," *Renewable Energy,* vol. 80, pp. 770-782, 2015.

[144] Y. Chu and C. F. M. Coimbra, "Short-term probabilistic forecasts for Direct Normal Irradiance," *Renewable Energy,* vol. 101, pp. 526-536, 2017.

[145] H. T. C. Pedro, C. F. M. Coimbra, M. David, and P. Lauret, "Assessment of machine learning techniques for deterministic and probabilistic intra-hour solar forecasts," *Renewable Energy,* vol. 123, pp. 191-203, 2018.

[146] E. Scolari, D. Torregrossa, J. Y. Le Boudec, and M. Paolone, "Ultra-Short-Term Prediction Intervals of Photovoltaic AC Active Power," Ecole Polytechnique Federale de Lausanne (EPFL), Lausanne, Switzerland, 2016.

[147] M. André, R. Perez, T. Soubdhan, J. Schlemmer, R. Calif, and S. Monjoly, "Preliminary assessment of two spatio-temporal forecasting technics for

hourly satellite-derived irradiance in a complex meteorological context," *Solar Energy,* vol. 177, pp. 703-712, 2019.

[148] R. Marquez and C. F. M. Coimbra, "Intra-hour DNI forecasting based on cloud tracking image analysis," *Solar Energy,* vol. 91, pp. 327-336, 2013.

[149] D. Yuyu, C. Xu, C. Fang, Z. Xiang, and Z. Hai, "Very-Short Term Forecast of Global Horizontal Irradiance Based on Ground-based sky imager and Lifted Condensation Level Calculation," in *China International Conference on Electricity Distribution (CICED 2014)*, Shenzen, 2014.

[150] H. Zhang, C. Zhang, and W. Li, "Short-term DNI Forecasting using Cloud History Patterns Matching," in *Seventh International Conference on Information Science and Technology*, Da Nang, Vietnam, April 19-19, 2017.

[151] C. W. Chow, B. Urquhart, M. Lave, A. Dominguez, J. Kleissl, J. Shields, and B. Washom, "Intra-hour forecasting with a total sky imager at the UC San Diego solar energy testbed," *Solar Energy,* vol. 85, pp. 2881-2893, 2011.

[152] P. Pawar, C. Cortés, K. Murray, and J. Kleissl, "Detecting clear sky images," *Solar Energy,* vol. 183, pp. 50-56, 2019.

[153] M. I. Gohari, B. Urquhart, H. Yang, B. Kurtz, D. Nguyen, C. W. Chow, M. Ghonima, and J. Kleissl, "Comparison of solar power output forecasting

performance of the Total Sky Imager and the University of California, San Diego Sky Imager," *Energy Procedia,* vol. 49, pp. 2340-2350, 2014.

[154] Yankee Environmental Systems, Inc., *BULLETIN TSI-440B,* Turner Falls, MA: Yankee Environmental Systems, Inc., 2003.

[155] W. Richardson, H. Krishnaswami, R. Vega, and M. Cervantes, "A Low Cost, Edge Computing, All-Sky Imager for Cloud Tracking and Intra-Hour Irradiance Forecasting," *Sustainability,* vol. 9, 2017.

[156] Y. Chu, H. T. C. Pedro, and C. F. M. Coimbra, "Hybrid intra-hour DNI forecasts with sky image processing enhanced by stochastic learning," *Solar Energy,* vol. 98, pp. 592-603, 2013.

[157] J. Alonso and F. J. Batlles, "Short and medium-term cloudiness forecasting using remote sensing techniques and sky camera imagery," *Energy,* vol. 73, pp. 890-897, 2014.

[158] S. R. West, D. Rowe, S. Sayeef, and A. Berry, "Short-term irradiance forecasting using skycams: Motivation and development," *Solar Energy,* vol. 110, pp. 188-207, 2014.

[159] J. Alonso-Montesinos, F. J. Batlles, and C. Portillo, "Solar irradiance forecasting at one-minute intervals for different sky conditions using sky

camera images," *Energy Conversion and Management,* vol. 105, pp. 1166-1177, 2015.

[160] H. Yang, B. Kurtz, D. Nguyen, B. Urquhart, C. W. Chow, M. Ghonima, and J. Kleissl, "Solar irradiance forecasting using a ground-based sky imager developed at UC San Diego," *Solar Energy,* vol. 103, pp. 502-524, 2014.

[161] EKO Instruments B.V., *New ASI-16 All-Sky Imager,* EKO Instruments B.V., 2017.

[162] D. Cañadillas, B. González-Díaz, J. Rodríguez, J. Rodríguez, and R. Guerrero-Lemus, "A low-cost two-camera sky-imager ground-based intra-hour solar forecasting system with cloud base height estimation capabilities working in a smart grid," in *2018 IEEE 7th World Conference on Photovoltaic Energy Conversion (WCPEC) (A Joint Conference of 45th IEEE PVSC, 28th PVSEC & 34th EU PVSEC*, Waikoloa, Hawaii, 2018.

[163] B. Nouri, S. Wilberta, L. Segura, P. Kuhn, N. Hanrieder, A. Kazantzidis, T. Schmidt, L. Zarzalejo, P. Blanc, and R. Pitz-Paal, "Determination of Cloud Transmittance for All Sky Imager Based Solar Nowcasting," *Solar Energy,* vol. 181, pp. 251-263, 2019.

[164] C. W. Chow, S. Belongie, and J. Kleissl, "Cloud motion and stability estimation for intra-hour solar forecasting," *Solar Energy,* vol. 115, pp. 645-655, 2015.

[165] C. Zhang, Y. Du, X. Chen, and E. G. Lim, "Cloud Motion Forecasting and Cloud Base Height Estimation Using Two Low-Cost Sky Cameras," in *2nd IEEE Conference on Energy Internet and Energy System Integration (EI2)*, Beijing, China, 20-22 Oct. 2018.

[166] D. M. L. H. Dissawa, M. P. B. Ekanayake, G. M. R. I. Godaliyadda, J. B. Ekanayake, and A. P. Agalgaonkar, "Cloud Motion Tracking for Short-Term On-Site Cloud Coverage Prediction," *2017 International Conference on Advances in ICT for Emerging Regions (ICTer),* pp. 332 - 337, 2017.

[167] M. J. Espinosa-Gavira, A. Agüera-Pérez, J. J. González de la Rosa, J. C. Palomares-Salas, and J. M. Sierra-Fernández, "An On-Line Low-Cost Irradiance Monitoring Network with Sub-Second Sampling Adapted to Small-Scale PV Systems," *Sensors,* vol. 18, p. 3405, 2018.

[168] R. J. Bessa, A. Trindade, A. Monteiro, V. Miranda, and C. S. P. Silva, "Solar Power Forecasting in Smart Grids Using Distributed Information," Institute for Systems and Computer Engineering, Technology and Science -Faculty of Engineering, University of Porto, Porto, Portugal, 2014.

[169] A. T. Lorenzo, W. F. Holmgreny, M. Leutholdz, C. K. Kimz, A. D. Croniny, and E. A. Bettertonz, "Short-Term PV Power Forecasts Based on a Real-Time Irradiance Monitoring Network," in *40th IEEE Photovoltaic Specialist Conference, PVSC 2014; Institute of Electrical and Electronics Engineers Inc.*, Denver, United States, 2014.

[170] J. L. Bosch, Y. Zheng, and J. Kleissl, "Deriving cloud velocity from an array of solar radiation measurements," *Solar Energy,* vol. 87, pp. 196-203, 2013.

[171] R. J. Bessa, A. Trindade, C. S. P. Silva, and V. Miranda, "Probabilistic solar power forecasting in smart grids using distributed information," *Electrical Power and Energy Systems,* vol. 72, pp. 16-23, 2015.

[172] J. S. Sánchez-García, E. Espinosa-Juárez, and J. J. Flores, "Short Term Photovoltaic Power Production Using a Hybrid of Nearest Neighbor and Artificial Neural Networks," in *2016 IEEE PES Transmission & Distribution Conference and Exposition*, Morelia, Mexico, 2016.

[173] J. Huang and R. J. Davy, "Predicting intra-hour variability of solar irradiance using hourly local weather forecasts," *Solar Energy,* vol. 139, pp. 633-639, 2016.

[174] C. Chen and U. T. Kartini, "k-Nearest Neighbor Neural Network Models for Very Short-Term Global Solar Irradiance Forecasting Based on Meteorological Data," *Energies,* vol. 10, pp. 186;1-18, 2017.

[175] F. J. Batllesa, J. Alonso, and G. López, "Cloud cover forecasting from METEOSAT data," *Energy Procedia,* vol. 57, pp. 1317-1326, 2014.

[176] P. Mathiesen, C. Collier, and J. Kleissl, "A high-resolution, cloud-assimilating numerical weather prediction model for solar irradiance forecasting," *Solar Energy,* vol. 92, pp. 47-61, 2013.

[177] A. Tascikaraoglu, B. M. Sanandaji, G. Chicco, V. Cocina, F. Spertino, O. Erdinc, N. G. Paterakis, and J. P. S. Catalao, "A Short-Term Spatio-Temporal Approach for Photovoltaic Power Forecasting," in *2016 Power Systems Computation Conference (PSCC)*, Genoa, Italy, 2016.

[178] S. Tiwariy, R. Sabzehgary, and M. Rasouli, "Short Term Solar Irradiance Forecast Using Numerical Weather Prediction (NWP) with Gradient Boost Regression," in *IEEE 9th International Symposium on Power Electronics for Distributed Generation*, 2018.

[179] J. Huang and M. Thatcher, "Assessing the value of simulated regional weather variability in solar forecasting using numerical weather prediction," *Solar Energy,* vol. 144, pp. 529-539, 2017.

[180] S. D. Millera, M. A. Rogersa, J. M. Haynesa, M. Senguptab, A. K. Heidinger, "Short-term solar irradiance forecasting via satellite/model coupling," *Solar Energy,* vol. 168, pp. 102-117, 2018.

[181] S. Devy, T. AlSkaify, M. Hossari, R. Godina, A. Louwen, and W. V. Sark, "Solar Irradiance Forecasting Using Triple Exponential Smoothing," in *2018 International Conference on Smart Energy Systems and Technologies (SEST)*, Sevilla, Spain, 2018.

[182] P. S. Loh, J. V. Chua, A. C. Tan, and C. I. Khaw, "Data-driven short-term forecasting of solar irradiance profile," *Energy Procedia,* vol. 143, pp. 572-578, 2017.

[183] H. Bouzgou and C. A. Gueymard, "Fast short-term global solar irradiance forecasting with wrapper mutual information," *Renewable Energy,* vol. 133, pp. 1055-1065, 2019.

[184] M. Jamaly and J. Kleissl, "Robust cloud motion estimation by spatio-temporal correlation analysis of irradiance data," *Solar Energy,* vol. 159, pp. 306-317, 2018.

[185] B. Kurtz, F. Mejia, and J. Kleissl, "A virtual sky imager testbed for solar energy forecasting," *Solar Energy,* vol. 158, pp. 753-759, 2017.

[186] D. Arpit, S. Jastrzębski, N. Ballas, D. Krueger, E. Bengio, M. S. Kanwal, T. Maharaj, A. Fischer, A. Courville, Y. Bengio, and S. Lacoste-Julien, "A Closer Look at Memorization in Deep Networks," in *Thirty-fourth International Conference on Machine Learning*, International Convention Centre, Sydney AUSTRALIA, 2017, Sun Aug 6th to Fri the 11th.

[187] C. Zhang, S. Bengio, M. Hardt, B. Recht, O. Vinyals, "Understanding Deep Learning Requires Re-Thinking Generalization," in *International Conference on Learning Representations*, Toulon, France, April 24 - 26, 2017.

[188] G. p. Plato, Writer, *Allegory of the Cave (Plato's Cave).* [Performance]. 514–520 AD.

[189] G. A. Carpenter, S. Grossberg, "A Massively Parallel Architecture for a Self-Organizing Neural Pattern Recognition Machine," *Computer Vision, Graphics, and Image Proceedings,* vol. 37, pp. 54-115, 1987.

[190] G. A. Carpenter and S. Grossberg, "Adaptive resonance Theory," MIT Press, Cambridge, Massachusetts, Revised: April, 2002.

[191] S. Grossberg, "Adaptive Resonance Theory: How a brain learns to consciously attend, learn, and recognize a changing world," *Neural Networks,* vol. 37, pp. 1-47, 2013.

[192] G. A. Carpenter and S. Grossberg, "ART 2: self-organization of stable category recognition codes for analog input patterns," *APPLIED OPTICS,* vol. 26, no. 23, pp. 4919-4930, 1987.

[193] B. Moore, "ART 1 and Pattern Clustering," in *1988 Connectionist Summer School*, 1988/08/01.

[194] M. J. Healy, R. D. Olingert, R. J. Young, T. P. Caudell, and K. W. Larson, "Modification of the ART-1 Architecture Based on Category Theoretic Design Principles," in *Proceedings of International Joint Conference on Neural Networks*, Montreal, Canada, July 31 - August 4, 2005.

[195] G. A. Carpenter, S. Grossberg, and D. B. Rosen, "Fuzzy ART: Fast Stable Learning and Categorization of Analog Patterns by an Adaptive Resonance System," *Neural Networks,* vol. 4, pp. 759-771, 1991.

[196] G. A. Carpenter, S. Grossberg, N. Markuzon, J. H. Reynolds, and D. B. Rosen, "Fuzzy ARTMAP: A Neural Network Architecture for Incremental Supervised Learning of Analog Multidimensional Maps," *TRANSACTIONS ON NEURAL NETWORKS,* vol. 3, pp. 698-713, 1992.

[197] T. P. Caudell and M. J. Healy, "Studies of inference rule creation using LAPART," in *Proceedings of IEEE 5th International Fuzzy Systems*, Sept. 1996.

[198] M. J. Healy, T. P. Caudell, and S. D. G. Smith, "A Neural Architecture for Pattern Sequence Verification Through Inferencing," *IEEE Transactions on Neural Networks,* vol. 4, no. 1, pp. 9-20, Jan 1993.

[199] M. J. Healy and T. P. Caudell, "Acquiring Rule Sets as a Product of Learning in a Logical Neural Architecture," *IEEE Transactions on Neural Networks,* vol. 8, no. 3, pp. 461-474, May 1997.

[200] G. Han, F. M. Ham, and L. V. Fausett, "Fuzzy Lapart Supervised Learning Through Inferencing For Stable Category Recognition," in *Proceedings of IEEE 5th International Fuzzy Systems*, New Orleans, LA, USA, June 26 - June 29,1994.

[201] T. P. Caudell and M. J. Healy, "Guaranteed Two-Pass Convergence for Supervised and Inferential Learning," *IEEE Transactions on Neural Networks,* vol. 9, no. 1, pp. 195-204, Jan. 1998.

[202] N. Blanc, D. Fisher and R. Spiller, "CCD vs CMOS - has CCD imaging come to an end?," *Photogrammetric Week 01,* pp. 131-137, 2001.

[203] A. Steele, *Sunscreen on back under normal and UV light.jpg,* https://commons.wikimedia.org/wiki/File:Sunscreen_on_back_under_normal_and_UV_light.jpg: Creative Commons CC0 1.0 Universal, 8 June 2013, 14:26.

[204] David, *File:Infrared HDR Palmer Park Colorado Springs.jpg,* Creative Commons Attribution 2.0 Generic, https://commons.wikimedia.org/wiki/ File:Infrared_HDR_Palmer_ Park_Colorado_Springs.jpg, 11 April 2010, 08:53.

[205] Life Pixel Infrared, "Infrared, UV & Forensic Photo Galleries; Infrared Photography Gallery & Ultraviolet Photography Gallery," LifePixel Infrared Photography IR Conversion, Modification & Scratched Sensor Repair, 16 October 2019. [Online]. Available: https://www.lifepixel.com/galleries. [Accessed 16 October 2019].

[206] A. R. Menicucci, T. P. Caudell, and A. A. Mammoli, "Apparatus and Method for Solar Energy Resource Micro-Forecasts For Solar Generation Sources and Utilities," U.S. Patent 9,921,339, 20 Mar., 2018.

[207] A. R. Menicucci, T. P. Caudell, and A. A. Mammoli, "Apparatus and Method for Solar Energy Micro-Forecasts for Solar Generation Sources and Utilities," U.S. Patent 10,345,486, 19 July., 2019.

[208] G. Wilensky, *Analysis of neural network issues: Scaling, enhanced nodal processing, comparison with standard classification,* DARPA Neural Network Program Review, Oct. 29-30, 1990.

[209] "Community Building and Natural Law," TransForm/Place, [Online]. Available: https://transformplace.org/community-building-and-natural-law/. [Accessed 20 03 2020].

[210] W. Thielicke and E. J. Stamhuis, "PIVlab – Towards User-friendly, Affordable and Accurate Digital Particle Image Velocimetry in MATLAB," *Journal of Open Research Software 2(1):e30, DOI: http://dx.doi.org/10.5334/jors.bl,* 2018.

[211] National Oceanic and Atmospheric Administration, "Aviation Weather Center," United States Department of Commerce, 2020. [Online]. Available: https://aviationweather.gov/metar/data?ids=KDEN&format=decoded&date=&hours=0. [Accessed 27 04 2020].

[212] V. de Bruyn, "le guide d'identification des nuages," Creative Commons Attribution-Share Alike 3.0 Unported, 12 January 2012. [Online]. Available: https://commons.wikimedia.org/wiki/File:Cloud_types_en.svg. [Accessed 22 03 2020].

[213] Fortune.com, "A Jaw-Dropping World Record Solar Price Was Just Bid in Abu Dhabi," [Online]. Available: http://fortune.com/2016/09/19/ world-record-solar-price-abu-dhabi/. [Accessed 19 May 2019].

[214] dieselgasturbine.com, "GE Cites Oxidation Problem In New HA Turbine," [Online]. Available: https://dieselgasturbine.com/ ge-cites-oxidation-problem-in-new-ha-turbine/. [Accessed 19 May 2019].

[215] The Wall Street Journal, "Is It Time to Deregulate All Electric Utilities?," *The Wall Street Journal,* 13 November 2016.

# Appendices

## Appendix A Relevant Search Terms for SIMF and Irradiance Forecasting

1. solar irradiance forecasts
2. solar forecasts
3. solar micro forecasts
4. hourly forecast
5. short term irradiance
6. intra-hour
7. very short-term solar forecasting
8. Very short term forecasting of the Global Horizontal Irradiance
9. short term forecast irradiance
10. Helioclim maps
11. Lucas Kanal
12. Gunnar Farneback  cross correlation wiki Implement in Fourier
13. Robust cloud motion

## Appendix B PIVLab Settings

The motivation for accurate cloud geometries was highlighted in the need for accurate velocity measurements. With accurate velocities, data can then be reduced, which also reduces the processing power required to make predictions. Velocities measurements were calculated with PIVLab 2.01. A list of all setting used is shown below in Table 10-1 for reference.

| **PIVLab Settings** | |
|---|---|
| Image Preporcessing CLAHE window size | 20 |
| FFT window | yes |
| Interrogation area | 40 |
| interrogation area Step | 30 |
| interrogation area Step, Pass 2 | 20 |
| interrogation area Step, Pass 3 | 15 |
| window deformation | SPLINE |
| sub-pixel | 2D Gauss |
| 5X repeated coorelation | yes |
| disable auto coorelation | yes |
| Post Processing, STD Dev. | 1.5 |

Table 10-1. Table of PIVLab 2.01 setting used by category.

## Appendix C Data Collection of Dates And Times Of Test

| Folder Name | Start Number | Finish Number | Total # samples | Total Time, Hours |
|---|---|---|---|---|
| 20180331_Anthony_A_Boulder | 0 | 715 | 715 | 1.99 |
| 20180331_Anthony_B_Boulder | 0 | 715 | 715 | 1.99 |
| 20180402_Anthony_B_Boulder | 0 | 1795 | 1795 | 4.99 |
| 20180404_Anthony_A_Boulder | 0 | 835 | 835 | 2.32 |
| 20180409_Anthony_B_Boulder | 0 | 1000 | 1000 | 2.78 |
| 20180410_Anthony_B_Boulder | 0 | 1075 | 1075 | 2.99 |
| 20180416_Anthony_A_Boulder | 0 | 1075 | 1075 | 2.99 |
| 20180418_Anthony_A_Boulder | 0 | 1075 | 1075 | 2.99 |
| 20180418_Anthony_B_Boulder | 0 | 1075 | 1075 | 2.99 |
| 20180419_Anthony_A_Boulder | 100 | 1075 | 975 | 2.71 |
| 20180419_Anthony_B_Boulder | 5 | 1075 | 1070 | 2.97 |
| 20180425_Anthony_A_Boulder | 300 | 1075 | 775 | 2.15 |
| 20180425_Anthony_B_Boulder | 0 | 1075 | 1075 | 2.99 |
| 20180426_Anthony_A_Boulder | 0 | 1075 | 1075 | 2.99 |
| 20180428_Anthony_A_Boulder | 0 | 1435 | 1435 | 3.99 |
| 20180430_Anthony_A_Boulder | 0 | 1430 | 1430 | 3.97 |
| 20180501_Anthony_A_Boulder | 0 | 770 | 770 | 2.14 |
| 20180504_Anthony_A_Boulder | 300 | 1795 | 1495 | 4.15 |
| 20180504_Anthony_B_Boulder | 0 | 1435 | 1435 | 3.99 |
| 20180505_Anthony_A_Boulder | 100 | 1615 | 1515 | 4.21 |
| 20180507_Anthony_A_Boulder | 500 | 2155 | 1655 | 4.60 |
| 20180509_Anthony_A_Boulder | 0 | 2155 | 2155 | 5.99 |
| 20180510_Anthony_A_Boulder | 0 | 2155 | 2155 | 5.99 |
| | | | Total Hours: | 78.82 |

Table 10-2, Listing of all days and times for data collected in Boulder Co.